Universitat Autònoma de Barcelona

Departament de Bioquímica i Biologia Molecular
Institut de Biotecnologia i de Biomedicina

Modelos proteicos para el estudio de la agregación amiloide *in vitro* e *in vivo*

Alba Espargaró Colomé

2012

Universitat Autònoma de Barcelona

Departament de Bioquímica i Biologia Molecular
Institut de Biotecnologia i de Biomedicina

Modelos proteicos para el estudio de la agregación amiloide *in vitro* e *in vivo*

Tesis doctoral presentada por Alba Espargaró Colomé para el grado de doctor en Bioquímica y Biología Molecular por la Universitat Autònoma de Barcelona

Tesis realizada en el Departamento de Bioquímica y Biología Molecular y en el Institut de Biotecnologia i de Biomedicina bajo la supervisión de Dr. Salvador Ventura y Dr. Raimon Sabaté

Alba Espargaró Colomé

Dr. Salvador Ventura Dr. Raimon Sabaté

Cerdanyola del Vallès 2012

CONTENIDO

LISTA DE ARTÍCULOS. 1

ABREVIACIONES. 3

RESUMEN 4

INTRODUCCIÓN. 7

De la secuencia a la estructura: Plegamiento proteico. 7

Espacio conformacional. 8

Proteínas intrínsecamente desestructuradas (IDPs) 9

Agregación proteica y enfermedades humanas. 9

Mecanismo de formación de los agregados amiloides. 13

Seeding y especificidad secuencial. 16

Especies intermediarias durante la formación de fibras amiloides 17

Elementos determinantes de la agregación proteica 18

Propiedades intrínsecas 18

Propiedades extrínsecas. 19

Regiones determinantes de la agregación. 20

Estructuras amiloides funcionales. 21

Priones. 22

Agregación en células bacterianas: Cuerpos de inclusión (IBs). 24

Propiedades de los cuerpos de inclusión. 24

Calidad proteica y equilibrio dinámico con chaperonas. 26

Modelos proteicos utilizados para el estudio de la agregación *in vitro* e *in vivo*. . . . 28

DISCUSIÓN. 30

BLOQUE I. **Estudio de la agregación proteica *in* vitro. Propiedades biofísicas de las fibras amiloides**. 30

CAPÍTULO I: Efecto de la secuencia y la composición aminoacídica en la formación amiloide. 30

CAPÍTULO II: Efecto del micro-entorno en la formación de fibras amiloides. 33

BLOQUE II. **Estudio de la agregación proteica *in vivo*. Propiedades biofísicas de los cuerpos de inclusión**. 35

CONCLUSIONES. 40
REFERENCIAS. 43

BLOQUE I: Estudio de la agregación proteica *in vitro*. Propiedades Biofísicas de las fibras amiloides.

Capítulo I: Efecto de la secuencia y la composición aminoacídica en la formación amiloide.

- Artículo 1
- Artículo 2

Capítulo II: Efecto del micro-entorno en la formación de fibras amiloides.

- Artículo 3
- Artículo 4
- Artículo 5

BLOQUE II: Estudio de la agregación proteica *in vivo*. Propiedades biofísicas de los cuerpos de inclusión.

- Artículo 6
- Artículo 7
- Artículo 8
- Artículo 9

LISTA DE ARTÍCULOS

Esta tesis está basada en los siguientes artículos:

1. **Native structure protects SUMO proteins from aggregation into amyloid fibrils**
   Sabaté R, Espargaró A, Graña-Montes R, Reverter D, Ventura S
   Biomacromolecules, Jun 2012; 13(6):1916-1926

2. **The role of protein sequence and amino acid composition in amyloid formation: scrambling and backward reading of IAPP amyloid fibrils**
   Sabaté R, Espargaró A, de Groot NS, Valle-Delgado JJ, Fernàndez-Busquets X, Ventura S
   Journal Molecular Biology, Nov 2010; 404(2):337-352

3. **Energy barriers for HET-s prion forming domain amyloid formation**
   Sabaté R, Castillo V, Espargaró A, Saupe SJ, Ventura S
   FEBS Journal, Sep 2009; 276(18):5053-5064

4. **Temperature dependence of the aggregation kinetics of Sup35 and Ure2p yeast prions**
   Sabaté R, Villar-Piqué A, Espargaró A, Ventura S
   Biomacromolecules, Feb 2012;3(2):474-483

5. **Effect of the surface charge of artificial model membranes on the aggregation of amyloid β-peptide**
   Sabaté R, Espargaró A, Barbosa-Barros L, Ventura S, Estelrich J
   Biochimie, Aug 2012;94(8):1730-1738

6. **Kinetic and thermodynamic stability of bacterial intracellular aggregates**
   Espargaró A, Sabaté R, Ventura S
   FEBS Letters, Oct 2008;582(25-26):3669-3673

7. **Characterization of the amyloid bacterial inclusion bodies of the HET-s fungal prion**
   Sabaté R, Espargaró A, Saupe SJ, Ventura S
   Microbial Cell Factories, Oct 2009;8:56

8. **Yeast prions forms infectious amyloid inclusion bodies in bacteria**
   Espargaró A, Villar-Piqué A, Sabaté R, Ventura S
   Microbial Cell Factories, Jun 2012;11(1):89

9. **Thioflavin-S staining coupled to flow cytometry. A screening tool to detect *in vivo* protein aggregation**
   Espargaró A, Sabaté R, Ventura S
   Molecular Biosystems, Aug 2012

Otros artículos publicados por Alba Espargaró no presentados en esta tesis:

1. **Using bacterial inclusión bodies to screen for amyloid aggregation inhibitors**
   Villar-Piqué A, Espargaró A, Sabaté R, de Groot NS, Ventura S
   Microbial Cell Factories, May 2012;11(1):55

2. **Aggregation of the neuroblastoma-associated mutant (S120G) of the human nucleoside diphosphate kinase-A/NM23-H1 into amyloid fibrils**
   Georgescauld F, Sabaté R, Espargaró A, Ventura S, Chaignepain S, Lacombe ML, Lascu I
   Naunyn Schmiedeberg's Archives of Pharmacology, Oct 2011;384(4-5):373-381

3. **Bacterial inclusion bodies of Alzheimer's disease β-amyloid peptides can be employed to study native-like aggregation intermediate states**
   Dasari M, Espargaró A, Sabaté R, Lopez del Amo JM, Fink U, Grelle G, Bieschke J, Ventura S, Reif B
   Chembiochem, Feb 2011;12(3):407-423

4. **Deciphering the role of the thermodynamic and kinetic stabilities of SH3 domains on their aggregation inside bacteria**
   Castillo V, Espargaró A, Gordo V, Vendrell J, Ventura S
   Proteomics, Dec 2010;10(23:4172-4185

5. **Studies on bacterial inclusion bodies**
   De Groot NS, Espargaró A, Morell M, Ventura S
   Future Microbiology, Aug 2008;3(4):423-435

6. **Inclusion bodies: specificity in their aggregation process and amyloid-like structure**
   Morell M, Bravo R, Espargaró A, Sisquella X, Avilés FX, Fernàndez-Busquets X, Ventura S
   Biochimica et Bhiophysica Acta, Oct 2008;783(10):1815-1825

7. **The in vivo and in vitro aggregation properties of globular proteins correlate with their conformational stability: the SH3 case**
   Espargaró A, Castillo V, de Groot NS, Ventura S
   Journal Molecular Biology, May 2008;378(5):1116-1131

8. **Study and selection of in vivo protein interactions by coupling biomolecular fluorescence complementation and flow cytometry**
   Morell M, Espargaró A, Aviles FX, Ventura S
   Nature Protocols, 2008;3(1):22-33

9. **Detection of transient protein-protein interactions by bimolecular fluorescence complementation: the Abl-SH3 case**
   Morell M, Espargaró A, Aviles FX, Ventura S
   Proteomics, Apr 2008;7(7):1023-1036

ABREVIACIONES

Å	Armstrong
AFM	Microscopia de fuerza atómica
CD	Dicroísmo Circular
CJD	Enfermedad de Creutzfeldt-Jakob
CR	Rojo Congo
FT-IR	Espectroscopia infrarroja con transformada de Fourier
HS	Hot spot
Hsp	Proteínas de choque térmico
IAPP	Péptido amiloide de los islotes
IB	Cuerpo de inclusión
IDPs	Proteínas intrínsecamente desestructuradas
mRNA	Ácido ribonucleico mensajero
MS	Espectrometría de masas
NMR	Resonancia magnética nuclear
PK	Proteinasa K
PrP	Proteína priónica
PrP^{C}	Proteína priónica celular
PrP^{SC}	Proteína priónica Scarpie (Infecciosa)
ssNMR	Resonancia magnética nuclear en estado solido
TEM	Microscopia electrónica de transmisión
Th-S	Tioflavina S
Th-T	Tioflavina T
TSEs	Encefalopatías espongiformes transmisibles

RESUMEN

Durante los últimos años la agregación proteica se ha convertido en un tema de elevada importancia en biología, biotecnología y medicina. Un número creciente de evidencias demuestran fehacientemente que el mal plegamiento de proteínas y su agregación, muchas veces en forma de fibras amiloides, conlleva la formación de depósitos celulares insolubles que son los responsables finales de un creciente número de enfermedades humanas. Este tipo de enfermedades, agrupadas bajo el concepto de enfermedades conformacionales, engloban una gran diversidad de afecciones tanto neurodegenerativas como sistémicas de las que cabria destacar enfermedades con una gran relevancia socioeconómica como pueden ser la enfermedad de Alzheimer, Parkinson, Huntington o la diabetes tipo II entre otras.

La producción recombinante en células bacterianas de las proteínas implicadas en este tipo de enfermedades da lugar, muchas veces, a la formación de agregados proteicos, denominados cuerpos de inclusión (IBs), que obstaculizan la obtención de éstas en su forma nativa. Aunque inicialmente se creyó que estos IBs eran simplemente agregados de proteínas plegadas de forma amorfa a causa de interacciones básicamente hidrofóbicas, recientes estudios han demostrado que éstos están compuestos mayoritariamente por proteínas recombinantes producidas que agregan adquiriendo conformaciones amiloides similares a las obtenidas en humanos. Este hecho hace que el estudio de estos IBs bacterianos pueda ser de vital importancia para la comprensión de las enfermedades conformacionales en humanos.

Esta tesis está centrada en el estudio de los procesos de agregación proteica y en la caracterización de los agregados formados tanto *in vitro* como *in vivo* utilizando como modelo varias proteínas y péptidos sin ningún tipo de homología secuencial ni estructural en un intento de abarcar un amplio abanico conformacional que ilustre el universo conformacional de las proteínas.

Son muchos los factores, tanto intrínsecos como extrínsecos a la cadena polipeptídica, que pueden influir en el proceso de formación de fibras amiloides *in vitro*. El estudio de la influencia de estos determinantes nos permite conocer las interacciones que dirigen la deposición proteica y proponer posibles mecanismos de agregación. Los resultados obtenidos nos han permitido estudiar en detalle el efecto que tienen algunos de estos factores esenciales sobre la agregación proteica, y como su efecto puede variar dependiendo de las características conformacionales de las proteínas. El estudio del efecto de estos determinantes nos ha permitido obtener información sobre las interacciones moleculares que dirigen la formación

de las fibras amiloides y de los posibles mecanismos que pueden seguir las proteínas, inicialmente solubles, para adquirir la estructura común en hoja β altamente ordenada.

Puesto que las células procariotas se han convertido en sistemas sencillos pero fisiológicamente relevantes para el estudio de la formación de estos agregados, la segunda parte de esta tesis se ha centrado en el estudio biofísico *in vivo* de los agregados formados en el interior celular utilizando células procariotas como modelo. Los resultados obtenidos demuestran que las proteínas presentes en IBs bacterianos muestran estructuras amiloides comparables a las obtenidas tanto *in vitro* como en organismos eucariotas, y que los factores estudiados *in vitro* también pueden afectar, de forma similar, a la formación amiloide *in vivo*.

INTRODUCCIÓN

INTRODUCCIÓN

DE LA SECUENCIA A LA ESTRUCTURA: PLEGAMIENTO PROTEICO

Las proteínas, elementos esenciales para la vida de los organismos, actúan como piezas estructurales y son la maquinaria que ejecuta las funciones celulares. Su extraordinaria diversidad y versatilidad funcional viene determinada por el gran número de conformaciones que pueden adquirir.

Las proteínas son cadenas polipeptídicas sintetizadas en los ribosomas siguiendo las instrucciones genéticas codificadas en los mRNA y formadas por la unión, mediante enlaces peptídicos, de unidades repetitivas llamadas aminoácidos. La distribución de estos "bloques estructurales" dentro de la cadena polipeptídica se conoce como estructura primaria y determina no tan solo la estructura funcional de la proteína sino también el camino que debe seguir para adquirirla (Baker 2000).

El plegamiento proteico es el proceso por el cual una cadena polipeptídica, en condiciones fisiológicas, adquiere la estructura nativa tridimensional. Tal y como fue observado por Levinthal en 1968, si la adquisición de la estructura nativa se basara en una búsqueda aleatoria entre el número total de posibles conformaciones, el tiempo que necesitaría sería astronómico; sin embargo, paradójicamente, las proteínas pueden plegar en segundos (Levinthal 1968; Zwanzig, Szabo et al. 1992). Así pues, el plegamiento de una proteína debe seguir vías cinéticas preferenciales donde las interacciones nativas sean mucho más estables y persistentes que las no nativas, facilitando la obtención de la estructura de mínima energía. Estás vías preferenciales limitan el chequeo a un número mínimo de posibles conformaciones favoreciendo el paso del estado desplegado a la estructura nativa (Wolynes, Onuchic et al. 1995; Dinner, Sali et al. 2000; Dobson 2003).Durante el proceso de plegamiento tienen lugar una serie de interacciones intramoleculares entre los diferentes aminoácidos que forman la cadena polipeptídica para dar lugar a la formación de la estructura secundaria. Según las características químicas de las cadenas laterales cada aminoácido presenta una tendencia determinada a participar en las diferentes interacciones posibles, dirigiendo de esta manera la estructura que debe adoptar la cadena polipeptídica (Creighton 1993). Existen varias estructuras secundarias, desde estructuras regulares como hélices α y hojas o giros β, a estructuras irregulares desestructuradas. La combinación espacial de estos elementos estructurales da lugar a la estructura terciaria o también conocida como estado nativo. Las interacciones que mantienen esta conformación nativa permiten sutiles fluctuaciones

conformacionales, necesarias para que las proteínas puedan realizar sus funciones biológicas (Dobson 2003). En algunos casos, diversas estructuras terciarias pueden ensamblarse entre sí mediante interacciones intermoleculares dando lugar a la formación de complejos proteicos. Estos complejos, formados por unidades de una misma o diferentes proteínas, forman las estructuras conocidas como cuaternarias (**Figura 1**).

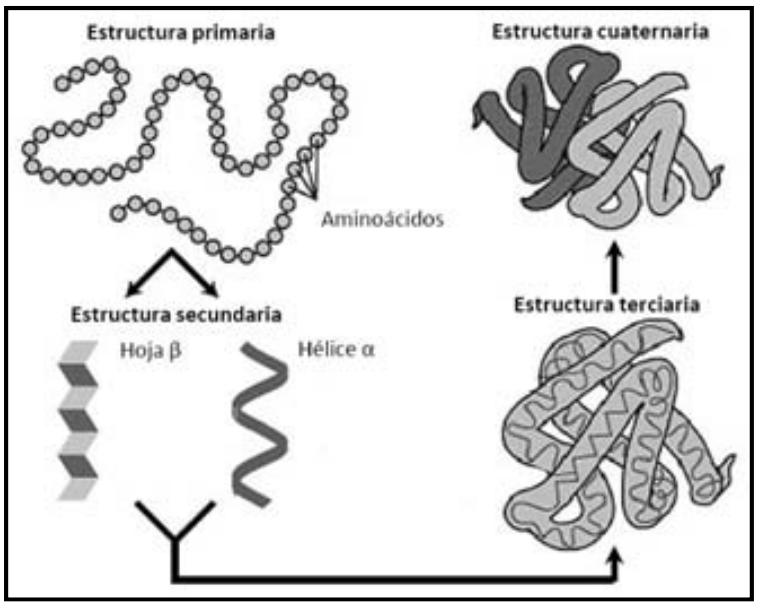

Figura 1. Representación de los diferentes niveles estructurales que puede adquirir una cadena polipeptídica. Figura adaptada de (www.umass.edu/molvis/workshop/imgs/protein-structure2.png)

Espacio conformacional

Para poder visualizar todo el espacio conformacional de una secuencia polipeptídica se introdujo el concepto de mapas energéticos (Dill and Chan 1997). Estos diagramas teóricos representan los diferentes estados de plegamiento y la multitud de vías paralelas que pueden seguir las cadenas polipeptídicas desde su estado desplegado, pasando por estados parcialmente plegados, hasta adquirir finalmente su configuración nativa. Cada cadena polipeptídica bajo unas condiciones determinadas tendrá un diagrama característico. Estos diagramas tridimensionales muchas veces se ilustran como bidimensionales para simplificar sus representaciones (Dobson 2003).

En el caso de proteínas pequeñas, estos mapas presentan forma de embudo indicando un plegamiento rápido y fiable hacia su estructura nativa (**Figura 2**) (Watters, Deka et al. 2007). Como podemos observar en la **figura 2** en la superficie se encuentran representados los diferentes caminos que una cadena polipeptídica puede seguir hasta llegar a su estructura nativa. El punto crítico de este proceso corresponde al estado de transición, la barrera energética que todas las proteínas deben superar para adquirir su estado nativo. Actualmente se considera que el paso fundamental del proceso de plegamiento es la formación de una serie de interacciones entre un número reducido de residuos (**figura 2** esferas amarillas) para

formar el núcleo de plegamiento a partir del cual el resto de la estructura colapsa rápidamente hacia el estado nativo (Fersht 2000; Dobson 2003).

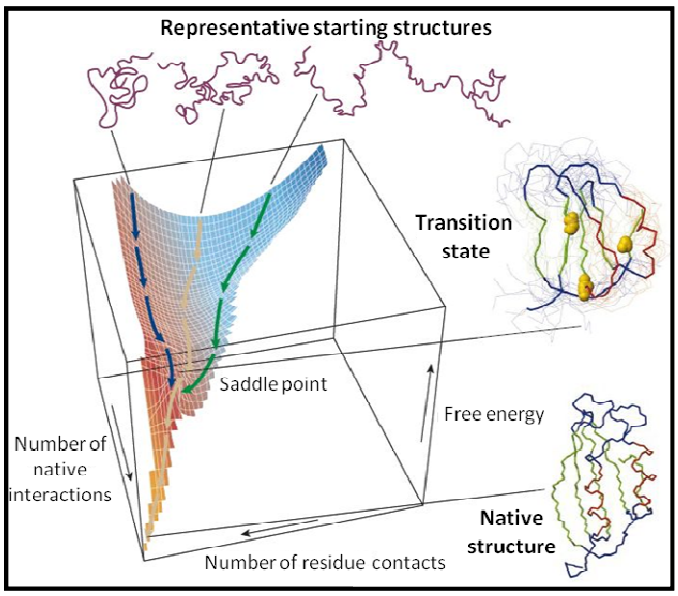

Figura 2. Mapa energético esquemático del plegamiento de una proteína. La superficie deriva de una simulación computacional de un modelo altamente simplificado del plegamiento de una proteína pequeña (Dobson 2003).

Proteínas intrínsecamente desestructuradas (IDPs)

Ha sido una idea ampliamente aceptada en la ciencia de las proteínas que la adquisición de la estructura tridimensional es un requisito fundamental para que estas realicen su función biológica. Contrariamente, se ha ido constatando que existen muchas proteínas funcionales total o parcialmente desplegadas en las que el hecho de no presentar ninguna estructura tridimensional definida es esencial para que puedan realizar sus funciones (Brown, Takayama et al. 2002). En la actualidad, hay irrefutables evidencias de que los estados desestructurados, comunes en todos los organismos vivos, son esenciales para funciones celulares básicas (Dunker, Silman et al. 2008).

La presencia de proteínas desordenadas es común en los tres reinos, tanto en eubacterias, arqueobacterias como en organismos multicelulares. Así, más del 25% de las proteínas de los genomas de eucariotas contienen regiones desordenadas de unos 50 aminoácidos aproximadamente las cuales evolucionan más rápidamente que las secuencias ordenadas (Brown, Takayama et al. 2002; Dunker, Silman et al. 2008).

AGREGACIÓN PROTEICA Y ENFERMEDADES HUMANAS

El citoplasma de una célula es un entorno altamente "poblado", donde la concentración total de macromoléculas puede superar los 400 $mg \cdot mL^{-1}$. Este hecho implica que entre el 5% y el 40% del volumen celular total se encuentra físicamente ocupado por macromoléculas (Ellis and Minton 2003). En este entorno, *in vivo*, se podría decir que el

plegamiento de proteínas es un reto extraordinario, donde las colisiones constantes entre moléculas, la elevada concentración proteica y el delicado equilibrio entre expresión y plegamiento deben ser considerados (Jahn and Radford 2008).

Las células han desarrollado estrategias para que el proceso de plegamiento de una proteína culmine en la formación de su estructura nativa funcional. Este es el caso de las chaperonas moleculares, proteínas presentes en todas las células y compartimentos celulares, que asisten el correcto plegamiento de las proteínas (Dobson 2003; Sabate, de Groot et al. 2010). En ciertas ocasiones, cuando todos estos esfuerzos no son suficientes, pueden producirse errores durante el proceso de plegamiento que pueden culminar en la formación de agregados proteicos. Morfológicamente estos agregados pueden presentar distintas conformaciones desde estructuras amorfas a agregados altamente organizados llamados amiloides.

Los agregados amorfos, que presentan una apariencia granular al ser observados mediante microscopia electrónica, están mayoritariamente formados por cadenas polipeptídicas desordenadas aunque también pueden presentar estructuras ricas en hoja β (Morell, Bravo et al. 2008; Wang, Maji et al. 2008). Por el contrario, las fibras amiloides son agregados proteicos en forma de filamentos que presentan estructuras altamente ordenadas y repetitivas con un núcleo común formado por hojas β orientados perpendicularmente al eje de la fibra formando una estructura conocida como β-cruzada. Estas estructuras fibrilares, con diámetros alrededor de 10 nm y longitudes desde nanómetros a varios micrómetros, pueden estar formadas por un filamento individual aunque a menudo son la asociación de múltiples filamentos girando, como si de una cuerda se tratara, en torno al eje de la fibra (Carulla, Caddy et al. 2005; Chiti and Dobson 2006; Kodali and Wetzel 2007).

Son muchas las técnicas analíticas utilizadas en la detección y en la caracterización estructural de estos depósitos fibrilares. Entre ellas se encuentra la tinción con colorantes específicos como las tioflavinas S y T (Th-S y Th-T) las cuales experimentan un cambio en su espectro de fluorescencia en presencia de amiloides y el Rojo Congo (CR) que sufre un desplazamiento batocrómico en su espectro con posible birrefringencia. Por otro lado, la identificación directa de la morfología de las fibras es posible mediante varias técnicas como la microscopia electrónica de transmisión (TEM) y más recientemente por microscopia de fuerza atómica (AFM) (Serpell, Sunde et al. 2000; Chiti and Dobson 2006), y la estructura secundaria a través del incremento del mínimo observado a ~217 nm (característico de una estructura secundaria en hoja β) mediante dicroísmo circular (CD), por el incremento/aparición de la banda β-intermolecular a ~1628 cm^{-1} mediante espectroscopia infrarroja con transformada de Fourier (FT-IR) o la detección de β-cruzada con reflexiones a 4.7 Å y 10 Å por difracción de

rayos X (Sunde, Serpell et al. 1997). Muchas veces estos estudios son complementados con otras técnicas como la proteólisis limitada que permite determinar regiones β, la espectrometría de masas (MS) o mediante el intercambio hidrógeno/deuterio (H/D) (Tycko 2006; Kodali and Wetzel 2007; Sabate, Baxa et al. 2007; Sawaya, Sambashivan et al. 2007; Wasmer, Lange et al. 2008; Tycko 2011) (**Figura 3**).

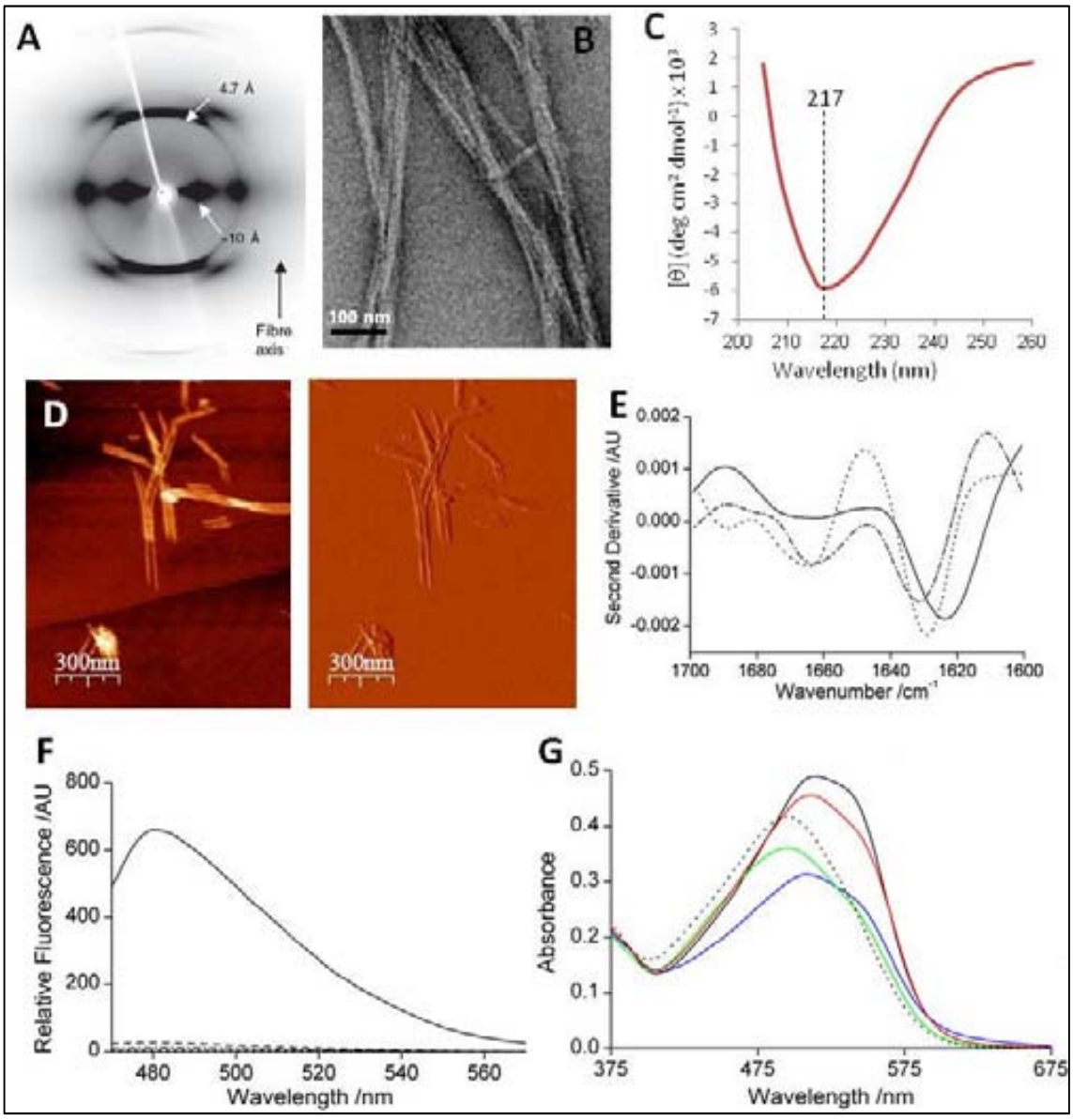

Figura 3: Métodos de identificación de fibras amiloides. **A**) Patrón de difracción de rayos X de las fibras formadas por el péptido amiloide de los islotes (IAPP) (Makin, Atkins et al. 2005). **B**) Imágenes obtenidas por TEM de fibras amiloides formadas por el prion HET-s (Sabate, Baxa et al. 2007). **C**) Dicroísmo circular en el UV lejano de fibras formadas por un dominio SH3. Adaptado de (Espargaro, Castillo et al. 2008). **D**) Imágenes obtenidas por AFM de fibras formadas por IAPP. **E**) Representación de la segunda derivada del espectro obtenido mediante FT-IR. **F**) Aumento de la fluorescencia intrínseca de Th-T en presencia de fibras amiloides. **G**) Cambio del espectro de absorción del CR al unirse a fibras amiloides. En **E**), **F**) y **G**) las diferentes líneas son los valores obtenidos por fibras de HET-s formadas a diferentes pHs (Sabate, Baxa et al. 2007).

Aunque las estructuras amiloides no pueden ser resueltas por los sistemas clásicos de análisis de proteínas (Thompson 2003), en la actualidad la resolución a nivel atómico de la estructura de las fibras amiloides ha sido posible gracias a técnicas como la cristalografía de rayos X y la resonancia magnética nuclear en estado sólido (ssNMR) (Petkova, Buntkowsky et al. 2004; Makin, Atkins et al. 2005; Nelson, Sawaya et al. 2005; Wasmer, Lange et al. 2008).

Durante los últimos años se ha puesto en evidencia la implicación de estas estructuras amiloides en un número creciente de patologías agrupadas actualmente bajo el término de enfermedades conformacionales (Chiti and Dobson 2006). Dentro de estas patologías se incluyen desde enfermedades tanto neurodegenerativas como sistémicas, como el Alzheimer, el Parkinson, encefalopatías espongiformes y la diabetes tipo II, donde la formación de agregados intra o extracelulares es la causa final de la enfermedad, hasta estados patológicos, como la fibrosis quística y algunos tipos de cáncer, donde un problema en la eficiencia de plegamiento puede dar lugar a una disminución de la cantidad de proteína necesaria para realizar su función (Dobson 2003; Chiti and Dobson 2006; Georgescauld, Sabate et al. 2011). Aunque en la actualidad se conocen más de 40 enfermedades humanas asociadas a la formación de estos agregados fibrilares, el hecho que este número esté claramente en aumento confiere una importancia vital al estudio exhaustivo del plegamiento proteico y su implicación en este tipo de enfermedades (**Tabla 1**).

Proteína	**Estructura nativa**	**Enfermedad**
Péptido β amiloide	Desestructurada	Alzheimer
α-Sinucleína	Desestructurada	Parkinson
β2-microglobulina	Globular (hojas β)	Amiloidosis relacionada con diálisis
Huntingtina	Variable (poliGln)	Huntington
Immunoglobulina dominio V_L	Globular (hojas β)	Amiloidosis asociada a cadenas ligeras
Polipéptido amiloide de los islotes	Desestructurada	Diabetes tipo II
Lisozima	Globular (hélices α, hojas β)	Amiloidosis sistémica hereditaria
Proteína priónica	Globular (hélices α, hojas β)	Creutzfeldt-Jakob
Transtirretina	Globular (hojas β)	Amiloidosis sistémica senil

Tabla 1. Principales proteínas relacionadas con la formación de fibras amiloides implicadas en enfermedades humanas. Figura adaptada de (Bhak, Choe et al. 2009).

La gran diversidad de proteínas implicadas en estas patologías y la gran variedad estructural que presentan (desde péptidos nativamente desestructurados, proteínas con una extensa estructura en hélice α o con una estructura total o parcial en hoja β hasta proteínas con ambas conformaciones, tanto hélices α como hojas β) junto con el hecho de que estas estructuras no se limitan únicamente a proteínas asociadas con los trastornos clínicos conocidos, sino que también pueden ser estructuras funcionales, sugiere que la formación de amiloides podría ser un proceso genérico en el universo proteico. Ya en los años 30 se observo que muchas proteínas podían existir en dos estados diferentes: La estructura globular nativa y una forma fibrilar producida en condiciones de temperatura y pH extremos. La observación a lo largo de los años de la existencia de estos dos estados para muchas proteínas, sugiere que cualquier proteína en determinadas condiciones podría formar fibras amiloides (Chiti, Webster et al. 1999; Dobson 2001; Dobson 2002; Fandrich and Dobson 2002).

Mecanismo de formación de los agregados amiloides

Durante el proceso de síntesis, y antes de adquirir su estructura nativa, las cadenas polipeptídicas pueden pasar por multitud de estados parcialmente desplegados que pueden escaparse de la vía de plegamiento (Jahn and Radford 2008). Desafortunadamente, los principios fisicoquímicos que facilitan la formación de enlaces intra e intermoleculares esenciales en las estructuras terciarias y cuaternarias también pueden participar en enlaces no nativos dando lugar a vías de plegamiento alternativas que pueden finalizar en la formación de agregados proteicos (**Figura 4**) (Castillo and Ventura 2009; Pastore and Temussi 2012).

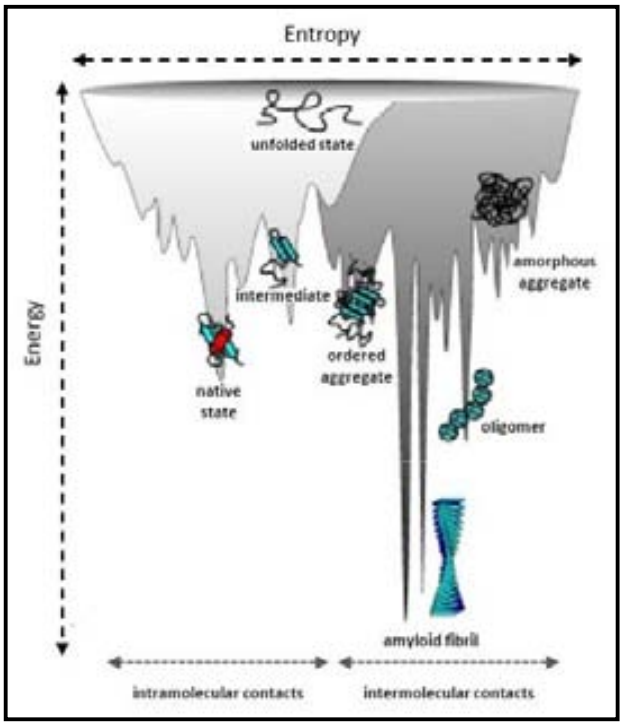

Figura 4. Representación de los mapas energéticos de las vías de plegamiento y agregación de una cadena polipeptídica. En la parte de la izquierda la adquisición de la estructura nativa a través de enlaces nativos, mientras que en la derecha observamos la formación de agregados proteicos mediante enlaces intermoleculares no nativos (Jahn and Radford 2008).

Estas interacciones no nativas, capaces de desencadenar la agregación proteica, pueden conllevar nuevos mínimos energéticos, menos definidos, constituidos por un amplio rango de estados oligoméricos que pueden derivar en mínimos energéticos más definidos, correspondientes a estructuras altamente organizadas como las protofibrillas o fibrillas. La energía mínima de las fibras amiloides maduras normalmente es menor que la del estado nativo, haciendo de éstas estructuras altamente estables (Wetzel 2006).

Independientemente de la estructura inicial de cada proteína implicada, todas las fibras amiloides presentan un patrón estructural común. Esto implica que las proteínas deben sufrir un desplegamiento total o parcial de su estructura nativa, permitiendo así la exposición de regiones determinadas que favorecen la reorganización estructural y la formación de nuevas interacciones que finalizaran en la formación de agregados proteicos (Chiti, Webster et al. 1999). En el caso de proteínas con estructura cuaternaria en condiciones nativas, la formación de agregados proteicos suele producirse previa disociación de las diferentes unidades proteicas (monómeros) que forman la proteína nativa (Azevedo, Pereira et al. 2011). No obstante, cabe resaltar que los péptidos o proteínas con capacidad agregacional no tienen porque poseer una estructura globular definida. En el caso de enfermedades como la diabetes tipo II, el Alzheimer o el Parkinson las proteínas involucradas son intrínsecamente desestructuradas (IDP). En estos casos el proceso de agregación viene determinado por el auto-ensamblaje directo de las conformaciones nativas (Chiti, Webster et al. 1999). Así pues, el enorme abanico de proteínas que pueden agregar formando estructuras amiloides y su gran diversidad estructural implica la existencia de diversos mecanismos de ensamblaje, desde proteínas totalmente o parcialmente desnaturalizadas (Ferguson, Becker et al. 2006), hasta proteínas en su estado nativo **(Figura 5)** (Plakoutsi, Bemporad et al. 2005).

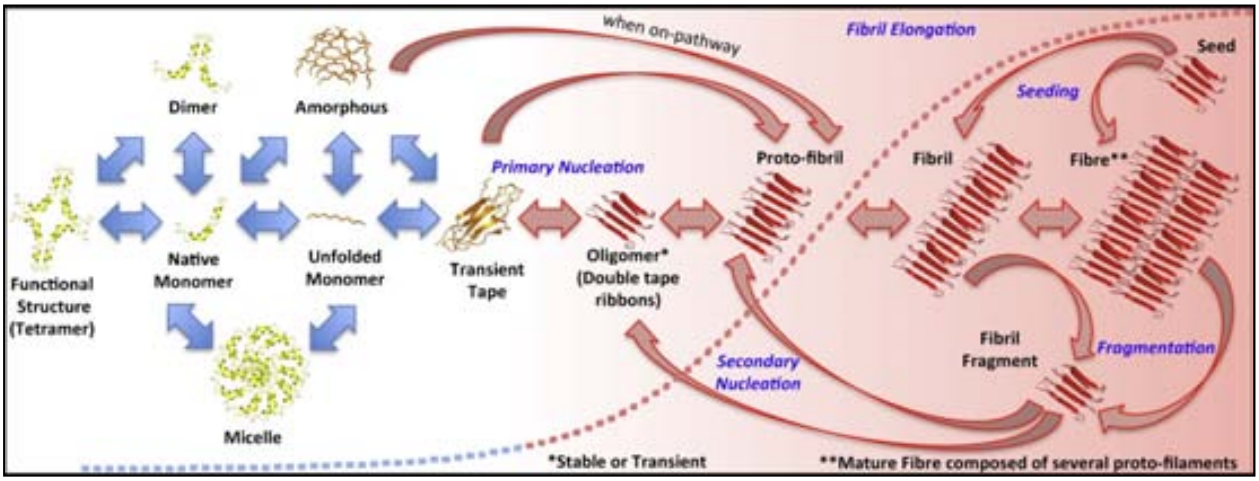

Figura 5. Visión esquemática de la formación de fibras amiloides (Invernizzi, Papaleo et al. 2012)

En las últimas décadas se han propuesto diferentes modelos para explicar las cinéticas de formación amiloide (Serio, Cashikar et al. 2000). Sin embargo, actualmente está ampliamente consensuado que la fibrilogénesis sigue un mecanismo de nucleación-polimerización, que es dependiente de la concentración y el tiempo (Jarrett and Lansbury 1993; Harper and Lansbury 1997; Lomakin, Teplow et al. 1997; Chiti and Dobson 2006; Bhak, Choe et al. 2009). Este mecanismo consta de tres fases: 1) En la primera fase, conocida como fase de latencia o de nucleación, las especies solubles se asocian para formar las primeras especies con conformación en hoja β que actuaran como núcleo de la reacción en un proceso termodinámicamente desfavorable. Este proceso está gobernado por múltiples equilibrios entre posibles especies solubles, desde estructuras monoméricas a estructuras formadas por un número *n* de monómeros o "micelas" que actúan como reservorios de monómeros (Yong, Lomakin et al. 2002; Sabate and Estelrich 2005; Bernstein, Dupuis et al. 2009; Jin, Shepardson et al. 2011). 2) La segunda fase, denominada fase exponencial o fase de crecimiento, es una fase termodinámicamente favorable en la que el núcleo crece rápidamente mediante la adición de las especies solubles para formar las fibras. En esta fase, pueden encontrarse una gran diversidad de especies multiméricas, desde protofibrillas a fibras, interrelacionadas en múltiples equilibrios. 3) Finalmente, en la fase estacionaria, donde prácticamente se han agotado las reservas de especies solubles susceptibles de ser asociadas a las fibras, los agregados fibrilares ordenados pueden mantenerse en equilibrio con la pequeña (a veces ínfima) cantidad de especies solubles. La drástica reducción de la adición de nuevos monómeros a las fibrillas formadas junto con el incremento de contactos interfibrilares favorecen la maduración de las fibras mediante la asociación de las fibrillas ya formadas (**Figura 5**) (Jarrett and Lansbury 1993; Bhak, Choe et al. 2009).

En ausencia de fibras o núcleos preformados, este proceso cinético de conversión de péptidos y/o proteínas a estructuras amiloides suele verse como una reacción sigmoidea controlada por dos parámetros cinéticos, la velocidad de nucleación y la velocidad de elongación o crecimiento (Jarrett and Lansbury 1993; Lomakin, Teplow et al. 1997; Munishkina, Henriques et al. 2004). Aunque diversos modelos pueden explicar este tipo de reacciones (Pallitto and Murphy 2001; Cohen, Vendruscolo et al. 2011; Cohen, Vendruscolo et al. 2011; Cohen, Vendruscolo et al. 2011), el hecho que el proceso precise de la formación de un núcleo a través del cual empezará a crecer la fibra sugiere que la agregación podría ser explicada por un modelo de reacción autocatalítica. Mediante esta aproximación podemos estudiar la formación de fibras de manera simple mediante un análisis matemático el cual nos permite obtener información sobre los parámetros cinéticos de la reacción (Sabate, Gallardo et al. 2003).

A pesar de que inicialmente las fibras maduras fueron consideradas como estructuras rígidas representando el punto final del proceso de agregación, estudios recientes han demostrado que son estructuras dinámicas que sufren continuamente un reciclaje molecular mediante un proceso de asociación y disociación dentro de la propia fibra (Carulla, Caddy et al. 2005) y pueden experimentar fragmentaciones (Tanaka, Collins et al. 2006). Este último fenómeno tiene un gran impacto en las cinéticas de ensamblaje ya que la ruptura de las fibras preformadas da lugar a la formación de nuevos núcleos de crecimiento acelerando de esta manera la reacción de polimerización a causa de esta nucleación secundaria (Knowles, Waudby et al. 2009). Este incremento de pequeñas partículas fibrilares no únicamente afecta las cinéticas de agregación sino que, como se ha demostrado recientemente, puede existir una relación directa entre la tasa de fragmentación y la toxicidad debido a la capacidad de estas partículas por interaccionar con las membranas celulares (Xue, Hellewell et al. 2010). En el caso de proteínas priónicas ha sido demostrado que un incremento en la fragmentación produce un aumento en el número de eventos de nucleación que aumentan drásticamente la capacidad prion (Tanaka, Collins et al. 2006). Independientemente de la fragmentación, existen otros aspectos capaces de afectar la fase de crecimiento fibrilar dando lugar a reacciones secundarias de nucleación. Estas nuevas etapas de nucleación pueden venir determinadas por la presencia de superficies naturales, como membranas celulares, o artificiales capaces de promover la agregación (Zhu, Souillac et al. 2002) y la capacidad de formar nuevas fibras mediante ramificaciones de las ya existentes, así como el crecimiento en la superficie de fibras ya formadas (Harper, Lieber et al. 1997; Andersen, Yagi et al. 2009).

Seeding **y especificidad secuencial**

En los procesos de agregación amiloide, la formación del núcleo, proceso termodinámicamente desfavorable, requiere un tiempo que puede ser reducido o incluso eliminado mediante la adición de agregados preformados, *seeds,* los cuales actúan como núcleos induciendo la agregación inmediatamente en un proceso conocido como *seeding* (**Figura 6**).

La formación de fibras amiloides es un proceso altamente específico que tiene lugar entre cadenas polipeptídicas idénticas o con una muy elevada homología. Estudios experimentales han mostrado que a medida que se reduce la identidad secuencial entre proteína soluble y agregada en forma amiloide también se disminuye la eficiencia de la reacción o *seeding* (Krebs, Morozova-Roche et al. 2004). Esta especificidad concuerda con el hecho que los depósitos proteicos relacionados con patologías conformacionales están

principalmente compuestos de una única proteína, la proteína implicada en la patología, en lugar de encontrar diferentes cadenas polipeptídicas (Dobson 2001).

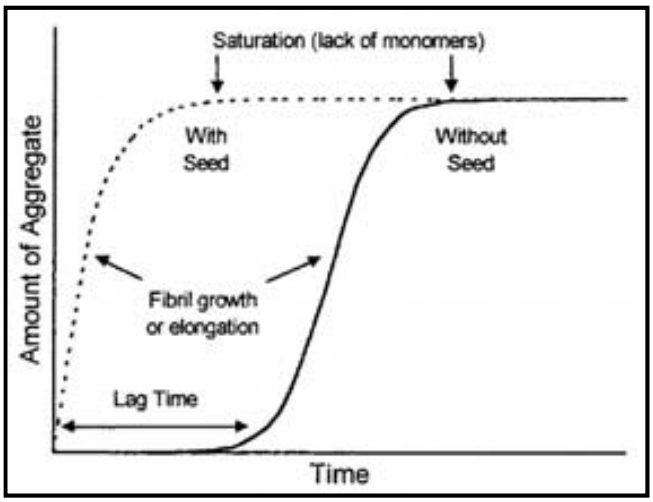

Figura 6. Representación de una cinética de formación de fibras amiloides. La línea continua representa la curva sigmoidea que se obtiene con las tres fases representadas: la fase de nucleación o fase de latencia, la fase de elongación y por último el equilibrio. La línea discontinua muestra el efecto de la presencia de agregados amiloides preformados, mostrando la eliminación de la fase de nucleación y la formación de fibras de manera inmediata (Sabate, Gallardo et al. 2003).

Especies intermediarias durante la formación de fibras amiloides

Durante el proceso de formación de fibras amiloides se han podido identificar y caracterizar diferentes estructuras intermediarias (Walsh, Lomakin et al. 1997; Lashuel, Hartley et al. 2002). Inicialmente, la toxicidad asociada al proceso de formación de fibras amiloides fue atribuida a las fibras maduras. No obstante, la información obtenida durante los últimos años indica que las fibras maduras son especies biológicas relativamente inertes y muy estables mientras que especies intermediarias, como los oligómeros o las protofibrillas, podrían ser las causantes del efecto citotóxico (Bucciantini, Giannoni et al. 2002; Kodali and Wetzel 2007; Uversky 2010; Bieschke, Herbst et al. 2011). Los oligómeros pueden ser definidos como especies de discreto tamaño, relativamente flexibles y muchas veces esferoides, que mantienen las características principales de los amiloides (Kodali and Wetzel 2007; Uversky 2010). Su caracterización durante el proceso de agregación de α-sinucleína mediante FT-IR, CD y unión de Th-T ha permitido determinar que son estructuras compactas y ordenadas en hoja β, con regiones hidrofóbicas expuestas al solvente (Kaylor, Bodner et al. 2005; Dusa, Kaylor et al. 2006). Existen varios mecanismos de citotoxicidad posibles relacionados con la deposición proteica. Debido a sus propiedades intrínsecas y a sus características estructurales, los oligómeros pueden interaccionar con las membranas celulares formando poros que pueden alterar el flujo de iones afectando la homeostasis y finalmente provocando disfunción celular y posible apoptosis o muerte celular (Lashuel, Hartley et al. 2002; Uversky 2010; van Rooijen, Claessens et al. 2010). Alternativamente, se ha propuesto otro posible mecanismo donde los oligómeros interaccionan con receptores de membrana provocando errores en la señalización intracelular (Uversky 2010).

ELEMENTOS DETERMINANTES DE LA AGREGACIÓN PROTEICA

Tal y como se ha comentado anteriormente en la mayoría de casos el proceso de agregación requiere la desestabilización de la estructura nativa, pudiendo así decir que la tendencia a formar estructuras amiloides está altamente relacionada con la estabilidad del estado nativo (Hurle, Helms et al. 1994; Espargaro, Castillo et al. 2008). Sin embargo, la estabilidad proteica no es suficiente para explicar la agregación de las proteínas globulares y mucho menos la agregación de los péptidos y proteínas que no poseen ninguna estructura nativa determinada.

Los determinantes de la agregación son muchos y variados ya que estos engloban propiedades intrínsecas de la cadena polipeptídica, basadas en las diferentes propiedades fisicoquímicas de los aminoácidos que la forman, y las características del entorno en el que se encuentra el péptido o proteína en cuestión.

Propiedades intrínsecas

Los principales factores intrínsecos de una cadena polipeptidica están basados en factores como la carga, la hidrofobicidad, los patrones de residuos polares y apolares, y la tendencia a pasar de estructuras en hélice α a hojas β de cada uno de los aminoácidos que la forman (Chiti, Stefani et al. 2003; DuBay, Pawar et al. 2004; de Groot, Aviles et al. 2006).

Uno de los efectos más importantes involucrado en el plegamiento de proteínas es el colapso hidrofóbico donde los residuos apolares son enterrados en el interior de la estructura nativa generando el núcleo hidrofóbico (Chiti, Stefani et al. 2003; Dyson, Wright et al. 2006). Las interacciones hidrofóbicas juegan un papel crucial, no únicamente en la adquisición del estado nativo de proteínas globulares sino también en la formación de las fibras amiloides (Bolognesi, Kumita et al. 2010). La desestabilización total o parcial de proteínas globulares puede dejar expuestos estos residuos hidrofóbicos favoreciendo la formación de interacciones intermoleculares y su posible agregación. En concordancia, se ha podido observar que un aumento en la hidrofobicidad se traduce en un incremento de la agregación (Chiti, Taddei et al. 2002; Calamai, Taddei et al. 2003).

Otra característica importante es la alternancia de residuos hidrofóbicos y hidrofílicos que puede favorecer la formación de hojas β altamente empaquetadas. En este sentido, se ha observado que al diseñar secuencias *de novo* donde se alternaban residuos polares (Lys, His Glu, Gln, Asp y Asn) con residuos no polares (Met, Leu, Ile, Val y Phe) éstas forman fibras con gran facilidad disponiendo los residuos hidrofóbicos protegidos en el interior y los hidrofílicos expuestos en el exterior de las fibras (West, Wang et al. 1999; Wang and Hecht 2002).

Otro factor que influye en la agregación es la carga. Se ha observado que la tasa de agregación de una cadena polipeptídica es inversamente proporcional al valor absoluto de la carga neta, de esta manera mutaciones que disminuyen la carga neta de la proteína acercándola a la neutralidad favorecen su agregación. Este factor se puede explicar de manera simple teniendo en cuenta que si incrementamos la repulsión electroestática entre distintas moléculas desfavoreceremos el auto-ensamblaje (Chiti, Taddei et al. 2002; DuBay, Pawar et al. 2004).

Propiedades extrínsecas

Muchos de los factores comentados anteriormente pueden verse alterados por cambios en el entorno proteico. Variaciones de pH, temperatura, fuerza iónica o concentración de la proteína pueden afectar drásticamente el plegamiento o agregación de las proteínas. Por ejemplo, cambios en el pH del medio pueden producir variaciones en la carga neta de las proteínas aumentando o disminuyendo su tendencia a agregar (Uversky, Li et al. 2001), o el aumento de temperatura puede favorecer la desestabilización de la estructura nativa dando lugar a la aparición de estados parcialmente desplegados que permiten la exposición al solvente de regiones hidrofóbicas anteriormente protegidas (Nielsen, Khurana et al. 2001).

Estas variaciones no afectan solamente al plegamiento de proteínas sino que también pueden alterar el proceso de agregación y formación amiloide tanto cinética, termodinámica como estructuralmente (Lopez De La Paz, Goldie et al. 2002; Kumar, Mohanty et al. 2007). Por ejemplo, el aumento de la concentración y la temperatura puede favorecer la formación de fibras amiloides; tanto la temperatura como el incremento en la concentración de proteína incrementan el número de contactos entre moléculas acelerando el proceso de nucleación (paso limitante en la formación de fibras amiloides) y por tanto reduciendo la fase de latencia (Nielsen, Khurana et al. 2001).

Aunque, como se ha expuesto anteriormente, las interacciones hidrofóbicas son muy importantes en la formación de fibras amiloides, también las interacciones electroestáticas juegan un papel importante en estos procesos de agregación (Nielsen, Khurana et al. 2001). Así pues, parámetros como el pH y la fuerza iónica también pueden influir en este tipo de procesos interfiriendo en la estabilidad de las distintas conformaciones. Por ejemplo, un aumento de la fuerza iónica puede traducirse en la disminución del tiempo necesario para la formación del núcleo debido a la reducción de las repulsiones entre las cargas de las cadenas laterales aminoacídicas entre monómeros (Nielsen, Khurana et al. 2001). Estudios realizados con la proteína priónica HET-s y el péptido β amiloide han mostrado que cambios en el pH y/o la fuerza iónica dan lugar a variaciones en las interacciones que estabilizan estructuras

determinadas dando lugar a la obtención de nuevas conformaciones (Petkova, Buntkowsky et al. 2004; Sabate, Baxa et al. 2007). Estas variaciones morfológicas pueden ser debidas a factores como la repulsión entre cadenas laterales cargadas, la disrupción o formación de puentes salinos y/o la destrucción de interacciones para dar lugar a la formación de otras nuevas.

Regiones determinantes de la agregación

Aunque gran parte de la secuencia de una proteína esté implicada en la formación de las estructuras fibrilares, hay evidencias claras de que algunas secuencias cortas de aminoácidos tienen más tendencia a agregar que otras (Lopez de la Paz and Serrano 2004; Sanchez de Groot, Pallares et al. 2005). Resultados experimentales han demostrado la existencia de regiones formadas por un número reducido de aminoácidos que pueden actuar tanto como inductores (Ivanova, Sawaya et al. 2004; Ventura, Zurdo et al. 2004; Esteras-Chopo, Serrano et al. 2005) como inhibidores (Buell, Tartaglia et al. 2009) de la agregación. Estas cortas secuencias capaces de conducir la agregación de largas cadenas polipeptídicas se conocen como *Hot Spots* (HSs). La composición de estos HSs es rica en residuos hidrofóbicos alifáticos (Val, Leu y Ile) y en residuos aromáticos (Phe, Trp y Tyr) (Rousseau, Serrano et al. 2006; Monsellier, Ramazzotti et al. 2008). Normalmente estos HSs se encuentran flanqueados por residuos específicos que tienen la función de contrarrestar la alta tendencia a agregar aumentando la eficiencia de plegado. Estas regiones, denominadas *gatekeepers*, que flanquean los HSs, son ricas en residuos cargados (Asp, Glu, Lys y Arg) y también en Pro (Rousseau, Serrano et al. 2006; Monsellier, Ramazzotti et al. 2008). En proteínas globulares, estas regiones de agregación se encuentran normalmente enterradas en el interior de la estructura nativa formando parte del núcleo hidrofóbico, envueltas en la red de contactos que estabilizan la estructura nativa o formando parte de la superficie de interacción entre proteínas dando lugar a la estructura cuaternaria (Vendruscolo, Paci et al. 2003; Castillo and Ventura 2009).

Gracias a todo el conocimiento acumulado sobre la estructura de las fibras amiloides y las fuerzas que promueven y estabilizan su formación se han desarrollado diferentes algoritmos capaces de identificar las secuencias amiloidogénicas de una proteína y predecir la tendencia a agregar de ésta (Castillo, Grana-Montes et al. 2011). Hoy en día existen aproximadamente 14 programas de predicción de zonas de agregación que podríamos dividir en dos categorías principales: los modelos empíricos y los modelos basados en la estructura (Belli, Ramazzotti et al. 2011).

Los modelos empíricos están basados en resultados experimentales donde las predicciones vienen determinadas principalmente por las propiedades fisicoquímicas de los aminoácidos, como por ejemplo hidrofobicidad, carga, tendencia a formar estructuras β y solubilidad (Belli, Ramazzotti et al. 2011). Dentro de este grupo se encuentran diferentes algoritmos como TANGO (Fernandez-Escamilla, Rousseau et al. 2004) y su actualización WALTZ (Maurer-Stroh, Debulpaep et al. 2010), AGGRESCAN (Conchillo-Sole, de Groot et al. 2007) o Zyggregator (Tartaglia and Vendruscolo 2008). Por otro lado, los modelos basados en la estructura tratan de identificar los factores determinantes de la agregación mediante la observación de las estructuras en 3D existentes de los diferentes péptidos que adoptan estructura fibrilar (Belli, Ramazzotti et al. 2011). En este grupo encontramos programas como PASTA (Trovato, Chiti et al. 2006), BETASCAN (Bryan, Menke et al. 2009) o Zipper DB (Nelson, Sawaya et al. 2005).

ESTRUCTURAS AMILOIDES FUNCIONALES

Clásicamente, los amiloides han sido considerados como estructuras cuaternarias formadas como respuesta a un error durante el proceso de plegamiento de las proteínas. El gran número de proteínas capaces de adquirir esta estructura cuaternaria parece sugerir que estas estructuras pueden venir determinadas por propiedades intrínsecas de las cadenas polipeptídicas (Dobson 2003). Así pues, no es de extrañar que la naturaleza emplee estas conformaciones para propósitos funcionales en una gran variedad de organismos, desde bacterias a humanos (Kelly and Balch 2003). Debido a sus propiedades estructurales, su gran compactación y su elevada resistencia, los amiloides son considerados como un excelente material para construir estructuras biológicas (Fowler, Koulov et al. 2007).

Dentro de estos amiloides estructurales encontramos algunos muy bien caracterizados como el caso de la proteína *Curli*, empleada por bacterias como *Escherichia coli* como amiloide extracelular creando una matriz proteica que permite la adhesión, la colonización de superficies inertes y la unión a proteínas del huésped (Chapman, Robinson et al. 2002). Otro ejemplo son las proteínas *Chaplin* producidas por la bacteria *Streptomyces coelicolor* que revisten las hifas de la bacteria permitiendo de esta manera la dispersión de las esporas para dar lugar a la colonización (Claessen, Rink et al. 2003).

También se han encontrado amiloides funcionales en animales, que son utilizados para realizar funciones biológicas específicas y especializadas, siempre bajo condiciones altamente reguladas (Chiti and Dobson 2006). En este sentido, uno de los descubrimientos, sin duda, más sorprendentes fue el descubrimiento de la proteína *Pmel17* en humanos. Esta proteína da

lugar a la formación de estrías intraluminales fibrosas en el interior de los melanosomas, estos orgánulos, relacionados con el lisosoma, se diferencian a melanocitos para permitir la producción epidérmica del pigmento melanina. Este material fibroso que permite la formación de los gránulos de melanina muestra analogías significantes con las fibras amiloides (Berson, Theos et al. 2003).

PRIONES

El concepto prión, que proviene de la teoría "**pr**ote**i**n-**on**ly" fue introducido por el Premio Nobel Stanley B. Prusiner en 1982 al descubrir que el agente infeccioso que producía la enfermedad de scarpie en ovejas y cabras era realmente una proteína (Prusiner 1982). Así pues, los priones son realmente proteínas naturales, que después de una conversión conformacional, se auto-ensamblan en estructuras amiloides ricas en hoja β auto-perpetuándose *in vivo*. La idea de que una conformación proteica pueda replicarse a sí misma y servir como elemento genético explica un conjunto de inusuales enfermedades neurodegenerativas conocidas como encefalopatías espongiformes transmisibles (TSEs), entre las cuales se encuentra la enfermedad de Creutzfeldt-Jakob (CJD) (Chien, Weissman et al. 2004). Estas enfermedades pueden ser genéticas, infecciosas o esporádicas. Hoy en día las TSEs han sido identificadas en un amplio número de mamíferos (Chien, Weissman et al. 2004; Caughey and Baron 2006) y presentan un gran espectro de manifestaciones clínicas, entre ellas se encuentra la demencia, ataxia, insomnio, paraplejia y parestesia (Prusiner 2001).

La proteína priónica (PrP), codificada por el gen *Prnp* altamente conservado en mamíferos, consta de 209 aminoácidos y se encuentra normalmente anclada en la membrana celular (Colby and Prusiner 2011). La proteína puede encontrarse en dos conformaciones diferentes, la forma fisiológica normal (PrP^{C}) y la isoforma causante de la enfermedad (PrP^{Sc}) que actúa estimulando la conversión de PrP^{C} a la conformación infecciosa. Estas dos conformaciones de PrP son idénticas en composición pero presentan una gran diferencia en su estructura tridimensional. Mientras que PrP^{C} es rica en hélices α y pobre en estructura β, PrP^{Sc} posee mucha más estructura en hoja β. Esta transición estructural entre hélices α y hojas β en PrP es el evento fundamental de las enfermedades priónicas (Prusiner 2001; Chien, Weissman et al. 2004; Caughey and Baron 2006).

Las proteínas priónicas no son exclusivas de mamíferos (Chien, Weissman et al. 2004). Así, en levadura encontramos dos de los priones más estudiados: [*URE3*] y [PSI^{+}]. Estos dos priones pueden ser definidos como genes no cromosómicos de *Saccharomyces cerevisiae* que

codifican para las proteínas Ure2 y Sup35 respectivamente, proporcionando un mecanismo para la generación de diversidad fenotípica y heredable, dependiendo de la conformación que adopten (soluble o fibrilar). Mientras que Ure2 es un regulador del catabolismo del nitrógeno, Sup35 es una subunidad del factor terminador de la traducción de los mRNA; no obstante, la forma fibrilar de ambos promueve la supervivencia en ambientes determinados y la evolución de nuevos fenotipos (Halfmann, Jarosz et al. 2012). El hecho de si estos priones son perjudiciales o beneficiosos ha sido motivo de controversia, ya que [*PSI*$^{+}$] y [*URE3*] raramente se han encontrado en levaduras naturales, sugiriendo así que podrían ser perniciosos (McGlinchey, Kryndushkin et al. 2011; Wickner, Edskes et al. 2011); sin embargo, estudios recientes han permitido localizar estos priones en la naturaleza mostrando la posibilidad que podrían ser beneficiosos (Halfmann, Jarosz et al. 2012). Uno de los priones mejor caracterizados es el prion [*Het-s*] del hongo filamentoso *Podospora anserina.* Este prion actúa como sistema de protección natural y está involucrado en el control de la muerte celular programada llamada incompatibilidad heterocarión, controlada genéticamente (Coustou, Deleu et al. 1997; Maddelein, Dos Reis et al. 2002). Cuando las hifas de colonias adyacentes se encuentran, estas pueden fusionarse y compartir el contenido celular (nutrientes y citoplasma) generando células multinucleadas, llamadas heterocarión, esenciales para el apareamiento y el crecimiento vegetativo del hongo. La incompatibilidad heterocarión es muy común en hongos filamentosos y tiene lugar cuando dos cepas con distinto genotipo intentan fusionarse (Balguerie, Dos Reis et al. 2004). La proteína HET-s, presenta dos variantes fenotípicas: HET-s y HET-S. HET-s existe en forma soluble (HET-s*) y en forma amiloide (HET-s) mientras que HET-S solo existe en forma soluble. Mientras que la fusión puede llevarse a cabo entre colonias genéticamente idénticas (HET-S-HET-S o HET-s-HET-s) sólo HET-s* puede fusionarse con HET-S (Coustou, Deleu et al. 1997; Maddelein, Dos Reis et al. 2002).

Diferentes estudios han revelado que la capacidad de propagación de los priones viene determinada por dos mecanismos claramente diferenciados: el primero es la velocidad de crecimiento de la fibra mediante el ensamblaje de la proteína a las partículas priónicas ya existentes y el segundo es la capacidad de fragmentación de las fibras formadas generando de esta manera nuevas partículas priónicas (*seeds*) esenciales para la infección y la propagación (Tuite and Koloteva-Levin 2004; Tanaka, Collins et al. 2006). El fenómeno de fragmentación, esencial para la propagación de los priones, está claramente asociada con diversos grupos de chaperonas como Hsp40, Hsp70 y Hsp104 (Sondheimer and Lindquist 2000; Chernoff 2004). Así, un crecimiento rápido asociado a una gran capacidad de fragmentación favorece la aparición y propagación del prión (**Figura 7**).

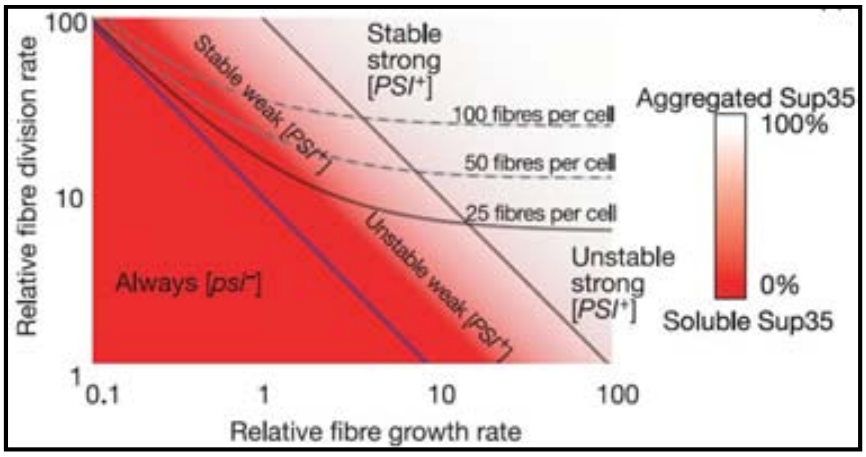

Figura 7. Representación gráfica del efecto de la tasa de crecimiento y la fragmentación de los diferentes fenotipos en la propagación del prion [*PSI*$^{+}$]. El fenotipo [*PSI*$^{+}$] es el resultado de la agregación de Sup35 mientras que [*psi*$^{-}$] es la forma soluble. Los estados de agregación de Sup35 se encuentran representados mediante un gradiente de color donde por debajo de la línea azul la propagación del prión no es posible. (Tanaka, Collins et al. 2006).

AGREGACIÓN EN CÉLULAS BACTERIANAS: CUERPOS DE INCLUSIÓN (IBs)

En la industria biotecnológica, las bacterias han sido ampliamente utilizadas para la producción de proteínas recombinantes que no necesitan modificaciones post-traduccionales. Sin embargo, las células bacterianas, organismos relativamente simples, pueden ser utilizados también como modelos para poder obtener información crucial sobre la agregación proteica y la relación entre ésta y la maquinaria de control celular. *Escherichia coli* es el organismo procariota más utilizado en la producción de proteína recombinante debido a su rápido crecimiento en medios de cultivo económicos, su capacidad de conseguir una elevada concentración celular y la posibilidad de obtener grandes cantidades de proteína. Esta producción proteica implica altas velocidades de traducción proporcionando de esta manera un suministro continuo de polipéptidos desplegados que muchas veces saturan la maquinaria de control celular. Ésta saturación puede comportar la acumulación de la proteína recombinante en depósitos proteicos llamados cuerpos de inclusión (IBs) (de Groot, Sabate et al. 2009). La formación de IBs es uno de los principales problemas en la producción proteica y es responsable de la restricción en la producción de muchas proteínas relevantes terapéuticamente (Ventura and Villaverde 2006).

Propiedades de los cuerpos de inclusión

Mediante microscopia de contraste de fases, los IBs pueden verse como partículas densas y refractantes con un diámetro aproximado de 1 µm situadas tanto en el citoplasma

como en el periplasma de las bacterias (Ventura and Villaverde 2006). Inicialmente los IBs fueron considerados como depósitos proteicos inactivos sin ninguna estructura determinada; no obstante, esta opinión ha cambiado rotundamente durante los últimos años (de Groot, Sabate et al. 2009).

Debido a la gran variabilidad de proteínas (en secuencia, estructura, tamaño y origen) que dan lugar a la formación de IBs durante su expresión en células procariotas, es fácil pensar que es un proceso dirigido por interacciones intermoleculares no específicas entre especies nacientes parcialmente desplegadas. Durante el proceso de expresión de proteínas recombinantes se observa la presencia de un número reducido de IBs (normalmente uno) con una elevada pureza proteica, donde en algunos casos la presencia de la proteína recombinante puede alcanzar el 90% de la masa total (Carrio, Corchero et al. 1998). Además, la coexpresión de dos proteínas en una misma bacteria da como resultado la formación de dos IBs diferenciados cada uno de ellos enriquecido con una de las dos proteínas (Hart, Rinas et al. 1990; Morell, Bravo et al. 2008). Estas características en la formación de IBs y su capacidad *in vitro* de ser utilizados como *seeds* para acelerar el proceso de agregación de la misma proteína soluble (Carrio, Gonzalez-Montalban et al. 2005) denotan que su proceso de formación viene determinado por interacciones específicas.

En los últimos años, estos agregados inicialmente considerados como amorfos y sin estructura molecular definida han podido ser estudiados en detalle confirmando que estos depósitos presentan características comunes a los agregados amiloides presentes en enfermedades humanas. Así pues, los IBs unen colorantes específicos de fibras amiloides como Th-T, Th-S y CR, y mediante FT-IR se ha podido observar que presentan espectros característicos de hojas β intermoleculares (Carrio, Gonzalez-Montalban et al. 2005) y que esta estructura β va aumentando durante su proceso de formación (Doglia, Ami et al. 2008). En concordancia con esta idea se ha podido observar mediante microscopia la presencia de fibras amiloides en IBs tanto parcialmente degradados con proteinasa K (Morell, Bravo et al. 2008) como en condiciones nativas (**Figura 8**). También estudios realizados mediante difracción de rayos X y NMR han confirmado la presencia de estructuras en hoja β cruzada (Wang, Maji et al. 2008; Wasmer, Benkemoun et al. 2009). Así pues, se ha podido confirmar de forma fehaciente que los IBs bacterianos comparten muchas características estructurales y funcionales de los agregados amiloides (de Groot, Sabate et al. 2009; Dasari, Espargaro et al. 2011).

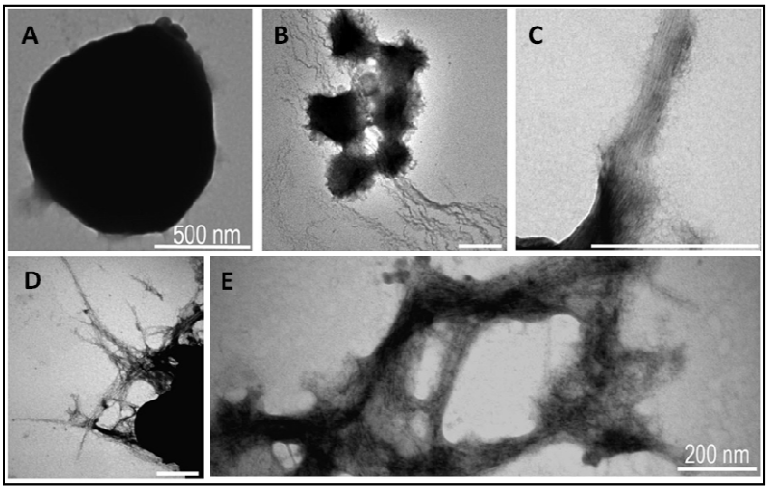

Figura 8. Imágenes de microscopia electrónica de transmisión de IBs parcialmente degradados con proteinasa K (PK). En la imagen A tenemos un IB purificado. Las barras representan 500 nm en A, B y C y 200 nm en D y E. Figura adaptada de (Morell, Bravo et al. 2008).

Aunque la gran mayoría de la proteína presentes en los IBs se encuentra agregada en estructura β, también se ha observado la presencia de estructuras parcialmente desplegadas y proteínas con estructura nativa (Carrio, Gonzalez-Montalban et al. 2005; Ami, Natalello et al. 2006; Ventura and Villaverde 2006). Aunque la distribución en el interior de los IBs de estas estructuras no se conoce todavía, su presencia podría explicar la detección de actividad proteica en estos depósitos bacterianos (Tokatlidis, Dhurjati et al. 1991; Garcia-Fruitos, Gonzalez-Montalban et al. 2005; Garcia-Fruitos, Aris et al. 2007). Esta actividad determina que la agregación de las proteínas recombinantes en el interior de los IBs no necesariamente implica una completa desactivación. En este mismo sentido, se ha observado la coexistencia de polipéptidos activos y correctamente plegados con una organización molecular en hoja β sugiriendo que las zonas de la cadena polipéptidica involucradas en esta estructura no necesariamente perturban la conformación de todos los dominios de la proteína y de esta manera podría mantener el centro activo correctamente plegado y funcional (Garcia-Fruitos, Gonzalez-Montalban et al. 2005). Esta nueva visión de los IBs y sus características abren la posibilidad de poder utilizarlos directamente como biocatalizadores sin la necesidad de purificar previamente la proteína o como nano-partículas (Garcia-Fruitos, Vazquez et al. 2012).

Calidad proteica y equilibrio dinámico con chaperonas

En el interior de una célula bacteriana existe una mezcla compleja de conformaciones proteicas donde solubilidad no implica necesariamente actividad proteica, de la misma manera en el interior de un IB también existen diferentes conformaciones de una misma proteína. Si tenemos en cuenta que el crecimiento volumétrico del IB tiene lugar durante la sobre-expresión de la proteína recombinante, esta heterogeneidad de conformaciones sería el resultado de un desequilibrio entre la deposición proteica y la eliminación de ésta mediante un

intercambio continuo entre las formas solubles e insolubles de las proteínas recombinantes (Carrio, Corchero et al. 1999). Debido a este equilibrio dinámico, en ausencia de síntesis proteica, los IBs citoplasmáticos son casi totalmente desintegrados en pocas horas (Carrio and Villaverde 2001; Gonzalez-Montalban, Garcia-Fruitos et al. 2006) sugiriendo que los IBs actúan como reservorios proteicos de los que se puede extraer proteína recombinante. Así pues, podríamos decir que los IBs podrían ser definidos como reservorios de proteínas, siendo el resultado de la incapacidad de las chaperonas y proteasas para procesar grandes cantidades de proteína mal plegada, donde éstas quedan agrupadas hasta que pueden ser liberadas para poder volver a entrar dentro del control de calidad proteico de la célula cuando sea posible (Carrio and Villaverde 2003). Este equilibrio dinámico entre la fracción agregada y la fracción soluble viene dirigido por un complejo sistema de control de calidad celular donde están implicados los procesos de desagregación, desplegamiento y reactivación proteica (**Figura 9**) (Carrio and Villaverde 2003; Gonzalez-Montalban, Garcia-Fruitos et al. 2006; Garcia-Fruitos, Martinez-Alonso et al. 2007; Sabate, de Groot et al. 2010).

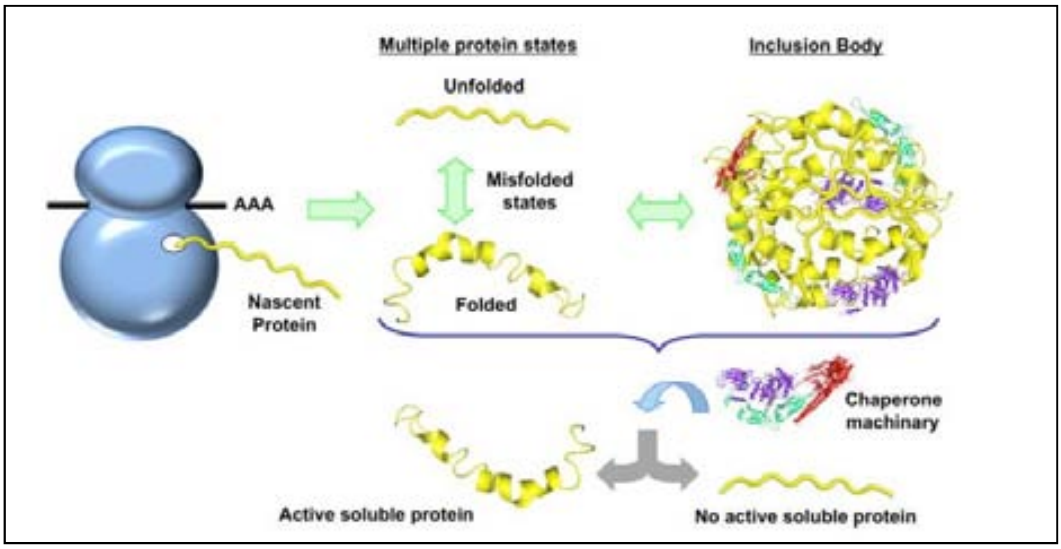

Figura 9. Conformaciones posibles que puede adoptar una proteína en el interior de una célula bacteriana. Una vez la proteína ha sido sintetizada ésta puede adquirir la estructura nativa de manera espontánea o mediante la asistencia de chaperonas. Esta estructura soluble puede agregar mediante interacciones selectivas en el interior del IB, donde pueden coexistir diferentes conformaciones. La maquinaria de calidad proteica puede actuar tanto en las conformaciones solubles como insolubles promoviendo de esta manera un equilibrio dinámico entre fracción soluble e insoluble. Este conjunto de acciones da como resultado la existencia de estructuras proteicas tanto funcionales como inactivas en ambas fracciones (Sabate, de Groot et al. 2010).

MODELOS PROTEICOS UTILIZADOS PARA EL ESTUDIO DE LA AGREGACIÓN *IN VITRO* E *IN VIVO*

Son muchas las proteínas, sin ninguna homología secuencial ni estructural, que pueden auto-ensamblarse formando estructuras amiloides. Entre ellas no únicamente encontramos proteínas asociadas a enfermedades sino también proteínas sin ninguna relación con estas patologías. En esta tesis hemos caracterizado cinética, termodinámica y estructuralmente los agregados formados *in vitro* e *in vivo* de varios péptidos y proteínas modelo.

Por un lado se ha estudiado el proceso de agregación de dos péptidos nativamente desestructurados involucrados con enfermedades conformacionales. El primero de ellos es el péptido amiloide de los islotes (IAPP) que es secretado junto a la insulina por las células β pancreáticas actuando como regulador de la homeostasis de la glucosa, la agregación de este péptido está ampliamente asociada con la diabetes tipo II (Westermark, Andersson et al. 2011). A parte de IAPP también se ha trabajado con el péptido β amiloide, directamente relacionado con la enfermedad de Alzheimer, la demencia más común en adultos (Ballard, Gauthier et al. 2011).

Tal y como se ha comentado anteriormente un gran número de evidencias sugieren que la capacidad de formar fibras amiloides podría ser una propiedad intrínseca y genérica de las cadenas polipeptídicas (Dobson 2003), de esta manera se ha decidido trabajar con SUMO una proteína globular y altamente soluble presente en todos los organismos eucariotas e involucrada en una gran variedad de procesos celulares (Hay 2005). El estudio de esta proteína nos permite ampliar el conocimiento sobre las características que dirigen la agregación de esta clase de proteínas.

Para finalizar hemos trabajado con los priones de *Saccharomyces cerevisiae* [*PSI*$^{+}$] y [*URE3*] y el prión [*Het-s*] del hongo filamentoso *Podospora anserina*. Estos tres priones están muy bien caracterizados y son un excelente modelo para entender los procesos de agregación de los priones infecciosos relacionados con enfermedades.

El estudio de este amplio abanico de péptidos y proteínas nos permite obtener una visión general sobre los procesos de agregación tanto *in vitro* como *in vivo* y ampliar el conocimiento de los mecanismos de formación amiloide.

DISCUSIÓN

BLOQUE I. ESTUDIO DE LA AGREGACIÓN PROTEICA *IN VITRO*. PROPIEDADES BIOFÍSICAS DE LAS FIBRAS AMILOIDES.

El creciente número de trastornos clínicos causados por un mal plegamiento proteico y la formación de fibras amiloides o agregados relacionados con éstas hace que el estudio biofísico de la formación de este tipo de depósitos proteicos sea particularmente atractivo por varios aspectos: En primer lugar estudios *in vitro* de la formación de fibras amiloides permiten, de forma más simple, obtener información esencial para la posterior aplicación y/o comprensión de este tipo de procesos *in vivo*. En segundo lugar los estudios cinéticos y termodinámicos permiten determinar la estructura de este tipo de agregados así como el mecanismo que sigue cada proteína para adquirir la estructura amiloide.

En este primer bloque se han empleado entornos *in vitro* controlados para estudiar los cambios conformacionales que sufren algunos péptidos y/o proteínas al pasar de su estado monomérico soluble a agregados amiloides altamente ordenados. Los resultados obtenidos aportan nuevos conocimientos sobre los mecanismos de formación, las estructuras de los agregados formados así como el papel que juegan diferentes factores internos y externos durante el proceso de agregación.

Los factores determinantes de la agregación son muchos y muy variados, englobando propiedades intrínsecas de la cadena polipeptídica y características del entorno en el que se encuentra el péptido o proteína. Este primer bloque se encuentra dividido en dos capítulos, el primero de ellos basado en el efecto de las propiedades intrínsecas de la cadena polipeptídica y el segundo en el efecto que tienen alteraciones del entorno durante el proceso de agregación.

Para llevar a cabo estos estudios se han utilizado como modelo proteínas y péptidos que no presentan ninguna homología secuencial ni estructural para poder obtener una visión global del efecto de los diferentes determinantes en el proceso de agregación.

CAPÍTULO I: Efecto de la secuencia y la composición aminoacídica en la formación amiloide

El hecho de que un gran número de proteínas sin ninguna homología secuencial ni estructural sean capaces de auto-ensamblarse formando estructuras ricas en hoja β parece indicar que las restricciones que dirigen el plegamiento proteico no son aplicables a la formación de fibras amiloides (Chiti and Dobson 2006; Fernandez-Busquets, de Groot et al. 2008). Las proteínas involucradas en la formación de fibras amiloides pueden ser desde proteínas globulares, con una estructura tridimensional bien definida, hasta proteínas

nativamente desestructuradas. En los dos casos la secuencia y la composición aminoacídica juegan un papel vital durante todo el proceso de agregación.

En este primer capítulo hemos trabajado con tres variantes de la proteína SUMO, una proteína globular altamente soluble, implicada en una gran variedad de procesos celulares y con tres péptidos, intrínsecamente desestructurados, derivados del péptido amiloide de los islotes (IAPP), la acumulación del cual en forma de agregados amiloides está fuertemente relacionada con la degeneración de las células β pancreáticas en la diabetes tipo II (Clark, Cooper et al. 1987).

En proteínas globulares, la agregación en forma de fibras amiloides está altamente favorecida cuando su estructura nativa se ve parcial o totalmente desestabilizada dejando expuestas al solvente zonas altamente amiloidogénicas que previamente se encontraban en el interior proteico (Ivanova, Sawaya et al. 2004; Ventura, Zurdo et al. 2004). Las proteínas SUMO, consideradas como "ubiquitin-like" muestran una estructura común. Dos de las proteínas SUMO estudiadas presentan una elevada homología con una identidad secuencial del 95 %, mientras que la tercera de ellas únicamente presenta un 45 % de identidad secuencial respecto a las otras dos; ésta diferencia secuencial se traduce en diferencias importantes que afectan a la estabilidad de la proteína siendo significativamente inferior frente desnaturalización térmica, con una temperatura de fusión (T_m) aproximada de 52 ºC respecto a los 68 ºC que presentan las otras dos proteínas. La reducción de la estabilidad junto con la presencia de más regiones potencialmente amiloidogénicas favorecen el proceso de agregación de esta proteína. No obstante, y a pesar de estas diferencias, las tres proteínas SUMO estudiadas dan lugar a la formación de agregados si son incubadas en sus respectivas T_m, condiciones de parcial desestabilización. En general las regiones que se encuentran en interfaces tienen más tendencia a agregar (Pechmann, Levy et al. 2009), sugiriendo que la formación de complejos funcionales y la formación de estructuras cuaternarias pueden competir en el interior celular donde las interacciones funcionales representan un camino competitivo a la agregación (Pastore and Temussi 2012). El estudio de estas tres variantes de la proteína SUMO permite demostrar que las mismas regiones utilizadas para establecer las interacciones funcionales y específicas en su estado nativo son las capaces de nuclear el proceso de agregación amiloide. Estos agregados presentan diferencias importantes entre ellos, desde composición en estructura β, diferencias en la unión de colorantes específicos como CR, Th-T y Th-S hasta diferencias morfológicas observadas mediante microscopia electrónica de transmisión (TEM). Así pues, las diferencias secuenciales entre proteínas de la misma familia, aun teniendo una estructura común, afectan directamente tanto a la

estabilidad del estado nativo como a los agregados formados bajo condiciones parcialmente desestabilizantes.

Por otro lado, el hecho de que proteínas esenciales y altamente solubles como SUMO puedan formar agregados amiloides da soporte a la visión de que las proteínas globulares no pueden abolir completamente la competencia entre el plegamiento productivo y la agregación. Así pues, mutaciones genéticas capaces de disminuir la estabilidad de SUMO podría tener graves consecuencias puesto que la disrupción de las vías de SUMO es letal en mamíferos y levaduras. Los resultados obtenidos confirman que la tendencia a agregar es una propiedad intrínseca de, sino todas, la gran mayoría de las cadenas polipeptídicas y que esta tendencia está ligada tanto a la secuencia de la cadena polipeptídica como a las propiedades conformacionales de las proteínas, donde la estabilidad conformacional de la estructura nativa juega un papel vital protegiendo las proteínas de la agregación.

Demostrada la importancia de la estructura terciaria y/o cuaternaria en proteínas globulares nos centramos en el estudio de péptidos intrínsecamente desestructurados (IDPs). El estudio de la agregación de IDPs como el IAPP y sus dos variantes nos ha permitido estudiar el papel que juegan la secuencia, la composición aminoacídica y la dirección de la cadena polipeptídica en la formación de fibras amiloides. Los tres péptidos estudiados forman fibras amiloides bajo condiciones determinadas; no obstante, aun teniendo la misma composición aminoacídica los agregados formados presentan diferencias estructurales, de estabilidad, unen colorantes específicos de distinta manera y poseen citotoxicidades características. Estos estudios nos demuestran que la distribución de las cadenas laterales a lo largo de la secuencia juega un papel esencial, tal y como ocurre en el plegamiento proteico, no únicamente en la estructura final del agregado sino también en el camino que sigue para adquirirlo desde su estado monomérico. La falta de fuertes regiones que dirijan la agregación, otorgando una baja tendencia a agregar a la cadena polipeptídica, como sucede en el caso del péptido diseñado, hace que el proceso de fibrilación se vea ralentizado aunque no se puede evita el auto-ensamblaje, dando lugar también a la formación de estructuras macromoleculares estables. Por otro lado, el estudio de la secuencia reversa muestra inequívocamente que la cadena polipeptídica tiene definitivamente una direccionalidad; así pues, dos péptidos con la misma composición aminoacídica y el mismo perfil hidrofóbico forman fibras amiloides distintas entre sí, mostrando que las fibras obtenidas por una proteína natural y su versión reversa probablemente no son más similares en su estructura que las formadas por dos péptidos amiloides sin relación secuencial. El estudio confirma que, aparte del perfil hidrofóbico y de la presencia de zonas amiloidogénicas, la dirección de la cadena polipeptídica promueve diferencias tanto en el mecanismo de agregación como en la estructura de las fibras maduras.

Los resultados de este primer capítulo nos permiten confirmar que, tanto en proteínas globulares como en proteínas intrínsecamente desestructuradas, la tendencia a formar estructuras amiloides se encuentra altamente ligada a la secuencia y a las propiedades conformacionales de las proteínas, donde regiones específicas de la cadena polipeptídica son las encargadas de dirigir la vía de auto-ensamblaje y de definir la estructura final de estos agregados.

CAPÍTULO II: Efecto del micro-entorno en la formación de fibras amiloides

No únicamente las propiedades intrínsecas a la cadena polipeptídica influyen en el proceso de agregación sino que cambios en el medio o micro-entorno celular pueden jugar un papel determinante en este proceso. Se ha observado que variaciones en parámetros como agitación, pH, temperatura, concentración proteica y fuerza iónica no afectan solamente al plegamiento de proteínas sino que también pueden alterar el proceso de agregación y formación amiloide tanto cinética, termodinámica como estructuralmente (Lopez De La Paz, Goldie et al. 2002; Kumar, Mohanty et al. 2007).

Este segundo capítulo está basado en el estudio del efecto de la temperatura y la agitación durante el proceso de agregación, utilizando como modelos proteicos las proteínas priónicas Sup35 y Ure2 de la levadura *Saccharomyces cerevisiae* y Het-s del hongo filamentoso *Podospora anserina*. Los tres priones elegidos representan modelos simples que pueden ser utilizados para la comprensión y la obtención de información esencial del comportamiento de los priones relacionados con enfermedades en mamíferos. Por otro lado, y con la finalidad de estudiar el efecto de las membranas (que inequívocamente forman parte del entorno celular en los procesos de auto-ensamblaje amiloide), también hemos estudiado el efecto de la presencia de membranas artificiales (liposomas) durante el proceso de agregación del péptido β amiloide, directamente relacionado con la enfermedad de Alzheimer (Ballard, Gauthier et al. 2011).

Los resultados obtenidos indican, en todos los casos, que tanto la estructura final de las fibras como la transición desde su estado monomérico a una estructura en hoja β ordenada es altamente dependiente de la temperatura y de la agitación en el caso de HET-s. Estas variaciones afectan de manera característica a cada una de las proteínas priónicas estudiadas mostrando que la formación de fibras amiloides, aun siguiendo un mecanismo de nucleación común, depende de varios factores como la naturaleza del núcleo que dará paso al inicio del proceso y de las propiedades de la proteína soluble que será incorporada a los extremos de las

fibras. Dependiendo de la naturaleza de la proteína cada uno de estos factores influirá de una manera determinada.

Uno de los principales interrogantes sobre la formación de fibras amiloides es el mecanismo que siguen las proteínas para adquirir esta estructura altamente ordenada a partir de su estado monomérico. El estudio del efecto de factores como la temperatura y la agitación nos permiten obtener información sobre los parámetros cinéticos y termodinámicos de la formación de fibras amiloides así como de las vías de auto-ensamblaje. La caracterización de estos parámetros junto con las propiedades conformacionales de las fibras amiloides obtenidas hacen posible la comprensión de los principios básicos de los mecanismos y las interacciones que promueven el auto-ensamblaje durante los procesos de fibrilación permitiendo proponer un modelo de agregación para cada uno de los priones estudiados.

Los estudios realizados muestran que las vías por las que diferentes proteínas priónicas, inicialmente solubles, llegan a adquirir estados amiloides difieren de forma significativa, al menos en términos cinéticos y termodinámicos.

No únicamente los parámetros comentados anteriormente pueden influir durante los procesos de agregación. En entornos celulares, donde la concentración de macromoléculas es muy elevada, las colisiones y las interacciones entre moléculas son constantes. El conocimiento del mecanismo de auto-ensamblaje de una proteína o péptido nos permite determinar como se ve influido éste por la presencia de otras moléculas como por ejemplo membranas lipídicas. Uno de los mecanismos propuestos para la neurotoxicidad del péptido β amiloide (Aβ) es su capacidad disruptiva de membranas celulares y la despolarización de éstas mediada por la formación de canales iónicos o por un aumento en la conductancia de la membrana en general (Arispe, Pollard et al. 1993; Arispe, Rojas et al. 1993; Lin, Bhatia et al. 2001; Kayed, Sokolov et al. 2004; Demuro, Mina et al. 2005); estos factores dan como resultado una alteración de la homeostasis y una desregulación de la transducción de señal neuronal que conduce a la muerte celular (Arispe, Pollard et al. 1993; Lashuel, Hartley et al. 2002; Florent-Bechard, Desbene et al. 2009). La utilización de liposomas como modelo de membrana biológica permite determinar de forma simple los parámetros cinéticos clarificando el mecanismo y las consecuencias de la interacción de Aβ con membranas lipídicas. A su tiempo, la utilización de liposomas con diferente carga superficial nos ha permitido identificar el efecto de la carga de la bicapa en la agregación amiloide. Los resultados muestran que el proceso de agregación de Aβ40 se ve ralentizado por la presencia de liposomas y que este efecto es dependiente de la carga. El hecho que el principal efecto sea sobre el proceso de nucleación, manteniendo el proceso de elongación relativamente intacto, indica que la interacción se podría producir antes de la formación de las fibras, produciéndose la

incorporación de monómeros de Aβ40 en la membrana liposomal y promoviendo así su disrupción. Estos resultados fomentan la visión de que son los primeros estadios de la agregación los causantes de la citotoxicidad celular, ya que estos son los capaces de interaccionar con las membranas lipídicas y provocar daño celular.

BLOQUE II. ESTUDIO DE LA AGREGACIÓN PROTEICA *IN VIVO*. PROPIEDADES BIOFÍSICAS DE LOS CUERPOS DE INCLUSIÓN.

El estudio *in vivo* de la agregación amiloide es un proceso altamente complejo. La formación de cuerpos de inclusión (IBs) en el interior de células bacterianas ha sido tradicionalmente relacionada con la formación de interacciones hidrofóbicas no específicas entre cadenas polipeptídicas total o parcialmente desplegadas. En los últimos años esta visión ha cambiado radicalmente debido al gran número de evidencias que sugieren que estos depósitos intracelulares comparten características estructurales con las altamente ordenadas y en muchos casos patógenas fibras amiloides (Carrio, Gonzalez-Montalban et al. 2005; Doglia, Ami et al. 2008; Morell, Bravo et al. 2008; Wang, Maji et al. 2008). Así pues, la fehaciente demostración que los agregados proteicos resultantes de la expresión recombinante de proteínas amiloides en organismos procariotas comparten muchas de las propiedades y características amiloides de la agregación producida en organismos superiores hace de éstos, modelos ideales para poder estudiar la agregación amiloide *in vivo*.

Este segundo bloque está centrado en el estudio biofísico y fisicoquímico de los agregados formados *in vivo* por el péptido amiloide Aβ42 y un mutante de éste con baja capacidad de agregación (de Groot, Aviles et al. 2006), los priones de *Saccharomyces cerevisiae* [*PSI*$^{+}$] y [*URE3*], y el prion de *Podospora anserina* [*Het-s*], que codifican las proteínas Sup35p, Ure2p y HET-s respectivamente.

Siguiendo las evidencias anteriormente mencionadas, se procedió a la confirmación de la presencia amiloide en los IBs de las proteínas seleccionadas. En una primera fase se determinó mediante CD y FT-IR la estructura secundaria de los IBs, comprobando que éstos presentaban espectros muy parecidos a los obtenidos al estudiar las fibras amiloides relacionadas con enfermedades humanas, y confirmando que estos depósitos proteicos contenían una arquitectura rica en hoja β. La presencia de estructura secundaria regular en el interior de los IBs implica la existencia de interacciones específicas entre las cadenas polipeptídicas que los forman, estabilizando la estructura del agregado de la misma manera que ocurre en fibras amiloides. Para confirmar este punto calculamos la estabilidad conformacional de los IBs frente a desnaturalización química. Las diferencias en estabilidad observadas indican que, aunque poseen una morfología común y una estructura secundaria rica en hoja β, estos agregados intracelulares formados por diferentes cadenas polipeptídicas no deben ser tratados como entidades únicas, sino que la estructura depende de propiedades intrínsecas y especificas de las proteínas que los forman, hasta tal punto que una única mutación puntual puede alterar drásticament la estabilidad de estos agregados.

Para poder afirmar que la estructura rica en hoja β se encontraba organizada en una estructura amiloide utilizamos los colorantes Rojo Congo (CR), Thioflavina T (Th-T) y Thioflavina S (Th-S) considerados como específicos y de elección en la detección de estructuras amilodes. En presencia de IBs formados por las proteínas a estudio se observó que la absorbancia de CR aumentaba y el máximo se desplazaba hacia longitudes de onda mayores apareciendo la banda específica amiloide, aumentaba la emisión de fluorescencia de Th-T y la tinción con Th-S permitía mostrar las zonas ricas en material fibrilar apareciendo la fluorescencia color verde característica de las fibras amiloides. Así pues, y en consonancia con la estructura secundaria observada y la existencia de interacciones selectivas, la unión de colorantes específicos indica que los IBs estudiados poseen estructura amiloide. Otra característica importante de las fibras amiloides es su capacidad de acelerar la conversión de sus respectivas especies solubles a fibras amiloides. En el trabajo realizado hemos podido determinar cuantitativamente que los IBs purificados tienen efectos muy similares a los producidos por las fibras amiloides y actúan reduciendo la fase de latencia de manera selectiva, ya que la formación amiloide se ve acelerada únicamente por IBs homólogos a la proteína soluble. Esto confirma que, del mismo modo que en las fibras amiloides, existe un reconocimiento específico entre las especies solubles y los IBs.

Los resultados obtenidos indican que los contactos intra- e inter-moleculares característicos de las fibras amiloides de cada una de las proteínas estudiadas están también presentes, al menos, en una fracción de las cadenas polipeptídicas que se encuentran en el interior de los agregados intracelulares formados en bacteria. La caracterización biofísica de los agregados formados por los distintos priones estudiados sugiere que estas proteínas podrían tener acceso a conformaciones priónicas cuando son expresadas de manera recombinante en bacterias. Una de las características principales de las proteínas priónicas es su capacidad de auto-perpetuarse *in vivo* y por lo tanto de infectar. Debido a las propiedades amiloides de las cadenas polipeptídicas que se encuentran en el interior de los IBs estudiados estas podrían producir dicha infección. En el caso de la proteína Sup35 esta propiedad puede ser evaluada mediante el estudio de la conversión de células de levadura [*psi*$^{-}$] a [*PSI*$^{+}$]. Para comprobar esta suposición se realizaron los consiguientes estudios que confirmaron la capacidad de infección de los IBs de Sup35 demostrando la formación de conformaciones priónicas en el interior bacteriano, donde la maquinaria proteica natural de las bacterias es suficiente para formar estas variantes infecciosas *per se*. En el bloque anterior observamos como la temperatura de formación de los agregados priónicos *in vitro* influye en las propiedades conformacionales de las fibras obtenidas. Ha sido demostrado que la temperatura puede alterar las propiedades de Sup35 como prión dando lugar a la obtención de diferentes

fenotipos [*PSI*$^{+}$] (Tanaka, Collins et al. 2006). En nuestro caso, y en concordancia con estos resultados, la reducción de la temperatura de expresión de 37 ºC a 18 ºC produce un aumento significativo de la proporción de colonias con un fuerte fenotipo [*PSI*$^{+}$], sugiriendo que las propiedades infectivas de las proteínas priónicas producidas en bacterias pueden ser moduladas mediante la regulación de las condiciones de producción. El hecho que los IBs presenten conformaciones infecciosas en su interior fácilmente modulables, los elevados niveles de proteína que acumulan y su fácil purificación, sugiere que éstos podrían ser una fuente fácil y rápida de obtener un amplio abanico de partículas priónicas.

Tal y como hemos podido observar, parece ser que la estructura fibrilar obtenida in *vitro* es conservada en los IBs, confirmando la observación anterior de que las bacterias son capaces de producir conformaciones priónicas en el interior de los depósitos proteicos y pueden ser moduladas mediante las condiciones de expresión. Todos estos resultados sugieren claramente que las células bacterianas pueden ser utilizadas como un sistema rápido, simple y biológicamente relevante para el estudio *in vivo* del auto-ensamblaje proteico, la toxicidad y la infectividad de proteínas amiloides. Es conocido que la formación de estructuras priónicas infecciosas está altamente relacionada con la maquinaria celular (Chien, Weissman et al. 2004), así pues las bacterias pueden ser consideradas como sistemas también idoneas para el estudi del efecto de chaperonas como ClpB (homologa a Hsp104), chaperonas eucariotas recombinantes y compuestos anti-aagregacionales durante el proceso de formación de los amiloides en sistemas celulares.

Siguiendo este propósito, hemos desarrollado un método rápido, cuantitativo y no invasivo para la detección *in vivo* de los agregados intracelulares formados en bacterias. Aunque muchos colorantes son útiles para la detección de amiloides los más utilizados son el CR, Th-T y Th-S. El método desarrollado está basado en la habilidad de la Th-S para penetrar las membranas celulares y unirse a los depósitos proteicos. Con el afán de demostrar la universalidad del método, para este estudio se decidió trabajar con varios modelos amiloidogénicos sin ninguna relación estructural ni secuencial entre ellos y detectar la unión de Th-S mediante varios métodos como microscopia óptica de fluorescencia, microscopia confocal y espectrofluorometría, confirmando así que la unión *in vivo* de Th-S es dependiente de la agregación pero independiente del tipo de proteína, pudiendo ser fácilmente monitorizada. A pesar de su fácil detección estos métodos no sirven para análisis a gran escala. Es por este motivo que se ha utilizado la citometría de flujo como método de elección que permite analizar poblaciones enteras de células en muy poco tiempo (Morell, Espargaro et al. 2008), permitiendo determinar la presencia de agregados amiloides en células bacterianas marcadas con Th-S de forma rápida, con un elevado rendimiento cuantitativo, no invasivo,

sensible y selectivo sin la necesidad de marcadores proteicos como por ejemplo la GFP que podrían influir en el proceso de agregación.

CONCLUSIONES

CONCLUSIONES

BLOQUE I: ESTUDIO DE LA AGREGACIÓN PROTEICA *IN VITRO*. PROPIEDADES BIOFÍSICAS DE LAS FIBRAS AMILOIDES.

CAPÍTULO I: Efecto de la secuencia y la composición aminoacídica en la formación amiloide

1. Tanto en proteínas estructuradas como en proteínas intrínsecamente desestructuradas la secuencia polipeptídica y la composición aminoacídica juegan un papel esencial no únicamente durante todo su proceso de agregación sino también en la estructura final de los agregados amiloides obtenidos.
2. En el caso de proteínas globulares la estabilidad de su estructura nativa ejerce un papel protector frente la agregación ya que las interacciones funcionales representan un camino competitivo a ésta.
3. Regiones específicas de la cadena polipeptídica son las encargadas de dirigir la vía de auto-ensamblaje y de definir la estructura final de los agregados.

CAPÍTULO II: Efecto del micro-entorno en la formación de fibras amiloides

1. Los factores externos estudiados afectan tanto la cinética de agregación como la estructura de los agregados obtenidos de manera característica para cada una de las proteínas estudiadas.
2. La obtención de los parámetros cinéticos y termodinámicos junto con las propiedades conformacionales de las fibras amiloides obtenidas nos permiten obtener información esencial sobre el mecanismo y las interacciones que promueven el auto-ensamblaje proteico y poder proponer modelos de agregación.
3. Los resultados obtenidos indican que, aun y adquiriendo estructuras finales comunes, las vías por las que diferentes proteínas adquieren esta estructura difiere significativamente.
4. Independientemente del mecanismo de agregación puede dilucidarse una relación directa entre la velocidad del proceso de agregación y la formación de agregados amorfos o fibras altamente organizadas.

BLOQUE II. ESTUDIO DE LA AGREGACIÓN PROTEICA *IN VIVO*. PROPIEDADES BIOFÍSICAS DE LOS CUERPOS DE INCLUSIÓN.

1. La estructura de los IBs estudiados depende de las propiedades intrínsecas de las cadenas polipeptídicas de las cuales están mayoritariamente formados. Así pues, se puede observar una relación directa entre la estabilidad específica de los IBs y la estabilidad de las fibras amiloides formadas por cada proteína.
2. Los IBs presentan estructuras ricas en hoja β y comparten muchas características en común con las fibras amiloides obtenidas *in vitro*.
3. Factores externos como la temperatura no únicamente afectan a los agregados *in vitro* sino que también determinan los agregados formados *in vivo*, mostrando que, en el caso de proteínas con capacidad priónica, el interior bacteriano permite la formación de estructuras amiloides infecciosas modulables mediante las condiciones de formación tal y como puede suceder *in vitro*.
4. Los estudios realizados validan los sistemas bacterianos como modelos rápidos, simples y de relevancia biológica para el estudio de la agregación proteica.
5. Se ha desarrollado un método rápido, cuantitativo y no invasivo para la detección *in vivo* de los agregados intracelulares formados en bacterias bajo la consideración que los agregados formados mantienen las propiedades y características de las fibras amiloides.

REFERENCIAS

Ami, D., A. Natalello, et al. (2006). "Structural analysis of protein inclusion bodies by Fourier transform infrared microspectroscopy." Biochim Biophys Acta 1764(4): 793-9.

Andersen, C. B., H. Yagi, et al. (2009). "Branching in amyloid fibril growth." Biophys J 96(4): 1529-36.

Arispe, N., H. B. Pollard, et al. (1993). "Giant multilevel cation channels formed by Alzheimer disease amyloid beta-protein [A beta P-(1-40)] in bilayer membranes." Proc Natl Acad Sci U S A 90(22): 10573-7.

Arispe, N., E. Rojas, et al. (1993). "Alzheimer disease amyloid beta protein forms calcium channels in bilayer membranes: blockade by tromethamine and aluminum." Proc Natl Acad Sci U S A 90(2): 567-71.

Azevedo, E. P., H. M. Pereira, et al. (2011). "Dissecting the structure, thermodynamic stability, and aggregation properties of the A25T transthyretin (A25T-TTR) variant involved in leptomeningeal amyloidosis: identifying protein partners that co-aggregate during A25T-TTR fibrillogenesis in cerebrospinal fluid." Biochemistry 50(51): 11070-83.

Baker, D. (2000). "A surprising simplicity to protein folding." Nature 405(6782): 39-42.

Balguerie, A., S. Dos Reis, et al. (2004). "The sequences appended to the amyloid core region of the HET-s prion protein determine higher-order aggregate organization in vivo." J Cell Sci 117(Pt 12): 2599-610.

Ballard, C., S. Gauthier, et al. (2011). "Alzheimer's disease." Lancet 377(9770): 1019-31.

Belli, M., M. Ramazzotti, et al. (2011). "Prediction of amyloid aggregation in vivo." EMBO Rep 12(7): 657-63.

Bernstein, S. L., N. F. Dupuis, et al. (2009). "Amyloid-beta protein oligomerization and the importance of tetramers and dodecamers in the aetiology of Alzheimer's disease." Nat Chem 1(4): 326-31.

Berson, J. F., A. C. Theos, et al. (2003). "Proprotein convertase cleavage liberates a fibrillogenic fragment of a resident glycoprotein to initiate melanosome biogenesis." J Cell Biol 161(3): 521-33.

Bhak, G., Y. J. Choe, et al. (2009). "Mechanism of amyloidogenesis: nucleation-dependent fibrillation versus double-concerted fibrillation." BMB Rep 42(9): 541-51.

Bieschke, J., M. Herbst, et al. (2011). "Small-molecule conversion of toxic oligomers to nontoxic beta-sheet-rich amyloid fibrils." Nat Chem Biol 8(1): 93-101.

Bolognesi, B., J. R. Kumita, et al. (2010). "ANS binding reveals common features of cytotoxic amyloid species." ACS Chem Biol 5(8): 735-40.

Brown, C. J., S. Takayama, et al. (2002). "Evolutionary rate heterogeneity in proteins with long disordered regions." J Mol Evol 55(1): 104-10.

Bryan, A. W., Jr., M. Menke, et al. (2009). "BETASCAN: probable beta-amyloids identified by pairwise probabilistic analysis." PLoS Comput Biol 5(3): e1000333.

Bucciantini, M., E. Giannoni, et al. (2002). "Inherent toxicity of aggregates implies a common mechanism for protein misfolding diseases." Nature 416(6880): 507-11.

Buell, A. K., G. G. Tartaglia, et al. (2009). "Position-dependent electrostatic protection against protein aggregation." Chembiochem 10(8): 1309-12.

Calamai, M., N. Taddei, et al. (2003). "Relative influence of hydrophobicity and net charge in the aggregation of two homologous proteins." Biochemistry 42(51): 15078-83.

Carrio, M., N. Gonzalez-Montalban, et al. (2005). "Amyloid-like properties of bacterial inclusion bodies." J Mol Biol 347(5): 1025-37.

Carrio, M. M., J. L. Corchero, et al. (1998). "Dynamics of in vivo protein aggregation: building inclusion bodies in recombinant bacteria." FEMS Microbiol Lett 169(1): 9-15.

Carrio, M. M., J. L. Corchero, et al. (1999). "Proteolytic digestion of bacterial inclusion body proteins during dynamic transition between soluble and insoluble forms." Biochim Biophys Acta 1434(1): 170-6.

Carrio, M. M. and A. Villaverde (2001). "Protein aggregation as bacterial inclusion bodies is reversible." FEBS Lett 489(1): 29-33.

Carrio, M. M. and A. Villaverde (2003). "Role of molecular chaperones in inclusion body formation." FEBS Lett 537(1-3): 215-21.

Carulla, N., G. L. Caddy, et al. (2005). "Molecular recycling within amyloid fibrils." Nature 436(7050): 554-8.

Castillo, V., R. Grana-Montes, et al. (2011). "Prediction of the aggregation propensity of proteins from the primary sequence: aggregation properties of proteomes." Biotechnol J 6(6): 674-85.

Castillo, V. and S. Ventura (2009). "Amyloidogenic regions and interaction surfaces overlap in globular proteins related to conformational diseases." PLoS Comput Biol 5(8): e1000476.

Caughey, B. and G. S. Baron (2006). "Prions and their partners in crime." Nature 443(7113): 803-10.

Claessen, D., R. Rink, et al. (2003). "A novel class of secreted hydrophobic proteins is involved in aerial hyphae formation in Streptomyces coelicolor by forming amyloid-like fibrils." Genes Dev 17(14): 1714-26.

Clark, A., G. J. Cooper, et al. (1987). "Islet amyloid formed from diabetes-associated peptide may be pathogenic in type-2 diabetes." Lancet 2(8553): 231-4.

Cohen, S. I., M. Vendruscolo, et al. (2011). "Nucleated polymerization with secondary pathways. III. Equilibrium behavior and oligomer populations." J Chem Phys 135(6): 065107.

Cohen, S. I., M. Vendruscolo, et al. (2011). "Nucleated polymerization with secondary pathways. II. Determination of self-consistent solutions to growth processes described by non-linear master equations." J Chem Phys 135(6): 065106.

Cohen, S. I., M. Vendruscolo, et al. (2011). "Nucleated polymerization with secondary pathways. I. Time evolution of the principal moments." J Chem Phys 135(6): 065105.

Colby, D. W. and S. B. Prusiner (2011). "Prions." Cold Spring Harb Perspect Biol 3(1): a006833.

Conchillo-Sole, O., N. S. de Groot, et al. (2007). "AGGRESCAN: a server for the prediction and evaluation of "hot spots" of aggregation in polypeptides." BMC Bioinformatics 8: 65.

Coustou, V., C. Deleu, et al. (1997). "The protein product of the het-s heterokaryon incompatibility gene of the fungus Podospora anserina behaves as a prion analog." Proc Natl Acad Sci U S A 94(18): 9773-8.

Creighton, T. E. (1993). "Proteins: structures and molecular properties." W.H.Freeman.

Chapman, M. R., L. S. Robinson, et al. (2002). "Role of Escherichia coli curli operons in directing amyloid fiber formation." Science 295(5556): 851-5.

Chernoff, Y. O. (2004). "Amyloidogenic domains, prions and structural inheritance: rudiments of early life or recent acquisition?" Curr Opin Chem Biol 8(6): 665-71.

Chien, P., J. S. Weissman, et al. (2004). "Emerging principles of conformation-based prion inheritance." Annu Rev Biochem 73: 617-56.

Chiti, F. and C. M. Dobson (2006). "Protein misfolding, functional amyloid, and human disease." Annu Rev Biochem 75: 333-66.

Chiti, F., M. Stefani, et al. (2003). "Rationalization of the effects of mutations on peptide and protein aggregation rates." Nature 424(6950): 805-8.

Chiti, F., N. Taddei, et al. (2002). "Kinetic partitioning of protein folding and aggregation." Nat Struct Biol 9(2): 137-43.

Chiti, F., P. Webster, et al. (1999). "Designing conditions for in vitro formation of amyloid protofilaments and fibrils." Proc Natl Acad Sci U S A 96(7): 3590-4.

Dasari, M., A. Espargaro, et al. (2011). "Bacterial Inclusion Bodies of Alzheimer's Disease beta-Amyloid Peptides Can Be Employed To Study Native-Like Aggregation Intermediate States." Chembiochem.

de Groot, N. S., F. X. Aviles, et al. (2006). "Mutagenesis of the central hydrophobic cluster in Abeta42 Alzheimer's peptide. Side-chain properties correlate with aggregation propensities." FEBS J 273(3): 658-68.

de Groot, N. S., R. Sabate, et al. (2009). "Amyloids in bacterial inclusion bodies." Trends Biochem Sci 34(8): 408-16.

Demuro, A., E. Mina, et al. (2005). "Calcium dysregulation and membrane disruption as a ubiquitous neurotoxic mechanism of soluble amyloid oligomers." J Biol Chem 280(17): 17294-300.

Dill, K. A. and H. S. Chan (1997). "From Levinthal to pathways to funnels." Nat Struct Biol 4(1): 10-9.

Dinner, A. R., A. Sali, et al. (2000). "Understanding protein folding via free-energy surfaces from theory and experiment." Trends Biochem Sci 25(7): 331-9.

Dobson, C. M. (2001). "The structural basis of protein folding and its links with human disease." Philos Trans R Soc Lond B Biol Sci 356(1406): 133-45.

Dobson, C. M. (2002). "Getting out of shape." Nature 418(6899): 729-30.

Dobson, C. M. (2003). "Protein folding and misfolding." Nature 426(6968): 884-90.

Doglia, S. M., D. Ami, et al. (2008). "Fourier transform infrared spectroscopy analysis of the conformational quality of recombinant proteins within inclusion bodies." Biotechnol J 3(2): 193-201.

DuBay, K. F., A. P. Pawar, et al. (2004). "Prediction of the absolute aggregation rates of amyloidogenic polypeptide chains." J Mol Biol 341(5): 1317-26.

Dunker, A. K., I. Silman, et al. (2008). "Function and structure of inherently disordered proteins." Curr Opin Struct Biol 18(6): 756-64.

Dusa, A., J. Kaylor, et al. (2006). "Characterization of oligomers during alpha-synuclein aggregation using intrinsic tryptophan fluorescence." Biochemistry 45(8): 2752-60.

Dyson, H. J., P. E. Wright, et al. (2006). "The role of hydrophobic interactions in initiation and propagation of protein folding." Proc Natl Acad Sci U S A 103(35): 13057-61.

Ellis, R. J. and A. P. Minton (2003). "Cell biology: join the crowd." Nature 425(6953): 27-8.

Espargaro, A., V. Castillo, et al. (2008). "The in vivo and in vitro aggregation properties of globular proteins correlate with their conformational stability: the SH3 case." J Mol Biol 378(5): 1116-31.

Esteras-Chopo, A., L. Serrano, et al. (2005). "The amyloid stretch hypothesis: recruiting proteins toward the dark side." Proc Natl Acad Sci U S A 102(46): 16672-7.

Fandrich, M. and C. M. Dobson (2002). "The behaviour of polyamino acids reveals an inverse side chain effect in amyloid structure formation." EMBO J 21(21): 5682-90.

Ferguson, N., J. Becker, et al. (2006). "General structural motifs of amyloid protofilaments." Proc Natl Acad Sci U S A 103(44): 16248-53.

Fernandez-Busquets, X., N. S. de Groot, et al. (2008). "Recent structural and computational insights into conformational diseases." Curr Med Chem 15(13): 1336-49.

Fernandez-Escamilla, A. M., F. Rousseau, et al. (2004). "Prediction of sequence-dependent and mutational effects on the aggregation of peptides and proteins." Nat Biotechnol 22(10): 1302-6.

Fersht, A. R. (2000). "Transition-state structure as a unifying basis in protein-folding mechanisms: contact order, chain topology, stability, and the extended nucleus mechanism." Proc Natl Acad Sci U S A 97(4): 1525-9.

Florent-Bechard, S., C. Desbene, et al. (2009). "The essential role of lipids in Alzheimer's disease." Biochimie 91(6): 804-9.

Fowler, D. M., A. V. Koulov, et al. (2007). "Functional amyloid--from bacteria to humans." Trends Biochem Sci 32(5): 217-24.

Garcia-Fruitos, E., A. Aris, et al. (2007). "Localization of functional polypeptides in bacterial inclusion bodies." Appl Environ Microbiol 73(1): 289-94.

Garcia-Fruitos, E., N. Gonzalez-Montalban, et al. (2005). "Aggregation as bacterial inclusion bodies does not imply inactivation of enzymes and fluorescent proteins." Microb Cell Fact 4: 27.

Garcia-Fruitos, E., M. Martinez-Alonso, et al. (2007). "Divergent genetic control of protein solubility and conformational quality in Escherichia coli." J Mol Biol 374(1): 195-205.

Garcia-Fruitos, E., E. Vazquez, et al. (2012). "Bacterial inclusion bodies: making gold from waste." Trends Biotechnol 30(2): 65-70.

Georgescauld, F., R. Sabate, et al. (2011). "Aggregation of the neuroblastoma-associated mutant (S120G) of the human nucleoside diphosphate kinase-A/NM23-H1 into amyloid fibrils." Naunyn Schmiedebergs Arch Pharmacol 384(4-5): 373-81.

Gonzalez-Montalban, N., E. Garcia-Fruitos, et al. (2006). "The chaperone DnaK controls the fractioning of functional protein between soluble and insoluble cell fractions in inclusion body-forming cells." Microb Cell Fact 5: 26.

Halfmann, R., D. F. Jarosz, et al. (2012). "Prions are a common mechanism for phenotypic inheritance in wild yeasts." Nature 482(7385): 363-8.

Harper, J. D. and P. T. Lansbury, Jr. (1997). "Models of amyloid seeding in Alzheimer's disease and scrapie: mechanistic truths and physiological consequences of the time-dependent solubility of amyloid proteins." Annu Rev Biochem 66: 385-407.

Harper, J. D., C. M. Lieber, et al. (1997). "Atomic force microscopic imaging of seeded fibril formation and fibril branching by the Alzheimer's disease amyloid-beta protein." Chem Biol 4(12): 951-9.

Hart, R. A., U. Rinas, et al. (1990). "Protein composition of Vitreoscilla hemoglobin inclusion bodies produced in Escherichia coli." J Biol Chem 265(21): 12728-33.

Hay, R. T. (2005). "SUMO: a history of modification." Mol Cell 18(1): 1-12.

Hurle, M. R., L. R. Helms, et al. (1994). "A role for destabilizing amino acid replacements in light-chain amyloidosis." Proc Natl Acad Sci U S A 91(12): 5446-50.

Invernizzi, G., E. Papaleo, et al. (2012). "Protein aggregation: mechanisms and functional consequences." Int J Biochem Cell Biol 44(9): 1541-54.

Ivanova, M. I., M. R. Sawaya, et al. (2004). "An amyloid-forming segment of beta2-microglobulin suggests a molecular model for the fibril." Proc Natl Acad Sci U S A 101(29): 10584-9.

Jahn, T. R. and S. E. Radford (2008). "Folding versus aggregation: polypeptide conformations on competing pathways." Arch Biochem Biophys 469(1): 100-17.

Jarrett, J. T. and P. T. Lansbury, Jr. (1993). "Seeding "one-dimensional crystallization" of amyloid: a pathogenic mechanism in Alzheimer's disease and scrapie?" Cell 73(6): 1055-8.

Jin, M., N. Shepardson, et al. (2011). "Soluble amyloid beta-protein dimers isolated from Alzheimer cortex directly induce Tau hyperphosphorylation and neuritic degeneration." Proc Natl Acad Sci U S A 108(14): 5819-24.

Kayed, R., Y. Sokolov, et al. (2004). "Permeabilization of lipid bilayers is a common conformation-dependent activity of soluble amyloid oligomers in protein misfolding diseases." J Biol Chem 279(45): 46363-6.

Kaylor, J., N. Bodner, et al. (2005). "Characterization of oligomeric intermediates in alpha-synuclein fibrillation: FRET studies of Y125W/Y133F/Y136F alpha-synuclein." J Mol Biol 353(2): 357-72.

Kelly, J. W. and W. E. Balch (2003). "Amyloid as a natural product." J Cell Biol 161(3): 461-2.

Knowles, T. P., C. A. Waudby, et al. (2009). "An analytical solution to the kinetics of breakable filament assembly." Science 326(5959): 1533-7.

Kodali, R. and R. Wetzel (2007). "Polymorphism in the intermediates and products of amyloid assembly." Curr Opin Struct Biol 17(1): 48-57.

Krebs, M. R., L. A. Morozova-Roche, et al. (2004). "Observation of sequence specificity in the seeding of protein amyloid fibrils." Protein Sci 13(7): 1933-8.

Kumar, S., S. K. Mohanty, et al. (2007). "Mechanism of formation of amyloid protofibrils of barstar from soluble oligomers: evidence for multiple steps and lateral association coupled to conformational conversion." J Mol Biol 367(4): 1186-204.

Lashuel, H. A., D. Hartley, et al. (2002). "Neurodegenerative disease: amyloid pores from pathogenic mutations." Nature 418(6895): 291.

Levinthal, C. (1968). "Are there pathways for protein folding?" J Chim Phys 65: 44-45.

Lin, H., R. Bhatia, et al. (2001). "Amyloid beta protein forms ion channels: implications for Alzheimer's disease pathophysiology." FASEB J 15(13): 2433-44.

Lomakin, A., D. B. Teplow, et al. (1997). "Kinetic theory of fibrillogenesis of amyloid beta-protein." Proc Natl Acad Sci U S A 94(15): 7942-7.

Lopez De La Paz, M., K. Goldie, et al. (2002). "De novo designed peptide-based amyloid fibrils." Proc Natl Acad Sci U S A 99(25): 16052-7.

Lopez de la Paz, M. and L. Serrano (2004). "Sequence determinants of amyloid fibril formation." Proc Natl Acad Sci U S A 101(1): 87-92.

Maddelein, M. L., S. Dos Reis, et al. (2002). "Amyloid aggregates of the HET-s prion protein are infectious." Proc Natl Acad Sci U S A 99(11): 7402-7.

Makin, O. S., E. Atkins, et al. (2005). "Molecular basis for amyloid fibril formation and stability." Proc Natl Acad Sci U S A 102(2): 315-20.

Maurer-Stroh, S., M. Debulpaep, et al. (2010). "Exploring the sequence determinants of amyloid structure using position-specific scoring matrices." Nat Methods 7(3): 237-42.

McGlinchey, R. P., D. Kryndushkin, et al. (2011). "Suicidal [PSI+] is a lethal yeast prion." Proc Natl Acad Sci U S A 108(13): 5337-41.

Monsellier, E., M. Ramazzotti, et al. (2008). "Aggregation propensity of the human proteome." PLoS Comput Biol 4(10): e1000199.

Morell, M., R. Bravo, et al. (2008). "Inclusion bodies: specificity in their aggregation process and amyloid-like structure." Biochim Biophys Acta 1783(10): 1815-25.

Morell, M., A. Espargaro, et al. (2008). "Study and selection of in vivo protein interactions by coupling bimolecular fluorescence complementation and flow cytometry." Nat Protoc 3(1): 22-33.

Munishkina, L. A., J. Henriques, et al. (2004). "Role of protein-water interactions and electrostatics in alpha-synuclein fibril formation." Biochemistry 43(11): 3289-300.

Nelson, R., M. R. Sawaya, et al. (2005). "Structure of the cross-beta spine of amyloid-like fibrils." Nature 435(7043): 773-8.

Nielsen, L., R. Khurana, et al. (2001). "Effect of environmental factors on the kinetics of insulin fibril formation: elucidation of the molecular mechanism." Biochemistry 40(20): 6036-46.

Pallitto, M. M. and R. M. Murphy (2001). "A mathematical model of the kinetics of beta-amyloid fibril growth from the denatured state." Biophys J 81(3): 1805-22.

Pastore, A. and P. A. Temussi (2012). "The two faces of Janus: functional interactions and protein aggregation." Curr Opin Struct Biol 22(1): 30-7.

Pechmann, S., E. D. Levy, et al. (2009). "Physicochemical principles that regulate the competition between functional and dysfunctional association of proteins." Proc Natl Acad Sci U S A 106(25): 10159-64.

Petkova, A. T., G. Buntkowsky, et al. (2004). "Solid state NMR reveals a pH-dependent antiparallel beta-sheet registry in fibrils formed by a beta-amyloid peptide." J Mol Biol 335(1): 247-60.

Plakoutsi, G., F. Bemporad, et al. (2005). "Evidence for a mechanism of amyloid formation involving molecular reorganisation within native-like precursor aggregates." J Mol Biol 351(4): 910-22.

Prusiner, S. B. (1982). "Novel proteinaceous infectious particles cause scrapie." Science 216(4542): 136-44.

Prusiner, S. B. (2001). "Shattuck lecture--neurodegenerative diseases and prions." N Engl J Med 344(20): 1516-26.

Rousseau, F., L. Serrano, et al. (2006). "How evolutionary pressure against protein aggregation shaped chaperone specificity." J Mol Biol 355(5): 1037-47.

Sabate, R., U. Baxa, et al. (2007). "Prion and non-prion amyloids of the HET-s prion forming domain." J Mol Biol 370(4): 768-83.

Sabate, R., N. S. de Groot, et al. (2010). "Protein folding and aggregation in bacteria." Cell Mol Life Sci 67(16): 2695-715.

Sabate, R. and J. Estelrich (2005). "Evidence of the existence of micelles in the fibrillogenesis of beta-amyloid peptide." J Phys Chem B 109(21): 11027-32.

Sabate, R., M. Gallardo, et al. (2003). "An autocatalytic reaction as a model for the kinetics of the aggregation of beta-amyloid." Biopolymers 71(2): 190-5.

Sanchez de Groot, N., I. Pallares, et al. (2005). "Prediction of "hot spots" of aggregation in disease-linked polypeptides." BMC Struct Biol 5: 18.

Sawaya, M. R., S. Sambashivan, et al. (2007). "Atomic structures of amyloid cross-beta spines reveal varied steric zippers." Nature 447(7143): 453-7.

Serio, T. R., A. G. Cashikar, et al. (2000). "Nucleated conformational conversion and the replication of conformational information by a prion determinant." Science 289(5483): 1317-21.

Serpell, L. C., M. Sunde, et al. (2000). "The protofilament substructure of amyloid fibrils." J Mol Biol 300(5): 1033-9.

Sondheimer, N. and S. Lindquist (2000). "Rnq1: an epigenetic modifier of protein function in yeast." Mol Cell 5(1): 163-72.

Sunde, M., L. C. Serpell, et al. (1997). "Common core structure of amyloid fibrils by synchrotron X-ray diffraction." J Mol Biol 273(3): 729-39.

Tanaka, M., S. R. Collins, et al. (2006). "The physical basis of how prion conformations determine strain phenotypes." Nature 442(7102): 585-9.

Tartaglia, G. G. and M. Vendruscolo (2008). "The Zyggregator method for predicting protein aggregation propensities." Chem Soc Rev 37(7): 1395-401.

Thompson, L. K. (2003). "Unraveling the secrets of Alzheimer's beta-amyloid fibrils." Proc Natl Acad Sci U S A 100(2): 383-5.

Tokatlidis, K., P. Dhurjati, et al. (1991). "High activity of inclusion bodies formed in Escherichia coli overproducing Clostridium thermocellum endoglucanase D." FEBS Lett 282(1): 205-8.

Trovato, A., F. Chiti, et al. (2006). "Insight into the structure of amyloid fibrils from the analysis of globular proteins." PLoS Comput Biol 2(12): e170.

Tuite, M. F. and N. Koloteva-Levin (2004). "Propagating prions in fungi and mammals." Mol Cell 14(5): 541-52.

Tycko, R. (2006). "Characterization of amyloid structures at the molecular level by solid state nuclear magnetic resonance spectroscopy." Methods Enzymol 413: 103-22.

Tycko, R. (2011). "Solid-state NMR studies of amyloid fibril structure." Annu Rev Phys Chem 62: 279-99.

Uversky, V. N. (2010). "Mysterious oligomerization of the amyloidogenic proteins." FEBS J 277(14): 2940-53.

Uversky, V. N., J. Li, et al. (2001). "Evidence for a partially folded intermediate in alpha-synuclein fibril formation." J Biol Chem 276(14): 10737-44.

van Rooijen, B. D., M. M. Claessens, et al. (2010). "Membrane Permeabilization by Oligomeric alpha-Synuclein: In Search of the Mechanism." PLoS One 5(12): e14292.

Vendruscolo, M., E. Paci, et al. (2003). "Structures and relative free energies of partially folded states of proteins." Proc Natl Acad Sci U S A 100(25): 14817-21.

Ventura, S. and A. Villaverde (2006). "Protein quality in bacterial inclusion bodies." Trends Biotechnol 24(4): 179-85.

Ventura, S., J. Zurdo, et al. (2004). "Short amino acid stretches can mediate amyloid formation in globular proteins: the Src homology 3 (SH3) case." Proc Natl Acad Sci U S A 101(19): 7258-63.

Walsh, D. M., A. Lomakin, et al. (1997). "Amyloid beta-protein fibrillogenesis. Detection of a protofibrillar intermediate." J Biol Chem 272(35): 22364-72.

Wang, L., S. K. Maji, et al. (2008). "Bacterial inclusion bodies contain amyloid-like structure." PLoS Biol 6(8): e195.

Wang, W. and M. H. Hecht (2002). "Rationally designed mutations convert de novo amyloid-like fibrils into monomeric beta-sheet proteins." Proc Natl Acad Sci U S A 99(5): 2760-5.

Wasmer, C., L. Benkemoun, et al. (2009). "Solid-state NMR spectroscopy reveals that E. coli inclusion bodies of HET-s(218-289) are amyloids." Angew Chem Int Ed Engl 48(26): 4858-60.

Wasmer, C., A. Lange, et al. (2008). "Amyloid fibrils of the HET-s(218-289) prion form a beta solenoid with a triangular hydrophobic core." Science 319(5869): 1523-6.

Watters, A. L., P. Deka, et al. (2007). "The highly cooperative folding of small naturally occurring proteins is likely the result of natural selection." Cell 128(3): 613-24.

West, M. W., W. Wang, et al. (1999). "De novo amyloid proteins from designed combinatorial libraries." Proc Natl Acad Sci U S A 96(20): 11211-6.

Westermark, P., A. Andersson, et al. (2011). "Islet amyloid polypeptide, islet amyloid, and diabetes mellitus." Physiol Rev 91(3): 795-826.

Wetzel, R. (2006). "Kinetics and thermodynamics of amyloid fibril assembly." Acc Chem Res 39(9): 671-9.

Wickner, R. B., H. K. Edskes, et al. (2011). "The yeast prions [PSI+] and [URE3] are molecular degenerative diseases." Prion 5(4).

Wolynes, P. G., J. N. Onuchic, et al. (1995). "Navigating the folding routes." Science 267(5204): 1619-20.

Xue, W. F., A. L. Hellewell, et al. (2010). "Fibril fragmentation in amyloid assembly and cytotoxicity: when size matters." Prion 4(1): 20-5.

Yong, W., A. Lomakin, et al. (2002). "Structure determination of micelle-like intermediates in amyloid beta -protein fibril assembly by using small angle neutron scattering." Proc Natl Acad Sci U S A 99(1): 150-4.

Zhu, M., P. O. Souillac, et al. (2002). "Surface-catalyzed amyloid fibril formation." J Biol Chem 277(52): 50914-22.

Zwanzig, R., A. Szabo, et al. (1992). "Levinthal's paradox." Proc Natl Acad Sci U S A 89(1): 20-2.

BLOQUE I: Estudio de la agregación proteica *in vitro.* Propiedades biofísicas de las fibras amiloides.

CAPITULO I: Efecto de la secuencia y la composición aminoacídica en la formación amiloide.

doi:10.1016/j.jmb.2010.09.052 J. Mol. Biol. (2010) 404, 337–352

Contents lists available at www.sciencedirect.com

Journal of Molecular Biology

journal homepage: http://ees.elsevier.com.jmb

The Role of Protein Sequence and Amino Acid Composition in Amyloid Formation: Scrambling and Backward Reading of IAPP Amyloid Fibrils

Raimon Sabaté[1]†, Alba Espargaró[1]†, Natalia S. de Groot[1], Juan José Valle-Delgado[2,3], Xavier Fernàndez-Busquets[2,3] and Salvador Ventura[1]*

[1]*Departament de Bioquímica i Biologia Molecular and Institut de Biotecnologia i de Biomedicina, Universitat Autònoma de Barcelona, 08193 Bellaterra, Barcelona, Spain*
[2]*Nanobioengineering Group, Institute for Bioengineering of Catalonia, Baldiri Reixac 10-12, E-08028 Barcelona, Spain*
[3]*Biomolecular Interactions Team, Nanoscience and Nanotechnology Institute, University of Barcelona, Parc Científic de Barcelona, Baldiri Reixac 10-12, E-08028 Barcelona, Spain*

Received 22 April 2010; received in revised form 31 July 2010; accepted 22 September 2010
Available online 29 September 2010

Edited by S. Radford

Keywords:
amyloid formation;
protein aggregation;
protein sequence;
islet amyloid polypeptide;
retro proteins

The specific functional structure of natural proteins is determined by the way in which amino acids are sequentially connected in the polypeptide. The tight sequence/structure relationship governing protein folding does not seem to apply to amyloid fibril formation because many proteins without any sequence relationship have been shown to assemble into very similar β-sheet-enriched structures. Here, we have characterized the aggregation kinetics, seeding ability, morphology, conformation, stability, and toxicity of amyloid fibrils formed by a 20-residue domain of the islet amyloid polypeptide (IAPP), as well as of a backward and scrambled version of this peptide. The three IAPP peptides readily aggregate into ordered, β-sheet-enriched, amyloid-like fibrils. However, the mechanism of formation and the structural and functional properties of aggregates formed from these three peptides are different in such a way that they do not cross-seed each other despite sharing a common amino acid composition. The results confirm that, as for globular proteins, highly specific polypeptide sequential traits govern the assembly pathway, final fine structure, and cytotoxic properties of amyloid conformations.

Introduction

The primary sequence of a protein encodes not only its specific functional three-dimensional structure but also the pathway that it follows from the unfolded state to the native conformation.[1] This information implies that a polypeptide with the same amino acid composition as a naturally occurring protein but with a randomized distribution of the residues would not attain the same native structure and probably would not fold at all. Retro proteins illustrate an extreme example of this situation. Native proteins are generally not palin-

*Corresponding author. E-mail address: salvador.ventura@uab.es.

† R.S. and A.E. contributed equally to this work.

Abbreviations used: IAPP, islet amyloid polypeptide; TEM, transmission electron microscopy; AFM, atomic force microscopy; FTIR, Fourier transform infrared spectroscopy; Th-T, thioflavin-T; CR, Congo red; Gdn–HCl, guanidine hydrochloride; ATR, attenuated total reflectance; DMEM, Dulbecco's modified Eagle's medium.

dromic; therefore, reading a protein sequence backwards provides a new polypeptide that does not align with its parent sequence.[2] In a retro protein, the dihedral angles φ and ψ correspond to the angles −ψ and −φ in the original protein, respectively. Reversal of peptide bond direction achieves a mirroring of side-chain positions in conformational space.[2] This property gave rise to speculation that, as a result of the folding process, a retro protein might adopt the mirror image structure of the native fold.[3] However, it has been shown as a general rule that retro versions do not fold into the compact, stable, and soluble conformations characteristic of natural globular proteins despite their common hydrophobic/hydrophilic pattern, global amino acid composition, and possible tertiary contacts.[4]

The strong constraints that the protein primary sequence imposes on the conformation of globular native proteins might not necessarily apply to the formation of amyloid fibril structures because a large number of both disease-related proteins and nontoxic proteins have been shown to convert into amyloid without any need for sequential or structural homology.[5,6] In fact, it is assumed that the formation of amyloid fibrils is an intrinsic and generic polypeptide property.[7] Goldschmidt *et al.* recently addressed the validity of such an assumption by investigating the molecular properties of the universe of proteins capable of forming amyloid fibrils.[8] Their results support previous findings suggesting that the propensity to form amyloid fibrils is highly dependent on the protein sequence,[9,10] in agreement with the observation that amyloidogenic segments of the amyloid-β peptide and the prion protein lose their amyloid propensity when they are scrambled.[11,12] However, scrambled variants of the yeast Ure2p and Sup35 prions, in which the order of amino acids in the prion domain was randomized, formed prions *in vivo* and amyloid fibrils *in vitro*,[13,14] suggesting that, at least in these particular cases, amino acid composition might be relevant to amyloid assembly. In this context, pioneering studies demonstrated that the absolute aggregation rates of amyloidogenic polypeptides can be approximated by using simple physicochemical parameters to describe the properties of polypeptide chains.[15] Later on, it was shown that explicitly taking into consideration the presence of specific aggregation-prone sequences improves the accuracy of the predictions, as demonstrated for scrambled versions of the N-terminal peptide of horse heart apomyoglobin.[16] Accordingly, although scrambled and natural versions of the NM region of the Sup35p prion form amyloids, they exhibit different aggregation kinetics. These data indicate that even in the particular case in which the ability to form amyloids is determined by the amino acid composition, the distribution of side chains might modulate the rate of conversion into amyloid structures.[17]

Together with the study of the aggregation properties of natural amyloid proteins and peptides and their scrambled versions, an analysis of the effect of backbone direction on the amyloid properties of polypeptides might prove very useful in deciphering the extent of sequence specificity required for amyloid assembly. However, this remains an essentially unexplored issue. In the present work, we have addressed the role of amino acid sequence and composition in amyloid formation using the islet amyloid polypeptide (IAPP) as model.

IAPP is stored in insulin-secretory granules and secreted by pancreatic β-cells acting, together with insulin, as regulator of glucose homeostasis.[18] The formation of IAPP aggregates is strongly associated with β-cell degeneration in type 2 diabetes[19] because more than 90% of patients exhibit IAPP amyloid upon autopsy. Furthermore, the level of islet amyloid appears to correlate with the severity of the disease.[19] Here, we study the aggregation kinetics, seeding ability, morphology, conformation, stability, and toxicity of amyloid fibrils formed by a 20-residue domain of IAPP, as well as of a backward and scrambled version of this peptide.

Results

Predicted aggregation propensities of IAPP peptides

Mature IAPP consists of 37 residues, contains a disulfide bridge between cysteine 2 and cysteine 7, and has an amidated C-terminus. Secondary structure predictions using the algorithm CSSP2[20] indicate that the IAPP region with the highest β-sheet propensity comprises residues 13–29 (data not shown). This includes the 20–29 region, which is considered to be the central amyloidogenic module of the polypeptide,[21] and it overlaps with the 10–19 segment, which has also been shown to be important for IAPP fibrillogenesis.[22–24] In the present work, we have addressed the amyloidogenic properties of a peptide corresponding to the IAPP 10–29 sequence stretch named WT. Different models have been recently proposed for the conformation of IAPP in the fibrillar state based on molecular modeling,[25] NMR,[26] and X-ray[27] results. In all of these models, the 10–29 IAPP segment is embedded in the main β-sheet structure.

Several algorithms have been developed to identify amyloidogenic protein sequences and to predict the aggregation propensities of proteins.[15,28–34] Here, theoretical aggregation-prone regions in WT were predicted using three different methods: TANGO,[28] AGGRESCAN,[30] and the algorithm of Zhang *et al.* (here named PRE-AMYL).[33] TANGO, AGGRESCAN, and PRE-AMYL consistently pre-

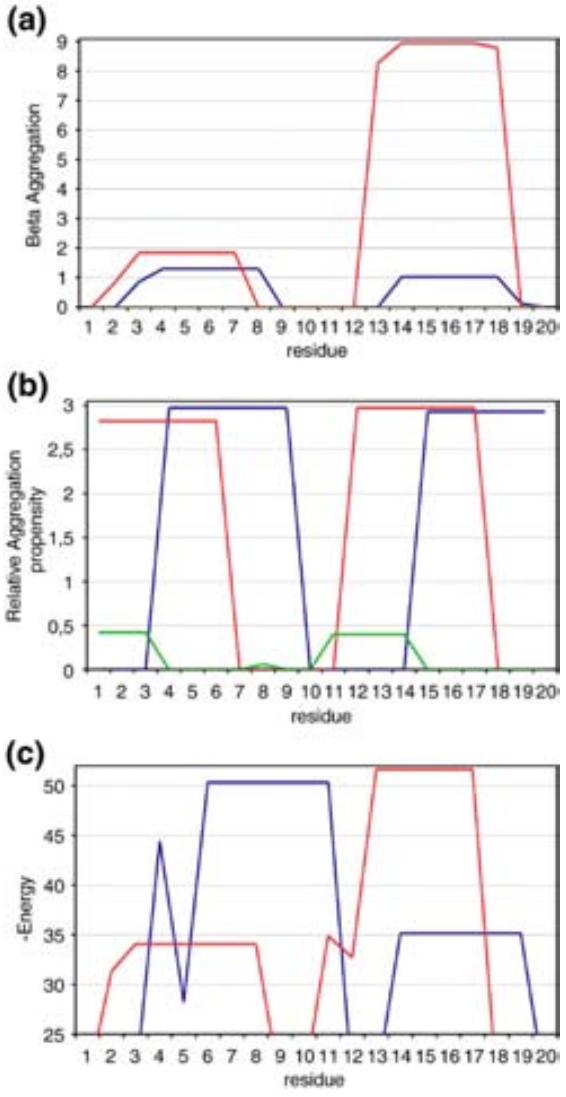

Fig. 1. Aggregation propensity profiles of IAPP peptides. Aggregation propensities were calculated according to (a) TANGO,[28] (b) AGGRESCAN,[30] and (c) Zhang *et al.*[33] The profiles correspond to WT (blue), RETRO (red), and DESIGN (green) peptides. The aggregation propensity of DESIGN is below the detection threshold in (a) and (c).

dicted two aggregation-prone regions in WT, in good agreement with experimental data. The consensus prediction suggests that the first aggregating region spans residues 12–17 (LANFLV), and the second aggregating region is composed of residues 23–28 (FGAILS) (Fig. 1).

To assess the influence, if any, of backbone direction on protein aggregation, we synthesized a retro version of WT, here named RETRO (Table 1). Two aggregating regions were suggested by TANGO, AGGRESCAN, and PRE-AMYL; the consensus prediction suggests that the first region includes residues 27–23 (using WT nomenclature) (LIAGF) and that the second region is composed of residues 17–13 (VLFNA). AGGRESCAN and PRE-AMYL provided predictions essentially symmetric to those obtained for WT (Fig. 1) and, accordingly, very similar aggregation propensities for both peptides (Table 1). TANGO predicted both regions—but especially the second one (VLFNAL)—to be more aggregation-prone in RETRO than in WT (Fig. 1); in fact, it anticipates a 5-fold faster aggregation rate for the backward sequence.

To study the role of the specific sequence in protein aggregation instead of simply the overall amino acid composition, we used TANGO as a benchmark to design a peptide, named DESIGN, that is devoid of any aggregation-prone regions despite sharing the same amino acid composition as WT and RETRO (Fig. 1 and Table 1). No aggregating segments were predicted by PRE-AMYL in this peptide (Fig. 1 and Table 1). AGGRESCAN detected short (<5 residues) and weak aggregation-prone stretches (Fig. 1) and a 6-fold reduction in aggregation tendency relative to WT (Table 1).

We performed a BLAST homology analysis with the RETRO and DESIGN sequences. Very high *E*-values, which indicate that the sequences are not homologous to any natural protein sequence, were obtained in both cases (see Materials and Methods).

Formation of amyloid fibrils by IAPP peptides

We incubated 100 μM solutions of the different peptides in 10 mM sodium acetate (pH 5.5) for 24 h at room temperature with agitation at 1000 rpm. This buffer has been previously shown to be

Table 1. Predicted aggregation propensities of WT, RETRO, and DESIGN peptides according to the default parameters of the algorithms used

Peptide	Sequence	TANGO[a]	AGGRESCAN[b]	Zhang *et al.*[c]
DESIGN	LIQSAFGNNVHLSRFNSSAL	0.0	0.040	0.0
WT	QRLANFLVHSSNNFGAILSS	12.69	0.295	−29.30
RETRO	SSLIAGFNNSSHVLFNALRQ	63.0	0.290	−28.09

[a] β-Aggregation (higher values correspond to higher aggregation propensities).[28]
[b] Area of the profile above the threshold per residue (higher values correspond to higher aggregation propensities).[30]
[c] Average of energy values below the threshold (lower values correspond to higher aggregation propensities).[33]

adequate for the study of IAPP fibrillogenesis.[22,35] Incubated peptide solutions were imaged using transmission electron microscopy (TEM). All three peptides formed amyloid-like fibrillar structures despite their different predicted aggregation properties. The individual samples of the three peptides exhibited significant fibrillar polymorphism, as analyzed by TEM. Representative images of the macromolecular structures formed by the three peptides are shown in Fig. 2. The WT fibrillar assemblies were shorter than those formed by DESIGN and RETRO peptides. The widths of the observed individual protofibrils were ~6–8 nm for WT, ~7–9 nm for DESIGN, and ~8–10 nm for RETRO. They appeared eventually associated to form stacks, bundles, or helical structures.

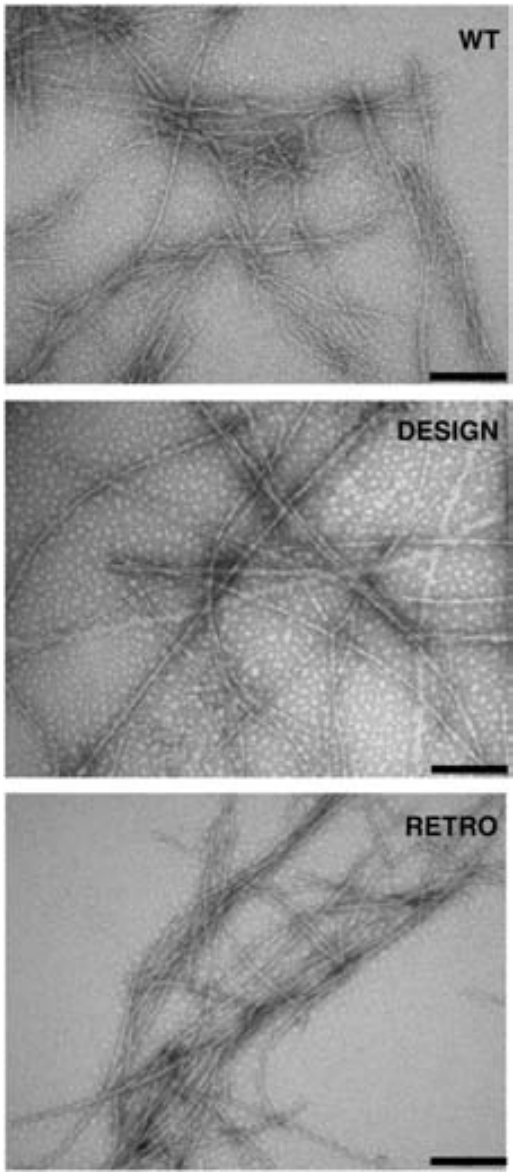

Fig. 2. Electron micrographs of the amyloid fibrils formed by WT, DESIGN, and RETRO peptides in 10 mM sodium acetate (pH 5.5) at room temperature with agitation at 1000 rpm. The scale bar represents 200 nm.

Tapping-mode atomic force microscopy (AFM) of highly oriented pyrolytic graphite (HOPG) was also used to visualize aggregating peptides. Two types of structures were observed in all three samples: ribbon-like protofibrils (Fig. 3a–c) and larger fibrils formed by the parallel association of protofibrils (Fig. 3d–f). Protofibril heights were ~1.5 nm for WT and ~1.0 nm for DESIGN and RETRO. The widths of protofibrils were ~10 nm for WT and DESIGN and ~12 nm for RETRO. By analogy to our previous data obtained with the amyloid-β 1–42 peptide,[36] the fibrillar structures 7–10 nm across, as observed by TEM, might correspond to twisted protofibrils, an artifact probably induced by dehydration of TEM samples. Protofibrils reached a length of several hundred nanometers and, in the case of WT and RETRO, had a tendency to form parallel assemblies, whereas DESIGN protofibrils were more disordered. WT fibrils were often fragmented, but DESIGN fibrils were always observed as completely straight structures up to several micrometers long. The conversion of protofibrils into fibrils was observed to be incomplete according to AFM images that showed a protofibril layer (most evident in Fig. 3f) on top of which the fibrils were deposited.

Fourier transform infrared spectroscopy analysis of secondary structure in the amyloid fibrils formed by IAPP peptides

The secondary structure of the different peptides in the fibrillar state was evaluated by Fourier transform infrared spectroscopy (FTIR) (Fig. 4). Deconvolution of the absorbance spectrum in the amide I region allowed us to identify the individual secondary structure components and their relative contribution to the main signal. The analysis indicates that despite the presence of a common β-sheet signature, the fibrils display important secondary structure differences, which refer to both the proportion and conformation of β-sheets and the turns and loops that might connect β-strands (Table 2).

A comparison of the spectra of mature fibrils with the spectra from peptide solutions 5 min after the initiation of aggregation at 25 °C (Supporting Information, Fig. S1)—when no significant binding to thioflavin-T (Th-T) is yet detected—allowed us to monitor the main structural changes occurring upon fibril formation. At the beginning of the reaction, the spectra of all peptides are dominated by a band at ~1654 cm^{-1} (Table 2), which has been assigned to both α-helical and unstructured regions.

In WT, intermolecular β-sheet forms early in the reaction, as indicated by a band at 1626 cm^{-1} and a second band at 1697 cm^{-1}, which is thought to result

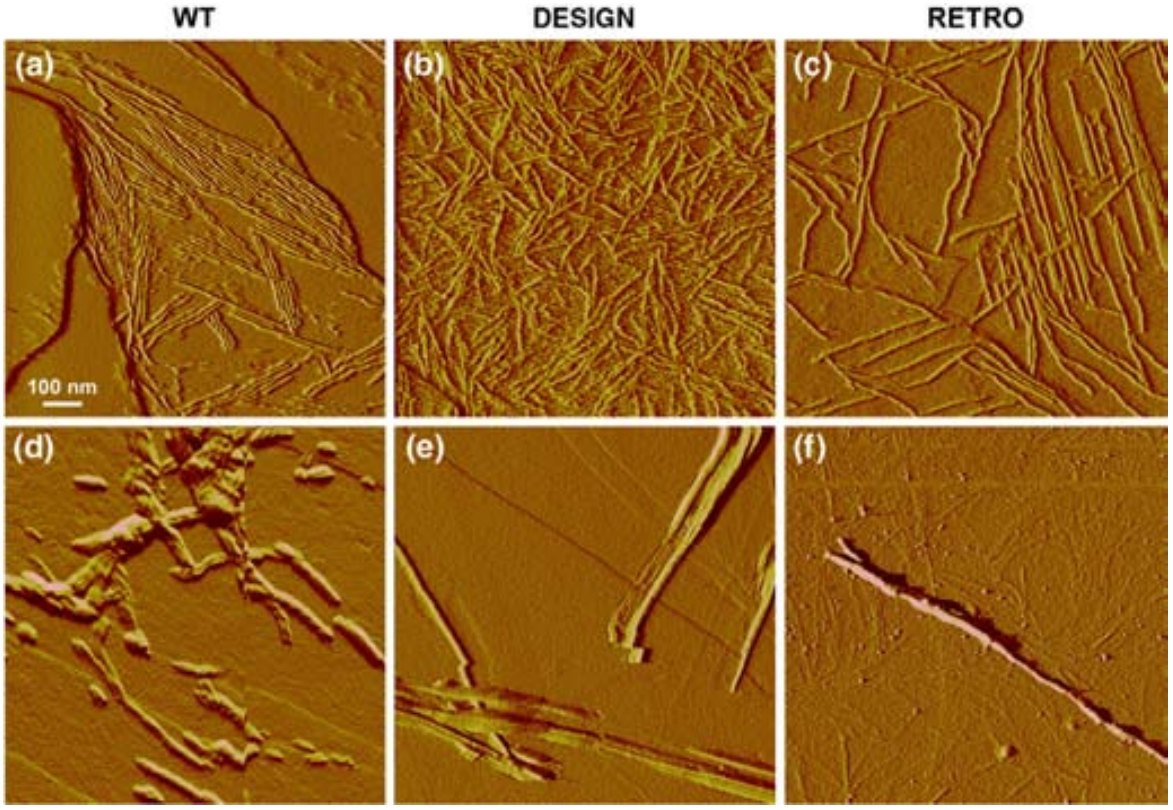

Fig. 3. Amplitude AFM images of the structures formed by WT, DESIGN, and RETRO peptides in 10 mM sodium acetate (pH 5.5) at room temperature with agitation at 1000 rpm. (a–c) Protofibrils. (d–f) Fibrils deposited on top of a protofibril layer.

from the splitting of the first signal. In addition, an important band at 1683 cm^{-1} is detected (Table 2). This band has been assigned to both β-turns and β-sheets and, accordingly, its position shifts coordinately with the 1624–1629 cm^{-1} signals in several of the peptides upon fibrillation (Table 2). The formation of mature fibrils in WT entails a complete conversion of non-β-regions into β-sheets and β-turn elements (Table 2).

The main components in the initial spectrum of RETRO correspond to those already described for WT (Table 2). However, the intermolecular β-sheet band is smaller and shifted to ~1629 cm^{-1}, suggesting a slower and looser self-assembly. Interestingly, in contrast to WT, the mature fibrils solution for RETRO still contains a significant amount of non-β-structure, and the characteristic WT β-turn band at ~1670 cm^{-1} is not detected (Table 2).

The initial spectrum of DESIGN presents a signal at 1632 cm^{-1}, which is usually assigned to intramolecular β-sheets, and lacks any intermolecular β-sheet band, which suggests the presence of a monomeric β-hairpin-like structure. The other bands present at 5 min correspond to those seen previously in the WT spectrum (Table 2). After fibrillation, the characteristic intermolecular β-sheet signal at 1624 cm^{-1} appears. However, the putative intramolecular β-sheet is still detected (Table 2). Also, the initial non-β-signals at 1654 cm^{-1} disappear, and a β-turn signal at 1673 cm^{-1} dominates the spectrum (Table 2).

Amyloid dyes bind to the amyloid fibrils formed by IAPP peptides

The fibrils formed by the three peptides bind to the amyloid diagnostic dye Congo red (CR), as evidenced by an increase in absorbance signal and a shift of the spectrum towards higher wavelengths (Fig. 5a). In addition, the difference spectrum between the dye in the presence of fibrils and the dye in the absence of fibrils allows the detection of the characteristic amyloid band at ~541 nm (Fig. 5b). Importantly, the different fibrils induce differential changes in the CR spectrum with a DESIGN>RETRO>WT effect. This supports the existence of structural differences in the fibrils. To further confirm this point, we performed titration to determine the interaction between the dye and the three different fibrils (Supporting Information, Table S1 and Fig. S2). We measured the maximum CR binding (B_{max}) values of 3.24, 4.95, and 4.69 μM, and

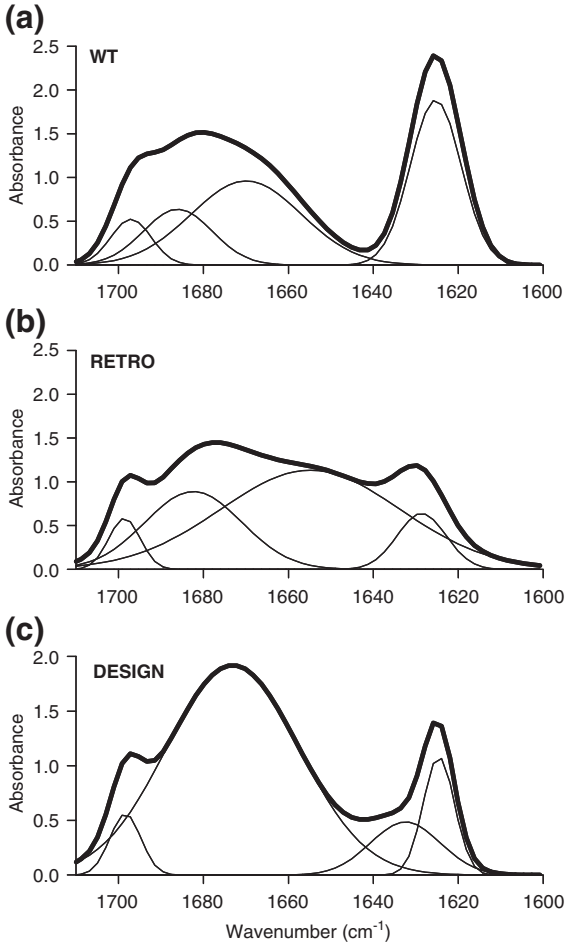

Fig. 4. Analysis of the secondary structures of WT (a), RETRO (b), and DESIGN (c) amyloid fibrils by ATR-FTIR. Absorbance spectra of the amide I region (continuous thick lines) showing the component bands (continuous thin lines). The sum of individual spectral components after Fourier self-deconvolution closely matches the experimental data.

apparent K_d values of 2.74, 3.93, and 3.29 μM, for 10 μM WT, RETRO, and DESIGN fibrils, respectively.

We further explored the binding of the fibrillar structures to Th-T. In the presence of amyloid fibrils, Th-T undergoes an enhancement of its fluorescence emission relative to that of the free dye.[37] All three fibrils bind to Th-T but induce differential changes in fluorescence with WT>RETRO>DESIGN (Fig. 5c). We measured Th-T B_{max} values of 0.41, 5.22, and 43.13 μM, and apparent K_d values of 16.4, 27.4, and 91.7 μM, for 25 μM WT, RETRO, and DESIGN fibrils, respectively (Supporting Information, Table S1 and Fig. S3). Overall, the binding to CR and Th-T supports the existence of conformational differences in the fibrils formed by these peptides.

Conformational stability of the amyloid fibrils formed by IAPP peptides

Secondary structure and dye binding data combine to indicate that the structure is stabilized by different contacts in the fibrils formed from the three peptides; therefore, these structures might display specific stability features. We characterized the conformational stabilities of the different fibrils under chemical denaturation with guanidine hydrochloride (Gdn–HCl). After fibril denaturation, the reduction in Th-T fluorescence signal was monitored. We assumed a two-state model in which the peptide is either in a fibrillar state, which contributes to fluorescence, or in a soluble state, which adds no contribution to the signal. The denaturation curves could be fitted accurately to the two-state model. Accordingly, cooperative-like denaturation behavior could be observed for all of the fibrils (Fig. 6). From the data in Table 3, it can be clearly inferred that the fibrils formed by the three related peptides exhibit dramatic differences in stability. DESIGN fibrils display a much higher stability against chemical denaturation ($\Delta G = 19$ kJ mol^{-1}) and a higher denaturation cooperativity ($m = 7.2$ kJ M^{-1} mol^{-1}) than WT fibrils ($\Delta G = 6$ kJ mol^{-1} and $m = 4.5$ kJ M^{-1} mol^{-1}). RETRO fibrils display intermediate values of stability and cooperativity ($\Delta G = 10$ kJ mol^{-1} and $m = 5.3$ kJ M^{-1} mol^{-1}).

Proteolytically protected core in the amyloid fibrils formed by IAPP peptides

Proteinase K is an endolytic serine protease that finds application in the mapping of polypeptide regions in the core of amyloid fibrils due to its strong preference for hydrolyzing unstructured protein regions. We tested whether the detected differences in secondary structure and stability imply different sensitivities to proteolysis. Mass spectrometry analysis after prolonged proteinase K treatment indicates that, in all three cases, essentially all of the peptide sequences are protected from digestion (2175 Da) (Supporting Information, Fig. S4). In the case of DESIGN, small amounts of peptide fragment 8–20 (1458 Da), peptide fragment 3–15 (1478 Da), and peptide fragment 6–20 (1660 Da) could be detected, which might suggest a slightly reduced protection of peptide tails in the fibrils.

Fibril formation kinetics of IAPP peptides

We studied the temperature dependence of the fibril nucleation rate constant (k_n) and the elongation rate constant (k_e) to decipher if IAPP peptides aggregate through different pathways. After the conversion of peptides into amyloid structures, the increase in Th-T fluorescence signal was monitored.[38]

Table 2. Secondary structure bands in the deconvoluted absorbance FTIR spectra of WT, RETRO, and DESIGN aggregated peptide solutions

	Bands (cm^{-1})[a]	Initial area[b] (%)	Final area[c] (%)	Structure
WT	1626, **1625**	8	36	β-Sheet (inter)
	1656	65	ND	Loop/turn/bend/helix
	1670	ND	40	β-Turn
	1683, **1686**	24	16	β-Turn
	1697, **1697**	3	8	β-Sheet/β-turn
RETRO	1629, **1628**	6	11	β-Sheet (inter)
	1654, **1655**	64	57	Loop/turn/bend/helix
	1681, **1683**	28	26	β-Turn
	1698, **1698**	2	6	β-Sheet/β-turn
DESIGN	**1624**	ND	11	β-Sheet (inter)
	1632, **1633**	7	10	β-Sheet (intra)
	1654	55	ND	Loop/turn/bend/helix
	1679, **1673**	35	75	β-Turn
	1698, **1698**	3	5	β-Sheet/β-turn

ND, corresponding band not detected at this time point.
[a] The positions of the bands in IAPP peptide solutions 5 min after the initiation of the aggregation reaction are shown in regular font. Those detected after 24 h of reaction, wherein the presence of abundant fibrils is evident in all solutions, are shown in boldface.
[b] Area of the bands in IAPP peptide solutions 5 min after the initiation of the aggregation reaction.
[c] Area of the bands in IAPP peptide solutions 24 h after the initiation of the aggregation reaction.

Plotting the absolute fluorescence at 480 nm against time results in sigmoidal curves that are characterized by three kinetic steps: a lag phase, an exponential growth phase, and a plateau phase. This sigmoidal curve resembles the behavior found in the polymerization of other amyloidogenic proteins and is best described by the nucleation-dependent polymerization model.[39,40] In all cases, the lag phase, the conformational transition rate, and the complete reaction time were sensitive to temperature (Fig. 7). Table S2 of Supporting Information summarizes the values obtained at each temperature for the different peptides. The k_n for WT is 3.7 times higher than the k_n for RETRO and 17.4 times higher than the k_n for DESIGN. Differences in the elongation step were also detected, with the k_e values of WT being 4.0 and 9.5 times higher than the k_e values of RETRO and DESIGN, respectively. As a result of accelerated nucleation and elongation rates, the fibrillization reaction of WT is completed ~4 and ~15 times faster than in the RETRO and DESIGN peptides, respectively.

Not only are k_n and k_e different between IAPP peptides but they also exhibit different dependences on the temperature. For WT, RETRO, and DESIGN, k_n increments by factors of 7.4, 1.1, and 2.5, respectively, when temperature is increased from 37 to 49 °C (Supporting Information, Table S2). The k_e values for the WT, RETRO, and DESIGN peptides are increased by multiples of 1.6, 3.6, and 3.2, respectively, in the same temperature range. This differential effect of temperature on the rate constants suggests that the species involved in the different aggregation pathways possess different conformational properties.

Energy barriers to IAPP peptides in amyloid fibril elongation

We calculated the activation energies (E_A) (see Materials and Methods) for elongation reactions (Table 4). For WT, an E_A of 24.38 kJ mol^{-1} was calculated, suggesting a diffusion-controlled process.[41] For the RETRO and DESIGN peptides, E_A values of 69.73 and 78.45 kJ mol^{-1} were obtained, respectively. Such high values of E_A suggest that significant conformational changes are associated with fibril elongation in these cases. To estimate the relative contributions of activation enthalpy and entropy to the elongation rates, we applied the transition-state theory (see Materials and Methods). The thermodynamic parameters derived from the analysis are shown in Table 4. The higher enthalpic terms and the positive entropy values for RETRO and DESIGN elongation reactions confirm that their fibrillation pathways differ significantly from that of the WT peptide.

Seeding of amyloid formation in IAPP peptides

The rate of fibril formation by an amyloidogenic protein is enhanced by the addition of preformed fibrils, a phenomenon known as seeding. Seeding displays a high specificity, and protein aggregation can be nucleated by homologous fibrils, but not by fibrils from unrelated proteins.[42] Seeding and cross-seeding experiments were performed to test if this selectivity also applies in the case of IAPP peptides. The aggregation reactions were performed at 15 μM for initially soluble peptide concentrations in the absence or in the presence of 1.5 μM preformed

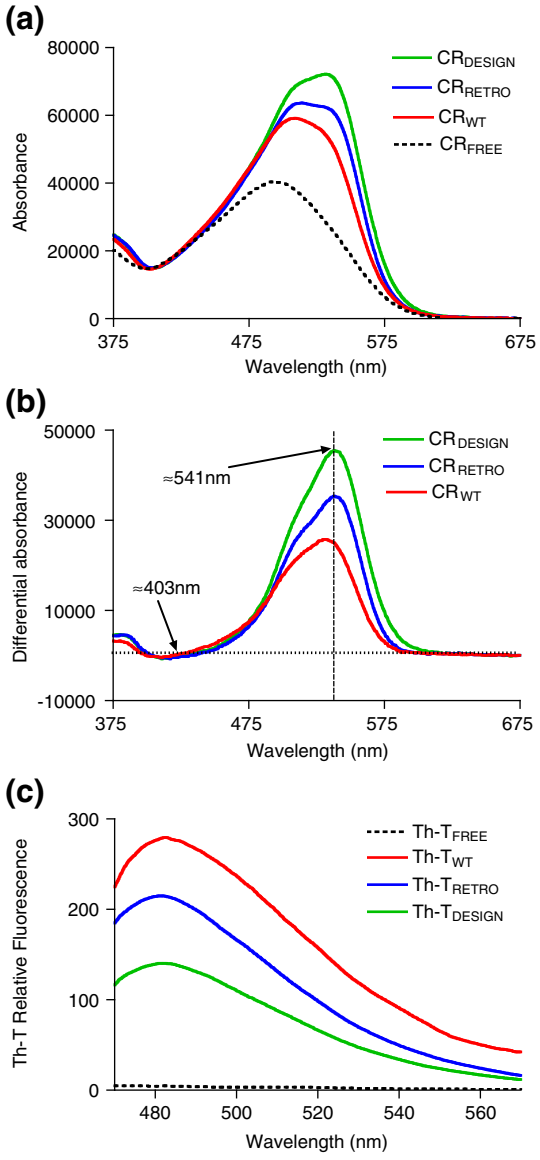

Fig. 5. Specific dye binding to WT, RETRO, and DESIGN amyloid fibrils. (a and b) CR spectral changes upon binding to aggregated peptides monitored by UV/Vis spectroscopy. In (a), note the shift in λ_{max} and the increase in CR absorbance when bound to different peptides. In (b), note the difference absorbance spectra of CR in the presence and in the absence of fibrils, showing in all cases the characteristic amyloid band at ~541 nm. (c) Fluorescence emission spectrum of 30 μM Th-T in the presence of 25 μM of each aggregated peptide when excited at 445 nm; note the maximum at ~480 nm.

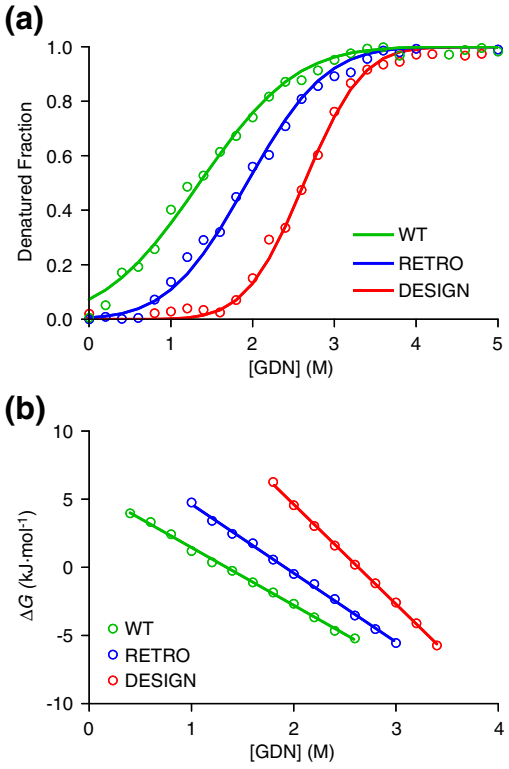

Fig. 6. Conformational stability of WT, RETRO, and DESIGN amyloid fibrils. Equilibrium Gdn–HCl denaturation curves for amyloid fibrils at pH 5.5 and 25 °C monitored by changes in Th-T relative fluorescence at 480 nm upon excitation at 445 nm. The fraction of denatured fibrils (a) and the changes in $\Delta G*$ (b) as a function of Gdn–HCl concentration are shown. The thermodynamic parameters are given in Table 3.

homologous or heterologous fibrils (Fig. 8). The assays were performed at 25 , 37 , and 49 °C for the WT, RETRO, and DESIGN peptides, respectively, to obtain similar reaction times. In all cases, the presence of preformed homologous fibrils shortened the lag phase, increased k_n, and reduced the total time of the reaction (Supporting Information, Table S3). Importantly, in all of the cases, the presence of preformed heterologous amyloid fibrils had a negligible effect on the kinetic parameters of the fibrillization reaction, indicating that cross-seeding was absent; therefore, there were no specific interactions between the sequentially related IAPP amyloid peptides and/or the compositionally related IAPP amyloid peptides.

Table 3. Thermodynamic fibril denaturation parameters at pH 5.5 and 25 °C

	WT	RETRO	DESIGN
m (kJ M^{-1} mol^{-1})[a]	4.49 ± 0.01	5.32 ± 0.52	7.24 ± 0.48
$m_{1/2}$ (M)[b]	1.348 ± 0.003	1.928 ± 0.008	2.623 ± 0.017
ΔG (H_2O) (kJ mol^{-1})[c]	6.06 ± 0.03	10.25 ± 1.04	18.99 ± 1.39

[a] Dependence of the Gibbs energy of fibril denaturation with Gdn–HCl.
[b] Midpoint of fibril denaturation with Gdn–HCl.
[c] Gibbs energy for fibril denaturation.

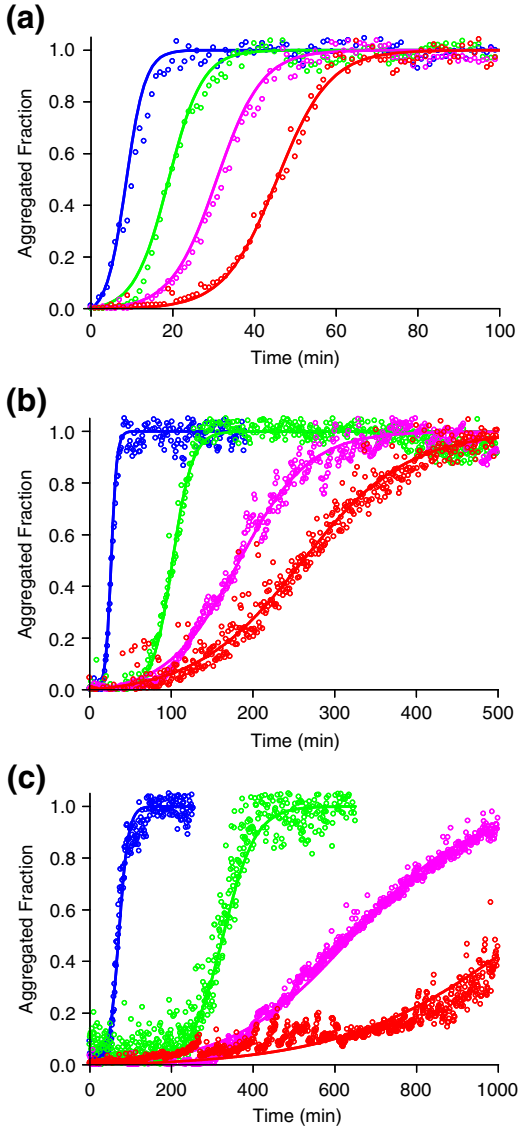

Fig. 7. Aggregation kinetics of WT (a), RETRO (b), and DESIGN (c) peptides. The fibrillar fraction of peptides is represented as a function of time. The aggregation reactions have been performed at 13 °C (red), 25 °C (pink), 37 °C (green), and 49 °C (blue) with agitation.

Cytotoxicity of the amyloid fibrils formed by IAPP peptides

Human IAPP is among the most amyloidogenic peptides known, and its fibrils have been found to be cytotoxic to a variety of cell types.[43] To explore if the different conformational features of IAPP peptides fibrils provide them with different cytotoxicities, we assayed their effect on cultured neuroblastoma cells from the SH-SY5Y cell line at 10 μM concentration after a 48-h exposure. All amyloid preparations decreased cell viability. However, WT fibrils were less cytotoxic than RETRO fibrils and especially DESIGN fibrils, which reduced cellular viability to ~40% of that in the control culture (Fig. 9). Similar trends in the viability of SH-SY5Y cells were observed after a 24-h exposure to IAPP peptides fibrils (data not shown).

Discussion

In the present work, we have addressed the influence of the primary sequence and amino acid composition on the assembly pathway, conformation, and function of amyloid fibrils by using a domain of the diabetes-associated IAPP peptides as model.

The molecular interactions driving protein aggregation are thought to be mechanistically related to those shaping protein folding routes.[44] Nucleation of amyloid fibril growth involves the formation of a series of high-energy oligomers. Oligomers of sufficient size slowly convert into fibril nuclei, which then permit rapid elongation by the addition of monomers to the ends of the fibrils. The lag phase reflects the time required for the formation of such nuclei. The collapse of hydrophobic residues inside a buried core appears as a crucial event in the initiation of protein folding;[45–48] similarly, a "coalescence and reorganization" model has been recently proposed for amyloid formation.[49–51] In this model, the self-assembly process is initiated by hydrophobic collapse and followed by molecular reorganization to form a more stable oligomer that displays a hydrogen-bonded core and exposes the initially buried hydrophobic side chains. The effect of polypeptide hydrophobicity on the initial steps of aggregation appears to be modulated by the distribution of nonpolar residues in the sequence. In this way, sequences with alternation between hydrophobic residues and hydrophilic residues[52] have been shown to act as nucleating regions for amyloid assembly.[10,15,53,54] Also, Monsellier *et al.* recently showed that the progressive clustering of the most hydrophobic/amyloidogenic residues in a sequence results in increased elongation rates and shorter lag phases.[16] Clustering of aggregation-prone residues might, on one hand, strengthen intermolecular interactions between monomers, resulting in the formation of small critical nuclei, and, on the other hand, increase the probability of

Table 4. Thermodynamic parameters of the elongation phase of WT, RETRO, and DESIGN amyloid fibril formation

	WT	RETRO	DESIGN
E_A (kJ mol^{-1})	24.38	69.73	78.45
ΔH^* (kJ mol^{-1})	22.08	67.42	76.15
ΔS^* (J K^{-1})	−63.04	71.12	90.61
$T\Delta S^*$ (kJ mol^{-1})	−18.79	21.19	27.00
ΔG_{298}^* (kJ mol^{-1})	40.86	46.23	49.15

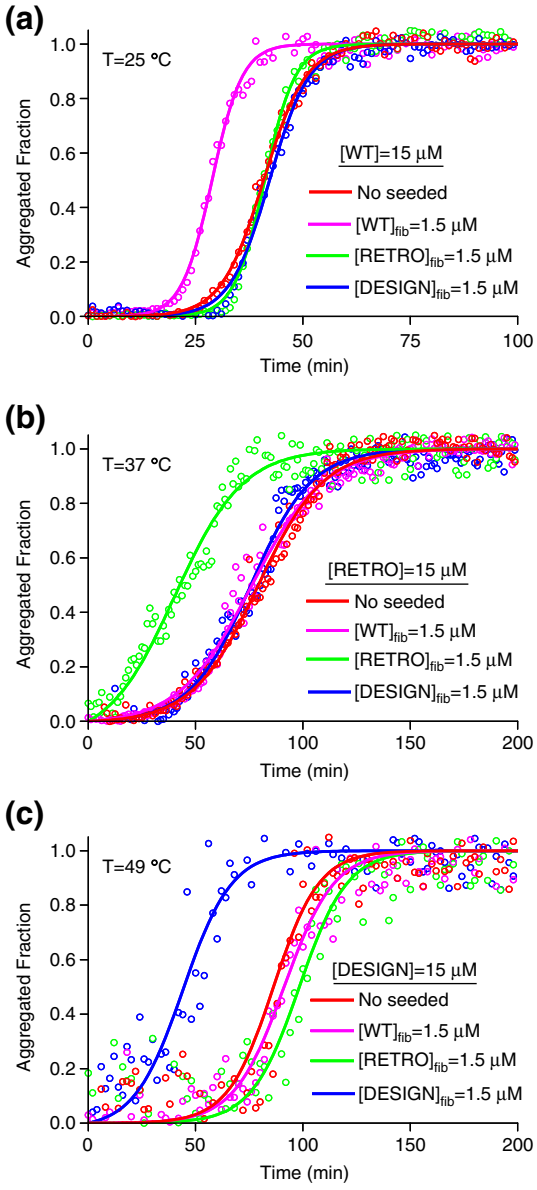

Fig. 8. Seeding and cross-seeding kinetics of WT (a), RETRO (b), and DESIGN (c) peptides in the presence of 10% of preformed WT, RETRO, and DESIGN fibrils. The fibrillar fraction of peptides is represented as a function of time. Note that, in all cases, the formation of amyloid fibrils is accelerated only by the addition of homologous preformed fibrils. The aggregation reactions have been performed at 25, 37, and 49 °C for WT, RETRO, and DESIGN peptides, respectively, with agitation.

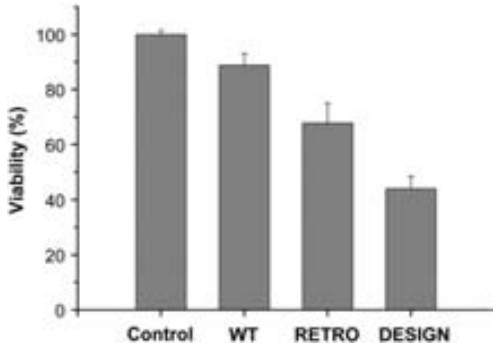

Fig. 9. Viability analysis of SH-SY5Y cells exposed to WT, RETRO, and DESIGN amyloid fibrils for 48 h. Error bars indicate ± SE ($n = 6$). One hundred percent cell viability was assigned to control samples corresponding to cells incubated in peptide free DMEM.

productive collisions between monomers. These two effects would result in faster nucleation reactions.[16] This mechanism might explain why DESIGN, in which amyloidogenic residues are more scattered throughout the sequence than in the WT and RETRO sequences, displays the longest lag phase and the lowest elongation rate among the analyzed IAPP peptides. The slow aggregation process of the DESIGN peptide is captured by the different prediction algorithms used in the present study, which in all cases predict aggregation propensities below the respective thresholds and indicate that the programs are sensitive to fibril formation rates. Nevertheless, DESIGN does finally slowly self-assemble into amyloid-like conformations. This indicates that even when the aggregation propensity of a polypeptide is intrinsically low, it might still explore conformational landscapes, leading to self-assembly into stable macromolecular structures.

The elongation of DESIGN fibrils differs significantly from the WT sequence in terms of energy. The low-energy barrier to the WT sequence indicates a facilitated diffusion-controlled growth process. This is in contrast to the high-energy barriers exhibited by DESIGN, which suggests that the monomer requires a chemical transformation before it can be accommodated at the growing fibril ends. The entropic and enthalpic contributions to the elongation reactions are also significantly different. In WT, two cooperative effects of similar magnitude appear to control fibril formation, as the reaction is unfavorable from both enthalpic and entropic points of view. In contrast, the free energy of elongation for DESIGN results from the difference between a larger activation energy and a favorable entropic contribution. In this case, the activated and inactive states significantly differ in energy. The different aggregation landscapes explored by the WT and DESIGN peptides, which share a common amino acid composition, result in the formation of macromolecular structures that differ in secondary structure content, stability, dye binding properties, and toxicity. These differences provide further support to the view that the distribution of side chains in the sequence, as it occurs in protein folding, plays a

pivotal role in determining the conformational features of the aggregated state and the way in which this state is reached from the initial monomeric state.

The amino acid sequence has a definite directionality, with the backbone of peptidic bonds running through the sequence from the N-terminus to the C-terminus. This implies that if one retains the sequence of side chains but reverses the direction in which the backbone runs through the sequence, an entirely new protein would be obtained. Still, this protein would retain the exact sequence of side chains and, accordingly, the same hydrophobic/hydrophilic pattern and clustering of amyloidogenic residues, which are two properties that, as discussed above, might determine both the structural properties of the aggregated state and the self-assembly pathway. Although the effect of retro transformations on the folding and native structure of proteins has been studied for different protein models,[3,4] the effect on the process of amyloid formation has remained essentially unexplored; the WT/RETRO pair is one of the few systems for which it has been characterized.

The lag phase for amyloid formation is significantly longer in RETRO than in WT, indicating that backbone reversal promotes conformational differences as early as the nucleation stage and at either the monomeric level or the oligomeric level. The population of structurally different species during the nucleation of RETRO and WT is further supported by the strikingly different dependences of their respective nucleation rates on temperature. The β-sheet conformation is the basic structural element of most amyloid fibrils and ordered oligomers.[50] It is important to consider how this conformation will respond to the changes in dihedral angles caused by a retro transformation. This question can be addressed by considering the coordinates of any point from within the region defining the β-structure in the Ramachandran plot and by transforming its dihedral angles to see where it lies after the transformation.[2–4] It turns out that the coordinates of most transformed points continue to lie within the same region of the map. Thus, a retro version would appear to be able to conserve the β-sheet structure if the original protein populates such a conformation. Our data argue that other properties, in addition to hydrophobic profile and linear β-sheet propensities, are relevant to the formation of the initial self-assembly-competent conformations of the WT and RETRO peptides. The differences between the nucleation stages of these two polypeptides can be understood if the initial self-assembly of one or both of these fragments does not occur from an initial extended linear conformation but instead contains one or more turns. Unlike in β-sheets, turn regions read backwards would result in turn propensities rarely observed in natural proteins,[55] implying that WT and RETRO could not share a similar initial overall conformation and, therefore, would likely display different conformational tendencies to pack into amyloid tertiary and/or quaternary structures. Accordingly, not only the nucleation step but also the elongation step of WT and RETRO amyloid formation are different, at least in energetic terms. The elongation of RETRO mechanistically resembles that of DESIGN in both the relative contribution of enthalpic and entropic factors and the high-energy barrier present in the elongation reaction. These similarities indicate that, in contrast to WT, the active and inactive states of RETRO significantly differ in energy. To the best of our knowledge, RETRO and DESIGN represent the only amyloidogenic nonnatural sequences for which the energy barriers to amyloid formation have been calculated. It is attractive to envision, although speculative, that the self-assembly reactions of natural sequences might be kinetically optimized relative to those of nonnatural proteins. This efficiency would result from the fact that the intramolecular folding of functional globular proteins and the intermolecular assembly of toxic amyloid structures rely ultimately on the same type of chemical interactions and physical laws; therefore, folding cannot be optimized by evolution independently of aggregation.[56]

Overall, the different aggregation pathways followed by WT and RETRO result in the formation of conformationally unrelated fibrils, as demonstrated by their different secondary structure contents, resistance to chemical denaturation, binding to CR or Th-T, and cytotoxicities. Accordingly, none of the preformed fibrils is able to cross-seed the aggregation of the reverted peptide. Although other peptide models should be analyzed to confirm this view, our data suggest that even though the succession of side chains is a major determinant of the ordered aggregation of a polypeptide, the amyloid fibrils formed by a natural protein and its retro version are probably not any more similar in structure than those formed by two sequentially unrelated amyloidogenic peptides. Importantly, the computational approaches used failed to predict the relative aggregation properties of the RETRO and WT peptides and indicated that the algorithms are mostly insensitive to chain direction. The reason for this mistaken insensitivity is that, in general, aggregation prediction algorithms analyze the self-assembly properties of linear amino acid sequences without taking into account the effects of backbone reversal at the conformational level, either in the nucleation stage or in the elongation stage of the aggregation process. Although, in principle, the integration of fast secondary structure predictions into these programs might be useful for this task, it turns out that most of these predictions are also insensitive to the direction of the polypeptide chain, implying that more complex and time-consuming

structurally based approaches should be implemented to refine aggregation propensity predictions. Interestingly enough, the first steps in this direction have already been taken with notable success.[57]

Materials and Methods

Peptides and preparation

WT (QRLANFLVHSSNNFGAILSS), RETRO (SSLIAGFNNSSHVLFNALRQ), and DESIGN (LIQSAFGNNVHLSRFNSSAL) peptides were obtained from EZ Biolab, Inc. (Carmel, IN). The identity and homogeneity of the peptides were reevaluated in our laboratory by an Ultraflex MALDI-TOF mass spectrometer (Bruker Daltonics) operating in linear mode under 20 kV and were found to be >95% in all cases, in accordance with the manufacturer's specifications. Peptide stock solution was prepared at 5 mM in 1,1,1,3,3,3-hexafluoro-2-propanol, centrifuged at 15,000*g* and 4 °C for 15 min, and, finally, filtered through Millex-GV 0. 22-μm filters in order to remove the possible residual quantity of high aggregates. Stock solutions were divided into aliquots (20 μL per Eppendorf tube), and 1,1,1,3,3,3-hexafluoro-2-propanol was removed by evaporation under a gentle stream of nitrogen, leaving a slight film. Finally, the samples were stored at −80 °C. When required, the samples were resuspended in 50 μL of anhydrous dimethyl sulfoxide and sonicated for 10 min. Sonication was crucial for removing any trace of undissolved seeds that may resist solubilization. This preparation yielded amylins in monomeric form. Aliquots of amylins were added to 100 μM acetate buffer (pH 5.5) and 850 μM MilliQ water, yielding a final peptide concentration of 100 μM.

Prediction of amyloid sequence stretches and aggregation propensities

Theoretical aggregation-prone regions in WT, RETRO, and DESIGN were predicted using three different methods: (1) TANGO‡,[28] which is based on the physicochemical principles underlying β-sheet formation, extended by the assumption that the core regions of an aggregate are fully buried; (2) AGGRESCAN§,[30] which uses an aggregation propensity scale for natural amino acids derived from *in vivo* experiments; and (3) the approach developed by Zhang *et al.*[33] (here named PRE-AMYL‖), which uses the microcrystal fibrillar structure of the prion hexapeptide NNQQNY[58] as template and a residue-based statistical potential to identify amyloidogenic fragments of proteins.

Search for homologous natural sequences

Homology searches were performed, using BLASTp¶, against a database of nonredundant protein sequences (nr). The best expectation (*E*) value for WT is 10^{-9}, since it corresponds to the natural human IAPP sequence. In contrast, RETRO and DESIGN sequences rendered the best *E* values of 2.4 and 26, respectively, indicating that no significantly homologous sequences exist in nature.

Secondary structure determination

Attenuated total reflectance (ATR) FTIR analysis was performed using a Bruker Tensor 27 FTIR Spectrometer (Bruker Optics, Inc.) with a Golden Gate MKII ATR accessory. Each spectrum consists of 20 independent scans, measured at a spectral resolution of 2 cm^{-1} within the range 1800–1500 cm^{-1}. All spectral data were acquired and normalized using the OPUS MIR Tensor 27 software. Second derivatives of the spectra were used to determine the frequencies at which the different spectral components were located.

Chemical denaturation

Protein stability in the presence of Gdn–HCl was studied at pH 5.5. The fraction of denatured protein (f_D) was calculated from fitted values using the equation $f_D = 1 - ((y_D - y)/(y_D - y_N))$, where y_D and y_N are the fluorescence maximum wavelengths of the denatured and native proteins, respectively, and y is the fluorescence maximum wavelength of protein as a function of denaturant concentration. A nonlinear least-squares analysis was used to fit the denaturation curves to the equation:

$$f_D = \frac{(y_N + m_N[D]) + (y_D + m_D[D])e^{\{A([D]-m_{1/2})/RT\}}}{1 + e^{\{A([D]-m_{1/2})/RT\}}} \quad (1)$$

where y represents the observed Th-T relative fluorescence emission at 480 nm upon excitation at 445 nm, y_N and y_D are the intercepts of the pretransition and posttransition baselines, m_N and m_D are the slopes of the pretransition and posttransition baselines, [D] is the Gdn–HCl concentration, $m_{1/2}$ is the Gdn–HCl concentration at the midpoint of the curve, and A is a constant generated by the fitting.[59]

Limited proteolysis

Aggregated peptides (35 μg mL^{-1}) were digested with 35 μg mL^{-1} proteinase K (pH 7) in phosphate-buffered saline for 60 min at 37 °C. Reactions were stopped by the addition of 2 vol of urea at 10 M. Then the samples were diluted in MilliQ water and analyzed by mass spectrometry following the α-cyano-4-hydroxycinnamic acid affinity sample preparation protocol with a 600-μm AnchorChip™ MALDI sample support in an Ultraflex MALDI-TOF spectrometer (Bruker Daltonics).

Th-T binding assays

Th-T binding to different aggregated peptides was measured on a Varian spectrofluorometer (Cary Eclipse) from 470 to 570 nm at 25 °C using an excitation wavelength of 445 nm. A slit width of 5 nm was used, and the maximum of emission (at 480 nm) was recorded. A fixed

‡ http://tango.crg.es/
§ http://bioinf.uab.es/aggrescan/
‖ ftp://mdl.ipc.pku.edu.cn/pub/software/pre-amyl/
¶ http://www.ncbi.nlm.nih.gov/

amount of Th-T or peptide was mixed with varying concentrations of peptide and Th-T, respectively. Aggregated peptide binding was calculated using the typical one-site binding equation (saturation binding curve): $y = (B_{max}x)/(K_d + x)$, where y is concentration of Th-T bound to peptides, B_{max} is the maximum number of binding sites expressed in concentration, x is the Th-T concentration, and K_d is the process constant.

CR binding assays

CR interaction with different aggregated peptides was recorded using a Cary 100 (Varian) UV/Vis spectrophotometer in the range 375–675 nm using a matched pair of quartz cuvettes of 1 cm optical length placed in a thermostated cell holder at 25 °C. A fixed amount of CR or peptide was mixed with varying concentrations of peptide and CR, respectively. In order to detect a typical amyloid band at ~541 nm, we analyzed the differential CR spectrum. Aggregated peptide binding was calculated using the typical one-site binding equation, as previously indicated for Th-T binding.

Atomic force microscopy

Images of the fibrils formed by the WT, RETRO, and DESIGN peptides were obtained with a multimode atomic force microscope (Veeco Instruments, Inc., Santa Barbara, CA) equipped with a 12-μm scanner (E-scanner). The images were taken in liquid media using a liquid cell without the O-ring seal. About 50 μL of peptide solution was deposited on cleaved HOPG (NT-MDT Co., Moscow, Russia) and allowed to adsorb for about 20 min before the measurements were started. The peptide samples had been previously centrifuged and resuspended in double-deionized water after the removal of the supernatant. This process was carried out three times to eliminate dimethyl sulfoxide from the incubation buffer, which was observed to adsorb on HOPG. Veeco NP-S probes were used to scan the samples in tapping mode at a scan rate of 0.5 or 1 Hz.

Transmission electron microscopy

Fibrillar peptide suspensions were centrifuged, and the insoluble part was resuspended in water, placed on carbon-coated copper grids, and left for 5 min. The grids were then washed twice with distilled water, stained with 2% (wt/vol) uranyl acetate for another 2 min, and washed with distilled water before analysis with a Hitachi H-7000 transmission electron microscope operating at an accelerating voltage of 75 kV.

Aggregation, seeding, and cross-seeding tests

Peptide aggregation from a soluble monomer was monitored by measuring the transition from the nonaggregated state to the aggregated state by relative Th-T fluorescence at 480 nm upon excitation at 445 nm. In the seeding and cross-seeding assays, a solution of aggregated peptides (representing 10% of monomer peptide) was also added. All experiments were carried out with a soluble monomer concentration of 15 μM.

The peptide aggregation process may be studied as an autocatalytic reaction[60] using the equation:

$$f = \frac{\rho\{e^{[(1+\rho)kt]} - 1\}}{1 + \rho\{e^{[(1+\rho)kt]}\}} \quad (2)$$

under the boundary conditions of $t=0$ and $f=0$, where $k = k_e a$ (a is the protein concentration) and ρ represents the dimensionless value describing the ratio of k_n to k.[60] By nonlinear regression of f (aggregated fraction) against t (time; in minutes), values of ρ and k can be easily obtained and, from them, the rate constants k_e (elongation constant) and k_n (nucleation constant). The extrapolation of the growth portion of the sigmoid curve to abscissa ($f=0$) and to the highest ordinate value of the fitted plot afforded two values of time (t_0 and t_1), which correspond to the lag time and the time at which the aggregation was almost completed.

Determination of thermodynamic parameters

When the logarithm of the elongation rate constant is represented as a function of inverse temperature, these data points fit well with a straight line, suggesting that both processes follow the Arrhenius law:

$$k = Ae^{-E_A/RT} \quad (3)$$

where A is the preexponential or frequency factor, E_A is the activation energy, and T is the absolute temperature (in Kelvin). Taking the natural log of both sides of Eq. (1), one obtains:

$$\ln k = -E_A/RT + lnA \quad (4)$$

By plotting ln k *versus* $1/T$, one obtains a linear relationship, and one can determine E_A from the slope ($-E_A/R$) and A from the y-intercept.

In order to estimate the relative contributions of activation enthalpy and entropy to the elongation rate, we have applied the transition-state theory.[61] The elongation rate can be expressed as:

$$k_e = k_e^0 e^{-\Delta G^*/k_B T} \quad (5)$$

where k_e is the elongation rate, k_e^0 is the preexponential factor for the elongation rate, ΔG^* is the standard Gibbs free energy of activation, and k_B is the Boltzmann factor. From the theory, we can assume that k^0 is proportional to the number concentration and DR_H, where $D = k_B T/(6\pi\eta R_H)$ is the diffusion coefficient of an object whose sphere of influence is R_H and with medium viscosity η. The preexponential factors can be expressed as:

$$k_e^0 = \frac{1.33 k_B T N_A}{\eta} \quad (6)$$

where N_A is the Avogadro number and c is the molar concentration.

The order of magnitude of both enthalpy cost and entropy cost associated with the elongation process can be estimated from the expression:

$$N_A k_B ln\left(\frac{k_e}{k_e^0}\right) = \Delta S^* - \Delta H^* T \quad (7)$$

The Gibbs free energy of activation can be determined by:

$$\Delta G^* = \Delta H^* - T\Delta S^* \quad (8)$$

Cell viability assays

The toxicity of fibrils was tested on cultured neuroblastoma cells (SH-SY5Y cell line). Cells were plated at 50,000 cells mL^{-1} on 96-well plates in 100 μL of Dulbecco's modified Eagle's medium (DMEM; Biological Industries, Israel) supplemented with 4.5 mg L^{-1} D-glucose, 2 mM L-glutamine, 50 μg mL^{-1} penicillin, 50 μg mL^{-1} streptomycin, and 10% fetal bovine serum. After 24 h of incubation at 37 °C and 5% CO_2 atmosphere, the medium was substituted with 90 μL of peptide-containing solutions prepared by a 10× dilution of 100 μM aggregated peptide samples in DMEM. Incubation was resumed for 24 or 48 h. Then, 10 μL of 4-[3-(4-iodophenyl)-2-(4-nitrophenyl)-2*H*-5-tetrazolio]-1,3-benzene disulfonate labelling reagent (Roche Diagnostics GmbH, Germany) was added to each well, and the plate was incubated under the same conditions for 1 h. The tetrazolium salt 4-[3-(4-iodophenyl)-2-(4-nitrophenyl)-2*H*-5-tetrazolio]-1,3-benzene disulfonate labelling reagent was cleaved to formazan by mitochondrial dehydrogenases. The amount of formazan dye formed is a measure of enzyme activity, which directly correlates with the number of metabolically active cells in the culture. Formazan dye formation was quantified by measuring the absorbance of the samples (prepared in sextuplicate for each experiment) at 440 nm and 37 °C using a Benchmark Plus Microplate Spectrophotometer (Bio-Rad Laboratories). One hundred percent cell viability was assigned to the absorbance of the control samples of cells incubated in peptide-free DMEM.

Acknowledgements

This work was supported by grants BIO2007-68046, BIO2005-01591, BIO2008-01184, and CSD2006-00012 (including FEDER funds) from Ministerio de Ciencia e Innovación, Spain, and by grant 2009-SGR 760 from AGAUR (Generalitat de Catalunya). A.E. and N.S.G. were the beneficiaries of an FPI fellowship awarded by the Spanish Ministry. R.S. was the beneficiary of an I3 contract (Universidad Autonoma de Barcelona-Generalitat de Catalunya). J.J.V.D. was the beneficiary of a contract from the Juan de la Cierva Programme from Ministerio de Ciencia e Innovación (Spain). S.V. was granted an Institució Catalana de Recerca i Estudis Avançats Academia award. We thank the Scientific and Technical Services of the University of Barcelona for technical assistance.

Supplementary Data

Supplementary data associated with this article can be found, in the online version, at doi:10.1016/j.jmb.2010.09.052

References

1. Travaglini-Allocatelli, C., Ivarsson, Y., Jemth, P. & Gianni, S. (2009). Folding and stability of globular proteins and implications for function. *Curr. Opin. Struct. Biol.* **19**, 3–7.
2. Olszewski, K. A., Kolinski, A. & Skolnick, J. (1996). Does a backwardly read protein sequence have a unique native state? *Protein Eng.* **9**, 5–14.
3. Guptasarma, P. (1992). Reversal of peptide backbone direction may result in the mirroring of protein structure. *FEBS Lett.* **310**, 205–210.
4. Lacroix, E., Viguera, A. R. & Serrano, L. (1998). Reading protein sequences backwards. *Fold. Des.* **3**, 79–85.
5. Fernandez-Busquets, X., de Groot, N. S., Fernandez, D. & Ventura, S. (2008). Recent structural and computational insights into conformational diseases. *Curr. Med. Chem.* **15**, 1336–1349.
6. Chiti, F. & Dobson, C. M. (2006). Protein misfolding, functional amyloid, and human disease. *Annu. Rev. Biochem.* **75**, 333–366.
7. Dobson, C. M. (2003). Protein folding and misfolding. *Nature*, **426**, 884–890.
8. Goldschmidt, L., Teng, P. K., Riek, R. & Eisenberg, D. (2010). Identifying the amylome, proteins capable of forming amyloid-like fibrils. *Proc. Natl Acad. Sci. USA*, **107**, 3487–3492.
9. Chiti, F., Calamai, M., Taddei, N., Stefani, M., Ramponi, G. & Dobson, C. M. (2002). Studies of the aggregation of mutant proteins *in vitro* provide insights into the genetics of amyloid diseases. *Proc. Natl Acad. Sci. USA*, **99**, 16419–16426.
10. Ventura, S., Zurdo, J., Narayanan, S., Parreno, M., Mangues, R., Reif, B. *et al.* (2004). Short amino acid stretches can mediate amyloid formation in globular proteins: the Src homology 3 (SH3) case. *Proc. Natl Acad. Sci. USA*, **101**, 7258–7263.
11. Forloni, G., Lucca, E., Angeretti, N., Della Torre, P. & Salmona, M. (1997). Amidation of beta-amyloid peptide strongly reduced the amyloidogenic activity without alteration of the neurotoxicity. *J. Neurochem.* **69**, 2048–2054.
12. Selvaggini, C., De Gioia, L., Cantu, L., Ghibaudi, E., Diomede, L., Passerini, F. *et al.* (1993). Molecular characteristics of a protease-resistant, amyloidogenic and neurotoxic peptide homologous to residues 106–126 of the prion protein. *Biochem. Biophys. Res. Commun.* **194**, 1380–1386.
13. Ross, E. D., Baxa, U. & Wickner, R. B. (2004). Scrambled prion domains form prions and amyloid. *Mol. Cell. Biol.* **24**, 7206–7213.
14. Ross, E. D., Edskes, H. K., Terry, M. J. & Wickner, R. B. (2005). Primary sequence independence for prion formation. *Proc. Natl Acad. Sci. USA*, **102**, 12825–12830.
15. DuBay, K. F., Pawar, A. P., Chiti, F., Zurdo, J., Dobson, C. M. & Vendruscolo, M. (2004). Prediction of the absolute aggregation rates of amyloidogenic polypeptide chains. *J. Mol. Biol.* **341**, 1317–1326.
16. Monsellier, E., Ramazzotti, M., de Laureto, P. P., Tartaglia, G. G., Taddei, N., Fontana, A. *et al.* (2007). The distribution of residues in a polypeptide sequence is a determinant of aggregation optimized by evolution. *Biophys. J.* **93**, 4382–4391.

17. Liu, Y., Wei, H., Wang, J., Qu, J., Zhao, W. & Tao, H. (2007). Effects of randomizing the Sup35NM prion domain sequence on formation of amyloid fibrils *in vitro*. *Biochem. Biophys. Res. Commun.* **353**, 139–146.
18. Gebre-Medhin, S., Olofsson, C. & Mulder, H. (2000). Islet amyloid polypeptide in the islets of Langerhans: friend or foe? *Diabetologia*, **43**, 687–695.
19. Clark, A., Cooper, G. J., Lewis, C. E., Morris, J. F., Willis, A. C., Reid, K. B. & Turner, R. C. (1987). Islet amyloid formed from diabetes-associated peptide may be pathogenic in type-2 diabetes. *Lancet*, **2**, 231–234.
20. Yoon, S., Welsh, W. J., Jung, H. & Yoo, Y. D. (2007). CSSP2: an improved method for predicting contact-dependent secondary structure propensity. *Comput. Biol. Chem.* **31**, 373–377.
21. Moriarty, D. F. & Raleigh, D. P. (1999). Effects of sequential proline substitutions on amyloid formation by human amylin 20–29. *Biochemistry*, **38**, 1811–1818.
22. Tracz, S. M., Abedini, A., Driscoll, M. & Raleigh, D. P. (2004). Role of aromatic interactions in amyloid formation by peptides derived from human amylin. *Biochemistry*, **43**, 15901–15908.
23. Scrocchi, L. A., Ha, K., Chen, Y., Wu, L., Wang, F. & Fraser, P. E. (2003). Identification of minimal peptide sequences in the (8–20) domain of human islet amyloid polypeptide involved in fibrillogenesis. *J. Struct. Biol.* **141**, 218–227.
24. Gilead, S. & Gazit, E. (2008). The role of the 14–20 domain of the islet amyloid polypeptide in amyloid formation. *Exp. Diabetes Res.* **2008**, 256954.
25. Kajava, A. V., Aebi, U. & Steven, A. C. (2005). The parallel superpleated beta-structure as a model for amyloid fibrils of human amylin. *J. Mol. Biol.* **348**, 247–252.
26. Luca, S., Yau, W. M., Leapman, R. & Tycko, R. (2007). Peptide conformation and supramolecular organization in amylin fibrils: constraints from solid-state NMR. *Biochemistry*, **46**, 13505–13522.
27. Wiltzius, J. J., Sievers, S. A., Sawaya, M. R., Cascio, D., Popov, D., Riekel, C. & Eisenberg, D. (2008). Atomic structure of the cross-beta spine of islet amyloid polypeptide (amylin). *Protein Sci.* **17**, 1467–1474.
28. Fernandez-Escamilla, A. M., Rousseau, F., Schymkowitz, J. & Serrano, L. (2004). Prediction of sequence-dependent and mutational effects on the aggregation of peptides and proteins. *Nat. Biotechnol.* **22**, 1302–1306.
29. Tartaglia, G. G., Cavalli, A., Pellarin, R. & Caflisch, A. (2005). Prediction of aggregation rate and aggregation-prone segments in polypeptide sequences. *Protein Sci.* **14**, 2723–2734.
30. Conchillo-Sole, O., de Groot, N. S., Aviles, F. X., Vendrell, J., Daura, X. & Ventura, S. (2007). AGGRESCAN: a server for the prediction and evaluation of "hot spots" of aggregation in polypeptides. *BMC Bioinf.* **8**, 65.
31. Galzitskaya, O. V., Garbuzynskiy, S. O. & Lobanov, M. Y. (2006). Prediction of amyloidogenic and disordered regions in protein chains. *PLoS Comput. Biol.* **2**, e177.
32. Thompson, M. J., Sievers, S. A., Karanicolas, J., Ivanova, M. I., Baker, D. & Eisenberg, D. (2006). The 3D profile method for identifying fibril-forming segments of proteins. *Proc. Natl Acad. Sci. USA*, **103**, 4074–4078.
33. Zhang, Z., Chen, H. & Lai, L. (2007). Identification of amyloid fibril-forming segments based on structure and residue-based statistical potential. *Bioinformatics*, **23**, 2218–2225.
34. Trovato, A., Seno, F. & Tosatto, S. C. (2007). The PASTA server for protein aggregation prediction. *Protein Eng. Des. Sel.* **20**, 521–523.
35. Jaikaran, E. T., Higham, C. E., Serpell, L. C., Zurdo, J., Gross, M., Clark, A. & Fraser, P. E. (2001). Identification of a novel human islet amyloid polypeptide beta-sheet domain and factors influencing fibrillogenesis. *J. Mol. Biol.* **308**, 515–525.
36. Arimon, M., Diez-Perez, I., Kogan, M. J., Durany, N., Giralt, E., Sanz, F. & Fernandez-Busquets, X. (2005). Fine structure study of Abeta1–42 fibrillogenesis with atomic force microscopy. *FASEB J.* **19**, 1344–1346.
37. Khurana, R., Coleman, C., Ionescu-Zanetti, C., Carter, S. A., Krishna, V., Grover, R. K. *et al.* (2005). Mechanism of thioflavin T binding to amyloid fibrils. *J. Struct. Biol.* **151**, 229–238.
38. Ban, T., Yamaguchi, K. & Goto, Y. (2006). Direct observation of amyloid fibril growth, propagation, and adaptation. *Acc. Chem. Res.* **39**, 663–670.
39. Jarrett, J. T. & Lansbury, P. T., Jr. (1993). Seeding "one-dimensional crystallization" of amyloid: a pathogenic mechanism in Alzheimer's disease and scrapie? *Cell*, **73**, 1055–1058.
40. Munishkina, L. A., Henriques, J., Uversky, V. N. & Fink, A. L. (2004). Role of protein–water interactions and electrostatics in alpha-synuclein fibril formation. *Biochemistry*, **43**, 3289–3300.
41. Scheckel, K. G. & Sparks, D. L. (2000). Kinetics of the formation and dissolution of Ni precipitates in a gibbsite/amorphous silica mixture. *J. Colloid Interface Sci.* **229**, 222–229.
42. Krebs, M. R., Morozova-Roche, L. A., Daniel, K., Robinson, C. V. & Dobson, C. M. (2004). Observation of sequence specificity in the seeding of protein amyloid fibrils. *Protein Sci.* **13**, 1933–1938.
43. Lorenzo, A., Razzaboni, B., Weir, G. C. & Yankner, B. A. (1994). Pancreatic islet cell toxicity of amylin associated with type-2 diabetes mellitus. *Nature*, **368**, 756–760.
44. Bartlett, A. I. & Radford, S. E. (2009). An expanding arsenal of experimental methods yields an explosion of insights into protein folding mechanisms. *Nat. Struct. Mol. Biol.* **16**, 582–588.
45. Dill, K. A. (1985). Theory for the folding and stability of globular proteins. *Biochemistry*, **24**, 1501–1509.
46. Fersht, A. R. (1995). Optimization of rates of protein folding: the nucleation–condensation mechanism and its implications. *Proc. Natl Acad. Sci. USA*, **92**, 10869–10873.
47. Dyson, H. J., Wright, P. E. & Scheraga, H. A. (2006). The role of hydrophobic interactions in initiation and propagation of protein folding. *Proc. Natl Acad. Sci. USA*, **103**, 13057–13061.
48. Le Duff, C. S., Whittaker, S. B., Radford, S. E. & Moore, G. R. (2006). Characterisation of the conformational properties of urea-unfolded Im7: implications for the early stages of protein folding. *J. Mol. Biol.* **364**, 824–835.

49. Serio, T. R., Cashikar, A. G., Kowal, A. S., Sawicki, G. J., Moslehi, J. J., Serpell, L. *et al.* (2000). Nucleated conformational conversion and the replication of conformational information by a prion determinant. *Science*, **289**, 1317–1321.
50. Cheon, M., Chang, I., Mohanty, S., Luheshi, L. M., Dobson, C. M., Vendruscolo, M. & Favrin, G. (2007). Structural reorganisation and potential toxicity of oligomeric species formed during the assembly of amyloid fibrils. *PLoS Comput. Biol.* **3**, 1727–1738.
51. Bolognesi, B., Kumita, J. R., Barros, T., Esbjorner-Winters, E., Luheshi, L., Crowther, D. C. *et al.* (2010). ANS binding reveals common features of cytotoxic amyloid species. *ACS Chem. Biol.* **5**, 735–740.
52. Schwartz, R. & King, J. (2006). Frequencies of hydrophobic and hydrophilic runs and alternations in proteins of known structure. *Protein Sci.* **15**, 102–112.
53. de la Paz, M. L. & Serrano, L. (2004). Sequence determinants of amyloid fibril formation. *Proc. Natl Acad. Sci. USA*, **101**, 87–92.
54. West, M. W., Wang, W., Patterson, J., Mancias, J. D., Beasley, J. R. & Hecht, M. H. (1999). *De novo* amyloid proteins from designed combinatorial libraries. *Proc. Natl Acad. Sci. USA*, **96**, 11211–11216.
55. Wilmot, C. M. & Thornton, J. M. (1988). Analysis and prediction of the different types of beta-turn in proteins. *J. Mol. Biol.* **203**, 221–232.
56. Monsellier, E. & Chiti, F. (2007). Prevention of amyloid-like aggregation as a driving force of protein evolution. *EMBO Rep.* **8**, 737–742.
57. Tartaglia, G. G., Pawar, A. P., Campioni, S., Dobson, C. M., Chiti, F. & Vendruscolo, M. (2008). Prediction of aggregation-prone regions in structured proteins. *J. Mol. Biol.* **380**, 425–436.
58. Sawaya, M. R., Sambashivan, S., Nelson, R., Ivanova, M. I., Sievers, S. A., Apostol, M. I. *et al.* (2007). Atomic structures of amyloid cross-beta spines reveal varied steric zippers. *Nature*, **447**, 453–457.
59. Santoro, M. M. & Bolen, D. W. (1988). Unfolding free energy changes determined by the linear extrapolation method: 1. Unfolding of phenylmethanesulfonyl alpha-chymotrypsin using different denaturants. *Biochemistry*, **27**, 8063–8068.
60. Sabate, R., Gallardo, M. & Estelrich, J. (2003). An autocatalytic reaction as a model for the kinetics of the aggregation of beta-amyloid. *Biopolymers*, **71**, 190–195.
61. Mauro, M., Craparo, E. F., Podesta, A., Bulone, D., Carrotta, R., Martorana, V. *et al.* (2007). Kinetics of different processes in human insulin amyloid formation. *J. Mol. Biol.* **366**, 258–274.

Article

pubs.acs.org/Biomac

Native Structure Protects SUMO Proteins from Aggregation into Amyloid Fibrils

Raimon Sabate,[†,§] Alba Espargaro,[†] Ricardo Graña-Montes,[†,‡] David Reverter,[†,‡] and Salvador Ventura*[,†,‡]

[†]Institut de Biotecnologia i de Biomedicina and [‡]Departament de Bioquímica i Biologia Molecular, Universitat Autònoma de Barcelona, 08193 Bellaterra (Barcelona), Spain

[§]Departament de Fisicoquímica, Facultat de Farmàcia, Universitat de Barcelona, Avda. Joan XXIII s/n, E-08028-Barcelona, Spain

Supporting Information

ABSTRACT: SUMO proteins belong to the Ubiquitin-like protein family, all sharing a common fold and a similar mechanism of conjugation to target polypeptides. SUMO is ubiquitous in all eukaryotes and participates in many crucial pathways. Native SUMO proteins are highly soluble, a property that is exploited in biotechnology. Moreover, SUMO regulates the solubility of aggregation-prone proteins in neurodegenerative disorders. Despite these properties, we show here that human SUMO1, SUMO2, and SUMO3 proteins are at risk of aggregation into amyloid structures if their native conformation is perturbed. Aggregation is mediated by specific regions, which overlap with SUMO functional interfaces, illustrating a competition between function and aggregation. Aggregation of SUMOs might have important physiological implications because disruption of the SUMO pathway is lethal in different organisms. It appears that functional constraints make it difficult to avoid the competition between productive folding and deleterious aggregation in globular proteins, even for essential polypeptides.

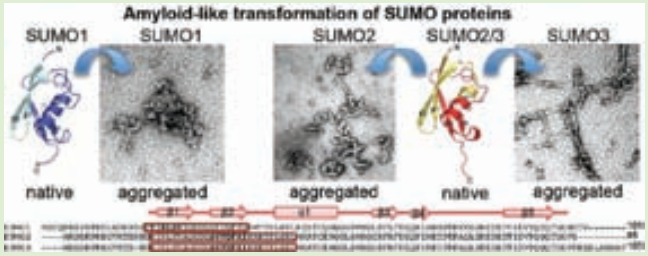

INTRODUCTION

To function, the large majority of proteins need to fold into a specific 3D conformation.[1] Only properly folded proteins remain soluble in the crowded cellular environment and are able to interact specifically with their targets.[2] The failure of proteins to fold properly, or to remain correctly folded, is associated with the impairment of essential cellular processes and is behind a wide range of human disorders in which proteins interact aberrantly to form insoluble aggregates.[3] The proteins involved in such pathologies are not sequentially or structurally related but in most cases self-assemble into amyloid fibrils, sharing a common cross-β-sheet motif.[4] Importantly, increasing evidence suggest that the ability to assemble into highly organized amyloid-like structures is not an unusual feature exhibited by a reduced set of proteins with special sequential or structural properties but rather a property shared by most, if not all, polypeptides occurring in both prokaryotic and eukaryotic organisms.[5−7] This implies that in addition to the native fold it would exist an alternative, stable, and ordered state accessible to all proteins. It appears that the set of noncovalent interactions that stabilize the native structure are also responsible for the formation of amyloids.[8] Therefore, both states compete within the cell, resulting in normal or aberrant biological behavior depending on whether the native or the aggregated state is populated.

The propensity to form amyloid structures is linked to both the sequential and conformational properties of proteins. As a general trend, evolution has endorsed globular proteins with solubility in their biological environments. However, when the stability of their native state is compromised and they become partially or completely unfolded they might expose previously protected aggregation-prone regions able to nucleate the fibrillation process.[9,10] Such amyloidogenic regions have been identified in most of the proteins involved in neurodegenerative and systemic amyloidogenic diseases.[11−14] There is now evidence that protein sequences have evolved to minimize their aggregation propensity.[15−18] This selective pressure is especially strong for proteins that exert essential cellular functions.[19−21] However, even globular proteins selected to be highly soluble might contain aggregation-"sensitive" stretches in their sequences because they seem to be also important in the folding of proteins into compact and stable conformations. In this sense, it has been recently shown that ubiquitin, a key player in eukaryotic intracellular protein degradation, which is considered to be a thermostable and very soluble globular protein, forms amyloid fibrils when its conformational stability is compromised.[22]

SUMO belongs to the Ubiquitin-like (Ubl) protein family. The Ubl protein family are small size (~10 KDa) post-translational modifiers, which are attached to protein substrates

Received: March 20, 2012
Revised: April 26, 2012
Published: May 4, 2012

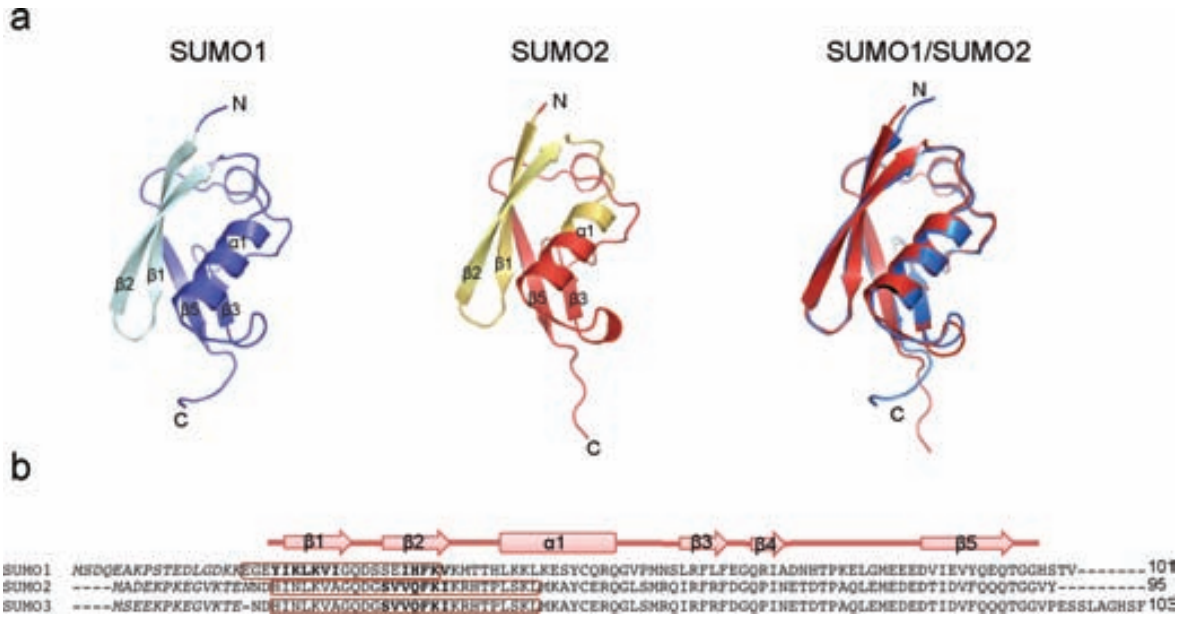

Figure 1. Structural comparison of SUMO1 and SUMO2. (a) Ribbon representation of the structures of SUMO1 (blue), SUMO2 (red), and the overlapping between SUMO1 and SUMO2. Labels represent the secondary structure elements and the N- and C-termini. (b) Structural alignment of sequences of SUMO1, SUMO2, and SUMO3. Residues in bold correspond to predicted amyloidogenic regions. Boxed sequences correspond to regions protected from proteolysis in the aggregated state.

via an isopeptide bond between its C-terminal glycine and a lysine residue of the substrate.[23] Despite the low degree of sequence homology displayed between the members of the family, they all share a common protein fold and a similar mechanism of conjugation. SUMO is the second most studied member of the Ubl family and can be attached to protein substrates via an enzymatic cascade of three enzymes (E1-E2-E3,) which is analogous to that in ubiquitin, and leads to the formation of the isopeptide bond.[24] This sumoylation process can be reversed by the action of specific SUMO proteases. In contrast with ubiquitin, which is mainly known in protein degradation via the 26S-proteasome, SUMO participates in a great variety of cellular processes, often by regulating protein−protein or protein−DNA interactions. Such processes include transcriptional regulation, nuclear transport, apoptosis, protein stability, maintenance of genome integrity, response to stress, signal transduction, and cell-cycle progression.[23,25−27] SUMO is present in all eukaryotes and has been proven to be essential in many organisms; that is, in *Saccharomyces cerevisiae*, defects in the sumoylation machinery lead to cell cycle arrest during the G2-M phase transition.[28]

In humans there are four different SUMO isoforms, SUMO1, SUMO2, SUMO3, and SUMO4. SUMO2 and SUMO3 are highly homologous, with an overall sequence identity of 95% and displaying sequence variation only in the N- and C-terminal extensions (they are sometimes referred as SUMO2/3) (Figure 1). In contrast SUMO1 shares only 43% of sequence identity with either SUMO2 or SUMO3 (Figure 1). SUMO4 does not seem to participate in the formation of conjugates in vivo, and it might be a pseudogene.[29] It has recently been shown that SUMO isoforms, namely, SUMO1 and SUMO2/3, are not redundant in the cell, some substrates can be exclusively modified by SUMO1 or by SUMO2/3, whereas some other substrates can be modified by both SUMO isoforms. In many cases, the biochemical regulation of this SUMO isoform specificity has not yet been revealed; presumably, the availability of the SUMO isoforms in the cell, the specific conjugation by the E3 SUMO ligase, or both may play a role in those processes.

Recent reports indicate that SUMO conjugation favors protein solubility.[30−33] SUMO has been involved recently in the regulation of the solubility of aggregation-prone proteins in neurodegenerative/conformational diseases. In this way, α-synuclein sumoylation inhibits its aggregation and toxicity, suggesting that defects in the SUMO pathway may contribute to the onset of aggregation-promoted disorders.[34] Because of their high stability and solubility, ubiquitin and SUMO proteins have become popular tags to enhance the recombinant protein expression and solubility in both prokaryotic and eukaryotic systems.[35] Here we show that despite these intrinsic properties, like ubiquitin, human SUMO proteins can form amyloid-like structures when their native structures are perturbed.

MATERIALS AND METHODS

SUMO Expression and Purification. Human Δ17-SUMO1 (residues 18−101), Δ14-SUMO2 (residues 15−95), and Δ13-SUMO3 (residues 14−103) named here as SUMO1, 2 and 3, respectively, were cloned into pET-28b to encode an N-terminal thrombin-cleavable hexahistidine fusion protein. Plasmids were transformed into *Escherichia coli* BL21(DE3) cells. Cultures were fermented in lysogeny broth (LB) medium at 37 °C to an OD_{600nm} of 0.5 to 0.6 before induction with 1 mM isopropyl-1-thio-β-D-galactopyranoside (IPTG) for 3 h at 37 °C; then, the cultures were centrifuged and the cell pellets were frozen at −20 °C. After cell lysis, SUMO proteins were purified under native conditions by affinity chromatography on a FF-Histrap histidine-tag resin (Amersham Biosicences, Uppsala, Sweden) using the required washing (20 mM Tris·HCl at pH 8, 0.5 M NaCl, 20 mM imidazole) and elution (20 mM Tris·HCl at pH 8, 0.5 M NaCl, 500 mM imidazole) buffers. The buffer was exchanged by gel filtration on a Sephadex G-25 column (Amersham Biosciences, Uppsala, Sweden) to phosphate-buffered saline (PBS) at a protein concentration of 2 $mg \cdot mL^{-1}$. To cleave the histidine-tag, we incubated SUMO fusions 16 h at room temperature with thrombin (Amersham Biosciences, Uppsala, Sweden) using 10 units per mg of recombinant protein. Histidine-tags were separated by gel filtration on a Sephadex G-25 column, and thrombin was removed

by filtration on Vivaspin 30 000 MWCO PES filter (Sartorius, Viva Science, Inc., Germany), where it is retained.

Secondary Structure Analysis. Circular dichroism (CD) spectra were measured at a spectral resolution of 1 cm^{-1} and 15 $nm \cdot min^{-1}$ scan rate and collected over the 200−250 nm wavelength range at 25 °C using a Jasco 810 spectropolarimeter with a quartz cell of 0.1 cm path length. Protein concentrations were 20 μM in PBS.

Attenuated total reflectance Fourier transform infrared spectroscopy (ATR FT-IR) analysis of SUMO proteins samples, in their soluble and aggregated states, was carried out using a Bruker Tensor 27 FT-IR spectrometer (Bruker Optics) with a Golden Gate MKII ATR accessory. Each spectrum consists of 16 scan accumulations measured at a spectral resolution of 2 cm^{-1} in a wavelength range between 1700 and 1500 cm^{-1}. Infrared spectra were fitted through overlapping Gaussian curves, and the amplitude, mass center, bandwidth at half of the maximum amplitude, and area for each Gaussian function were calculated employing a nonlinear peak-fitting program (PeakFit package, Systat Software, San Jose, CA).

Intrinsic Fluorescence. SUMO proteins fluorescence was measured in a Varian Cary Eclipse spectrofluorometer using an excitation wavelength of 275 nm and collecting the emission spectra between 280 and 380 nm. Slit widths were typically 5 nm for excitation and 10 nm for emission. Spectra were acquired at 1 nm intervals, 600 $nm \cdot min^{-1}$ rate, and 0.1 s averaging time. Protein concentrations were 20 μM in PBS.

Thermal Denaturation. Thermal denaturation was monitored by following CD signal at 217 nm and the intrinsic Tyr fluorescence (measuring Tyr emission at 305 nm after excitation at 275 nm) with a 0.1 °C temperature pitch and 2 min of temperature equilibration lapse between measures. Experimental data were fitted to a two-state transition curve, whose signals for the folded and unfolded states are dependent on the temperature, using the nonlinear least-squares algorithm provided with Prism (PeakFit package). Protein concentrations were 20 μM in PBS.

Amyloid-Specific Dye Staining. Congo-Red (CR) binding to SUMO aggregates obtained upon incubation at their melting temperature under agitation was recorded using a Cary-100 Varian spectrophotometer (Varian, Palo Alto, CA) in the 375−675 nm wavelength range using a matched pair of quartz cuvettes of 1 cm optical length placed in a thermostatted cell holder at 25 °C. To detect the typical amyloid band at ∼541 nm, differential CR spectra (10 μM) in the presence and absence of 20 μM of protein were used.

Thioflavin-T (Th-T) binding to SUMO proteins aggregates was recorded using a Varian spectrofluorometer (Cary Eclipse, Varian) with an excitation wavelength of 445 nm and an emission range between 470 and 570 nm. Th-T spectra at 25 μM in the absence and presence of 20 μM of protein in PBS at 25 °C were recorded. For optical microscopy analysis, SUMO proteins were incubated for 1 h in the presence of 125 μM of Thioflavin-S (Th−S), and the precipitated fractions, obtained by centrifugation at 14 000g for 5 min, were resuspended in PBS and placed on a microscope slide and sealed. Th−S fluorescence images of SUMO aggregates were obtained at 40-fold magnification under UV light with a fluorescence microscope (Leica Microsystems, Mannheim, Germany).

Bis-ANS Binding. The binding of 1 μM 4,4′-bis(1-anilinonaphthalene 8-sulfonate) (bis-ANS) to SUMO proteins was measured on a Varian spectrofluorimeter (Cary Eclipse, Palo Alto, CA). The samples, in PBS, were excited at 370 nm, and emission was measured between 400 and 600 nm with slit widths of 5 and 10 nm for excitation and emission, respectively. Thermal transition curves were obtained at a cooling rate of 1 °C/min by measuring bis-ANS emission at 480 nm after excitation at 370 nm.

Transmission Electron Microscopy. For negative staining, aggregated proteins were adsorbed to carbon-coated grids, rinsed with water, and stained with 2% (w/v) uranyl acetate. The samples were imaged in a Hitachi H-7000 transmission electron microscope (TEM) operating at an accelerating voltage of 75 kV.

Aggregation Assay (Seeding and Cross-Seeding Determinations). SUMO aggregation from soluble monomers was monitored by measuring the transition from nonaggregated to aggregated states by relative Th-T fluorescence at 480 nm when exciting at 445 nm. In the seeding and cross-seeding assays, a solution of aggregated peptides (representing 10% of soluble SUMO protein) was also added. All experiments were carried out with a soluble monomer concentration of 0.2 mg/mL at the temperature of melting (T_m) in PBS.

The SUMO aggregation process may be studied as an autocatalytic reaction using the equation

$$f = \frac{\rho\{e^{[(1+\rho)kt]} - 1\}}{1 + \rho\{e^{[(1+\rho)kt]}\}} \quad (1)$$

under the boundary condition of $t = 0$ and $f = 0$, where $k = k_e a$ (where a is the protein concentration) and ρ represents the dimensionless value to describe the ratio of k_n to k.[36] By nonlinear regression of f (aggregated fraction) against t (time in minutes), ρ and k values can be easily derived, and from them the rate constants, k_e (elongation constant) and k_n (nucleation constant), can be derived. The extrapolation of the growth portion of the sigmoid curve to the abscissa ($f = 0$), and to the highest ordinate value of the fitted plot, afforded two values of time (t_0 and t_1), which correspond to the lag time and to the time when aggregation is almost completed.

Limited Proteolysis of SUMO Proteins with Proteinase (PK). Aggregated SUMO proteins at 50 μM were digested with 2.5 $\mu g \cdot mL^{-1}$ of proteinase K (PK) in PBS for different times at 37 °C. Reactions were stopped by the addition of 1/3 volume of 3× SDS-PAGE loading buffer and heated at 100 °C for 10 min to be analyzed by SDS-PAGE gels (16% bis-acrilamide). To identify which specific protein regions were embedded in this core, 50 μM of native or heat-aggregated SUMO proteins were digested with PK (2.5 $\mu g \cdot mL^{-1}$) for 30 min at 37 °C in PBS buffer (pH 7.0), and the reactions were stopped by mixing with 1 volume of 10 M urea to dissolve preformed aggregates. After 10-fold dilution in milli-Q water, they were analyzed by mass spectrometry following the α-cyano-4-hydroxycinnamic acid affinity sample preparation protocol with a 600-μm AnchorChip MALDI sample support in an Ultraflex MALDI-TOF mass spectrometer (Bruker Daltonics, Germany).

RESULTS AND DISCUSSION

Spectral Properties of SUMO Proteins. We recombinantly express and purify human SUMO1, SUMO2, and SUMO3 proteins. The native 3D structures of these three SUMO isoforms have been shown to be highly similar to that of ubiquitin, all sharing a compact α/β structure consisting of 15% of α-helix, 35−45% of β-sheet, 25−35% of β-turns, and 10−15% of unordered residues[37−39] (Figure 1). In Figure 2a, we show their CD spectra in the far-UV region. The shapes of the three spectra are similar. As expected, SUMO2 and SUMO3 exhibit overlapping spectra, whereas SUMO1 exhibits higher molar ellipticity between 200 and 210 nm. Deconvolution of the spectra using the K2D3 software[40] suggests that the β-sheet signal (34−45%) is the main contributor to the spectra of SUMO proteins. However, the spectra deviate from that expected for a canonical α/β fold. This behavior is frequently observed in small proteins due to the contribution of aromatic or unfolded regions to the global spectra.[41,42]

We further address the secondary structure content of the three SUMO proteins using FT-IR spectroscopy. The amide I band essentially corresponds to the absorption of the carbonyl peptide bond group of the protein main chain and is, therefore, a sensitive marker of the protein secondary structure. The absorbance spectra of SUMO2 and SUMO3 are essentially identical (Figure 2b). Deconvolution of their spectra indicate that they result from the main contribution of three bands: 1632−1633 cm^{-1} corresponding to intramolecular β-sheet, 1647 cm^{-1} coming from α-helical conformations, and 1673 cm^{-1} attributable to the presence of β-turns. The absorbance

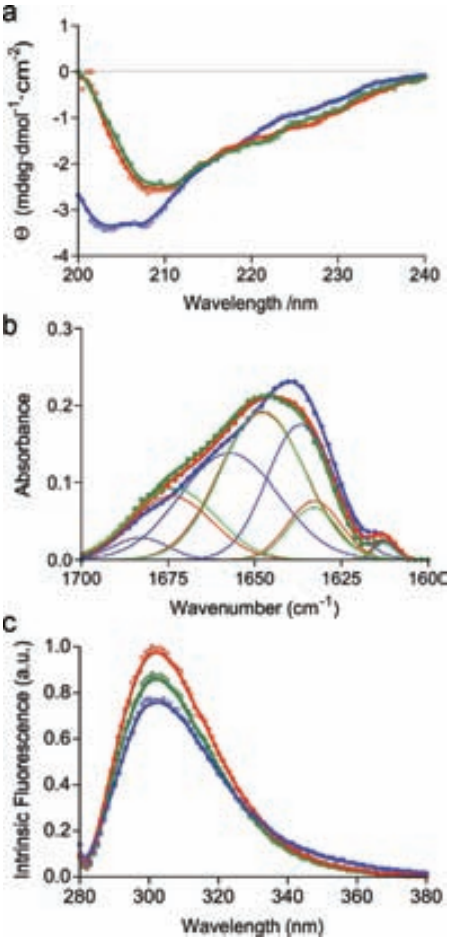

Figure 2. Spectral properties of native SUMO1 (in blue), SUMO2 (in red), and SUMO 3 (in green) proteins. Secondary structure followed by (a) CD and (b) FT-IR and (c) intrinsic fluorescence. Note in panel b the deconvolution of each SUMO spectrum.

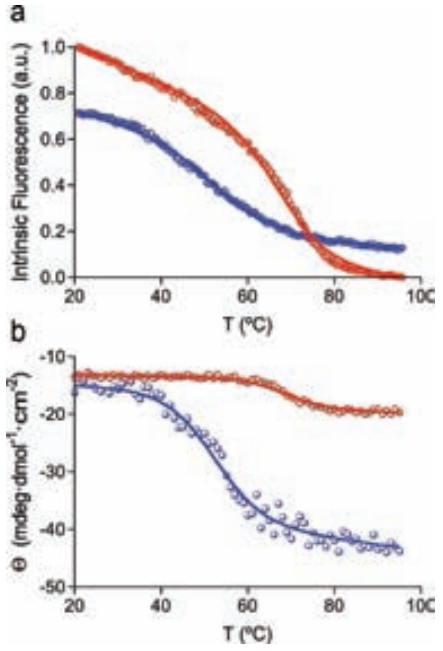

Figure 3. Thermal unfolding of SUMO1 (in blue) and SUMO2 (in red) proteins, followed by (a) intrinsic fluorescence change and (b) CD.

spectrum of SUMO1 differs from that of SUMO2/SUMO3 (Figure 2b). Although all SUMO proteins share the same secondary components, in SUMO1 the bands are red-shifted to 1636, 1657, and 1683 cm^{-1}.

SUMO1 contains three tyrosine (Tyr) residues at positions 21, 51, and 91. SUMO 2 has two Tyr at position 51 and 98 (SUMO1 numeration), and SUMO 3 displays a single Tyr residue at position 51 (SUMO1 numeration). No tryptophan residues are found in any of the SUMO proteins. We excite the different proteins at 275 nm and record their intrinsic fluorescence spectra between 280 and 380 nm. The shapes of all spectra are similar, all sharing the characteristic Tyr emission maximum at 302 nm (Figure 2c).

Thermal Unfolding of SUMO Proteins. The thermal stabilities of SUMO proteins are analyzed by monitoring Tyr intrinsic fluorescence and far-UV CD changes at 302 and 217 nm, respectively, from 20 to 95 °C. Because the spectroscopic analysis confirms previous data indicating that the globular domains of SUMO2 and SUMO3 are not only sequentially identical but also share the same structure, we selected only SUMO2 for stability analysis. The transition curves from heat-induced fluorescence emission changes in SUMO proteins are shown in Figure 3a. The thermal denaturation curves, followed by far-UV CD, are shown in Figure 3b. In both cases, a single cooperative transition is observed, and the data can be fitted to a two-state temperature-induced unfolding model ($R > 0.99$). Moreover, the T_m values calculated for the two proteins from the resulting CD and fluorescence curves are identical within the experimental error, and the corresponding denaturation curves can be overlapped (data not shown), indicating that the secondary and tertiary structures are lost simultaneously upon heating, thus supporting a two-state thermal unfolding mechanism for the two proteins. These data coincide to indicate that SUMO2 is significantly more stable (apparent $T_m \approx 68$ °C) than SUMO1 (apparent $T_m \approx 52$ °C) in front of thermal denaturation.

We explore the presence of exposed hydrophobic clusters in the native state of SUMO1 and SUMO2 by measuring their binding to bis-ANS, a dye that increases its fluorescence emission upon interaction with these regions.[43] Whereas SUMO1 exhibits a moderate binding to bis-ANS (Figure 4a), no binding is detected for SUMO2 (Figure 4b). This is consistent with the proportion of hydrophobic residues exposing more than 10% of their side chains surface to solvent in the two proteins according to the respective crystal structures: 11% in SUMO1 and only 6% in SUMO2/SUMO3 proteins. The bis-ANS binding to SUMO1 is lost upon incubation at 95 °C, supporting the fact that it is a characteristic of its folded state (Figure 4a). Despite the fact that no apparent precipitation is observed when heat-unfolded proteins at 95 °C are cooled to 20 °C at 20 μM concentration, both SUMO1 and SUMO2 experience a large increase in their binding to bis-ANS after this process, indicating that they cannot fully recover their native states and instead misfold into species that expose hydrophobic residues previously hidden in the core of the native structure (Figure 4a,b). Interestingly, this misfolding process during cooling appears to follow a two-state mechanism, with midpoint transitions at ~65 and ~60 °C for SUMO1 and SUMO2 (Figure 4c), respectively ($R > 0.99$), suggesting that the formation of the detected non-native hydrophobic clusters occurs in a cooperative-like manner. The

dx.doi.org/10.1021/bm3004385 | *Biomacromolecules* 2012, 13, 1916−1926

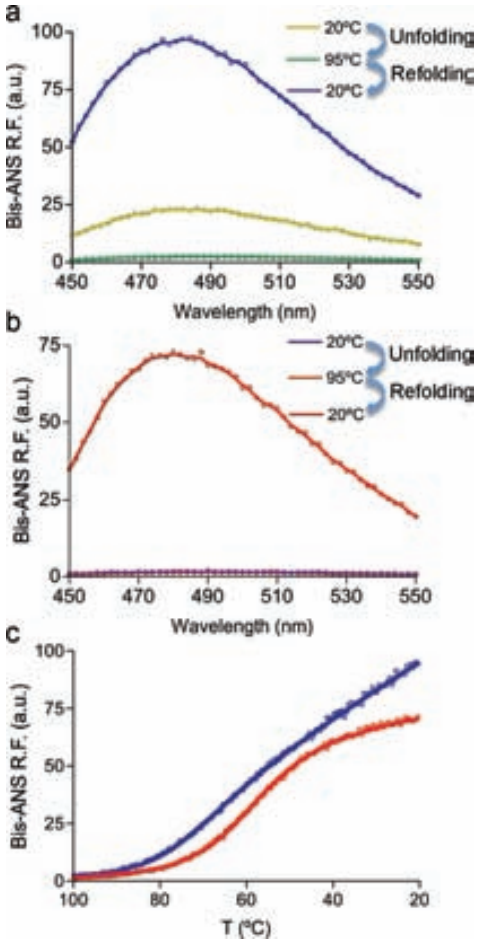

Figure 4. Binding of bis-ANS to soluble SUMO1 and SUMO2 proteins as a function of the temperature. Bis-ANS spectrum of (a) SUMO1 and (b) SUMO2 at 20 °C (lemon and violet), 95 °C (green and orange), and 20 °C after cooling down (blue and red). (c) SUMO 1 and 2 (in blue and red, respectively) refolding from 95 to 20 °C. The fit of the data to a two-state cooperative unfolding model is depicted as a continuous line.

observed midpoint temperatures for bis-ANS binding coincide with temperatures in which both proteins populate partially unfolded states, according to CD and fluorescence unfolding data.

SUMO Proteins Display Predicted Aggregation-Prone Regions. It is now accepted that specific and continuous protein segments nucleate amyloid-like reactions and participate in the formation of the β-core of the mature fibrils.[9,10] Different computational methods have been developed to predict those sequential stretches.[18,44] We used here AGGRESCAN[11] and PASTA,[14] two algorithms based on different principles, to identify if SUMO protein sequences display regions with potential amyloidogenicity that might act as specific nucleus in self-assembling reactions. We consider as potentially amyloidogenic only those regions predicted by both methods. In SUMO1, we detect stretches spanning residues 21−27 (YIKLKVI) in β-strand 1 and residues 34−38 (IHFKV) in β-strand 2 (Figure 1). In SUMO 2/SUMO3, we detect a single region corresponding to residues 32−38 (SVVQFKI) in β-strand 2 (SUMO1 numeration) (Figure 1). Most of the hydrophobic residues in the detected regions are at least partially buried, making difficult the establishment of extensive intermolecular interactions once the protein acquires its native structure, accounting for the solubility of these polypeptides. However, this does not exclude the fact that upon partial unfolding and solvent exposure the predicted regions can favor intermolecular contacts, resulting in hydrophobic clustering.

SUMO Proteins Self-Assemble into β-Sheet Enriched Structures. To explore the possibility that the detected amyloid-prone segments might promote self-assembly when the proteins are partially unfolded, we incubate the different proteins at 1 mg/mL concentration for 24 h under agitation at their melting temperatures: 52 and 68 °C for SUMO1 and SUMO2/SUMO3, respectively. At the end of the reaction, all of the solutions become cloudy, suggesting the presence of aggregates. The far-UV CD spectra of these samples differ significantly from those displayed by the native proteins, all exhibiting a minimum around 217 nm, which indicates enrichment in β-sheet secondary structure (Figure 5a). FT-IR

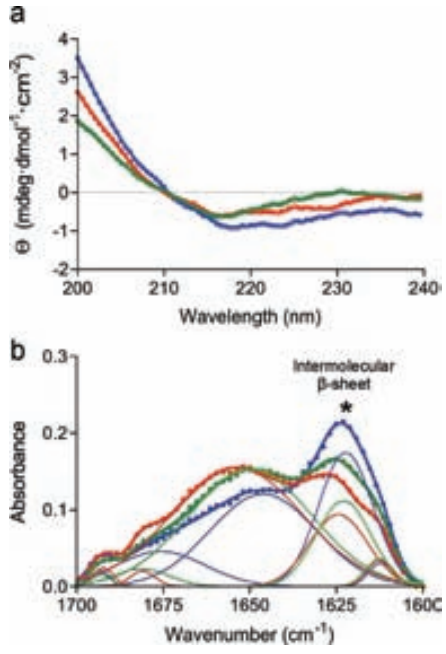

Figure 5. Secondary structure of aggregated SUMO1 (in blue), SUMO2 (in red), and SUMO 3 (in green) proteins followed by (a) CD and (b) ATR FT-IR. Note in panel b the deconvolution of each SUMO spectrum into its spectral components. Asterisk indicates the new intermolecular β-sheet band.

spectroscopy allows addressing more accurately structural features in aggregated proteins.[45] The spectra of aggregated SUMOs exhibit a new band in the amide I region at 1620−1625 cm^{-1}, typically attributed to the presence of intermolecular β-sheet secondary structure, which is accompanied by a minor band 1692 cm^{-1} corresponding to the splitting of the main β-sheet signal (Figure 5b). These two bands are considered to be a hallmark of the presence of amyloid structures.[45,46] Decovolution of the absorbance spectra indicates that the amyloid-like bands contribute to 37 and 23% of the total IR signal for SUMO1 and SUMO2/SUMO3, respectively.

SUMO Aggregates Display Amyloid-Like Properties. We used the amyloid-specific dyes Congo red (CR), thioflavin T (Th-T), and thioflavin S (Th−S) to analyze if the detected intermolecular β-sheet in aggregated SUMO proteins corresponds to amyloid-like assemblies. The absorbance of CR increases, and the spectrum maximum red shifts to 505−510

dx.doi.org/10.1021/bm3004385 | Biomacromolecules 2012, 13, 1916−1926

nm in the presence of aggregates of all SUMO proteins (Figure 6a). This spectral change corresponds to that promoted by

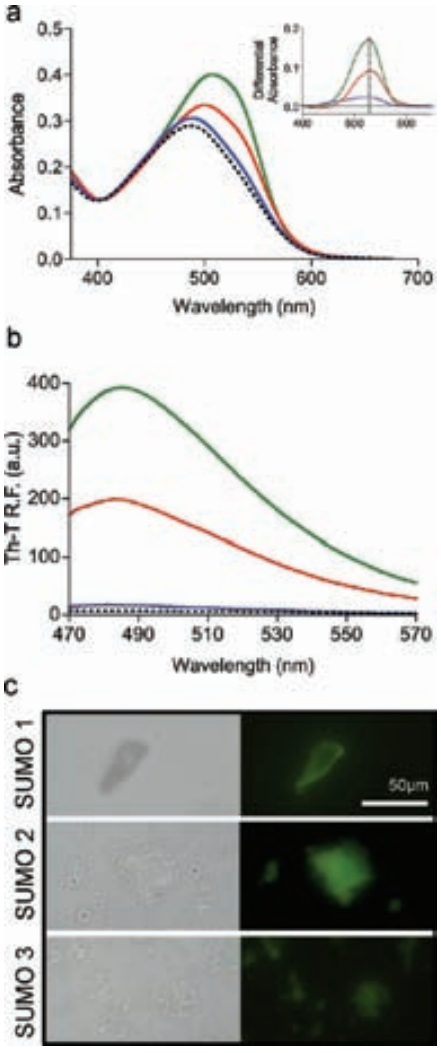

Figure 6. Binding of SUMO protein aggregates to specific amyloid-like dyes. (a) CR spectra; the inset shows the difference spectra displaying the typical 541 nm amyloid peak. (b) Th-T spectra displaying fluorescence enhancement at 482 nm when the dye is bound to amyloid-like aggregates. Spectra of free dyes (black dotted line), SUMO1 (in blue), SUMO2 (red), and SUMO3 (in green) are shown. (c) Th−S staining of SUMO aggregates under visible (on the left of each panel) and fluorescent (on the right of each panel) light.

different amyloid proteins in the aggregated state.[47] Moreover, the difference spectra of the dye in the presence and absence of SUMO proteins exhibit the characteristic amyloid band at ∼541 nm (Inset Figure 6a). However, not all of the SUMO aggregates bind to CR with the same affinity, with SUMO1 promoting only slight spectral changes and SUMO3 promoting a large increase in CR absorbance.

Th-T fluorescence emission is enhanced in the presence of amyloid fibrils.[48] The same behavior is observed upon incubation of Th-T with aggregated SUMO proteins. Again, the different aggregates induce differential changes in Th-T fluorescence (Figure 6b), with SUMO1 promoting only a two-fold increase in fluorescence at the ∼482 nm spectral maximum, whereas SUMO2 and SUMO3 promote 40- and 80-fold increases in fluorescence emission, respectively. For all SUMO aggregates, areas rich in fibrous material are stained with Th−S (Figure 6c) to yield green−yellow fluorescence against a dark background, as observed by fluorescence microscopy.

The morphological features of the species present in SUMO protein solutions incubated at melting temperatures are analyzed using TEM. As shown in Figure 7, in all cases we

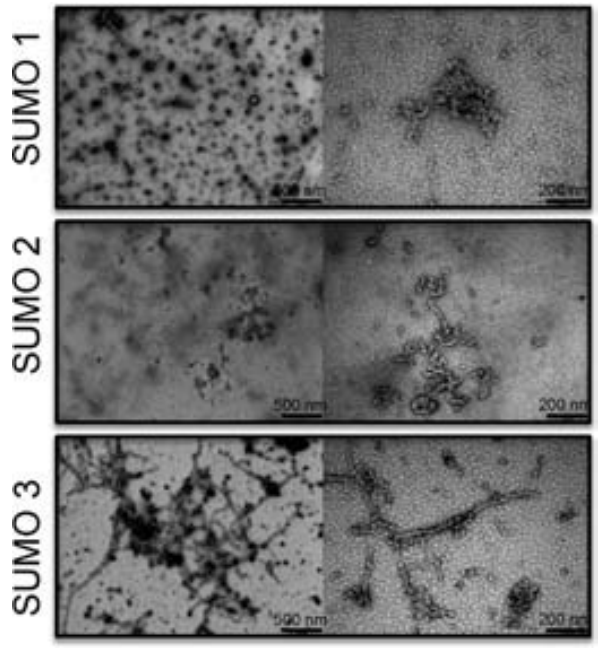

Figure 7. Transmission electron micrographs of SUMO1, SUMO2, and SUMO3 in the aggregated state.

detect the presence of protein aggregates. Nevertheless, the size and morphology of the aggregates are significantly different. SUMO1 forms abundant small oligomeric-like aggregates, which tend to clump together, whereas the aggregates formed by SUMO2 display protofibrillar morphology, and those formed by SUMO3 correspond to mature amyloid-like fibrils. Conformational properties of the different aggregates are well-correlated with their relative binding to amyloid-dyes. Interestingly, despite the fact that the SUMO3 C-terminal tail, which constitutes the only sequential difference between SUMO2 and SUMO3 proteins in our study, is not predicted to be amyloidogenic and has essentially a polar nature, it appears to be an important determinant of the conformational properties of the aggregated state.

The kinetics of amyloid fibril formation usually follow a sigmoidal curve that reflects a nucleation-dependent growth mechanism.[36,49] The assembly of SUMO proteins follows this kinetic scheme (Figure 8). The nucleation step of the amyloid assembly is shortened in the presence of preformed amyloid fibrils of the same protein that can act as seeds for the polymerization reaction.[50] To test whether preformed SUMO aggregates can seed the aggregation of the correspondent soluble proteins, we follow the aggregation kinetics of the proteins at 200 $\mu g \cdot mL^{-1}$ in the presence of 20 $\mu g \cdot mL^{-1}$ of preformed aggregates (Figure 8). A decrease in the lag time of the reaction and a concomitant increase in the nucleation constant (k_n), without a significant effect on the elongation rate (k_e), can be observed in all cases (Table S1 of the Supporting

dx.doi.org/10.1021/bm3004385 | Biomacromolecules 2012, 13, 1916−1926

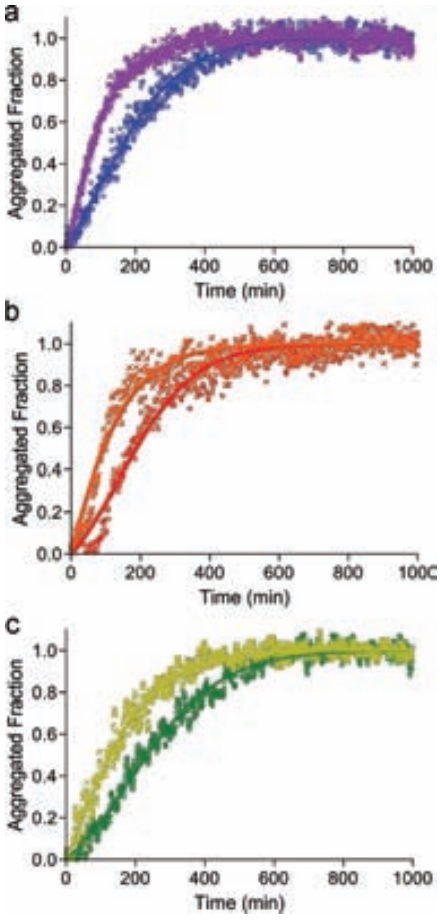

Figure 8. Aggregation kinetics of SUMO proteins. The fibrillar fraction of (a) SUMO1, (b) SUMO2, and (c) SUMO3 is represented as a function of time. The aggregation reactions have been performed in the absence (in blue, red, and green) and in presence (in violet, orange, and yellow, respectively) of 10% of preaggregated protein under agitation at melting temperatures.

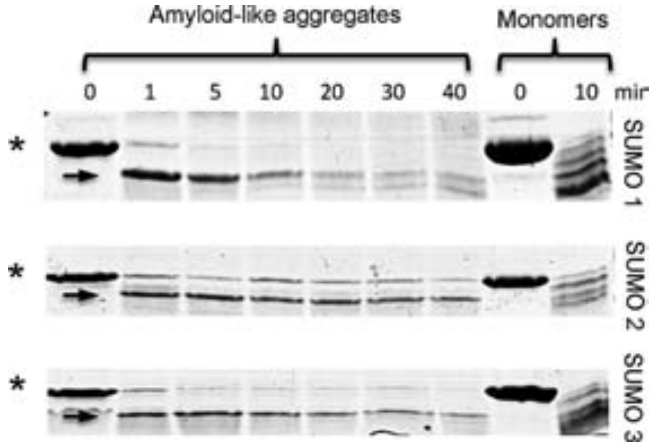

Figure 9. Limited proteolysis of soluble and aggregated SUMO proteins. Time course of proteinase K digestion of soluble and aggregated SUMO proteins, followed by SDS-PAGE. The digestions were carried out at pH 7.5 and 37 °C. Asterisk and black arrows indicate the weight of the native protein and the major resistant species, respectively.

Information), indicating that despite their different morphologies all SUMO aggregates can seed their aggregation reactions.

PK is a protease usually employed to map the protected core of amyloid fibrils because, despite its high activity for cleaving peptide bonds, it cannot attack the highly packed backbones in an amyloid β-sheet structure. Native SUMO proteins are incubated with PK, and the resulting products are analyzed by SDS-PAGE. A smear containing multiple bands is detectable for the three SUMO isoforms, suggesting an unspecific cleavage of these globular proteins (Figure 9). In contrast, treatment of SUMO-aggregated species with PK renders a major band that is selectively protected from digestion, suggesting that it might constitute the core of the detected intermolecular β-sheet structure (Figure 9). To identify which specific protein regions are embedded in this core, we analyze native or heat-aggregated SUMO proteins digested with PK by MALDI-TOF mass spectroscopy. We do not detect any protected protein fragment in PK digestions of native SUMO proteins. In contrast, the aggregated samples display major fragments of ~2600 and ~3000 kDa for SUMO1 and SUMO2/SUMO3, respectively. These fragments likely correspond to the most protected regions in the amyloid-like aggregates formed by SUMO proteins (Table 1 and Supporting Information). In SUMO1, this region contains residues 18−37 corresponding to β-strand 1 and β-strand 2 (SUMO1 numeration) and includes most of the predicted amyloidogenic residues in β-strand 1 (YIKLKVI) and β-strand 2 (IHFK). In SUMO2/SUMO3, the PK protected region consists of residues 20−47 (SUMO 1 numeration) and corresponds to β-strand 1, β-strand 2, and the beginning of the α-helix and includes the single amyloidogenic SVVQFKI sequence detected in the β-strand 2 of these two proteins (Figure 1). The preferential protection of the regions displaying the highest predicted amyloid propensity in SUMO proteins argues that, if exposed to solvent, they might act as effective nucleus for the formation of intermolecular β-sheets that would ultimately result in the aggregation of the proteins in which they are embedded. These sequences are characterized by a combination of hydrophobic and aromatic side chains and polar/charged residues, present in several of the amyloidogenic peptides identified in proteins linked to amyloid processes.[51] In both SUMO1 and SUMO2/SUMO3, the core of the detected amyloid-like structures includes β-strand 1 and β-strand 2. Interestingly enough, prediction of aggregation-prone regions in Smt3, the only SUMO protein in yeast, identifies β-strand 2 as the most amyloidogenic region despite the low sequential identity between yeast and human SUMO proteins. In fact, a BLAST analysis indicates that the detected aggregation-prone sequences are conserved in SUMO proteins across species (data not shown). A common observation in the amyloid fibrils formed by globular proteins linked to different disorders is that the parts of the molecule involved in aggregation used to be located in preformed β-strands, suggesting that local unfolding may allow anomalous intermolecular interaction between this preformed elements leading to the formation of an aggregated β-sheet structure.[52] This appears to be also the case for SUMO proteins. In fact, secondary structure predictions using the algorithm CSSP2[53] indicate that the sequences corresponding to the β-strand 2 display the highest intrinsic β-sheet propensities in human SUMO proteins; therefore, they might be ready to self-assemble in case it becomes exposed to solvent.

Amyloidogenic Regions and Functional Interaction Sites Overlap in SUMO Proteins. In addition to the observed propensity of SUMO isoforms to form β-sheet amyloid-like structures upon protein unfolding, it would be interesting to remark here the tendency of SUMO to form

Table 1. Mass Spectrometry Analysis of the Proteinase-K-Resistant Core of SUMO Protein Aggregates[a]

protein	position	sequence	experimental mass (Da)	theoretical mass (Da)	error (Da)
SUMO1	18−37	*HM*EGE**YIKLKV**IGQDSSE**IHFK**[b]	2588.301	2587.347	0.954
SUMO2	17−44	HINLKVAGQDG**SVVQFKI**KRHTPLSKL	3011.897	3012.735	0.838
SUMO3	17−44	HINLKVAGQDG**SVVQFKI**KRHTPLSKL	3011.854	3012.735	0.881

[a]Residues in bold correspond to predicted amyloidogenic regions. [b]Residues in italics correspond to residues of the His-tag-SUMO1 fusion remaining at the N-terminus of SUMO1 after cleavage with thrombin.

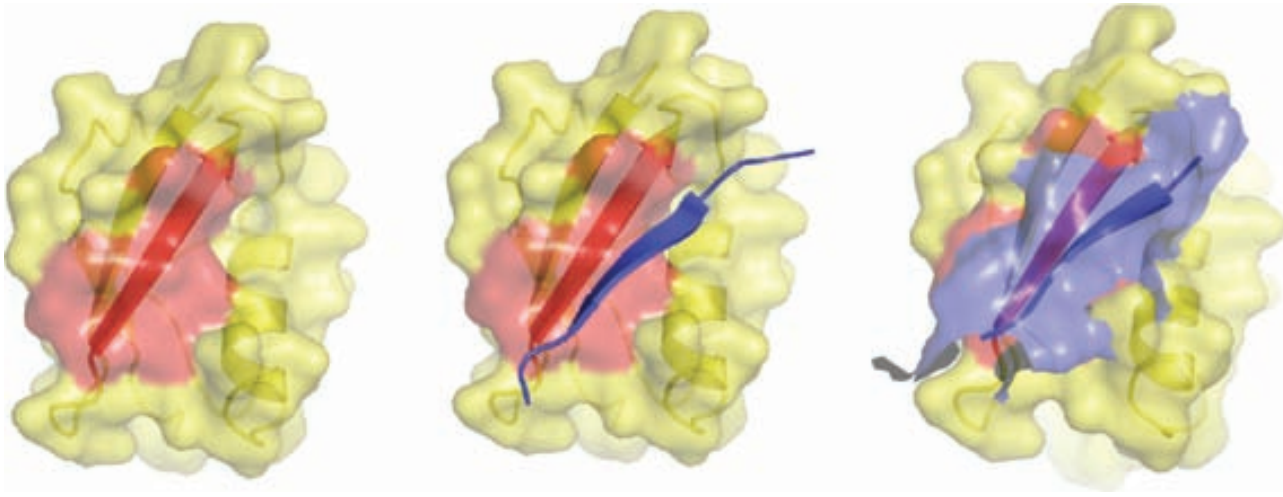

Figure 10. Interaction between SUMO and SUMO interaction motifs (SIMs). (a) Right, surface, and ribbon representation of SUMO-1. Red represents the SUMO b2 strand. Middle, same representation in complex with the SIM depicted as a blue strand. Left, surface representation of the interaction between SUMO-1 (red) and SIM (blue). PDB 1Z5S.

Table 2. Aggregation-Prone Stretches in Putative SIM Sequences, According to AGGRESCAN Predictions[a]

Uniprot Accesion Code	Name	SIM sequence
Q7Z333	SETX	SRGQ *VIII* SDSDDDDER
P23497	SP100	QASD *IIVI* SSEDSEGSTDVD
Q9NS56	TOPORS	RSPV *VIII* DSDSDKDSEVKED
Q8N3Z6	ZCCHC7 motif 2	REVM *IIEI* SSSEEEESTISE
	ZCCHC7 motif 1	NQKK *LIVL* SDSEVIQLSDG
Q9UJ78	ZMYM5 (ZNF237) motif 2	ISET *IV I* DDEEDIE
Q9UBW7	ZMYM2 (ZNF 198) motif 2	VSET IV I DDEEDME
Q9UKY1	ZHX1	SSTT *II I* DSSDETT
O75925	PIAS1	KNKK *VEVI* DLTI DSSSDEEEEEP
O75928	PIAS2	SKKK *VDVI* DLTI ESSSDEEEDPPAKRKC
Q9Y6X2	PIAS3	NKKK *VEVI* DLTI ESSSDEEDLPP
Q6PEW1	ZCCHC12	ADCN *VIEI* DDTL DDSDED *FILI* ES
Q8N2W9	PIAS4	PGAD *VIDL* TL DSSSSSEDEE
Q96B23	C18orf25 motif 2	SPAE *VIDL* TL DEDSRRKYL
Q6VMQ6	ATF7IP (MCAF)	DSSG *VIDL* TM DDEESGA
Q06265	EXOSC9 (PMSCL1)	KTDE *VIVI* TD SEEEE *VIIL* ND
Q96B23	C18orf25 motif 1	SSDSE *VEIV* GVQE

[a]Stretches corresponding to V/I-x-V/I−V/I or V/I−V/I-x-V/I/L SIM consensus are represented in italic letters. Aggregation-prone regions detected by AGGRESCAN appear shadowed. Putative gatekeeper residues are colored in red. SIMs sequences were obtained from ref 58.

intermolecular β-sheets under native conditions. So far, the only known SUMO interaction motif (SIM) displays an extended β-sheet structure, forming an extra intermolecular β-strand with β-strand 2 of SUMO and inserted in a hydrophobic groove created between β-strand 2 and α-helix of SUMO.[54−56]

The amyloidogenic IHFKV region in SUMO1 β-strand 2 is located at the native interface of the complex with its substrate RanGAP1 (PDB 1Z5S) (Figure 10) and is likely a major contributor to the complex stability according to the PISA server (http://www.ebi.ac.uk/msd-srv/prot_int/pistart.html).

dx.doi.org/10.1021/bm3004385 | *Biomacromolecules* 2012, 13, 1916−1926

Several other complexes between SUMO domains and protein fragments containing SIMs, with differential specificity toward SUMO1 or SUMO2/SUMO3 each, have been resolved by NMR spectroscopy, all of them showing a docking for the interaction motif onto SUMO structure identical to that previously mentioned.[54,57,58] Therefore, the same sequence used by SUMOs to establish specific functional interactions in the native state might nucleate its anomalous aggregation upon unfolding. Moreover, the RAnGAP1 SIM sequence at the complex interface also contains a nine-residue predicted amyloidogenic region (LDVLIVYGL), which is in contact with the amyloidogenic stretch in SUMO1 β-strand 2 (Figure 10). Interestingly enough, the consensus sequences for SIMs are considered to be V/I-x-V/I−V/I or V/I−V/I-x-V/I/L, where position two or three can be any amino acid. These consensus regions are highly hydrophobic and likely aggregation-prone. Accordingly, when we analyze the sequences of 19 putative SIMs, previously identified experimentally by yeast two-hybrid,[59] using AGGRESCAN, we detect amyloidogenic stretches in most of them (Table 2). The spatial coincidence of interaction sites and aggregating regions is not an anecdotic property of the SUMO/SIM system but rather a feature of many protein−protein interactions. In general, interface regions are more prone to aggregate than other surface regions.[60] This results from the fact that as in the case of SUMO the interactions that promote the formation of functional complexes, including hydrophobic and electrostatic forces, might also cause anomalous intermolecular association,[60] especially when the interfaces are located in preformed β-sheet secondary structure elements, suggesting that the formation of functional complexes and the aggregation of their individual subunits might compete in the cell. We have previously proposed that this can be one of the underlying reasons for the aggregation of a number of human globular proteins involved in different conformational diseases,[52] a view that has been further confirmed by other studies.[61,62] This evidence has led us to propose that normal and aberrant interactions are two sides of the same coin and that the function represents a competing pathway of aggregation.[63]

It has been shown that evolution uses different negative design strategies to fight against protein deposition.[16] One of them consists of placing amino acids that counteract aggregation at the flanks of protein sequences with high aggregation propensity. These residues are called gatekeepers,[15] and they reduce self-assembly using the repulsive effect of charge (Arg, Lys, Asp, and Glu), the entropic penalty on aggregate formation (Arg and Lys), or incompatibility with β-structure backbone conformation (Pro). In Table 2, we show that this type of residues is abundant at the flanks of the identified aggregating regions in SIMs. The presence of charged residues surrounding the consensus SIM motif has been proposed to be important for establishing specific interactions with SUMO proteins; however, these contacts are not evident in the structures solved so far, and their side chains tend to be disordered in NMR structures, suggesting that they might be instead important to decrease SIMs intrinsic aggregation propensities.

It is intriguing whether the natural tendency of SUMO proteins to form intermolecular β-sheet structures would result in pathological conditions in case their structural stability becomes compromised in the cell. Despite the fact that no evidence exists for this situation, a recent quantitative proteomics study in yeast has identified Smt3 (the SUMO2 analog) to be a member of the cellular subproteome that interacts with and is sequestered by the amyloid-like aggregates formed by both natural and artificial amyloidogenic sequences.[64] In the case of SMT3, these interactions occur prefermentation upon synthesis before adopting stably folded conformations,[64] where its amyloidogenic regions are likely exposed to solvent. The conserved aggregation-propensity of β-strand 2 suggests that it might mediate the detected interactions, arguing that despite the fact that we use here artificial conditions our data might be relevant to understand the amyloid toxicity resulting from the depletion of essential functional proteins like SUMO.[64]

CONCLUSIONS

SUMO proteins are highly soluble in their folded states. In the present work, we show, however, that they are at risk of aggregation into amyloid fibrils if the interactions sustaining their native structure are disturbed. This effect is likely initiated by the exposition to the solvent of aggregation-prone regions located at the N-terminus of the protein. The sequences in these protein segments have a high β-sheet intrinsic propensity that might favor the self-assembly into the detected intermolecular amyloid-like β-sheet structures. The fact that essential and highly soluble proteins like ubiquitin or SUMOs can populate the amyloid state provides strong support to the view that globular proteins cannot completely avoid the competition between their productive folding and their deleterious aggregation. In the case of SUMO, this likely results from the fact that the interactions that promote the formation of functional complexes through the establishment of intermolecular β-sheets might also contribute to cause aberrant intermolecular association. The soluble and functional state in SUMO proteins is maintained under physiological conditions thanks to the existence of intrinsic energy barriers that favor the folded state over unfolded or partially folded conformations. Nevertheless, genetic mutations that decrease SUMOs stability might allow the population of these aggregation susceptible states, with possible implications for cell physiology, because disruption of the SUMO pathway is lethal in mammals and in budding yeast. In the same manner, depletion in SUMO levels by amyloid-like interactions of nascent SUMO polypeptide chains with pre-existing aggregates might be a contributor to the recurrently observed toxicity of amyloid assemblies.

ASSOCIATED CONTENT

Supporting Information

Kinetic parameters of SUMOs aggregation reactions.

Limited PK digestion of aggregated SUMO proteins.

This material is available free of charge via the Internet at http://pubs.acs.org.

AUTHOR INFORMATION

Corresponding Author

*Tel: 34-93-5868147. Fax: 34-93-5811264. E-mail: salvador.ventura@uab.es.

Notes

The authors declare no competing financial interest.

ACKNOWLEDGMENTS

We thank Christopher D. Lima for reagents. This work was supported by BFU2010-14901 from Ministerio de Ciencia e Innovación (MCISpain) and 2009-SGR 760 from AGAUR

(Generalitat de Catalunya). R.S. and D. R. are the beneficiaries of a contract from the Ramón y Cajal Programme from MCISpain. S.V. has been granted an ICREA ACADEMIA award.

REFERENCES

(1) Dobson, C. M. Protein folding and misfolding. *Nature* **2003**, *426* (6968), 884−890.
(2) Daggett, V.; Fersht, A. R. Protein folding and binding: moving into unchartered territory. *Curr. Opin. Struct. Biol.* **2009**, *19* (1), 1−2.
(3) Chiti, F.; Dobson, C. M. Protein misfolding, functional amyloid, and human disease. *Annu. Rev. Biochem.* **2006**, *75*, 333−366.
(4) Nelson, R.; Eisenberg, D. Recent atomic models of amyloid fibril structure. *Curr. Opin. Struct. Biol.* **2006**, *16* (2), 260−265.
(5) Dobson, C. M. Principles of protein folding, misfolding and aggregation. *Semin. Cell. Dev. Biol.* **2004**, *15* (1), 3−16.
(6) Jahn, T. R.; Radford, S. E. The yin and yang of protein folding. *FEBS J.* **2005**, *272* (23), 5962−5970.
(7) de Groot, N. S.; Sabate, R.; Ventura, S. Amyloids in bacterial inclusion bodies. *Trends Biochem. Sci.* **2009**, *34* (8), 408−416.
(8) Linding, R.; Schymkowitz, J.; Rousseau, F.; Diella, F.; Serrano, L. A comparative study of the relationship between protein structure and beta-aggregation in globular and intrinsically disordered proteins. *J. Mol. Biol.* **2004**, *342*, 345−353.
(9) Ventura, S.; Zurdo, J.; Narayanan, S.; Parreno, M.; Mangues, R.; Reif, B.; Chiti, F.; Giannoni, E.; Dobson, C. M.; Aviles, F. X.; Serrano, L. Short amino acid stretches can mediate amyloid formation in globular proteins: the Src homology 3 (SH3) case. *Proc. Natl. Acad. Sci. U. S. A.* **2004**, *101* (19), 7258−7263.
(10) Ivanova, M. I.; Thompson, M. J.; Eisenberg, D. A systematic screen of beta(2)-microglobulin and insulin for amyloid-like segments. *Proc. Natl. Acad. Sci. U. S. A.* **2006**, *103* (11), 4079−4082.
(11) Conchillo-Sole, O.; de Groot, N. S.; Aviles, F. X.; Vendrell, J.; Daura, X.; Ventura, S. AGGRESCAN: a server for the prediction and evaluation of "hot spots" of aggregation in polypeptides. *BMC Bioinf.* **2007**, *8*, 65.
(12) Pawar, A. P.; Dubay, K. F.; Zurdo, J.; Chiti, F.; Vendruscolo, M.; Dobson, C. M. Prediction of "aggregation-prone" and "aggregation-susceptible" regions in proteins associated with neurodegenerative diseases. *J. Mol. Biol.* **2005**, *350* (2), 379−392.
(13) Tartaglia, G. G.; Vendruscolo, M. The Zyggregator method for predicting protein aggregation propensities. *Chem. Soc. Rev.* **2008**, *37* (7), 1395−1401.
(14) Trovato, A.; Seno, F.; Tosatto, S. C. The PASTA server for protein aggregation prediction. *Protein Eng., Des. Sel.* **2007**, *20* (10), 521−523.
(15) Rousseau, F.; Serrano, L.; Schymkowitz, J. W. How evolutionary pressure against protein aggregation shaped chaperone specificity. *J. Mol. Biol.* **2006**, *355* (5), 1037−47.
(16) Monsellier, E.; Chiti, F. Prevention of amyloid-like aggregation as a driving force of protein evolution. *EMBO Rep.* **2007**, *8* (8), 737−742.
(17) Tartaglia, G. G.; Pechmann, S.; Dobson, C. M.; Vendruscolo, M. Life on the edge: a link between gene expression levels and aggregation rates of human proteins. *Trends Biochem. Sci.* **2007**, *32* (5), 204−206.
(18) Castillo, V.; Grana-Montes, R.; Sabate, R.; Ventura, S. Prediction of the aggregation propensity of proteins from the primary sequence: aggregation properties of proteomes. *Biotechnol. J.* **2011**, *6* (6), 674−685.
(19) Tartaglia, G. G.; Caflisch, A. Computational analysis of the *S. cerevisiae* proteome reveals the function and cellular localization of the least and most amyloidogenic proteins. *Proteins* **2007**, *68* (1), 273−278.
(20) Chen, Y.; Dokholyan, N. V. Natural selection against protein aggregation on self-interacting and essential proteins in yeast, fly, and worm. *Mol. Biol. Evol.* **2008**, *25* (8), 1530−1533.
(21) de Groot, N. S.; Ventura, S. Protein aggregation profile of the bacterial cytosol. *PLoS One* **2010**, *5* (2), e9383.
(22) Arnesano, F.; Scintilla, S.; Calo, V.; Bonfrate, E.; Ingrosso, C.; Losacco, M.; Pellegrino, T.; Rizzarelli, E.; Natile, G. Copper-triggered aggregation of ubiquitin. *PLoS One* **2009**, *4* (9), e7052.
(23) Johnson, E. S. Protein modification by SUMO. *Annu. Rev. Biochem.* **2004**, *73*, 355−382.
(24) Hershko, A.; Ciechanover, A. The ubiquitin system. *Annu. Rev. Biochem.* **1998**, *67*, 425−479.
(25) Hay, R. T. SUMO: a history of modification. *Mol. Cell* **2005**, *18* (1), 1−12.
(26) Geiss-Friedlander, R.; Melchior, F. Concepts in sumoylation: a decade on. *Nat. Rev. Mol. Cell Biol.* **2007**, *8* (12), 947−956.
(27) Wilkinson, K. A.; Henley, J. M. Mechanisms, regulation and consequences of protein SUMOylation. *Biochem. J.* **2010**, *428* (2), 133−145.
(28) Li, S. J.; Hochstrasser, M. A new protease required for cell-cycle progression in yeast. *Nature* **1999**, *398* (6724), 246−251.
(29) Owerbach, D.; McKay, E. M.; Yeh, E. T.; Gabbay, K. H.; Bohren, K. M. A proline-90 residue unique to SUMO-4 prevents maturation and sumoylation. *Biochem. Biophys. Res. Commun.* **2005**, *337* (2), 517−520.
(30) Palacios, S.; Perez, L. H.; Welsch, S.; Schleich, S.; Chmielarska, K.; Melchior, F.; Locker, J. K. Quantitative SUMO-1 modification of a vaccinia virus protein is required for its specific localization and prevents its self-association. *Mol. Biol. Cell* **2005**, *16* (6), 2822−2835.
(31) Fei, E.; Jia, N.; Yan, M.; Ying, Z.; Sun, Q.; Wang, H.; Zhang, T.; Ma, X.; Ding, H.; Yao, X.; Shi, Y.; Wang, G. SUMO-1 modification increases human SOD1 stability and aggregation. *Biochem. Biophys. Res. Commun.* **2006**, *347* (2), 406−412.
(32) Mukherjee, S.; Thomas, M.; Dadgar, N.; Lieberman, A. P.; Iniguez-Lluhi, J. A. Small ubiquitin-like modifier (SUMO) modification of the androgen receptor attenuates polyglutamine-mediated aggregation. *J. Biol. Chem.* **2009**, *284* (32), 21296−21306.
(33) Janer, A.; Werner, A.; Takahashi-Fujigasaki, J.; Daret, A.; Fujigasaki, H.; Takada, K.; Duyckaerts, C.; Brice, A.; Dejean, A.; Sittler, A. SUMOylation attenuates the aggregation propensity and cellular toxicity of the polyglutamine expanded ataxin-7. *Hum. Mol. Genet.* **2010**, *19* (1), 181−195.
(34) Krumova, P.; Meulmeester, E.; Garrido, M.; Tirard, M.; Hsiao, H. H.; Bossis, G.; Urlaub, H.; Zweckstetter, M.; Kugler, S.; Melchior, F.; Bahr, M.; Weishaupt, J. H. Sumoylation inhibits alpha-synuclein aggregation and toxicity. *J. Cell Biol.* **2011**, *194* (1), 49−60.
(35) Peroutka Iii, R. J.; Orcutt, S. J.; Strickler, J. E.; Butt, T. R. SUMO fusion technology for enhanced protein expression and purification in prokaryotes and eukaryotes. *Methods Mol. Biol.* **2011**, *705*, 15−30.
(36) Sabate, R.; Gallardo, M.; Estelrich, J. An autocatalytic reaction as a model for the kinetics of the aggregation of beta-amyloid. *Biopolymers* **2003**, *71* (2), 190−195.
(37) Song, J.; Zhang, Z.; Hu, W.; Chen, Y. Small ubiquitin-like modifier (SUMO) recognition of a SUMO binding motif: a reversal of the bound orientation. *J. Biol. Chem.* **2005**, *280* (48), 40122−40129.
(38) Vijay-Kumar, S.; Bugg, C. E.; Cook, W. J. Structure of ubiquitin refined at 1.8 A resolution. *J. Mol. Biol.* **1987**, *194* (3), 531−544.
(39) Huang, W. C.; Ko, T. P.; Li, S. S.; Wang, A. H. Crystal structures of the human SUMO-2 protein at 1.6 and 1.2 A resolution: implication on the functional differences of SUMO proteins. *Eur. J. Biochem.* **2004**, *271* (20), 4114−4122.
(40) Louis-Jeune, C.; Andrade-Navarro, M. A.; Perez-Iratxeta, C. Prediction of protein secondary structure from circular dichroism using theoretically derived spectra. *Proteins* **2011**, *80* (2), 374−381.
(41) Grana-Montes, R.; de Groot, N. S.; Castillo, V.; Sancho, J.; Velazquez-Campoy, A.; Ventura, S. Contribution of disulfide bonds to stability, folding and amyloid fibril formation: The PI3-SH3 domain case. *Antioxid. Redox Signaling* **2012**, *16* (1), 1−15.
(42) Arolas, J. L.; Castillo, V.; Bronsoms, S.; Aviles, F. X.; Ventura, S. Designing out disulfide bonds of leech carboxypeptidase inhibitor: implications for its folding, stability and function. *J. Mol. Biol.* **2009**, *392* (2), 529−546.

(43) de Groot, N. S.; Parella, T.; Aviles, F. X.; Vendrell, J.; Ventura, S. Ile-phe dipeptide self-assembly: clues to amyloid formation. *Biophys. J.* **2007**, *92* (5), 1732−1741.
(44) Hamodrakas, S. J. Protein aggregation and amyloid fibril formation prediction software from primary sequence: towards controlling the formation of bacterial inclusion bodies. *FEBS J.* **2011**, *278* (14), 2428−2435.
(45) Zurdo, J.; Guijarro, J. I.; Dobson, C. M. Preparation and characterization of purified amyloid fibrils. *J. Am. Chem. Soc.* **2001**, *123* (33), 8141−8142.
(46) Zurdo, J.; Guijarro, J. I.; Jimenez, J. L.; Saibil, H. R.; Dobson, C. M. Dependence on solution conditions of aggregation and amyloid formation by an SH3 domain. *J. Mol. Biol.* **2001**, *311* (2), 325−340.
(47) Klunk, W. E.; Pettegrew, J. W.; Abraham, D. J. Quantitative evaluation of congo red binding to amyloid-like proteins with a beta-pleated sheet conformation. *J. Histochem. Cytochem.* **1989**, *37* (8), 1273−1281.
(48) LeVine, H., 3rd Thioflavine T interaction with synthetic Alzheimer's disease beta-amyloid peptides: detection of amyloid aggregation in solution. *Protein Sci.* **1993**, *2* (3), 404−410.
(49) Jarrett, J. T.; Lansbury, P. T. Amyloid fibril formation requires a chemically discriminating nucleation event: studies of an amyloidogenic sequence from the bacterial protein OsmB. *Biochemistry* **1992**, *31*, 12345−12352.
(50) Jarrett, J. T.; Berger, E. P.; Lansbury, P. T. The carboxy terminus of the beta amyloid protein is critical for the seeding of amyloid formation: implications for the pathogenesis of Alzheimer's disease. *Biochemistry* **1993**, *32*, 4693−4697.
(51) Konno, T.; Murata, K.; Nagayama, K. Amyloid-like aggregates of a plant protein: a case of a sweet-tasting protein, monellin. *FEBS Lett.* **1999**, *454* (1−2), 122−126.
(52) Castillo, V.; Ventura, S. Amyloidogenic regions and interaction surfaces overlap in globular proteins related to conformational diseases. *PLoS Comput. Biol.* **2009**, *5* (8), e1000476.
(53) Yoon, S.; Welsh, W. J.; Jung, H.; Yoo, Y. D. CSSP2: an improved method for predicting contact-dependent secondary structure propensity. *Comput. Biol. Chem.* **2007**, *31* (5−6), 373−377.
(54) Song, J.; Durrin, L. K.; Wilkinson, T. A.; Krontiris, T. G.; Chen, Y. Identification of a SUMO-binding motif that recognizes SUMO-modified proteins. *Proc. Natl. Acad. Sci. U. S. A.* **2004**, *101* (40), 14373−14378.
(55) Reverter, D.; Lima, C. D. Insights into E3 ligase activity revealed by a SUMO-RanGAP1-Ubc9-Nup358 complex. *Nature* **2005**, *435* (7042), 687−692.
(56) Baba, D.; Maita, N.; Jee, J. G.; Uchimura, Y.; Saitoh, H.; Sugasawa, K.; Hanaoka, F.; Tochio, H.; Hiroaki, H.; Shirakawa, M. Crystal structure of thymine DNA glycosylase conjugated to SUMO-1. *Nature* **2005**, *435* (7044), 979−982.
(57) Namanja, A. T.; Li, Y. J.; Su, Y.; Wong, S.; Lu, J.; Colson, L. T.; Wu, C.; Li, S. S.; Chen, Y. Insights into high affinity small ubiquitin-like modifier (SUMO) recognition by SUMO-interacting motifs (SIMs) revealed by a combination of NMR and peptide array analysis. *J. Biol. Chem.* **2012**, *287* (5), 3231−3240.
(58) Sekiyama, N.; Ikegami, T.; Yamane, T.; Ikeguchi, M.; Uchimura, Y.; Baba, D.; Ariyoshi, M.; Tochio, H.; Saitoh, H.; Shirakawa, M. Structure of the small ubiquitin-like modifier (SUMO)-interacting motif of MBD1-containing chromatin-associated factor 1 bound to SUMO-3. *J. Biol. Chem.* **2008**, *283* (51), 35966−35975.
(59) Hecker, C. M.; Rabiller, M.; Haglund, K.; Bayer, P.; Dikic, I. Specification of SUMO1- and SUMO2-interacting motifs. *J. Biol. Chem.* **2006**, *281* (23), 16117−16127.
(60) Pechmann, S.; Levy, E. D.; Tartaglia, G. G.; Vendruscolo, M. Physicochemical principles that regulate the competition between functional and dysfunctional association of proteins. *Proc. Natl. Acad. Sci. U. S. A.* **2009**, *106* (25), 10159−10164.
(61) Frousios, K. K.; Iconomidou, V. A.; Karletidi, C. M.; Hamodrakas, S. J. Amyloidogenic determinants are usually not buried. *BMC Struct. Biol.* **2009**, *9*, 44.
(62) Masino, L.; Nicastro, G.; Calder, L.; Vendruscolo, M.; Pastore, A. Functional interactions as a survival strategy against abnormal aggregation. *FASEB J.* **2011**, *25* (1), 45−54.
(63) Pastore, A.; Temussi, P. A. The two faces of Janus: functional interactions and protein aggregation. *Curr. Opin. Struct. Biol.* **2012**, *22* (1), 30−37.
(64) Olzscha, H.; Schermann, S. M.; Woerner, A. C.; Pinkert, S.; Hecht, M. H.; Tartaglia, G. G.; Vendruscolo, M.; Hayer-Hartl, M.; Hartl, F. U.; Vabulas, R. M. Amyloid-like aggregates sequester numerous metastable proteins with essential cellular functions. *Cell* **2011**, *144* (1), 67−78.

CAPITULO II: Efecto del micro-entorno en la formación de fibras amiloides.

the FEBS Journal

Energy barriers for HET-s prion forming domain amyloid formation

R. Sabaté[1], V. Castillo[1], A. Espargaró[1], Sven J. Saupe[2] and S. Ventura[1]

1 Departament de Bioquímica i Biologia Molecular and Institut de Biotecnologia i de Biomedicina, Universitat Autònoma de Barcelona, Spain
2 Laboratoire de Génétique Moléculaire des Champignons, Institut de Biochimie et de Génétique Cellulaires, UMR 5095 CNRS/Université de Bordeaux 2, France

Keywords
aggregation kinetics; amyloid; *Podospora anserina*; prion; protein aggregation

Correspondence
S. Ventura, Departament de Bioquímica i Biologia Molecular and Institut de Biotecnologia i de Biomedicina, Universitat Autònoma de Barcelona, 08193 Bellaterra, Barcelona, Spain
Fax: +34 93 5811264
Tel: +34 93 5868147
E-mail: salvador.ventura@uab.es
R. Sabaté, Departament de Bioquímica i Biologia Molecular and Institut de Biotecnologia i de Biomedicina, Universitat Autònoma de Barcelona, 08193 Bellaterra, Barcelona, Spain
Fax: +34 93 5811264
Tel: +34 93 5812154
E-mail: raimon.sabate@uab.cat

(Received 29 May 2009, revised 2 July 2009, accepted 7 July 2009)

doi:10.1111/j.1742-4658.2009.07202.x

The prion-forming domain comprising residues 218–289 of the fungal prion HET-s forms infectious amyloid fibrils at physiological pH. Because a high-resolution molecular model for the structure of these fibrils exists, it constitutes an attractive system with which to study the mechanism of amyloid assembly. Understanding aggregation under specific conditions requires a quantitative knowledge of the kinetics and thermodynamics of the self-assembly process. We report here the study of the temperature and agitation dependence of the HET-s(218–289) fibril nucleation (k_n) and elongation (k_e) rate constants at physiological pH. Over our temperature and agitation range, k_n and k_e increased 30-fold and three-fold, respectively. Both processes followed the Arrhenius law, allowing calculation of the thermodynamic activation parameters associated with them. The data confirm the nucleation reaction as the rate-limiting step of amyloid fibril formation. The formation of the nucleus appears to depend mainly on enthalpic factors, whereas both enthalpic and entropic effects contribute similarly to the energy barrier to fibril elongation. A kinetic model is proposed in which nucleation depends on the presence of an initially collapsed, but poorly structured, HET-s(218–289) state and in which the fibril tip models the conformation of the incoming monomers without substantial disorganization of its structure during the elongation process.

Introduction

Aggregation of misfolded proteins that escape the cellular quality control mechanisms to enter into amyloid structures is a common feature of a wide range of debilitating and increasingly prevalent diseases, such as Alzheimer's disease, Parkinson's disease, Huntington's disease, and prion diseases [1]. Prions are infectious proteins that are assembled as amyloid or amyloid-like structures that have a self-perpetuating capacity *in vivo* and thus turn into pathological infectious agents or protein-based genetic elements [2–4].

Fungal prions are infectious filamentous polymers of proteins. Among these prions are the [PSI^+], [URE3] and [PIN^+] yeast prions and the [Het-s] prion of the filamentous fungus *Podospora anserina* [5]. In its prion form, the HET-s protein participates in a fungal self-nonself recognition process called heterokaryon

Abbreviations
bis-ANS, 4,4′-bis(1-anilinonaphthalene 8-sulfonate); CR, Congo Red; FTIR, Fourier transformation IR; PFD, prion-forming domain; ThT, thioflavin-T; TEM, transmission electron microscopy.

incompatibility [6]. The HET-s prion displays a globular α-helical domain appended to a natively unfolded domain termed the prion-forming domain (PFD). This PFD is the C-terminal 218–289 fragment responsible for prion propagation and amyloid formation [7,8]. A combination of hydrogen exchange, solid-state NMR and proline-scanning mutagenesis data has been used to propose a structural model for the infectious amyloid fold of the HET-s PFD [9]. Recently, Wasmer *et al*. presented a structural model based on solid-state NMR restraints for amyloid fibrils from the PFD of HET-s. This is the only atomic-resolution structure of an infectious fibrillar state reported to date. On the basis of 134 intramolecular and intermolecular experimental distance restraints, they found that the HET-s PFD forms a left-handed β-solenoid, with each molecule forming two helical windings, a compact hydrophobic core, at least 23 hydrogen bonds, three salt bridges, and two asparagine ladders (Fig. 1) [10]. The model is supported by electron diffraction and microscopy studies. Electronic diffraction gives a prominent meridional reflection at 0.47 nm^{-1}, indicative of cross-β-structure, and scanning transmission electron microscopy (STEM) mass-per-length measurements have yielded 1.02 ± 0.16 subunits per 9.4 Å, which is in agreement with the predicted value in the model [11].

Agitation, pH, temperature, protein concentration and ionic strength have been shown to alter the structural morphology, kinetic characteristics and stability of fibrils [12–14]. This fibrillar polymorphism, which is being reported for an increasing number of proteins, probably reflects the fact that fibrils, in contrast to globular proteins, have not been under evolutionary constraints to retain a single active conformation [13]. In that context, it is noteworthy that in the case of [Het-s], which might represent an evolved adaptive prion with a function beneficial to the host cell, fibrils apparently show no polymorphism at physiological pH. A major unsolved question is how the basically disordered PFD of HET-s is transformed into the highly ordered fibrils characteristic of this domain. To contribute to decipher this mechanism we describe the effects of temperature and agitation on PFD fibrillation. The data allowed us to derive the thermodynamic parameters that characterize the process and propose a model for the aggregation of this infectious prion.

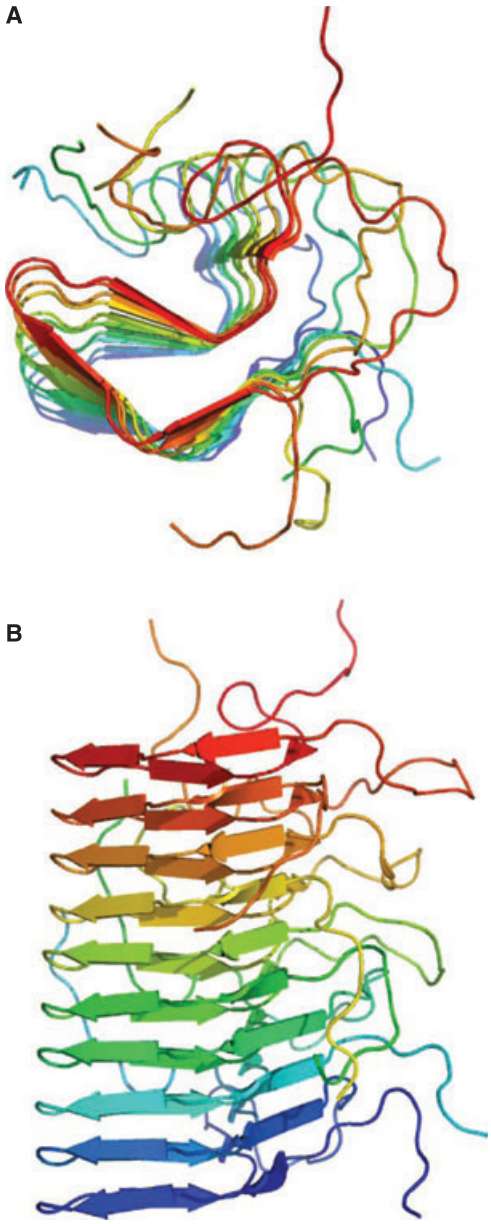

Fig. 1. Structure of the HET-s PFD fibrils. (A) Top view and (B) side view of the five central molecules of the lowest-energy structure of the HET-s PFD heptamer calculated from the NMR restraints.

Results and discussion

Conversion of soluble HET-s PFD into amyloid fibrils

The conversion of soluble HET-s PFD protein into amyloid structures can be easily followed by monitoring the changes in light-scattering signal by UV–visible spectroscopy in the range 240–400 nm. The polypeptide conformational changes occurring during this process were monitored by recording the far-UV CD spectrum in the range 200–250 nm at 5 min intervals. The monomeric form of HET-s PFD possesses a far-UV CD spectrum typical of an essentially unfolded polypeptide chain. In Fig. 2A, the overlaid CD spectra show the conformational transition from this unordered structure towards a β-sheet-enriched conforma-

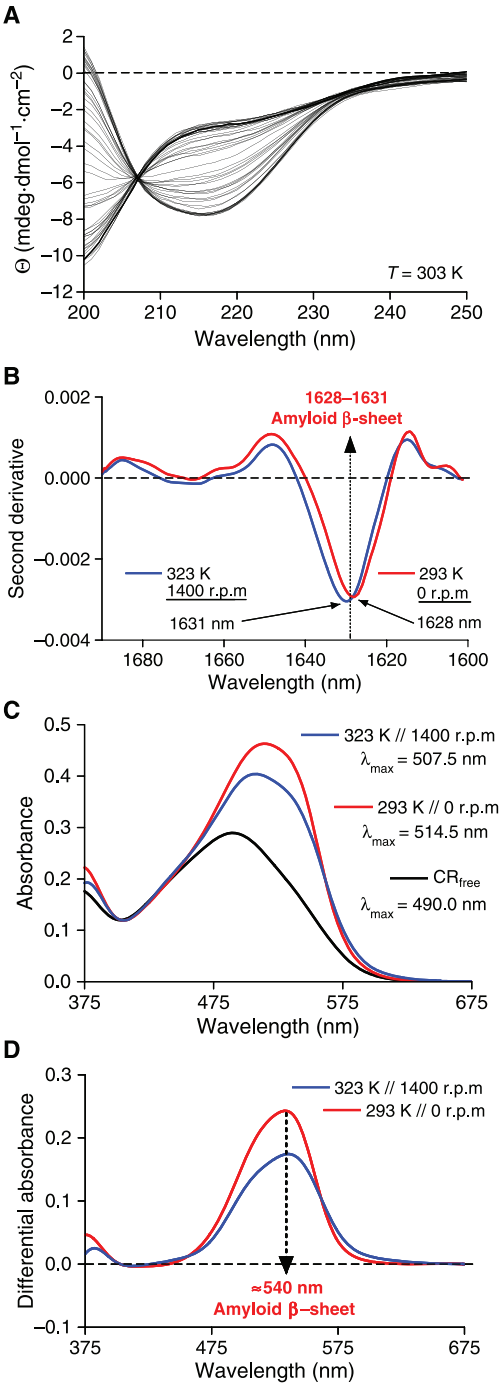

Fig. 2. Secondary structure and amyloid detection. (A) Conformational change of the HET-s PFD at 303 K followed by CD; CD spectra were recorded at time intervals of 5 min. (B) FTIR second derivative spectra of the HET-s PFD in the amide I region corresponding to β-sheet conformations. (C, D) Spectral changes produced by the interaction of aggregated HET-s PFD at different amyloid formation conditions with CR-specific amyloid dye. In (B), note the λ_{max} of the obtained HET-s PDF amyloid, and in (C), note the different absorbance at ~ 540 nm of the differential spectrum.

tion upon protein incubation at 303 K. The prevalence of β-sheet secondary structure after 6 h is clearly indicated by the presence of a characteristic, single negative band at 217 nm. The existence of an amyloid intermolecular β-sheet structure was confirmed by the detection of the typical ~ 1630 cm^{-1} peak in the amide I region of the IR spectrum (Fig. 2B) and by the presence of the characteristic peak at ~ 540 nm upon binding to Congo Red (CR) (Fig. 2C,D). Finally, imaging of the protein solution by STEM at the end of the reaction allows observation of the typical PFD 5 nm wide bundled or disordered fibrils. These structures display high prion infectivity [11,12].

Plotting the absolute CD value at 217 nm or the 400 to 280 nm absorbance ratio nm against time results in overlapping sigmoidal curves that are characterized by three kinetic steps: a lag phase, an exponential growth phase, and a plateau phase (Figs 3 and 4). This sigmoidal behaviour resembles that found for the polymerization of other amyloidogenic proteins, and is best described by the nucleation-dependent polymerization model [15,16], which invokes the formation of soluble oligomers that are thermodynamically unstable and

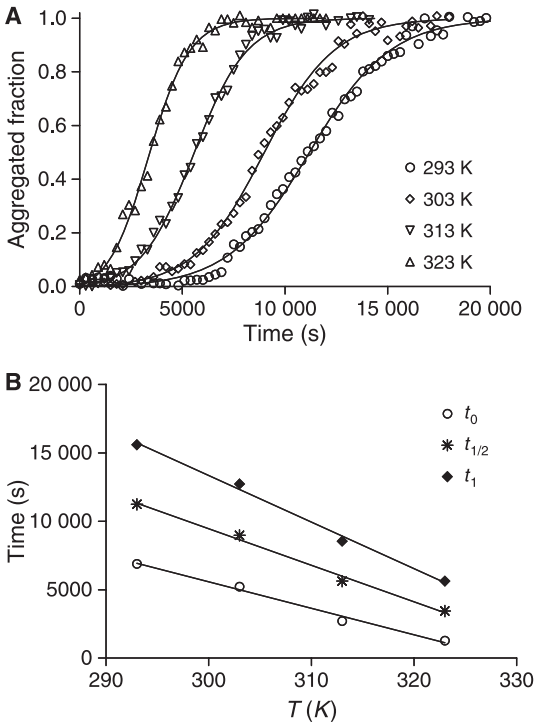

Fig. 3. Kinetics of aggregation of 10 μM of HET-s PFD at pH 7. (A) Normalized aggregation curve followed at 217 nm by CD at time intervals of 5 min. (B) Determination of lag time (t_0), half-time ($t_{1/2}$) and complete reaction time (t_1) from the plots of the fraction of fibrillar HET-s PFD as a function of time.

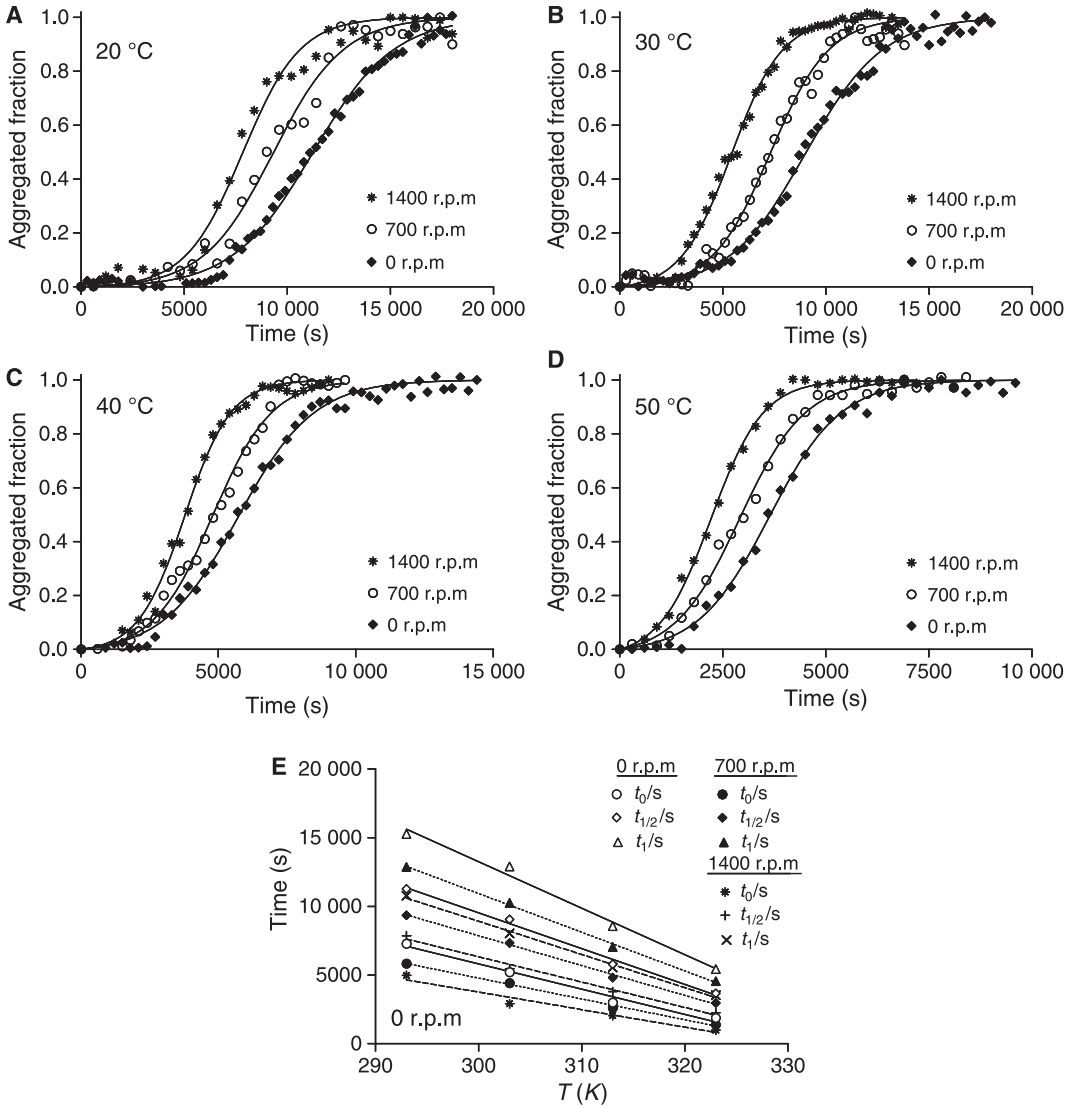

Fig. 4. Kinetics of aggregation of 10 μM HET-s PFD at pH 7 followed by light scattering. (A–D) The reactions were performed at 293, 303, 313 and 323 K at 0 r.p.m., 700 r.p.m. and 1400 r.p.m., and followed by recording the change in the scattering signal at 5 min time intervals. (E) Determination of lag time (t_0), half-time ($t_{1/2}$) and complete reaction time (t_1) from the plots representing the fraction of fibrillar HET-s PFD as a function of time.

represent the nuclei on which the polymerization or fibril growth spontaneously proceeds. During the lag phase, the secondary structure of the HET-s PFD did not significantly change, and then an exponential increase in β-sheet content was observed with a concomitant increase in the light-scattering signal, whose rate is defined by the slope of the linear trend of the sigmoid curve. Previous time-course experiments in which the binding of thioflavin-T (ThT) to the HET-s PFD was monitored by measuring ThT fluorescence anisotropy revealed that the binding of ThT was almost negligible in the lag phase, increased during the exponential phase, and reached a maximum at the plateau phase [17]. This observation, together with the reported changes in CD and scattering signals, suggests that β-sheet formation and aggregate formation may be concerted processes for this prion protein, as previously shown for polyglutamine extensions [18].

Effect of temperature and agitation on HET-s PFD fibrillation rates

The transition of the HET-s PFD from apparently disordered conformations to aggregated β-sheet

Table 1. Aggregation kinetic parameters.

Agitation (r.p.m.)	Parameter	*T* (K) 293	303	313	323
0	k_n ($10^6 \cdot s^{-1}$)	1.61	4.67	11.87	15.05
	k_e ($M^{-1} \cdot s^{-1}$)	50.69	58.10	75.24	96.31
	ck_e ($10^6 \cdot s^{-1}$)	506.90	581.00	752.40	963.10
	t_0 (s)	7270	5209	2993	1881
	$t_{1/2}$ (s)	11 263	9047	5768	3657
	t_1 (s)	15 257	12 884	8542	5433
700	k_n ($10^6 \cdot s^{-1}$)	2.39	4.05	10.83	30.83
	k_e (10^6 $M^{-1} \cdot s^{-1}$)	58.75	70.09	91.66	123.30
	ck_e ($10^6 \cdot s^{-1}$)	587.50	700.90	916.60	1233.00
	t_0 (s)	5831	4412	2602	1373
	$t_{1/2}$ (s)	9341	7330	4810	2957
	t_1 (s)	12 851	10 247	7017	4541
1400	k_n ($10^6 \cdot s^{-1}$)	2.50	9.94	13.36	45.72
	k_e (10^6 $M^{-1} \cdot s^{-1}$)	71.81	79.74	117.30	153.90
	ck_e ($10^6 \cdot s^{-1}$)	718.10	797.40	1173.00	1539.00
	t_0 (s)	4969	2905	2037	984
	$t_{1/2}$ (s)	7861	5466	3791	2258
	t_1 (s)	10 752	8027	5546	3531

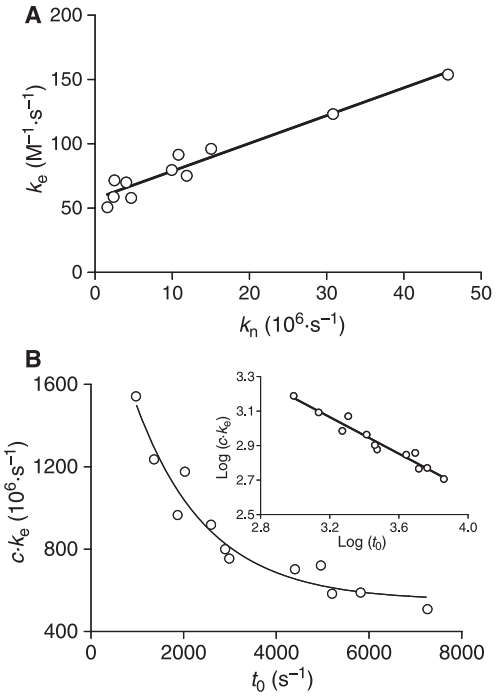

Fig. 5. Correlations between nucleation and elongation kinetic parameters. (A) Correlation between elongation and nucleation rates. (B) Correlation between the product of elongation rate and protein concentration as a lag time (t_0) function.

structures was dependent on the temperature and agitation. The lag phase, the conformational transition rate and the complete reaction time were exquisitely sensitive to these two factors (Figs 3 and 4). Table 1 summarizes the values obtained with each temperature and agitation regime. The nucleation of soluble HET-s PFD increases dramatically with increasing temperature and agitation. In consequence, all of the parameters relating to time (i.e. t_0, $t_{1/2}$, and t_1) are inversely proportional to temperature and agitation. The nucleation rate constant (k_n) is enhanced by a factor of 30 when the temperature rises from 293 K without agitation to 323 K with agitation at 1400 r.p.m. (Table 1). The elongation rate constant k_e approximately triples in this temperature and agitation range. As compared to ck_e, k_n is smaller in all experimental conditions, indicating that, in kinetic terms, nucleation is the rate-determining step in HET-s PFD amyloid fibril formation.

In the fibrillation of insulin, glucagon, and Aβ(1–40), a correlation between lag times and growth rates has been observed [19]. To determine whether this rule also applies for this fungal prion, we plotted k_e versus k_n for the different fibrillation reactions. A linear relationship between both constants was observed, confirming that acceleration of the nucleation process is associated with a higher elongation rate. (Fig. 5A). Accordingly, plotting ck_e against t_0 demonstrates a clear correlation of the absolute values of these two parameters, and therefore a kinetic proportionality between the efficiency of nucleus formation and the velocity of fibril elongation (Fig. 5B).

Energetic barriers to PFD HET-s amyloid formation

Figure 6A,B displays, on a logarithmic scale, the nucleation and elongation rate constants as a function of inverse temperature. These data points fit well with a straight line, suggesting that both processes follow the Arrhenius law:

$$k = Ae^{-E_A/RT} \quad (1)$$

where A is the pre-exponential or frequency factor, and E_A is the activation energy. Taking the natural log of both sides of Eqn (1), one obtains:

$$\ln k = -E_A/RT + \ln A \quad (2)$$

This implies that, in both cases, self-assembly is controlled by one single free energy barrier, associated with the activation of the intermediate state in the oligomerization and polymerization reactions. By plotting ln k versus $1/T$, a linear relationship is obtained, and one can determine E_A from the slope ($-E_A/R$) and A from the y-intercept. This equation assumes that E_A

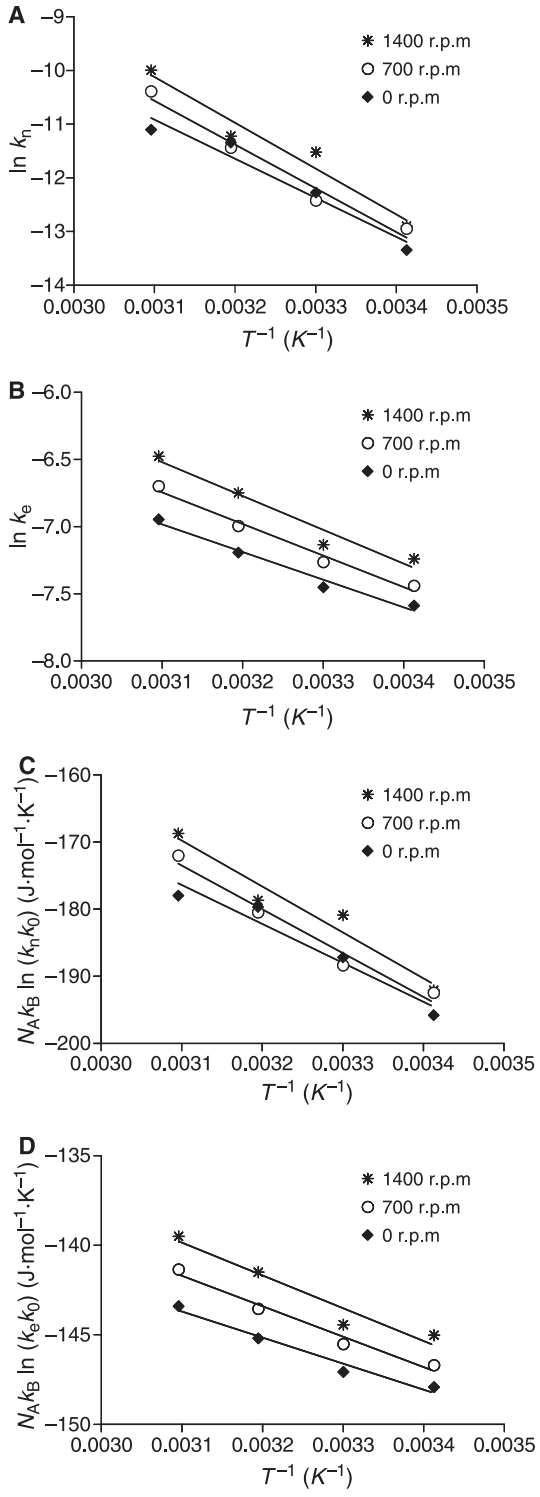

Fig. 6. Arrhenius plot of nucleation (A, C) and elongation (B, D) rates as a function of inverse temperature.

and A are constant or nearly constant with respect to temperature. The linearity of the display indicates that E_A is independent of the temperature. This observation does not exclude deviations from Arrhenius behaviour over wider temperature ranges, as can be the case for protein folding [20].

E_A values of 60–71 and 14–18 kJ·mol^{-1} for the nucleation and elongation process were calculated for the HET-s PFD. Energies of activation below 42 kJ·mol^{-1} generally indicate diffusion-controlled processes, whereas higher values imply a chemical reaction [21]. This suggests that, for the HET-s PFD, the nucleation is a thermodynamically unfavourable process linked to a chemical transformation, whereas diffusion might play a crucial role in fibril elongation. The E_A value for the nucleation of the HET-s PFD is four to five times lower than that reported for Aβ(1–40) [22], pointing to the existence of substantial differences in the nucleation mechanisms of different polypeptides. Accordingly, recent theoretical studies have suggested that the nucleation barriers depend both on the hydrophobicity and the β-sheet-forming propensity of the polypeptide [23]. Interestingly, the E_A value for the nucleation of the HET-s PFD is very close to that estimated for α-synuclein (72 kJ·mol^{-1}) [24].

The free energy barrier associated with the aggregation process can be estimated from the temperature dependence of the nucleation and elongation rates. To estimate the relative contributions of activation enthalpy and entropy in the nucleation and elongation rates, the transition state theory has been applied. The nucleation and elongation rates can be expressed as

$$k_n = k_n^0 e^{-\Delta G^*/k_B T} \text{and } k_e = k_e^0 e^{-\Delta G^*/k_B T} \quad (3)$$

where k_n and k_e are the nucleation and elongation rates, $k_n^0$and k_e^0 are the pre-exponential factors for the nucleation and elongation rates, ΔG^* is the standard Gibbs free energy of activation, k_B is the Boltzmann factor, and T is the absolute temperature in kelvins. From the theory, we can assume that k^0 is proportional to number concentration ρ and to DR_H, where $D = k_B T/(6\pi\eta R_H)$ is the diffusion coefficient of an object whose sphere of influence is R_H, at temperature T, and with medium viscosity η. The pre-exponential factors can be expressed as

$$k_n^0 = \frac{1.33 k_B T c N_A}{\eta} \text{ and } k_e^0 = \frac{1.33 k_B T N_A}{\eta} \quad (4)$$

when N_A is the Avogadro number and c is the molar concentration.

The order of magnitude of both the enthalpy and entropy costs associated with nucleation and elongation processes can be estimated from the expression

$$N_A k_B \ln\left(\frac{k_n}{k_n^0}\right) = \Delta S^* - \Delta H^* T \text{ and } N_A k_B \ln\left(\frac{k_e}{k_e^0}\right) = \Delta S^* - \Delta H^* T \quad (5)$$

for the nucleation and elongation rates, respectively (Fig. 6C,D). The Gibbs free energies of activation can be determined from:

$$\Delta G^* = \Delta H^* - T\Delta S^* \quad (6)$$

The thermodynamic activation parameters derived from the analysis are shown in Table 2. The absolute value for the Gibbs free energy of activation for HET-s PFD nucleus formation is estimated to be ~ 56 kJ·mol^{-1}. The barrier for nucleation is higher than that for elongation, with enthalpic ~ 63 kJ·mol^{-1} and entropic ($T\Delta S^*$) ~ 7 kJ·mol^{-1} contributions at 298 K. Therefore, the nucleation reaction is controlled by competition between two effects with different orders of magnitude: the process is entropically favourable but enthalpically unfavourable [20]. The nucleation process depends mainly on the enthalpic factor, suggesting that chemical transformation or conformational remodelling occurrs from the inactive to the activated state. Because the far-UV CD spectrum of the inactive HET-s state corresponds to a poorly structured polypeptide, it is difficult to envisage why structurally an increase in enthalpy and entropy is required to attain the activated state. A possibility is that, in spite of being devoid of any regular secondary structure, the basal state still has a compact monomeric or oligomeric structure that is disrupted in the aggregation-competent intermediate. One of the distinctive features of the HET-s PFD amyloid fibrils is the existence of a highly packed hydrophobic core. It is possible that these hydrophobic residues are unspecifically collapsed, either intramolecurlarly or intermolecularly, in the initial state. Changes in 4,4′-bis(1-anilinonaphthalene 8-sulfonate) (bis-ANS) fluorescence are frequently used to monitor the presence of solvent-exposed hydrophobic clusters in compacted states. In agreement with the above hypothesis, the HET-s PFD binds to bis-ANS with high affinity (Fig. 7A). Increasing the temperature decreases the population of this collapsed state, explaining why we observe increased aggregation rates and reduced lag times at higher temperatures (Fig. 7C,D). The interactions sustaining the collapsed structure would be rather weak, explaining why we obtain a rather low energy barrier for the nucleation process. However, as shown in Fig. 7B, the loss of this collapsed structure with increasing temperature is a cooperative process. Supporting evidence for this mechanism is also found in the effect of vigorous agitation. The effect of agitation on the kinetics of amyloid formation has been well characterized for insulin [25]. In that case, as reported here for the PFD, agitation occurred mainly in the nucleation stage. The enhanced rates of nucleation with strong agitation were proposed to arise from the increased amount of air–water interface. By analogy to insulin, the most probable effect of the air–water interface in the case of the HET-s PFD is that it promotes the partial disruption of the initial collapsed state, allowing the build-up of the critical species on the fibrillation pathway. Another effect proposed for agitation is an increase in fibril fragmentation, generating new ends that accelerate fibril formation. However, no evidence of fragmentation was observed for HET-s PFD fibrils by TEM, even at 1400 r.p.m. agitation (data not shown). Finally, the formation of a collapsed initial state allows us to explain the rather anomalous effect of salt on HET-s PFD fibrillation. We have shown previously that the presence of salt delays instead of accelerating HET-s PFD amyloid formation [12]. It is known that the addition of salts to polypeptides that are unstructured allows them to adopt more compact conformations and assemblies [26]. Accordingly, the binding to bis-ANS increases by four-fold in the presence of salt (data not shown), suggesting an increase in the population or compactness of the intramolecularly or intermolecularly collapsed species. This stabilization of the basal state is expected to result in lower nucleation rates. To address the nature of the HET-s PFD inactive state, we analysed the kinetics of HET-s PFD fibrillation in a range of concentrations from 2.5 μM to 100 μM in quiescent and agitated conditions. As shown in Fig. 8, the observed kinetic curves in this concentration range are very similar. Accordingly, we obtained similar values for the nucleation constants and lag times, showing that the rate of nucleus formation does not depend on the initial peptide concentration. This is in favour of an oligomeric basal state stabilized by intermolecular hydrophobic contacts.

We estimate the absolute value for the Gibbs free energy of activation of HET-s PFD amyloid fibril

Table 2. Thermodynamic activation parameters.

	Agitation (r.p.m.)					
	0		700		1400	
Process	k_n	k_e	k_n	k_e	k_n	k_e
E_A (kJ·mol^{-1})	60.3	16.9	67.5	19.3	70.7	20.7
ΔH^* (kJ·mol^{-1})	58.0	14.6	65.2	17.0	68.4	18.4
ΔS^* (J·K^{-1}·mol^{-1})	3.4	−98.5	28.8	−89.1	42.2	−82.9
$T\Delta S^*_{298}$ (kJ·mol^{-1})	1.0	−29.4	8.6	−26.5	12.6	−24.7
ΔG^*_{298} (kJ·mol^{-1})	57.0	43.9	56.7	43.5	55.8	43.1

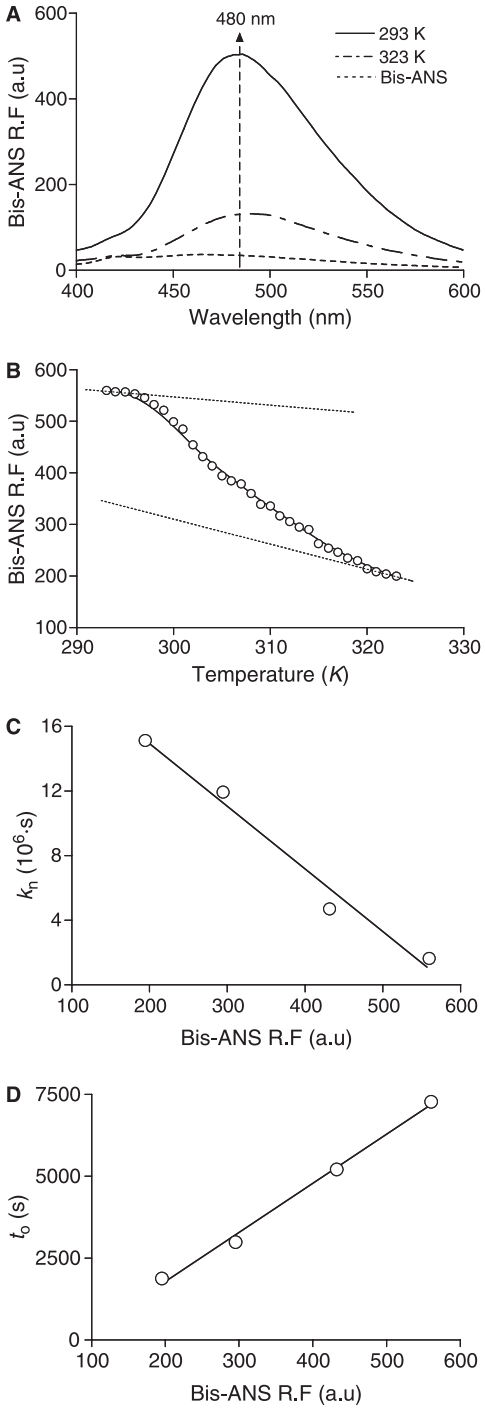

Fig. 7. Soluble HET-s PFD binding to bis-ANS as a function of the temperature. (A) Bis-ANS spectra of the initial state of the HET-s PFD at 293 and 323 K. Samples were excited at 370 nm. (B) Dependence of HET-s PFD binding to Bis-ANS on the temperature. The fit of the data to a two-state cooperative unfolding model is depicted as a continuous line. The initial and final baselines are shown as discontinuous lines, and deviate significantly from the experimental data, thus supporting the conclusion of cooperativity. (C, D) Linear relationship between bis-ANS signal and amyloid formation lag time (t_0). R.F, relative fluorescence; a.u, arbitrary units.

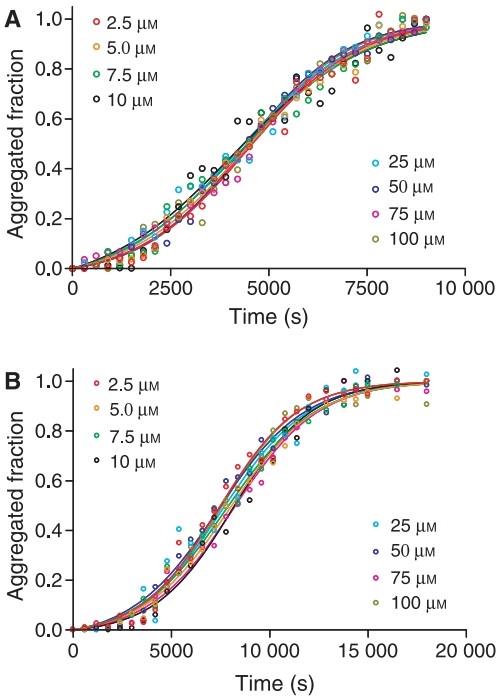

Fig. 8. Aggregation of the HET-s PFD as a function of peptide concentration (from 2.5 to 100 μM) in: (A) agitated (500 r.p.m.) and (B) quiescent conditions.

elongation to be ~ 44 kJ·mol^{-1}. The enthalpic ~ 17 kJ·mol^{-1} and entropic ($T\Delta S^*$) ~ -27 kJ·mol^{-1} contributions reveal that the rate of HET-s amyloid fibril formation appears to be controlled by two cooperative effects of similar magnitude. The reaction is unfavourable from both the enthalpic and entropic points of view. These values suggest that, as hypothesized previously, for HET-s the formation of the initial nucleus and the elongation of the fibrils probably follow different mechanisms. This is further supported by their different dependencies on the agitation and temperature conditions. Importantly, although the overall PFD HET-s Gibbs free energy of activation for the elongation reaction is similar to that found for Aβ (30 kJ·mol^{-1}), entropy appears to play an opposite role in these two elongation reactions. For Aβ, a $T\Delta S^*$ of 67 kJ·mol^{-1} was calculated. Because the authors proposed that soluble Aβ monomer probably did not possess a stable structure that could 'unfold' in the activation process, the calculated gain in entropy was attributed to unfolding of the organized fibril end to accommodate the addition of an incoming monomer [27]. Our data indicate that, for the PFD of HET-s, this is not the case, as a loss of entropy is calculated for the elongation process. The data suggest, rather, that the fibrils accommodate the incoming prion

monomers without substantial disorganization of their structure. The loss of translational, rotational and conformational energy of the polypeptide monomers upon binding to pre-existing fibrils would account for the calculated loss of entropy in the elongation process. Interestingly, a loss of entropy during α-synuclein elongation has also been proposed recently [28].

Effect of temperature on HET-s PFD fibril morphology

Alternative conformations of amyloidogenic proteins critically hinge on their multistep assembly pathways, which, in turn, are modulated by the fibrillation conditions [29]. We decided to investigate whether, in addition to aggregation kinetics, temperature affects the macroscopic morphology of HET-s PFD amyloid fibrils. Low temperature promotes the assembly of fibrillar structures (Fig. 9A). In contrast, high temperature induces the formation of apparently amorphous material (Fig. 9C,D). At intermediate temperatures, a mixture of ordered and disordered aggregates is observed (Fig. 9B). Interestingly, the formation of disordered aggregates at high temperature is a faster process than the aggregation in ordered bundles at low temperature. The acceleration of the fibrillation promoted by agitation has a similar effect on the fibril morphology (data not shown). A similar dependence of the fibril morphology on the temperature has been reported for barstar, insulin and α-synuclein amyloid fibrils [24,25,30]. Also, for the PI3-SH3 domain, pH values promoting fast aggregation reactions were shown to cause disorganized fibrillar structures, whereas pH values allowing slow polymerization led to well-ordered fibrils [31]. Therefore, it appears that, independently of the amyloidogenic model, a clear correlation between the overall rate of aggregation and the formation of largely amorphous protein aggregates or well-defined highly organized fibrils exists. In spite of the macroscopic differences between these aggregates, many studies have succeeded in approximating the energetic barriers of the aggregation process by treating them as related structural entities. This is probably the case for HET-s PFD aggregates, because, in spite of their different morphology, they display similar physicochemical properties, they can be easily interconverted, all them are infectious, and they undergo cross-seeding reactions.

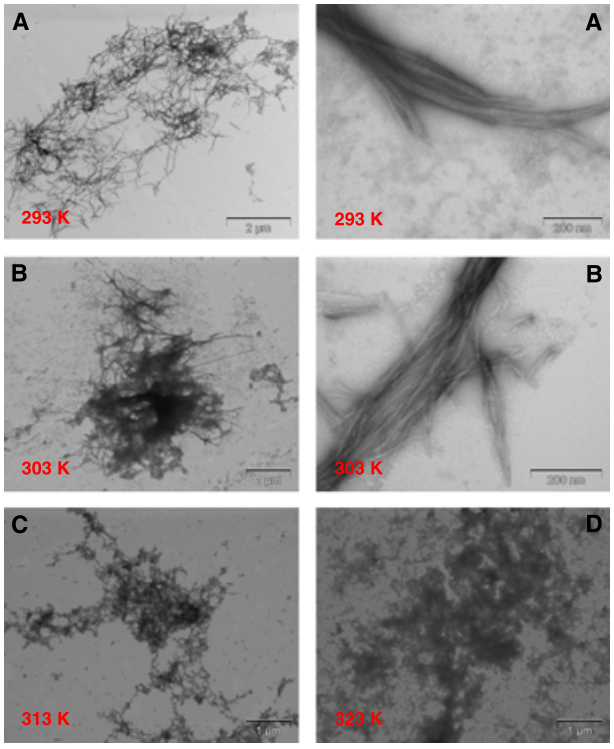

Fig. 9. Temperature effect on HET-s PFD aggregate morphology. Micrographs of 10 μM HET-s PFD at 293 K (A), 303 K (B), 313 K (C), and 323 K (D). A slow aggregation rate favours bundled fibril association, whereas a fast rate favours disordered fibrillar aggregates.

Conclusions

The kinetics of amyloid fibrillation are important for an understanding of the mechanism of amyloid self-assembly and for the eventual design of molecular inhibitors. The results of the present work contribute to our understanding of a few basic features of the molecular interactions and mechanisms that drive prion amyloid fibrillogenesis. The HET-s PFD is devoid of any regular secondary structure, but appears to be at least partially compact in solution. Disruption of this collapsed assembly appears to be a crucial event in the nucleation reaction of this prion protein. With knowledge of the high-resolution three-dimensional structure of HET-s PFD amyloid fibrils in their prion form [10], i.e. formed in the same conditions as in the present study, and the thermodynamic activation parameters associated with their elongation, one might propose a mechanism for the assembly of monomers on the tips of the prion fibrils. The HET-s prion domain amyloid is proposed to be an intramolecular parallel 'pseudo' in-register β-sheet dimer, but in some ways it also resembles a β-helix. In the fibril structure, each monomer forms two turns of the solenoid enclosing a well-defined,

triangular hydrophobic core. This structure implies that, very probably, the mechanism underlying elongation is not, as is often suggested, a primary conformational change of the prion protein followed by aggregation. The monomeric protein can hardly adopt the structure that it has in the fibril by itself, because approximately half of the backbone bonds that sustain its conformation in the fibril are intermolecular. Therefore, it is likely that the conformational change in the monomer coincides with, and is probably a consequence of, the new molecule joining the tip of the fibril. The data suggest that the incoming monomer, but not the receptor fibril, suffers a structural change in this process. The fact that the sequence identified as forming the next layer of the β-sheet is covalently attached to the one that has just joined the fibril tip certainly facilitates the conformational change, and would account for the reduced enthalpy of the process. In fact, the ability of the fibril tip to model the structure of the incoming monomer has been proposed to be the structural basis of prion inheritance [5].

Experimental procedures

HET-s expression, purification, and sample preparation

For expression of the HET-s PFD, 2 L of DYT medium was inoculated with an overnight culture of BL21(DE3) cells bearing the plasmid to be expressed at 37 °C. When an $D_{600\ nm}$ of 0.5–0.6 was reached, the bacteria were induced with 1 mM isopropyl thio-β-D-galactoside for 2 h at 37 °C, the cultures were centrifuged at 8000 ***g*** for 5 min, and the cell pellets were frozen at −20 °C.

HET-s PFD protein expressed as a C-terminal histidine-tagged construct in *Escherichia coli* was purified under denaturing conditions (6 M guanidine hydrochloride for 4 h at 25 °C) by affinity chromatography on Talon histidine-tag resin (ClonTech, Mountainview, CA, USA). Buffer was exchanged by gel filtration on a Sephadex G-25 column (Amersham, Uppsala, Sweden) for buffer A (40 mM anhydrous boric acid, 10 mM citric acid monohydrate, 6 mM NaCl) at pH 2. The aggregation kinetics at different temperatures and agitations were initiated by immediately mixing the solution in a 1 : 1 ratio with buffer (20 mM trisodium phosphate dodecahydrate, pH 12) obtaining a final pH of 7, using a final protein concentration of 10 μM.

CD spectroscopy determination

CD spectra obtained at a spectral resolution of 1 cm^{-1} and a scan rate of 15 $nm{\cdot}min^{-1}$ were collected in the wavelength range 200–250 nm at 293, 303, 313, and 323 K, using a Jasco 810 spectropolarimeter with a quartz cell of 0.1 cm path length, and values at 217 nm were recorded.

Fourier transformation IR (FTIR) spectroscopy determination

Attenuated total reflectance-FTIR spectroscopy analysis samples of HET-s fibrils were analysed using a Bruker Tensor 27 FTIR spectrometer (Bruker Optics Inc., Ettlingen, Germany) with a Golden Gate MKII attenuated total reflectance accessory. Each spectrum consisted of 125 independent scans, measured at a spectral resolution of 2 cm^{-1} within the 1800–1500 cm^{-1} range. All spectral data were acquired and normalized using OPUS MIR Tensor 27 software. Second derivatives of the spectra were used to determine the frequencies at which the different spectral components were located.

UV–visible spectroscopy by scattering determination

Absorbance at 280 nm (tryptophan/tyrosine peak plus scattering) or at 400 nm (scattering of the sample) was measured at 5 min intervals using a Cary-400 Varian spectrophotometer (Varian Inc., Palo Alto, CA, USA) at 293, 303, 313, and 323 K.

CR binding

CR binding to amyloid HET-s(218–289) aggregates obtained at different temperatures and agitation speeds were recorded using a Cary-100 Varian spectrophotometer (Varian Inc.) in range from 375 to 675 nm. The spectra of CR at 10 μM with or without aggregated protein formed by four Gaussian bands were deconvoluted, and the λ_{max} was determined.

Hydrophobic cluster determination

The binding of bis-ANS to initial HET-s(218–289) soluble species was measured on a Varian spectrofluorimeter (Cary Eclipse, Palo Alto, CA, USA) from 400 to 600 nm, using an excitation wavelength of 370 nm. A slit width of 10 nm used, and the maximum of emission, at 480 nm, was recorded. Thermal transition curves were obtained at a heating rate of 1 °C min^{-1} by measuring bis-ANS emission at 480 nm after excitation at 370 nm.

Electron microscopy

For negative staining, samples were adsorbed onto freshly glow-discharged carbon-coated grids, rinsed with water, and stained with 1% uranyl acetate. Samples of pH 7 fibrils

were usually sonicated briefly (5 s on a Kontes sonicator at about 60 W) to ensure optimal particle size. Micrographs were recorded with a Philips CM120 microscope.

Aggregation assay

For aggregation kinetics, we consider that nonaggregated HET-s PFD becomes aggregated, and in this transition is transformed from a mainly unstructured conformation to a predominantly β-sheet structure (amyloid form). This transition can be conveniently followed by CD. The CD spectra were determined from 200 to 250 nm every 5 min, and values at 217 nm were recorded. In parallel, UV–visible spectra from 240 to 400 nm were determined, and the absorbances at 280 nm (tryptophan/tyrosine peak plus scattering) and 400 nm (scattering of the sample) were recorded. These aggregation processes may be studied as an autocatalytic reaction using the equation

$$f = \frac{\rho\{\exp[(1+\rho)kt] - 1\}}{1 + \rho\exp[(1+\rho)kt]}. \quad (7)$$

under the boundary condition of $t = 0$ and $f = 0$, where $k = k_e c$ (where c is the protein concentration), and ρ represents the dimensionless value used to describe the ratio of k_n to k [32]. By nonlinear regression of f against t, values of ρ and k can be easily obtained, and from them the rate constants, k_e (elongation constant) and k_n (nucleation constant), can be determined.

The extrapolation of the linear portion of the sigmoid curve to the abscissa ($f = 0$), and to the highest ordinate value of the fitted plot, afforded two values of time (t_0 and t_1) that correspond to the lag time and to the time at which the aggregation was almost complete. The time at which half of the protein was aggregated (i.e. when $f = 0.5$) is the time of half-aggregation ($t_{1/2}$).

These aggregation assays were performed in a temperature range from 293 to 323 K and under three agitation conditions (0 r.p.m., 700 r.p.m., and 1400 r.p.m.). For each condition, the assay was repeated three times. A variation of $\sim 15\%$ in the observed aggregation constants was detected between replicates; the average of these values was used for calculation of the energy terms.

Acknowledgements

We thank F. X. Aviles and J. Vendrell for laboratory facilities. This work was supported by grants 2005-SGR00037 (Generalitat de Catalunya) and BIO2007-68046 (Spanish Ministry for Science and Innovation).

References

1 Dobson CM (2003) Protein folding and misfolding. *Nature* **426**, 884–890.
2 Caughey B & Baron GS (2006) Prions and their partners in crime. *Nature* **443**, 803–810.
3 Shorter J & Lindquist S (2005) Prions as adaptive conduits of memory and inheritance. *Nat Rev Genet* **6**, 435–450.
4 Prusiner SB (2001) Shattuck lecture – neurodegenerative diseases and prions. *N Engl J Med* **344**, 1516–1526.
5 Wickner RB, Shewmaker F, Kryndushkin D & Edskes HK (2008) Protein inheritance (prions) based on parallel in-register beta-sheet amyloid structures. *BioEssays* **30**, 955–964.
6 Coustou V, Deleu C, Saupe S & Begueret J (1997) The protein product of the het-s heterokaryon incompatibility gene of the fungus Podospora anserina behaves as a prion analog. *Proc Natl Acad Sci USA* **94**, 9773–9778.
7 Balguerie A, Dos Reis S, Ritter C, Chaignepain S, Coulary-Salin B, Forge V, Bathany K, Lascu I, Schmitter JM, Riek R *et al.* (2003) Domain organization and structure–function relationship of the HET-s prion protein of Podospora anserina. *EMBO J* **22**, 2071–2081.
8 Nazabal A, Dos Reis S, Bonneu M, Saupe SJ & Schmitter JM (2003) Conformational transition occurring upon amyloid aggregation of the HET-s prion protein of Podospora anserina analyzed by hydrogen/deuterium exchange and mass spectrometry. *Biochemistry* **42**, 8852–8861.
9 Ritter C, Maddelein ML, Siemer AB, Luhrs T, Ernst M, Meier BH, Saupe SJ & Riek R (2005) Correlation of structural elements and infectivity of the HET-s prion. *Nature* **435**, 844–848.
10 Wasmer C, Lange A, Van Melckebeke H, Siemer AB, Riek R & Meier BH (2008) Amyloid fibrils of the HET-s(218–289) prion form a beta solenoid with a triangular hydrophobic core. *Science* **319**, 1523–1526.
11 Sen A, Baxa U, Simon MN, Wall JS, Sabate R, Saupe SJ & Steven AC (2007) Mass analysis by scanning transmission electron microscopy and electron diffraction validate predictions of stacked beta-solenoid model of HET-s prion fibrils. *J Biol Chem* **282**, 5545–5550.
12 Sabate R, Baxa U, Benkemoun L, Sanchez de Groot N, Coulary-Salin B, Maddelein ML, Malato L, Ventura S, Steven AC & Saupe SJ (2007) Prion and non-prion amyloids of the HET-s prion forming domain. *J Mol Biol* **370**, 768–783.
13 Pedersen JS, Dikov D, Flink JL, Hjuler HA, Christiansen G & Otzen DE (2006) The changing face of glucagon fibrillation: structural polymorphism and conformational imprinting. *J Mol Biol* **355**, 501–523.
14 Ruschak AM & Miranker AD (2007) Fiber-dependent amyloid formation as catalysis of an existing reaction pathway. *Proc Natl Acad Sci USA* **104**, 12341–12346.
15 Jarrett JT & Lansbury PT Jr (1993) Seeding 'one-dimensional crystallization' of amyloid: a pathogenic mechanism in Alzheimer's disease and scrapie? *Cell* **73**, 1055–1058.

16 Munishkina LA, Henriques J, Uversky VN & Fink AL (2004) Role of protein–water interactions and electrostatics in alpha-synuclein fibril formation. *Biochemistry* **43**, 3289–3300.
17 Sabate R & Saupe SJ (2007) Thioflavin T fluorescence anisotropy: an alternative technique for the study of amyloid aggregation. *Biochem Biophys Res Commun* **360**, 135–138.
18 Wetzel R (2006) Kinetics and thermodynamics of amyloid fibril assembly. *Acc Chem Res* **39**, 671–679.
19 Fandrich M (2007) Absolute correlation between lag time and growth rate in the spontaneous formation of several amyloid-like aggregates and fibrils. *J Mol Biol* **365**, 1266–1270.
20 Fersht A (1999) *Structure and Mechanism in Protein Science. A Guide to Enzyme Catalysis and Protein Folding*. Freeman, New York, NY.
21 Scheckel KG & Sparks BL (2001) Temperature effects on nickel sorption kinetics at the mineral–water interface. *Soil Sci Soc Am J* **65**, 719–728.
22 Sabate R, Gallardo M & Estelrich J (2005) Temperature dependence of the nucleation constant rate in beta amyloid fibrillogenesis. *Int J Biol Macromol* **35**, 9–13.
23 Auer S, Dobson CM & Vendruscolo M (2007) Characterization of the nucleation barriers for protein aggregation and amyloid formation. *HFSP J* **1**, 137–146.
24 Uversky VN, Li J & Fink AL (2001) Evidence for a partially folded intermediate in alpha-synuclein fibril formation. *J Biol Chem* **276**, 10737–10744.
25 Nielsen L, Khurana R, Coats A, Frokjaer S, Brange J, Vyas S, Uversky VN & Fink AL (2001) Effect of environmental factors on the kinetics of insulin fibril formation: elucidation of the molecular mechanism. *Biochemistry* **40**, 6036–6046.
26 Fink AL, Calciano LJ, Goto Y, Kurotsu T & Palleros DR (1994) Classification of acid denaturation of proteins: intermediates and unfolded states. *Biochemistry* **33**, 12504–12511.
27 Kusumoto Y, Lomakin A, Teplow DB & Benedek GB (1998) Temperature dependence of amyloid beta-protein fibrillization. *Proc Natl Acad Sci USA* **95**, 12277–12282.
28 Morris AM & Finke RG (2009) Alpha-synuclein aggregation variable temperature and variable pH kinetic data: a re-analysis using the Finke–Watzky 2-step model of nucleation and autocatalytic growth. *Biophys Chem* **140**, 9–15.
29 Kelly JW (1998) The alternative conformations of amyloidogenic proteins and their multi-step assembly pathways. *Curr Opin Struct Biol* **8**, 101–106.
30 Kumar S, Mohanty SK & Udgaonkar JB (2007) Mechanism of formation of amyloid protofibrils of barstar from soluble oligomers: evidence for multiple steps and lateral association coupled to conformational conversion. *J Mol Biol* **367**, 1186–1204.
31 Zurdo J, Guijarro JI, Jimenez JL, Saibil HR & Dobson CM (2001) Dependence on solution conditions of aggregation and amyloid formation by an SH3 domain. *J Mol Biol* **311**, 325–340.
32 Sabate R, Gallardo M & Estelrich J (2003) An autocatalytic reaction as a model for the kinetics of the aggregation of beta-amyloid. *Biopolymers* **71**, 190–195.

Article

pubs.acs.org/Biomac

Temperature Dependence of the Aggregation Kinetics of Sup35 and Ure2p Yeast Prions

Raimon Sabaté,* Anna Villar-Piqué, Alba Espargaró, and Salvador Ventura*

Institut de Biotecnologia i de Biomedicina and Departament de Bioquímica i Biologia Molecular, Universitat Autònoma de Barcelona, 08193 Bellaterra (Barcelona), Spain

Supporting Information

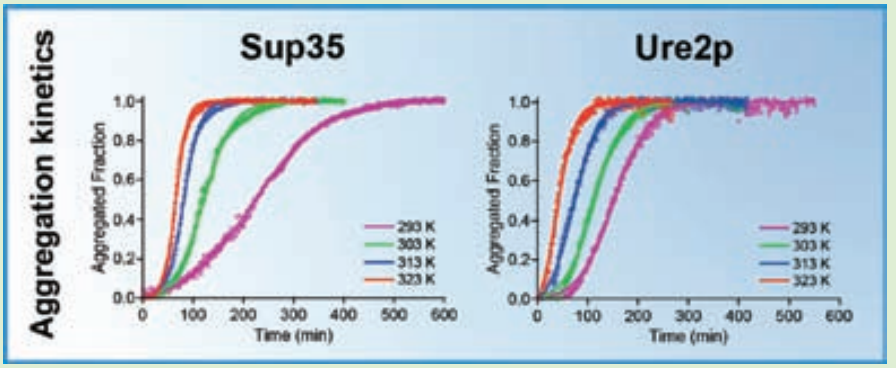

ABSTRACT: Fungal prions are protein-based genetic elements. Sup35 and Ure2p constitute the best-characterized prion proteins in the yeast *Saccharomyces cerevisiae*. No high-resolution molecular models of the amyloid conformations adopted by the prion domains of these proteins are available yet. A quantitative description of the kinetics and thermodynamics of their self-assembly processes might provide clues on the nature of the structural changes originating their heritable and transmissible phenotypes. Here we study the temperature dependence of Sup35 and Ure2p amyloid fibril nucleation and elongation reactions at physiological pH. Both processes follow the Arrhenius law, allowing calculation of their associated thermodynamic activation parameters. Although the Gibbs energies (ΔG^*) for the nucleation and elongation of both prions are similar, the enthalpic and entropic contributions to these two processes are dramatically different. In addition, the structural properties of the two types of prion fibrils exhibit different dependence on the polymerization temperature. Overall, we show here that the amyloidogenic pathways of Sup35 and Ure2p prions diverge significantly.

INTRODUCTION

Prions are naturally occurring proteins that, after a conformational conversion, self-assemble into β-sheet-enriched amyloid-like structures and become self-perpetuating in vivo, acting as pathological infectious agents or protein-based genetic elements.[1−3] Fungal prions provide an excellent model for the understanding of disease-linked mammalian prions. Interestingly, they do not seem to be associated with pathological states and may even confer evolutionary advantages.[4,5] Among these, we found the [PSI$^+$], [URE3], [RNQ$^+$], and [PIN$^+$] prions from *Saccharomyces cerevisiae* and the [Het-s] prion from the filamentous fungus *Podospora anserina*.[4,6−9] In the last years, increasing efforts have been devoted to the elucidation of the aggregation and prion features of these proteins. [PSI$^+$] and [URE3], the prion forms of Sup35 and Ure2p proteins, are the best-characterized prions in *Saccharomyces cerevisiae*. Nevertheless, in contrast with [Het-s],[10,11] no high-resolution structure of the infectious fibrils formed by these prions exists. In the absence of detailed structural information, a quantitative characterization of the kinetics and thermodynamics of their self-assembly processes might be of help in deciphering the nature of the conformational changes, leading to the formation of transmissible amyloid structures.

In this work, we report the study of the temperature dependence of amyloid yeast prions fibril nucleation (k_n) and elongation (k_e) rate constants at physiological pH. Over the studied temperature range, both processes followed the Arrhenius law, allowing calculation of the thermodynamic activation parameters associated with them and the specific contributions of enthalpic and entropic factors to each particular reaction, providing clues on the self-assembly mechanism of Sup35 and Ure2p. The data indicate that the polymerization reactions of these two yeast prions are significantly different.

Received: October 29, 2011
Revised: December 15, 2011

   dx.doi.org/10.1021/bm201527m | *Biomacromolecules* XXXX, XXX, XXX−XXX

MATERIALS AND METHODS

Protein Expression and Purification. The Sup35 NM fragment (residues 1−254) C-terminally tagged with 7x-histidine and the full-length Ure2p protein N-terminally tagged with 6x-histidine were expressed and purified essentially as previously described[12−14] (Supporting Information).

Aggregation Assays. Aggregation of initially soluble species was monitored by measuring the transition from nonaggregated to aggregated states according to the Thioflavin T (Th-T) fluorescence at 480 nm when excited at 445 nm. All experiments were carried at a protein concentration of 10 μM in native buffer (50 mM Tris·HCl, 150 mM NaCl at pH 7.4) under stirring conditions (∼1000 rpm with microstir bars). Sup35 and Ure2p aggregation processes were modeled as autocatalytic reactions as previously described[15] (Supporting Information). The amount of insoluble fibrillar material at the end of each reaction was quantified after centrifugation at 14 000g for 30 min. We determined 70−75 and 55−60% of insoluble material for Sup35 and Ure2p, respectively, independent of the assay temperature. Protein concentrations were calculated in the soluble fractions using absorbance at 280 nm. Because soluble fractions displayed slight turbidity, the residual scattering was corrected by subtracting the absorbance at 320 nm.

Thermodynamic Parameters Determination. When the logarithm of the nucleation or elongation rate constant is represented as a function of inverse temperature, these data points fit well with a linear function, suggesting that both processes follow the Arrhenius law

$$k = A\mathrm{e}^{-E_A/RT} \tag{1}$$

where A is the pre-exponential or frequency factor and E_A is activation energy. Taking the natural log of both sides of eq 1 one obtains

$$\ln k = -E_A/RT + \ln A \tag{2}$$

By plotting ln k versus $1/T$, a linear relationship is obtained and one can determine E_A from the slope ($-E_A/R$) and A from the y intercept.

To estimate the relative contributions of activation enthalpy and entropy in the nucleation and elongation rates, the transition-state theory has been applied. The nucleation and elongation rates can be expressed as

$$k_n = k_n^0\mathrm{e}^{-\Delta G^*/k_BT} \text{ and } k_e = k_e^0\mathrm{e}^{-\Delta G^*/k_BT} \tag{3}$$

where k_n and k_e are the nucleation and elongation rates, k_n^0 and k_e^0 are the pre-exponential factors for the nucleation and elongation rates, ΔG^* is the standard Gibbs energy of activation, k_B is the Boltzmann constant, and T is the absolute temperature in kelvin. From the theory, we can assume that k^0 is proportional to number concentration ρ and to DR_H, where $D = k_BT/(6\pi\eta R_H)$ is the diffusion coefficient of an object whose hydrodynamic radius is R_H, at temperature T and with medium viscosity coefficient η. The pre-exponential factors can be expressed as

$$k_n^0 = \frac{1.33k_BTcN_A}{\eta} \text{ and } k_e^0 = \frac{1.33k_BTN_A}{\eta} \tag{4}$$

where N_A is the Avogadro number and c is the molar concentration.

The order of magnitude of both the enthalpy and entropy costs associated to nucleation and elongation processes can be estimated from the expression

$$N_Ak_B\ln\left(\frac{k_n}{k_n^0}\right) = \Delta S_n^* - \frac{\Delta H_n^*}{T} \text{ and } N_Ak_B\ln\left(\frac{k_e}{k_e^0}\right) = \Delta S_e^* - \frac{\Delta H_e^*}{T} \tag{5}$$

for the nucleation and elongation rates. The Gibbs energies of activation can be determined by

$$\Delta G_n^* = \Delta H_n^* - T\Delta S_n^* \text{ and } \Delta G_e^* = \Delta H_e^* - T\Delta S_e^* \tag{6}$$

Transmission Electron Microscopy (TEM) Assays. For negative staining, amyloid fibrils were centrifuged, and the insoluble fraction was resuspended in water, placed on carbon-coated copper grids, and left to stand for 5 min. The grids were washed with distilled water and stained with 2% (w/v) uranyl acetate for another 2 min before analysis using a Hitachi (Tokyo, Japan) H-7000 transmission electron microscope operating at an accelerating voltage of 75 kV.

Congo Red Assay. Congo Red (CR) interaction with amyloid fibrils was tested using a Cary100 (Varian, Palo Alto, CA) UV/vis spectrophotometer by recording the absorbance spectra from 375 to 675 nm using a matched pair of quartz cuvettes of 1 cm optical length placed in a thermostatted cell holder at 25 °C. Final CR and protein concentrations were 10 μM in native buffer. Spectra were recorded after 2 of min equilibration, and solutions without protein and solutions without CR were used as negative controls. Binding of CR to 10 μM amylin amyloid fibril solution was used as positive control.

Thioflavin Assay. Th-T binding to yeast amyloid prions was recorded using a Varian spectrofluorometer (Cary Eclipse, Palo Alto, CA) with an excitation wavelength of 445 nm and emission range from 470 to 570 nm. Final Th-T and protein concentrations were 25 and 10 μM in native buffer, respectively. Spectra were recorded after 2 min of equilibration, and solutions without protein were used as negative controls. Binding of Th-T to 10 μM amylin amyloid fibril solution was used as positive control. Excitation and emission slit widths of 10 nm were used.

Limited Proteolysis of Yeast Prions with Proteinase K. Soluble or Ure2p fibrils (35 μM) formed at 293, 303, 313, and 323 K were digested with 0.5 μg·mL^{-1} of proteinase K in PBS for 10 min at 37 °C. Reactions were stopped by the addition of one volume of electrophoresis loading buffer and heated at 100 °C for 5 min. They were analyzed in 12% SDS-PAGE gels, followed by Coomassie Blue staining.

Temperature Dependence of Intrinsic Fluorescence. Thermal transition curves were obtained at a heating rate of 1 °C per min following the changes of intrinsic fluorescence at 335 and 360 nm when excited at 280 nm at an Ure2p concentration of 20 μM in a Varian spectrofluorometer (Cary Eclipse, Palo Alto, CA). Individual emission spectra were collected in the 300−400 nm range at 293, 303, 313, and 323 K. Excitation and emission slit widths of 10 nm were used. Experiments were carried out in native buffer.

Bis-ANS Binding. The binding of 1 μM bis-ANS to 10 μM of initial Sup35 and Ure2p soluble species was measured on a Varian spectrofluorimeter (Cary Eclipse, Palo Alto, CA) in the 400−600 nm emission range using an excitation wavelength of 370 nm. Thermal transition curves were obtained at a heating rate of 1 °C per min by measuring bis-ANS emission at 480 nm after excitation at 370 nm. Excitation and emission slit widths of 10 nm were used. Experiments were carried out in native buffer.

Secondary Structure Determination. Attenuated total reflectance Fourier transformed infrared ATR-FTIR spectroscopy analysis of yeast prion fibrils was performed using a Bruker Tensor 27 FTIR Spectrometer (Bruker Optics, Berlin, Germany) with a Golden Gate MKII ATR accessory. Each spectrum consists of 125 independent scans, measured at a spectral resolution of 2 cm^{-1}, within the 1800−1500 cm^{-1} range. All spectral data were acquired and normalized using the OPUS MIR Tensor 27 software. FTIR spectra were fitted to four overlapping Gaussian curves and the amplitude, center, and bandwidth at half of the maximum amplitude and area of each Gaussian function were calculated using a nonlinear peak fitting program (PeakFit package, Systat Software, San Jose, CA). Second derivatives of the spectra were also used to determine the frequencies at which the different spectral components were located.

dx.doi.org/10.1021/bm201527m | Biomacromolecules XXXX, XXX, XXX−XXX

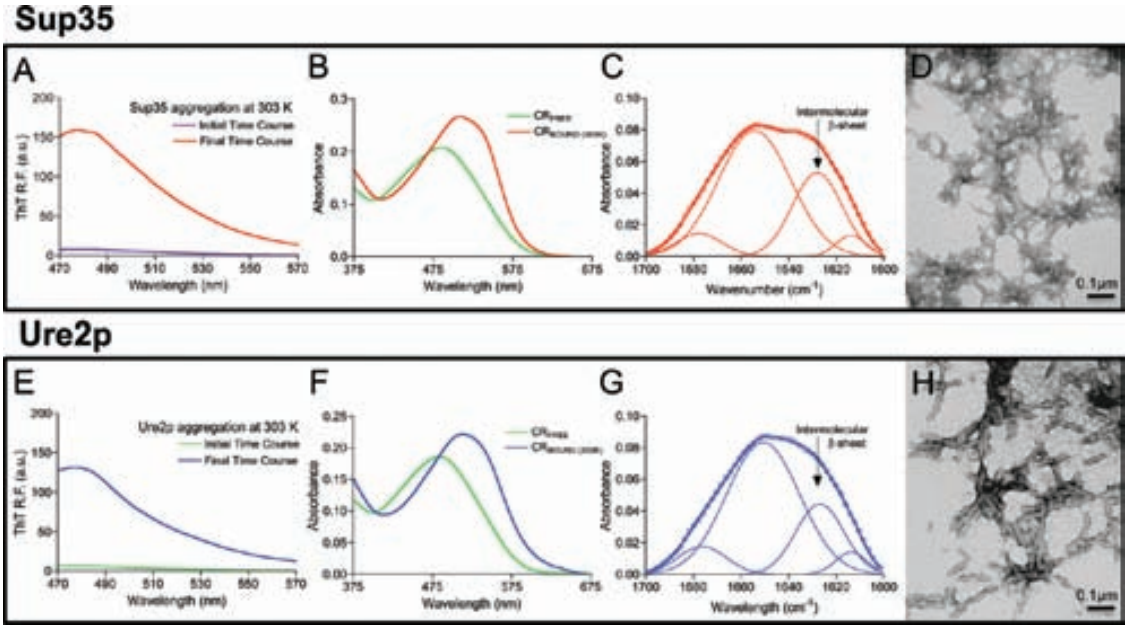

Figure 1. Amyloid structure determination. ThT fluorescence spectra taken at initial and final time points of the aggregation reactions of Sup35 (A) and Ure2p (E). (B,F) Spectral changes of CR produced by the interaction with Sup35 and Ure2p fibrils. Absorbance spectra of the amide I region (solid thick lines) of Sup35 (C) and Ure2p (G) showing the component bands (solid thin lines) obtained by ATR-FTIR spectroscopy. The sum of individual spectral components after Fourier self-deconvolution closely matches the experimental data. Electron micrographs showing Sup35 (D) and Ure2p (H) amyloid fibrils. Yeast prion fibrils were formed at 303 K.

RESULTS

Conversion of Soluble Sup35 and Ure2p into Amyloid Assemblies. The aggregation of Sup35 and Ure2p from their initially soluble states promotes a strong increase in the fluorescence emission of Th-T. (See Figure 1A,E.) The two types of aggregates also bind to CR, promoting a significant increase and red shift of the dye absorbance maximum. (See Figure 1B,F.) These Th-T and CR spectral changes are usually attributed to the formation of β-sheet enriched amyloid-like structures. The existence of a tightly packed intermolecular β-sheet structure in the aggregated states of Sup35 and Ure2p is confirmed by the presence of the characteristic band at 1625–1630 cm^{-1} in the amide I region of their respective infrared spectra, as monitored by ATR-FTIR spectroscopy. (See Figure 1C,G.) Moreover, the analysis of the aggregated solutions of both proteins by TEM evidence that the initially soluble polypeptides self-assemble into characteristic fibrillar structures (Figure 1D,H), which, as previously described, might be infective.[13,16,17]

The spectral changes promoted by the aggregation of both proteins in Th-T fluorescence allow tracking of this reaction by monitoring the changes in the emission of this dye in a time dependent manner. As shown in Figure 2, when the fractions of Sup35 and Ure2p aggregated species are plotted against time, we obtain two sigmoid curves characterized by three kinetic stages: (1) lag phase, (2) exponential growth phase, and (3) plateau phase. These phases, characteristic of most amyloid processes, reflect a nucleation-polymerization mechanism.[15,18]

Effect of Temperature on Sup35 and Ure2p Aggregation Rates. The aggregation reactions of Sup35 and Ure2p are sensitive to the temperature. (See Figure 2.) The nucleation (k_n) and elongation rate (k_e), lag time (t_0), half aggregation time ($t_{1/2}$). and final aggregation time (t_1) were calculated in the 293–323 K temperature range (Table 1). As shown in Figure 3A, an inverse exponential relationship is observed between the different reaction times and the temperature for Sup35. In contrast, the lag, exponential, and plateau times of the Ure2p fibrillation reaction decrease linearly with increasing temperature. (See Figure 3B.)

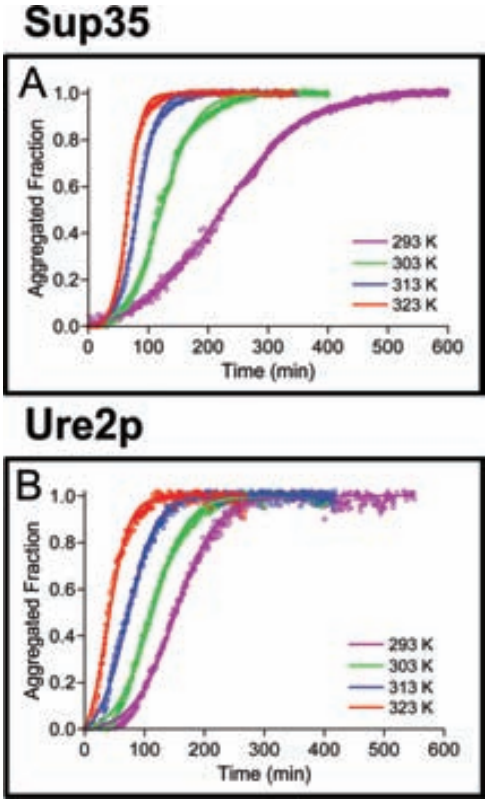

Figure 2. Aggregation kinetics of Sup35 (A) and Ure2p (B) at 20 μM and 293 (violet), 303 (green), 313 (blue), and 323 (red) under agitation conditions and pH 7.5, followed by Th-T fluorescence.

dx.doi.org/10.1021/bm201527m | Biomacromolecules XXXX, XXX, XXX–XXX

Table 1. Kinetic Parameters of Sup35 and Ure2p Aggregation Reactions

yeast prion	T (K)	293	303	313	323
Sup35	k_n ($10^6 \cdot s^{-1}$)	11.11	9.03	6.72	4.66
	k_e ($M^{-1} \cdot s^{-1}$)	10.83	28.00	50.93	72.66
	$c \cdot k_e$ ($10^6 \cdot s^{-1}$)	216.50	560.00	1018.50	1453.17
	t_0 (min)	84.8	62.4	48.2	41.7
	$t_{1/2}$ (min)	227.7	121.2	81.8	65.7
	t_1 (min)	370.5	180.0	115.3	89.8
Ure2p	k_n ($10^6 \cdot s^{-1}$)	6.14	12.30	35.48	99.06
	k_e ($M^{-1} \cdot s^{-1}$)	23.53	27.75	32.48	41.73
	$c \cdot k_e$ ($10^6 \cdot s^{-1}$)	470.67	555.00	649.50	834.50
	t_0 (min)	81.1	53.8	25.2	8.6
	$t_{1/2}$ (min)	152.5	113.3	73.8	42.0
	t_1 (min)	224.0	172.8	122.3	75.3

The duration of the lag phase for Ure2p decreases by 10-fold at 323 K relative to that observed at 293 K, whereas only a 2-fold reduction is detected for Sup35. The k_n for the Ure2p reaction increases by 16-fold in the measured temperature interval, whereas, surprisingly, for Sup35 we observe a 2-fold decrease in k_n in the same temperature range. In contrast, k_e increases by seven-fold for Sup35 and by only two-fold in Ure2p. As a result, although the elongation reaction ($t_0 - t_1$) is faster for Ure2p than for Sup35 at 293 K, this difference is progressively reduced at higher temperatures until at 323 K, the elongation reaction becomes faster for Sup35 than for Ure2p. As shown in Figure 3C, Sup35 exhibits an inverse relationship between the values of k_e and k_n at any given temperature. In contrast, these reaction constants are directly correlated for Ure2p. (See Figure 3D.) Therefore, whereas for Ure2p acceleration of the nucleation process is associated with a higher elongation rate, the opposite effect appears to occur for Sup35. Independently of the relationship between k_n and k_e, and as shown previously for the aggregation processes of other amyloidogenic proteins and peptides like insulin, glucagon, Aβ(1−40) or HET-s(218−289),[19,20] a correlation between lag times and growth rates exists for both yeast prion proteins as it becomes evident when plotting ck_e versus t_0. (See Figure 3E,F.)

Energy Barriers to Sup35 and Ure2p Amyloid Formation. When Sup35 and Ure2p k_n and k_e constants are plotted on a logarithmic scale as a function of the temperature, the data points fit well to a straight line (Figure S1 of the Supporting Information), suggesting that both processes follow the Arrhenius law (eq 2). Therefore, the self-assembly of both proteins appears to be controlled by a single Gibbs energy barrier in both nucleation and polymerization steps and in the

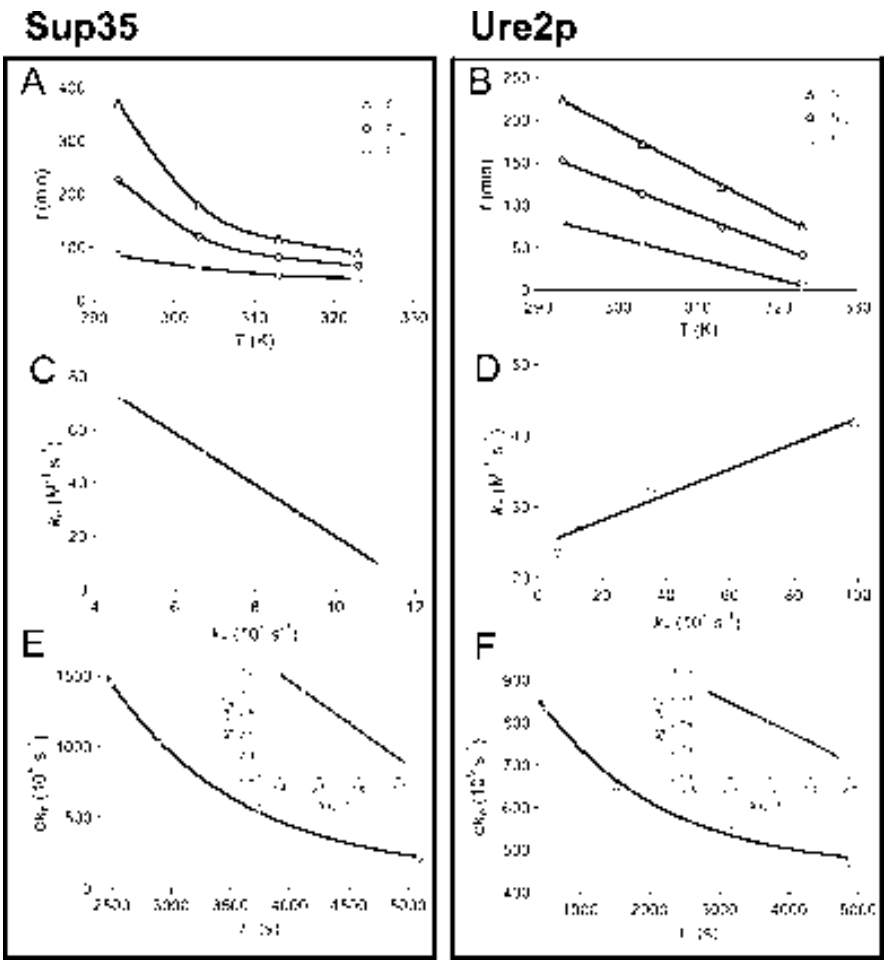

Figure 3. Kinetic parameters for the aggregation reactions of Sup35 and Ure2p. Changes in lag time (t_0), half time ($t_{1/2}$), and complete reaction time (t_1) for Sup35 (A) and Ure2p (B) aggregation as a function of the temperature. Correlations between nucleation and elongation kinetic parameters showed a relationship between elongation and nucleation rates in Sup35 (C) and Ure2p (D) and a correlation between the product of elongation rate and Sup35 (E) and Ure2p (F) concentrations as a lag time (t_0) function.

dx.doi.org/10.1021/bm201527m | Biomacromolecules XXXX, XXX, XXX−XXX

analyzed temperature range. The pre-exponential or frequency factor (A) and the activation energy (E_A) can be directly calculated from these plots (Table 2). The relative contributions of activation enthalpy and entropy in the nucleation and elongation rates have been determined by applying the transition-state theory (eq 5, Figure S2 of the Supporting Information, and Table 2). As expected, for both proteins, the Gibbs energy barrier is higher for the nucleation than for elongation stage. Similar ΔG^* values are obtained for the nucleation (~55 kJ·mol^{-1}) and elongation (~45 kJ·mol^{-1}) processes of both polypeptides. Interestingly, these values resemble those previously calculated for the Het-s prion-forming domain (PFD) with ΔG^* of 57 and 43 kJ·mol^{-1} for the nucleation and elongation stages, respectively.[20] Despite the similitude in ΔG^*, the activation energies for the nucleation and polymerization processes differ significantly in both proteins. E_A of 74 and −23 kJ·mol^{-1} for nucleation and E_A of 14 and 50 kJ·mol^{-1} for elongation reactions were calculated for Ure2p and Sup35 proteins, respectively. E_A below 42 kJ·mol^{-1} generally indicates diffusion-controlled processes, whereas higher values are assumed to involve a chemical reaction.[21] Accordingly, the nucleation of Ure2p appears to be a thermodynamically unfavorable process entailing a chemical transformation (i.e., a structural change), whereas the nucleation stage of Sup35 seems to be a favorable process without any apparent requirement for important structural rearrangements. As previously observed in HET-s PFD,[20] the elongation of Ure2p is a thermodynamically unfavorable reaction where diffusion might play a crucial role. In the case of Sup35, the elongation of the fibrils is also unfavorable but likely depends on conformational conversions.

Table 2. Thermodynamic Parameters of Sup35 and Ure2p Aggregation Reactions

yeast prion	Sup35		Ure2p	
process	k_n	k_e	k_n	k_e
E_A (kJ·mol^{-1})	−22.95	49.67	73.51	14.45
ΔH^* (kJ·mol^{-1})	−25.25	47.37	71.21	12.15
ΔS^* (J·K^{-1}·mol^{-1})	−265.5	7.737	57.34	−107.3
$T\Delta S^*_{298}$ (kJ·mol^{-1})	−79.12	2.31	17.09	−31.98
ΔG^*_{298} (kJ·mol^{-1})	53.55	46.19	55.02	44.26

To clarify the aggregation mechanisms of Sup35 and Ure2p, the relative contributions of enthalpy and entropy to the nucleation and elongation reactions were calculated (Table 2). Significant differences in ΔH^* and $T\Delta S^*$ contributions to the nucleation and elongation processes of yeast prions were observed. ΔH^* and $T\Delta S^*$ values of −25 and −79 kJ·mol^{-1} were calculated for the nucleation of Sup35, respectively. The same process in Ure2p exhibits ΔH^* and $T\Delta S^*$ values of 71 and 17 kJ·mol^{-1}, respectively. Therefore, although in both cases nucleation involves a competition between enthalpic and entropic effects, the signs of the calculated thermodynamic values suggest two different nucleation pathways. ΔH^* and $T\Delta S^*$ values of 47 and 2 kJ·mol^{-1} were obtained for the elongation process of Sup35, respectively. Ure2p elongation displays ΔH^* of 12 kJ·mol^{-1} and $T\Delta S^*$ of −32 kJ·mol^{-1}. Therefore, entropic and enthalpic effects compete in the elongation of Sup35 fibrils, whereas they act cooperatively on the elongation stage of Ure2p. These data suggest differences in the elongation mechanism.

Hydrophobic Clustering in Sup35 and Ure2p Soluble States. In amyloid processes, hydrophobic forces are thought to drive the initial unspecific condensation of monomers into oligomeric assemblies. Changes in the fluorescence spectrum of bis-ANS fluorescence are frequently used to detect the presence of solvent-exposed hydrophobic clusters. We analyzed the binding of the initially soluble states of Sup35 and Ure2p to this dye. As shown in Figure 4, soluble Sup35 binds to bis-ANS with high affinity, whereas Ure2p exhibits very low binding at the same concentration. This suggests the population of monomeric or oligomeric collapsed states in which hydrophobic residues seem to coalesce into clusters in the Sup35 soluble state. Apparently, these species are not significantly populated at the initial stages of Ure2p aggregation. Increasing the temperature results in a progressive decrease of the ability of Sup35 to bind bis-ANS, reflecting a decrease in the ensemble of collapsed conformations at higher temperatures. This decrease in bis-ANS fluorescence emission together with the reduction in the nucleation rates of Sup35 aggregation reactions at increasing temperatures, might suggest that the presence of hydrophobic surfaces could play an important role in the nucleation stage.

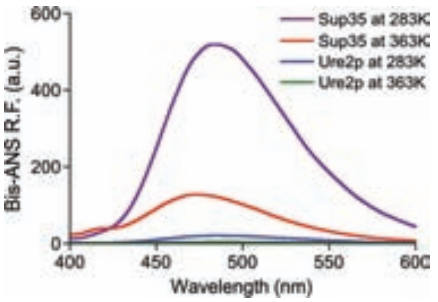

Figure 4. Binding of soluble Sup35 and Ure2p species to bis-ANS as a function of the temperature.

Effect of Temperature on Ure2p Conformation. The Sup35 NM (1−254) and Het-s PFD (218−289) regions typically used to study the aggregation and infective properties of the correspondent proteins correspond to the prion-forming domains of these molecules and are likely devoid of any significant regular secondary or tertiary structure in their respective monomeric states.[22−24] In contrast, the full-length protein, comprising both the prion unstructured region and a globular α-helical domain displaying a glutathione-S-transferase-like fold, has been used traditionally to study the aggregation and transmissibility of Ure2p, as is the case of the present study. Energetic calculations suggest that the nucleation step of Ure2p amyloid formation involves a structural rearrangement of the molecule. Therefore, we analyzed if the soluble structure of Ure2p experiences any detectable temperature-dependent conformational change by monitoring the intrinsic fluorescence of this protein. The fluorescence emission spectrum of Ure2p is dominated by the contribution of Trp residues with a maximum at ~335 nm (see Figure 5A). The emission maximum intensity decreases with increasing temperature following an apparently cooperative reaction that could be fitted to a two-state transition in the measured temperature range. This observation likely indicates a structural perturbation of the globular domain were Trp residues reside upon increasing the temperature. (See Figure 5A,B.) The detected changes in fluorescence exhibit a linear correlation with

dx.doi.org/10.1021/bm201527m | Biomacromolecules XXXX, XXX, XXX−XXX

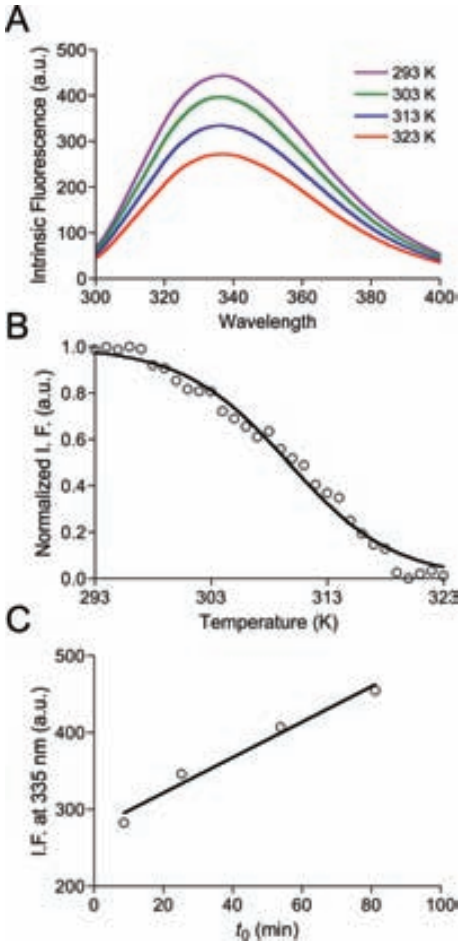

Figure 5. Conformation of Ure2p protein as a function of the temperature. (A) Fluorescence spectra of the initial soluble state of Ure2p at 293, 303, 313, and 323 K. (B) Dependence of Ure2p intrinsic fluorescence on the temperature. The fit of the data to a two-state cooperative unfolding model is depicted as a continuous line. (C) Logarithmic relationship between intrinsic fluorescence signal and nucleation constant (k_n). I.F., intrinsic fluorescence; a.u., arbitrary units.

measured lag phases at the different assayed temperatures (Figure 5C), suggesting that the observed temperature-dependent acceleration of the nucleation reaction might be associated with Ure2p conformational changes.

Effect of Temperature on the Conformation of Sup35 and Ure2p Fibrils. The structure of amyloid assemblies can be modulated by the aggregation conditions;[25] that is, in the HET-s PFD system, slow aggregation at low temperatures favors the formation of ordered fibrils, whereas the acceleration of the process by higher temperatures promotes the population of more disordered assemblies,[20] an effect that is well-documented for other amyloid proteins as barstar, insulin, or α-synuclein.[26−28] We assayed the properties of Sup35 and Ure2p fibrils formed in the 293−323 K temperature range using TEM and fluorescence microscopy. As shown in Figure 6A, Sup35 forms amyloid fibrils that can be visualized as fluorescent aggregates after staining with the amyloid binding dye Th−S under all conditions. Sup35 fibrils are small, associate into rather disordered aggregates, and do no exhibit detectable morphology changes with the temperature, as observed by TEM. This type of disordered fibril association under agitation conditions has been also described in the polymerization of the HET-s (218−289) prion.[29] The observed structures correspond to mature Sup35 assemblies in our experimental conditions because the fibrils formed upon 1 week of incubation under the same conditions displayed identical morphological properties (data not shown).

Although all Ure2p fibrils bind to Th−S, TEM micrographs show that their morphology display a clear temperature dependence. (See Figure 6B.) The analysis of 100 individual fibrils formed under each condition shows that the width of Ure2p fibrils remain practically invariable (23 ± 3 and 20 ± 4 nm for fibrils formed at 293 and 323K, respectively), whereas the fibril length is reduced as a function of the temperature, with lengths of 550 ± 220, 260 ± 90, 240 ± 90, and 130 ± 50 nm for fibrils formed at 293, 303, 313, and 323 K, respectively. In addition, whereas the fibrils formed at lower temperatures tend to associate laterally and to cluster, the assemblies formed at higher temperature appear, essentially, as isolated short fibrils.

We analyzed the secondary structure content of Sup35 and Ure2p fibrils formed at different temperatures (Figure 7A,D) by ATR-FTIR. Consistently with the uniform macroscopic appearance, no significant changes in the conformation of Sup35 fibrils were observed, as evidenced by the overlapping IR spectra. Deconvolution of the absorbance spectra in the amide I region allows us to confirm that the same structural components, almost exactly in the same proportions, are common to all Sup35 fibrils (Table S1 of the Supporting Information). In contrast, the ATR-FTIR spectra of Ure2p fibrils exhibit temperature dependence. Deconvolution of the spectra evidence changes in the secondary structure of the fibrils with the temperature. In this way, the intermolecular β-sheet component at 1605−1635 cm^{-1} steadily increases with the temperature, corresponding to 26% of the total signal in the amide I region in the fibrils formed at 293 K and 48% in those formed at 323 K; moreover the fibrils formed at 323 K lack the β-turn signal at ∼1675 cm^{-1} present in the other species (Table S1 of the Supporting Information). The detected β-sheet component proportions are in excellent agreement with those observed previously for Ure2p amyloid fibrils formed at 290 K under quiescent conditions (28%) and upon heating of these preformed fibrils at 333 K (46%).[30]

We quantified the binding of the different fibrils to Th-T (Figure 7B,E) and CR (Figure 7C,F). Sup35 fibrils display similar Th-T fluorescence spectra independently of the incubation temperature. In contrast, for Ure2p fibrils, Th-T fluorescence emission exhibits clear temperature dependence. Consistently with the detected increase in intermolecular β-sheet content, in Ure2p fibrils, Th-T emission increases significantly at higher temperatures. Exactly the same temperature dependence is observed for the binding of Ure2p fibrils to CR, whereas the binding of Sup35 fibrils formed at different temperatures renders essentially the same CR absorbance spectrum. The observed differences in Ure2p binding to amyloid dyes do not result from a different amount of aggregated material at the end of the reactions at the assayed temperatures because in all cases it comprises 55−60% of the total protein.

Overall, secondary structure analysis and amyloid binding properties indicate that the Sup35 fibrils formed at different temperatures are conformationally indistinguishable, whereas, apparently, an increasing proportion of the Ure2p polypeptide chain is incorporated into the cross-β sheet structure of its fibrils when the temperature is raised. Proteinase K (PK) is a

dx.doi.org/10.1021/bm201527m | *Biomacromolecules* XXXX, XXX, XXX−XXX

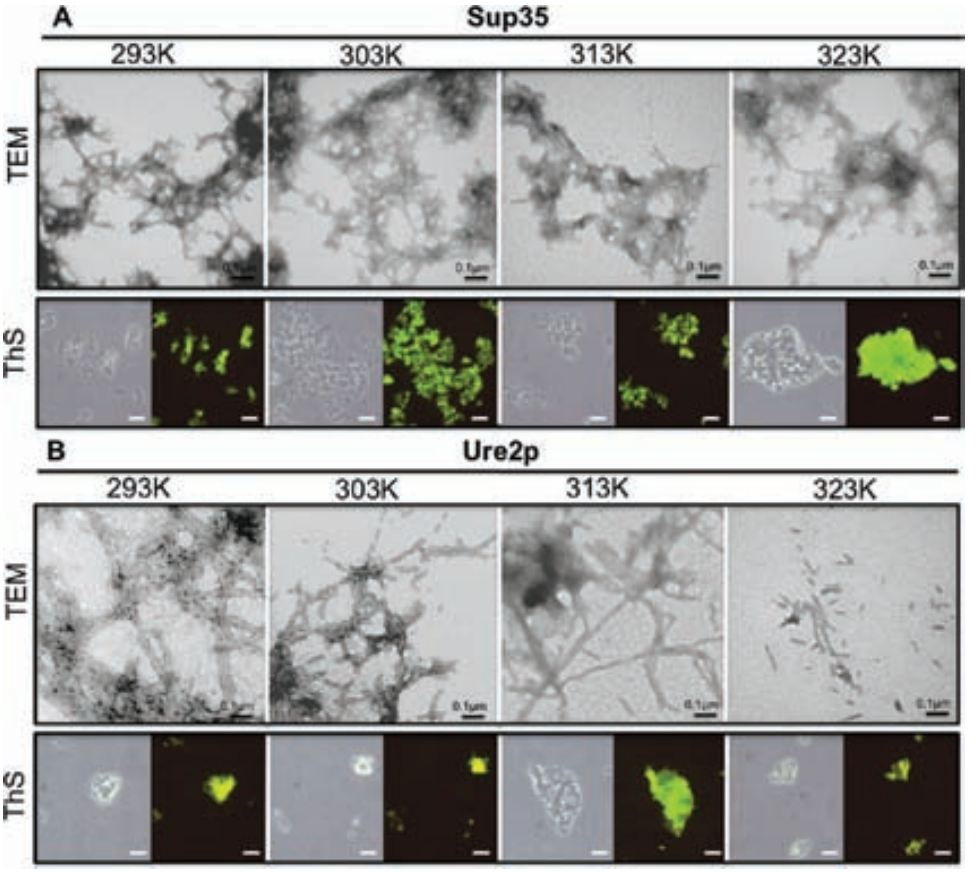

Figure 6. Effect of temperature on the morphology of Sup35 (A) and Ure2p (B) aggregates. Electronic micrographs (upper panels) and visualization of Th−S fluorescence (lower panels) of amyloid-like aggregates at 293 (A), 303 (B), 313 (C), and 323 K (D). In the lower panels, left series correspond to phase contrast microscopy and right series correspond to fluorescence microscopy under UV light; note that the scale bar for Th−S fluorescence visualization corresponds to 10 μm.

protease usually used to map the protected core of amyloid fibrils because despite its high activity for cleaving peptide bonds it cannot attack the highly packed backbones in an amyloid β-sheet structure. We analyzed the proportion of full-length Ure2p protected from proteolytic digestion at the different assayed temperatures (Figure 8). Under the conditions of the assay, soluble Ure2p is completely cut by the protease. Under the same conditions, the amount of full-length protein protected from digestion in the fibrils increases along with the temperature (Figure 8).

■ DISCUSSION

Prions are infectious proteins able to switch from an initially soluble conformation to an aggregated and transmissible amyloid state. Although a significant number of proteins are able to attain amyloidogenic conformations, only a reduced fraction of them have been shown to behave as prions. Characterization of the kinetic parameters governing amyloid fibrillation together with the conformational properties of the resulting amyloid fibrils might help us to understand basic features of the mechanism and interactions, promoting self-assembly during prion fibrillogenesis.

The final conformation of an amyloid fibril might depend both on the nature of the nucleus that acts a template and on the properties of the soluble protein that is incorporated at the fibril ends. In certain cases, the templating effect of the nucleus predominates,[31,32] whereas in other occasions are the structural characteristics of the soluble protein that exert the main control on the physical properties of the fibrils.[33] Interestingly, we observe that in the case of Sup35, although temperature affects the kinetics of both the nucleation and elongation stages, it has a negligible effect on the structural properties of the resulting fibrils, as assessed by Th-T and CR binding, TEM, and FTIR spectroscopy. This suggests that in the studied range the temperature does not significantly affect the overall conformational properties of the aggregated state or soluble Sup35 molecules, although differences can still exist on the molecular level. This is in excellent agreement with recent data indicating that the Sup35 oligomers formed in our temperature range share similar conformational properties and the resulting fibrils display similar infectiveness.[34]

The NM (1−254) domain used here, and in most studies, corresponds to the prion-forming domain of Sup35 and is not expected to adopt any regular secondary or tertiary structure in its monomeric form in solution.[35] However, its strong binding to bis-ANS indicates that given the essentially polar nature of this domain sequence, it can form at least partially collapsed states with clustered hydrophobic surfaces at the beginning of the aggregation reaction. This clustering might result from π-stacking interactions among the many tyrosine residues in the N region of Sup35. These results are in good agreement with single-molecule fluorescence resonance energy transfer (SM-FRET) and fluorescence correlation spectroscopy data on the structure and dynamics of monomeric NM.[36] SM-FRET experiments indicated that the N region of NM adopts a collapsed state corresponding to a multitude of interconverting

dx.doi.org/10.1021/bm201527m | Biomacromolecules XXXX, XXX, XXX−XXX

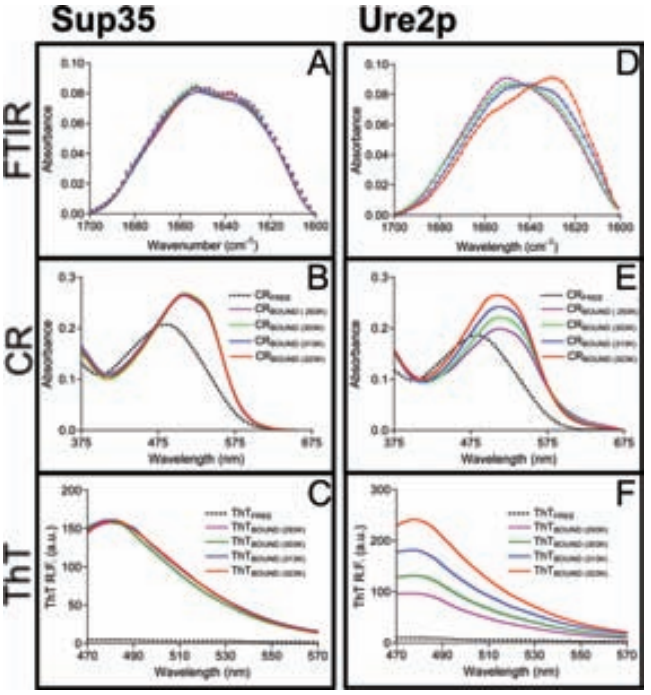

Figure 7. Effect of temperature on the secondary structure and amyloid properties of Sup35 (left) and Ure2p (right) aggregates. Absorbance spectra of the amide I region of panels A and D, CR (B,E), and Th-T (C, F) spectral changes upon binding to aggregated proteins of Sup35 and Ure2p prions, respectively, formed at 293 (violet), 303 (green), 313 (blue), and 323 (red); note the shift in λ_{max} and increase in absorbance of CR and in Th-T fluorescence (with a maximum at ~480 nm) in the presence of the different amyloid-like aggregates.

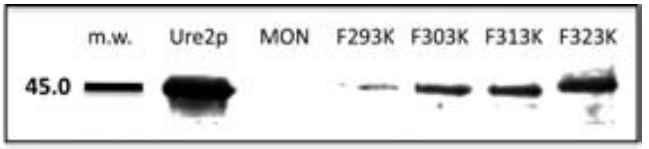

Figure 8. Resistance of Ure2p fibrils against proteolysis. Resistance of full-length Ure2p to proteinase K (PK) digestion in the fibrils formed at 293, 303, 313, and 323 K, as shown by SDS-PAGE. Ure2p and MON refer to the soluble Ure2p protein in the absence and presence of p*K*, respectively.

species, similar to the initial intermediates formed during the folding of globular proteins. The presence of denaturant was shown to decrease the compactness of the ensemble. Similarly, increasing the temperature decreases the presence of exposed hydrophobic clusters, with a concomitant reduction in the nucleation rates, suggesting that the population or the relative stability of this collapsed ensemble might play an important role in nucleus formation. The aggregation of Sup35 has been shown to be consistent with the nucleated conformational conversion mechanism.[37] Importantly, hydrophobic forces are thought to drive the initial condensation of monomers into amorphous oligomers entailing an increment in bis-ANS fluorescence, which might explain the observed relationship between bis-ANS binding and the nucleation rate. In this model, upon the initial collapse, polypeptides within the disordered oligomers realign slowly to establish hydrogen bonds that favor the formation of β-sheets. Like in protein folding, the formation of new noncovalent interactions would be favorable from the enthalpic point of view (ΔH^* = −25 kJ·mol^{-1}) but unfavorable entropically because the conformational fluctuations would be strongly reduced in the ordered oligomer relative to the initially loosely packed collapsed state, which might explain the negative $T\Delta S^*$ (−79 kJ·mol^{-1}) value for the nucleation stage of Sup35.

The large enthalpy change in the elongation of Sup35 indicates that the activated and inactive states for this reaction differ significantly in energy and together with the discrete increase in entropy suggests that a transition from an ordered and bound conformation to a more loose structure occurs during fibril growth. The sign of the enthalpic and entropic terms are identical to those reported for Aβ peptide elongation.[38] Like in the case of Aβ, Sup35 monomer is not expected to possess a regular and stable structure, which can unfold in the activation process. Instead, as proposed for Aβ,[38] a partial unfolding of the structured fibril end might occur to accommodate the incoming monomer, which would involve disruption of some noncovalent bonds among the fibril tip molecules with its corresponding activation energy. This unfolding would increase the system entropy, in agreement with the observed positive entropy term and observed dependence of the elongation rate on the temperature. Despite the fact that temperature increases the elongation speed by seven-fold, it does not change the fibrils overall physical properties, which supports incoming Sup35 molecules being template by a rather common pre-existent conformation at the fibril ends.[34]

The sign and magnitude of the observed changes in the nucleation and elongation constants of Ure2p with temperature are in good agreement with those reported previously by studying its aggregation kinetics at 298 and 310 K in different buffers.[39] Temperature induces important changes in the final physical properties of Ure2p fibrils, modifying their overall secondary structure content and specifically increasing the proportion of intermolecular β-sheet conformations. A similar increase in β-sheet content was observed when Ure2p fibrils preformed at 310 K were heated to 333 K.[30] This behavior has been interpreted as parts of Ure2p molecules being still flexible in the fibrils formed at low temperature; in such a way that the heat-induced structural rearrangement leads to the reorganization of Ure2p flexible regions within the fibrils into more rigid β-sheet structures.[30] The progressive incorporation of the full-length Ure2p protein in the protected fibrillar structure that we observe when fibril formation occurs at increasing temperatures is in agreement with this view and might reflect the transition from a state in which the prion domains of Ure2p form an amyloid core decorated with flexible, globular and functional domains[40] to a state in which the globular domains are at least partially incorporated in the main intermolecular β-sheet structure of the fibril.

The nucleation rate for Ure2p is highly dependent on the temperature. The thermodynamic parameters for the nucleation stage of Ure2p indicate that this reaction is mainly enthalpically driven (ΔH^* = 71 kJ·mol^{-1}), likely involving a conformational change in the soluble Ure2p species. This is in agreement with the observed temperature-dependent shift in Ure2p intrinsic fluorescence. This change in the local environment of Trp residues does not correspond to the denaturation of the globular domain because this process has been shown to occur only at higher temperature (~350 K) and exhibit a high ΔH_m (346 kJ·mol^{-1})[41] but would rather reflect partial unfolding or conformational fluctuations, which might favor the transient population of amyloidogenic intermediates

dx.doi.org/10.1021/bm201527m | *Biomacromolecules* XXXX, XXX, XXX−XXX

in Ure2p.[39] This view is consistent with the positive but small entropy change ($T\Delta S^*$ = 17 kJ·mol^{-1}) calculated for the nucleation reaction.

The effect of temperature in the elongation rate of Ure2p is rather small. Interestingly, Ure2p elongation displays values of ΔH^* (12 kJ·mol^{-1}) and $T\Delta S^*$ (−32 kJ·mol^{-1}), very close to those exhibited by *P. anserina* HET-s prion,[20] another protein in which the globular domain remains essentially folded in the fibrils at physiological temperature.[42] The elongation reaction is unfavorable from both the enthalpic and entropic points of view. The rate of Ure2p fibril elongation appears to be controlled by two cooperative effects of similar magnitude. In contrast with Sup35, a loss of entropy is calculated for the elongation process ($T\Delta S^*$= −32 kJ·mol^{-1}). The reduced ΔH^* value (ΔH^* = 12 kJ·mol^{-1}), suggests that the fibrils might accommodate the incoming Ure2p prion monomers without substantial disorganization of their initial structure, which is in agreement with the globular domain being essentially folded in the fibrils. The loss of translational, rotational and conformational energy of the polypeptide monomers, and especially of the unstructured and flexible prion Ure2p region, upon binding to pre-existing fibrils would account for the calculated loss of entropy in the elongation process, as shown recently for α-synuclein.[43]

CONCLUSIONS

Overall, the results in the present work suggest that the pathways by which different, initially soluble, prion proteins reach their amyloid states might diverge significantly, at least in kinetic and thermodynamic terms. The aggregation of both Sup35 and Ure2p prions depends on the presence of Gln/Asn-rich sequential stretches. However, our data indicate that specific sequential traits in these regions control the prion amyloid formation pathways as well as the structural features of the resulting aggregates, thus modulating the formation of infective conformations.

ASSOCIATED CONTENT

Supporting Information

Details of the Materials and Methods. This information is available free of charge via the Internet at http://pubs.acs.org/.

AUTHOR INFORMATION

Corresponding Author

*E-mail: Raimon.Sabate@uab.cat; Tel: 34-93-5868954; Fax: 34-93-5811264 (R.S.). E-mail: salvador.ventura@uab.es; Tel: 34-93-5868956; Fax: 34-93-5811264 (S.V.).

ACKNOWLEDGMENTS

This work was supported by BFU2010-14901 from Ministerio de Ciencia e Innovación (MCISpain) and 2009-SGR 760 from AGAUR (Generalitat de Catalunya). S.V. has been granted an ICREA ACADEMIA award. The funders had no role in study design, data collection and analysis, decision to publish, or preparation of the manuscript.

REFERENCES

(1) Prusiner, S. B. *N. Engl. J. Med.* **2001**, *344*, 1516−1526.
(2) Caughey, B.; Baron, G. S. *Nature* **2006**, *443*, 803−810.
(3) Shorter, J.; Lindquist, S. *Nat. Rev. Genet.* **2005**, *6*, 435−450.
(4) Cox, B. S.; Tuite, M. F.; McLaughlin, C. S. *Yeast* **1988**, *4*, 159−178.
(5) Lindquist, S.; Krobitsch, S.; Li, L.; Sondheimer, N. *Philos. Trans. R. Soc., B* **2001**, *356*, 169−176.
(6) Chernoff, Y. O. *Mutat. Res.* **2001**, *488*, 39−64.
(7) Wickner, R. B. *Science* **1994**, *264*, 566−569.
(8) Maddelein, M. L.; Dos Reis, S.; Duvezin-Caubet, S.; Coulary-Salin, B.; Saupe, S. J. *Proc. Natl. Acad. Sci. U.S.A.* **2002**, *99*, 7402−7477.
(9) Coustou, V.; Deleu, C.; Saupe, S.; Begueret, J. *Proc. Natl. Acad. Sci. U.S.A.* **1997**, *94*, 9773−9778.
(10) Ritter, C.; Maddelein, M. L.; Siemer, A. B.; Luhrs, T.; Ernst, M.; Meier, B. H.; Saupe, S. J.; Riek, R. *Nature* **2005**, *435*, 844−848.
(11) Wasmer, C.; Lange, A.; Van Melckebeke, H.; Siemer, A. B.; Riek, R.; Meier, B. H. *Science* **2008**, *319*, 1523−1526.
(12) DePace, A. H.; Santoso, A.; Hillner, P.; Weissman, J. S. *Cell* **1998**, *93*, 1241−1252.
(13) Tanaka, M.; Chien, P.; Naber, N.; Cooke, R.; Weissman, J. S. *Nature* **2004**, *428*, 323−328.
(14) Ross, E. D.; Baxa, U.; Wickner, R. B. *Mol. Cell. Biol.* **2004**, *24*, 7206−72013.
(15) Sabate, R.; Gallardo, M.; Estelrich, J. *Biopolymers* **2003**, *71*, 190−195.
(16) Tanaka, M.; Chien, P.; Yonekura, K.; Weissman, J. S. *Cell* **2005**, *121*, 49−62.
(17) Brachmann, A.; Baxa, U.; Wickner, R. B. *EMBO J.* **2005**, *24*, 3082−3092.
(18) Jarrett, J. T.; Lansbury, P. T. Jr. *Cell* **1993**, *73*, 1055−1058.
(19) Fandrich, M. *J. Mol. Biol.* **2007**, *365*, 1266−1270.
(20) Sabate, R.; Castillo, V.; Espargaro, A.; Saupe, S. J.; Ventura, S. *FEBS J.* **2009**, *276*, 5053−5064.
(21) Scheckel, K. G.; Sparks, B. L. *Soil Sci. Soc. Am. J.* **2001**, *65*, 719−728.
(22) Balguerie, A.; Dos Reis, S.; Ritter, C.; Chaignepain, S.; Coulary-Salin, B.; Forge, V.; Bathany, K.; Lascu, I.; Schmitter, J. M.; Riek, R.; Saupe, S. J. *EMBO J.* **2003**, *22*, 2071−2081.
(23) Goncharov, V. A. *Biophys. J.* **2005**, *89*, 4139−4148.
(24) Chiti, F.; Dobson, C. M. *Annu. Rev. Biochem.* **2006**, *75*, 333−366.
(25) Kelly, J. W. *Nat. Struct. Biol.* **2000**, *7*, 824−826.
(26) Kumar, S.; Mohanty, S. K.; Udgaonkar, J. B. *J. Mol. Biol.* **2007**, *367*, 1186−1204.
(27) Nielsen, L.; Khurana, R.; Coats, A.; Frokjaer, S.; Brange, J.; Vyas, S.; Uversky, V. N.; Fink, A. L. *Biochemistry* **2001**, *40*, 6036−6046.
(28) Uversky, V. N.; Li, J.; Fink, A. L. *J. Biol. Chem.* **2001**, *276*, 10737−10744.
(29) Sabate, R.; Baxa, U.; Benkemoun, L.; Sanchez de Groot, N.; Coulary-Salin, B.; Maddelein, M. L.; Malato, L.; Ventura, S.; Steven, A. C.; Saupe, S. J. *J. Mol. Biol.* **2007**, *370*, 768−783.
(30) Bousset, L.; Briki, F.; Doucet, J.; Melki, R. *J. Struct. Biol.* **2003**, *141*, 132−142.
(31) Petkova, A. T.; Leapman, R. D.; Guo, Z.; Yau, W. M.; Mattson, M. P.; Tycko, R. *Science* **2005**, *307*, 262−265.
(32) Tanaka, M.; Collins, S. R.; Toyama, B. H.; Weissman, J. S. *Nature* **2006**, *442*, 585−589.
(33) Devlin, G. L.; Knowles, T. P.; Squires, A.; McCammon, M. G.; Gras, S. L.; Nilsson, M. R.; Robinson, C. V.; Dobson, C. M.; MacPhee, C. E. *J. Mol. Biol.* **2006**, *360*, 497−509.
(34) Ohhashi, Y.; Ito, K.; Toyama, B. H.; Weissman, J. S.; Tanaka, M. *Nat. Chem. Biol.* **2010**, *6*, 225−230.
(35) Scheibel, T.; Lindquist, S. L. *Nat. Struct. Biol.* **2001**, *8*, 958−962.
(36) Mukhopadhyay, S.; Krishnan, R.; Lemke, E. A.; Lindquist, S.; Deniz, A. A. *Proc. Natl. Acad. Sci. U.S.A.* **2007**, *104*, 2649−2654.
(37) Carulla, N.; Zhou, M.; Arimon, M.; Gairi, M.; Giralt, E.; Robinson, C. V.; Dobson, C. M. *Proc. Natl. Acad. Sci. U.S.A.* **2009**, *106*, 7828−7833.
(38) Kusumoto, Y.; Lomakin, A.; Teplow, D. B.; Benedek, G. B. *Proc. Natl. Acad. Sci. U.S.A.* **1998**, *95*, 12277−12282.
(39) Zhu, L.; Zhang, X. J.; Wang, L. Y.; Zhou, J. M.; Perrett, S. *J. Mol. Biol.* **2003**, *328*, 235−254.
(40) Bousset, L.; Thomson, N. H.; Radford, S. E.; Melki, R. *EMBO J.* **2002**, *21*, 2903−2911.

(41) Baxa, U.; Ross, P. D.; Wickner, R. B.; Steven, A. C. *J. Mol. Biol.* **2004**, *339*, 259−264.
(42) Wasmer, C.; Schutz, A.; Loquet, A.; Buhtz, C.; Greenwald, J.; Riek, R.; Bockmann, A.; Meier, B. H. *J. Mol. Biol.* **2009**, *394*, 119−127.
(43) Morris, A. M.; Finke, R. G. *Biophys. Chem.* **2009**, *140*, 9−15.

Biochimie 94 (2012) 1730–1738

Contents lists available at SciVerse ScienceDirect

Biochimie

journal homepage: www.elsevier.com/locate/biochi

Research paper

Effect of the surface charge of artificial model membranes on the aggregation of amyloid β-peptide

Raimon Sabaté [a,b,**], Alba Espargaró [a], Lucyanna Barbosa-Barros [b], Salvador Ventura [a], Joan Estelrich [b,c,*]

[a] Departament de Bioquímica i Biologia Molecular and Institut de Biotecnologia i de Biomedicina, Universitat Autònoma de Barcelona, 08193-Bellaterra, Barcelona, Spain
[b] Departament de Fisicoquímica, Facultat de Farmàcia, Universitat de Barcelona, Avda. Joan XXIII s/n, E-08028-Barcelona, Catalonia, Spain
[c] Institut de Nanociència i Nanotecnologia (IN²UB), Spain

ARTICLE INFO

Article history:
Received 18 November 2011
Accepted 30 March 2012
Available online 20 April 2012

Keywords:
Amyloid
Oligomer
Fibrils
Liposome
Aggregation
Model membrane

ABSTRACT

The neurotoxicity effect of the β-amyloid (Aβ) peptide, the primary constituent of senile plaques in Alzheimer's disease, occurs through interactions with neuronal membranes. Here, we attempt to clarify the mechanisms and consequences of the interaction of Aβ with lipid membranes. We have used liposomes as a model of biological membrane, and have devoted particular attention to the bilayer charge effect. Our results show that insertion and surface association of peptide with membrane, increased in a membrane charge-dependent manner, lead to a reduction of Aβ soluble species, lag time elongation and an increase in the inter-molecular β-sheet ratio of amyloid fibrils. In addition, our findings suggest that the fine balance between peptide insertion and surface association modulates Aβ aggregation, influencing the amyloid fibrils concentration as well as their morphology.

1. Introduction

Protein folding into non-native states is usually associated with the conversion of peptides or proteins from their soluble and functional conformations into highly organized fibrillar aggregates, generally described as amyloid fibrils [1–3]. Alzheimer's disease (AD), one of the most common causes of adult dementia, has been directly related to the accumulation of β-amyloid (Aβ) peptides in the brain [4,5]. Although historically the mature Aβ fibrils were considered as responsible of the neuronal cell death [6], the low correlation between amyloid plaques load and the clinical severity of the disease [7,8] suggest that soluble assemblies of Aβ might be responsible for synaptic dysfunction in AD [9] and mature fibrils present in the tissue deposits might even act protective material [2,10]. Since it was been vastly shown that Aβ could interact with synthetic lipids *in vitro* [11–27], neuronal membranes have to play a significant role in the cytotoxic process. One proposed mechanism for Aβ neurotoxicity is membrane disruption and depolarization mediated by either ion-channel formation or an increase in overall membrane conductance, resulting in the alteration of ion homeostasis and deregulation of neuronal signal transduction, leading to cell death [28–38]. However, it is still unclear how the interaction of amyloid species with membranes causes disruption of the bilayer, leading to a disruption of membrane integrity.

Here we examined the influence of the surface charge of lipid membranes on the specificity of Aβ40 membrane binding, and how such a charge modifies peptide permeabilization. Since neuronal membranes, in not excited state, have a resting potential ranging from −70 to −80 mV, large unilamellar vesicles with a molar content in negatively charged lipids ranging from 0 to 50% were used as a biomimetic model alternative to natural cell membranes *in vivo*, in order to test the effect of membrane negative charge on Aβ40 aggregation. For this purpose, extruded liposomes of PC:PS 100:0 (molar ratio) (zwitterionic liposomes), PC:PS 75:25 (25% negative charge) and PC:PS 50:50 (50% negative charge) were prepared (PC: phosphatidylcholine and PS: phosphatidylserine). As the melting temperature of the phospholipids is well below room temperature, the liposomes formed are found in liquid crystal phase. Thus, we checked fluid liposome-induced changes in the Aβ40 aggregation rate as well as the consequences of the amyloid formation for membrane integrity.

* Corresponding author. Universitat de Barcelona, Avda, Departament de Fisicoquímica, Facultat de Farmàcia, Institut de Nanociència i Nanotecnologia (IN²UB), Joan XXIII s/n, E-08028 Barcelona, Catalonia, Spain. Tel.: +34 93 4024559; fax: +34 93 4035987.
** Corresponding author. Departament de Bioquímica i Biologia Molecular and Institut de Biotecnologia i de Biomedicina, Universitat Autònoma de Barcelona, 08193-Bellaterra, Barcelona, Spain. Tel.: +34 93 5862154; fax: +34 93 5811264.
E-mail addresses: raimon.sabate@uab.cat (R. Sabaté), joanestelrich@ub.edu (J. Estelrich).

0300-9084/$ – see front matter © 2012 Elsevier Masson SAS. All rights reserved.
doi:10.1016/j.biochi.2012.03.027

2. Materials and methods

2.1. Materials

Soybean phosphatidylcholine (PC) (Lipoid S-100) was a gift from Lipoid (Ludwigshafen, Germany) and phosphatidylserine (PS) from bovine spinal cord was obtained from Lipid Products (Nutfield, U.K.). The 1–40 fragment of Aβ peptide was obtained from Bachem (Bubendorf, Switzerland). Organic solvents were purchased from VWR (Darmstadt, Germany). Solutions were prepared in double-distilled water purified through a MilliQ system (Millipore, USA).

The identity and homogeneity of the peptide were re-evaluated in our laboratory by an Ultraflex MALDI-TOF mass spectrometer (Bruker Daltonics, Germany), operating in linear mode under 20 kV, and were found to be >95% in all cases, in accordance with the manufacturer's specifications. To obtain a soluble peptide stock solution, a solution of Aβ40 peptide in 1,1,1,3,3,3-hexafluoro-2-propanol (HFIP) was prepared at 2 mg mL^{-1}, was centrifuged at 15,000 *g* at 4 °C for 15 min and, finally, filtered through Millex-GV 0.22-μm filters (Millipore, USA) in order to remove the possible residual quantity of high aggregates. Stock solutions were divided into aliquots and HFIP was removed by evaporation under a gentle stream of nitrogen, leaving a slightly yellow film. The samples were kept overnight in a desiccator under vacuum. Finally, they were stored at −80 °C. When required, the samples were suspended in 50 μL of anhydrous dimethyl sulfoxide (DMSO) and bath-sonicated bubbling nitrogen gas for 15 min. Sonication was crucial for removing any trace of non-dissolved seeds that may resist solubilisation and the nitrogen bubbling for purge the residual traces of HFIP from the samples. It is known that HFIP can present cytotoxicity [39] and alter the lipid arrangement inducing membrane disruption [40]. However, the disruptive effect of HFIP affects mainly the saturated and/or gel-phase phospholipids. Since the main phospholipid used (PC) is unsaturated and its physical state is liquid crystal, HFIP does not alter our bilayers. Aliquots of soluble Aβ40 peptide were added to 100 μL aggregation buffer 10× (100 mM Tris·HCl, 5 mM of $MgCl_2$, 10 mM $CaCl_2$ pH 7.4) and 850 μL of MilliQ water (or liposomal solution), yielding a final peptide concentration of 20 μM.

2.2. Liposome preparation and characterization

Phospholipids dissolved at 20 mM concentration in a mixture (2:1, volume ratio) of chloroform and methanol were placed in a round-bottom flask and then dried in a rotary evaporator under reduced pressure at 40 °C to form a thin film on the flask. The film was hydrated with Tris–HCl buffer (10 mM, pH 7.4) to give a lipid concentration of 10 mM. Multilamellar liposomes (MLV) were formed by constant vortexing for 4 min in a vortex mixer followed by sonication in a Transsonic Digitals bath sonifier (Elma, Germany) for 10 min. MLV were downsized by extrusion at 40 °C in an Extruder device (Lipex Biomembranes, Canada) through polycarbonate membrane filters of variable pore size under nitrogen pressures of up to 55×10^5 N m^{-2} [41]. Liposomes were extruded in three steps: first through a 0.8 μm pore diameter filter, then through a 0.4 μm membrane and finally through a 0.2 μm filter. Three consecutive extrusions were performed at each step to render large unilamellar vesicles (LUVs). The mean and the distribution of the particle size were determined by dynamic light scattering at 25 °C with a Zetasizer NanoZS90 (Malvern, UK). For viscosity and the refractive index, water values were used.

2.3. Aggregation kinetics

The aggregation of Aβ40 from soluble material in the presence or absence of liposomes (1 mM) was followed by measuring the increased fluorescence of thioflavin-T (Th-T) when it binds to aggregate structures. Th-T has been observed to bind cross-β ladders as small as four to five strands corresponding to tetramer and pentamer of Aβ peptide. Hence, the enhancement of Th-T fluorescence is not observed with Aβ monomers and small oligomers [42]. A Cary Eclipse spectrofluorometer (Varian, Palo Alto, CA) was employed for measuring the fluorescent emission of Th-T at 480 nm after excitation at 445 nm. The spectra of Th-T at 25 μM without or in presence of 20 μM of Aβ40 aggregates were recorded. The sample was gently stirred during the measurements. All experiments were carried out at 37 °C. As the obtained curves present a sigmoidal shape, the mathematic model to follow the aggregation can be similar to the used for a catalytic reaction. A distinctive characteristic of any catalytic reaction lies in the fact that the process is performed at a variable concentration of catalyser. Here the "catalyser" would correspond to the initial peptide concentration. Based in the former assumption, the Aβ40 aggregation process was studied as an autocatalytic reaction using the equation

$$f = \rho \frac{e^{[(1+\rho)kt]} - 1}{1 + \rho \times e^{[(1+\rho)kt]}}$$

under the boundary condition of $t = 0$ and $f = 0$, where f is the fraction of initial peptide which has undergone an aggregation, k is a constant value related to $k_e a$ (when a is the protein concentration and k_e is the elongation constant) and ρ represents the dimensionless value to describe the ratio of k_n (nucleation constant) to k. By non-linear regression of f (aggregated fraction) against t (time), values of ρ and k can be obtained easily; and from these, the rate constants, k_e and k_n. The extrapolation of the growth portion of the sigmoid curve to the abscissa ($f = 0$), and to the highest ordinate value of the fitted plot, afforded two values of time (t_0 and t_1), which correspond to the lag time and to the time at which the aggregation was almost complete [43].

2.4. Secondary structure determination

Attenuated total reflectance Fourier transformed infrared spectroscopy (ATR-FTIR) analyses of Aβ40 aggregates were performed using a Bruker Tensor 27 FTIR Spectrometer (Bruker Optics, Ettingen, Germany) with a Golden Gate MKII ATR accessory. Each spectrum consists of 20 independent scans, measured at a spectral resolution of 1 cm^{-1} within the 1800–1500 cm^{-1} range. All spectral data were acquired and normalized with the OPUS MIR Tensor 27 software. FTIR spectra were fitted to four overlapping Gaussian curves and the amplitude, centre and bandwidth at half of the maximum amplitude and area of each Gaussian function were calculated using a non-linear peak-fitting program (PeakFit package, Systat Software, San Jose, CA). Second derivatives of the spectra were also used to determine the wavenumber at which the different spectral components were located.

2.5. Amyloid specific dyes staining

CR binding to Aβ40 aggregates (obtained at the final time of the aggregation) was tested with a Cary-100 Varian UV/Vis spectrophotometer (Varian, Palo Alto, CA) by recording the absorbance spectra from 375 to 675 nm at 25 °C. Spectra of CR at 5 μM in presence of Aβ40 and of Aβ40-liposomes were recorded and deconvoluted in four Gaussian bands. Finally, in order to detect the typical amyloid band at ~541 nm, the differential spectra for each Aβ40 aggregate were determined. For optical microscopy analysis, Aβ40 aggregates were incubated for 1 h in the presence of 50 μM CR and the precipitated fraction, obtained by centrifugation at 14,000 *g* for 5 min, was placed on a microscope slide and sealed. CR

birefringence was tested under cross-polarized light with an optic microscope (Leica DMRB, Heidelberg, Germany). For the centrifugation assay, after 15 min of incubation, the samples were centrifuged at 15,000 *g* for 30 min at room temperature. This method requires only knowing the molar absorptivity of free dye, because bound dye is physically separated from the free form. The supernatant, which contained the free dye, was discharged and the corresponding absorbance was measured from 375 to 675 nm.

The binding of Thioflavin-T (Th-T) to Aβ40 aggregates was recorded using an optical microscopy analysis. Aβ40 aggregates were incubated for 1 h in the presence of 125 μM of Th-T and the precipitated fraction, obtained by centrifugation at 14,000 *g* for 5 min, was placed on a microscope slide and sealed. Th-T relative fluorescence images of Aβ40 aggregates were obtained at 40-fold magnification under UV light in Leica fluorescence DMRB microscope (Leica Microsystems, Mannheim, Germany).

2.6. Transmission electronic microscopy (TEM)

The morphology of aggregates of Aβ40 was observed by Transmission electronic microscopy using a Hitachi H-7000 microscope operating at 75 kV. Aβ40 in fibrillar form was previously sonicated for a short time to ensure optimal particle size. The aggregates of Aβ40 were adsorbed to freshly glow-discharged carbon-coated grids, rinsed with water and stained with 2% (w/v) uranyl acetate.

2.7. Permeability studies

For these studies, liposomes were prepared by hydrating the dried lipids with an aqueous solution of calcein (CL) at 100 mM. At this concentration, CL is self-quenched and only low fluorescence is detected. After preparation of the liposomes, the non-encapsulated dye was eliminated by the mini-column centrifugation technique [44]. Liposomes were diluted to a final lipid concentration of 1 mM in presence of 20 μM of soluble Aβ40 peptide at 37 °C. If a consequence of the interaction of peptide with membrane, this undergoes a poration, calcein is released from the internal space and it becomes diluted and unquenched, thereby causing an increase in fluorescence. The percentage of CL released under the influence of Aβ40 was determined after measurement of the relative fluorescence intensity using λ_{ex} of 472 nm and λ_{em} of 516 nm. Dynamic light scattering was used to corroborate membrane disruption and liposome integrity. At the final time of each reaction we have added 10 μL of 10% Triton X-100 (TX-100) in order to disrupt the residual liposomes amount and determine the maximal relative fluorescence of the CL (showing 100% of liposome leakage).

2.8. Western blot

Amyloid-like aggregates of Aβ40 formed in absence or presence of liposomes were transferred onto PVDF membranes; and recombinant proteins, detected with an anti-oligomer antibody (Biosource, Camarillo, CA). The membranes were developed with the ECL method [45].

3. Results

3.1. Effect of artificial membranes on Aβ40 aggregation kinetics

The Th-T trace from amyloid formation is characterized by a sigmoidal curve shape. During the initial lag phase, oligomers are built up to the critical size detectable by Th-T and during the elongation phase the fluorescence intensity increases rapidly as fibrils elongate. As explained elsewhere [15], liposome composition alters the aggregation kinetics of Aβ40. As shown in Fig. 1, all of liposome systems checked delayed Aβ40 aggregation. The delay was greater in the presence of negatively charged liposomes. In this way, an increment from 21 to 53 min for t_0 (lag time, i.e. the time necessary to observe the first aggregates) was observed when comparing the aggregation of the peptide alone with that in the presence of liposomes with 50% negative charge. Similar increments were observed for $t_{1/2}$ and t_1 in the presence of charged liposomes (Table 1).

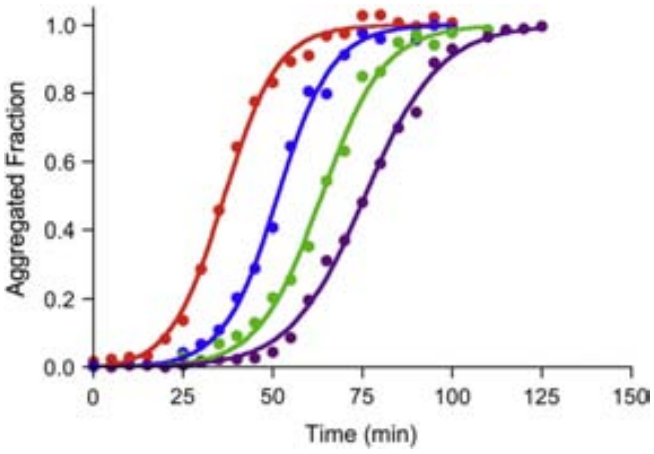

Fig. 1. Curves of aggregation of Aβ40 in absence (red) and in presence of PC:PS 100:0 (blue), PC:PS 75:25 (green) and PC:PS 50:50 (violet) liposomes. (For interpretation of the references to colour in this figure legend, the reader is referred to the web version of this article.)

The k_n of the Aβ40 aggregation reaction was reduced 7-fold in the presence of uncharged liposomes and 15-fold in presence of liposomes with 50% charge. The k_e remained practically constant regardless of the absence or presence of liposomes. The selective and dramatic alteration of k_n suggests that Aβ40 interaction with liposomes occurs at the initial stages of Aβ40 polymerization.

3.2. Presence of β-sheet structure in Aβ40 aggregates

To assess whether the presence of anionic and neutral liposomes alters the secondary structure of Aβ40 assemblies, the aggregates obtained in the final time course of each aggregation reaction were analysed by ATR-FTIR. In peptides and proteins, amide I region (around 1600–1700 cm^{-1}) is assigned to the C=O stretching mode of the peptide main chain. Native β-sheet proteins produce amide I peaks clustering between 1630 cm^{-1} and 1643 cm^{-1} (intra-molecular β-sheets), whereas amyloid fibrils present a band that extends from 1611 cm^{-1}–1630 cm^{-1} (inter-molecular β-sheets). A difference between the bands of both kinds of β-sheets is that the inter-molecular β-sheets bands are usually narrower that the observed for intra-molecular β-sheets [46]. As

Table 1
Kinetics of the aggregation of Aβ40 in the absence and presence of different types of liposomes. ck_e is the product of peptide concentration and the elongation constant. The kinetic parameters were obtained under the supposition that the aggregation follows an autocatalytic model.

Kinetic parameters	Aβ40			
Liposomes	–	PC:PS 100:0	PC:PS 75:25	PC:PS 50:50
t_0 (min)	21	37	45	53
$t_{1/2}$ (min)	35	51	64	76
t_1 (min)	51	65	84	99
k_n (10^6 s^{-1})	16.87	2.57	1.39	1.14
k_e (M^{-1} s^{-1})	60.00	59.28	51.23	43.17
ck_e (10^3 M^{-1} s^{-1})	2.21	2.19	1.89	1.59

shown in Fig. 2, and more clearly in Fig. 2a, all Aβ40 aggregates had a main band at ~1630 cm^{-1} in the amide I region, suggesting that they display similar inter-β-strand hydrogen bonds.

Fitting analysis was done on the amide I band contour using four overlapping Gaussian curves, as shown in Fig. 2a. Peak positions of each deconvoluted band are related to specific secondary structure elements (Table 2). It can be observed that the aggregate content in β-sheet inter-molecular structure increased from 36% in the absence of liposomes to ~57% in their presence.

Therefore, although all of aggregates displayed characteristic inter-molecular β-sheet structures, the β-sheet content of the aggregates formed in presence of liposomes is significantly larger than that in the aggregates formed by the peptide alone.

3.3. Amyloid-like properties of Aβ40 aggregates

To determine whether the β-sheet structure detected in Aβ40 aggregates in both the absence and presence of liposomes corresponds to an amyloid-like conformation, the binding of these aggregates to the widely used amyloid diagnosis dyes, Congo Red (CR) and Thioflavin-T (Th-T), was studied. As Congo-Red (CR) does not directly interfere with phospholipids of bilayers [47], it allows study of Aβ40 fibrillation in presence of liposomes. All Aβ40 aggregates bound to CR, as shown by an increase in the absorbance of the dye and by a shift of the maxima towards higher wavelengths (Fig. 3a). Moreover, the differential spectrum (the spectrum of Aβ bound to CR minus the spectrum of CR alone) (Fig. 3b) showed

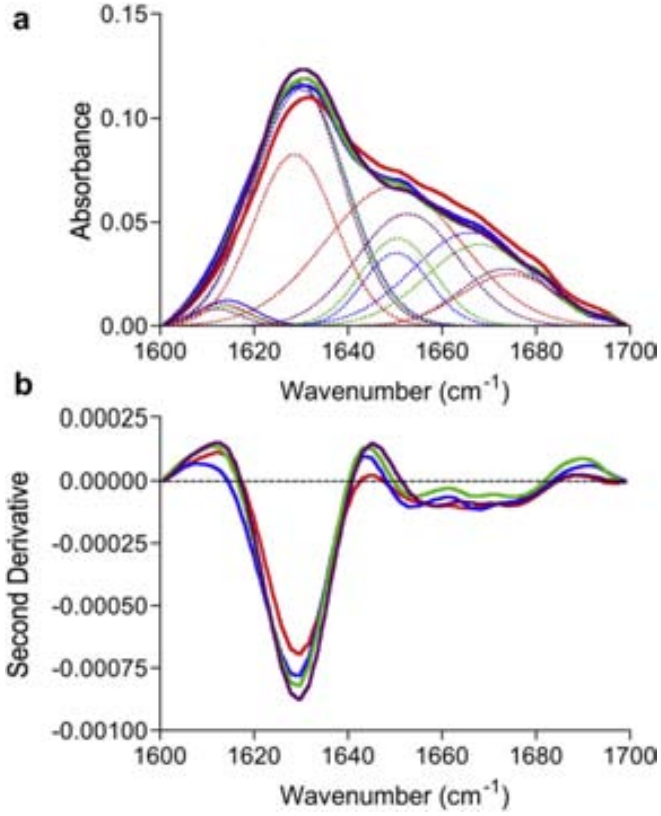

Fig. 2. Secondary structure of Aβ40 determined by ATR-FTIR spectroscopy in absence (red) and in presence of PC:PS 100:0 (blue), PC:PS 75:25 (green) and PC:PS 50:50 (violet) liposomes. (a) Absorbance in the amide I region as a function of wavelength. FTIR spectra were fitted to four overlapping Gaussian. The sum of the four bands overlaps the experimental data closely. (b) Second derivative of the spectra showed in (a). (For interpretation of the references to colour in this figure legend, the reader is referred to the web version of this article.)

Table 2
Assignment of secondary structure of Aβ in the fitted FTIR spectra in absence and presence of liposomes.

Aβ40		Band (cm^{-1})	Area (%)	Structure
Liposomes	–	1613	3	Side chain
		1628	36	β-sheet (inter)
		1650	61	Loop/β-turn/bend/α-helix
		1674		
	PC:PS 100:0	1614	4	Side chain
		1630	56	β-sheet (inter)
		1650	40	Loop/β-turn/bend/α-helix
		1666		
	PC:PS 75:25	1614	3	Side chain
		1630	57	β-sheet (inter)
		1651	40	Loop/β-turn/bend/α-helix
		1668		
	PC:PS 50:50	1612	2	Side chain
		1629	58	β-sheet (inter)
		1653	40	Loop/β-turn/bend/α-helix
		1674		

a band at ~ 541 nm characteristic of amyloids. As confirmed by centrifugation (Fig. 3c), the differences observed in the CR spectrum, with a PC:PS 0:0 > PC:PS 50:50 > PC:PS 75:25 > PC:PS 100:0 effect, are directly related to amyloid fibril concentration in the different samples. In addition, all Aβ40 amyloid-like aggregates display CR birefringence on incubation with CR and illumination under cross-polarized light in an optical microscope (data not shown). To further confirm the presence of amyloid-like fibrils, the binding of these Aβ40 aggregates to Th-T was tested. Th-T becomes fluorescent in the presence of aggregated, but not soluble, amyloid [48]. Thus, its fluorescence can be used to monitor the aggregation process. Aβ40 aggregates bound to Th-T induced differential changes in Th-T relative fluorescence in the same manner as in CR (Fig. 3d). Furthermore, all samples had Th-T fluorescence staining, observable by optical fluorescence microscopy (data not shown).

In summary, although the Aβ40 aggregates formed in absence of liposomes displayed fewer inter-molecular β-sheets (as detected by ATR-FTIR) than those formed in presence of liposomes, the final concentration of amyloid fibrils was higher in absence than in presence of liposomes.

3.4. Aβ40 fibril morphology

Transmission electron microscopy (TEM) monitors the morphology of protein aggregates and, more specifically, the presence of amyloid-like fibrils in aggregated samples. As shown in Fig. 4 and Supplementary 1, although all Aβ40 aggregates corresponded to amyloid-like fibrillar structures, micrographs showed a variety of morphologies. Thus, whereas Aβ40 fibrils formed in absence of liposomes displayed macroscopically well-formed fibrils (Fig. 4a), Aβ40 fibrils formed in presence of liposomes were macroscopically more disordered, with a concomitant reduction in fibrillar size when the negative charge of liposomes increased (see Fig. 4b–d). The reduction in size entails an increase in the number of fibrils for a given fibril mass.

3.5. Effect of Aβ40 presence on the integrity of artificial membranes

Proteins can induce the aggregation of liposomes through a bridging mechanism [49]. Concretely, this fact has been observed for Aβ40, Aβ42, human amylin and prion (106–126) peptides [50]. However, this effect is extremely dependent on the medium where liposomes are suspended, on the presence of G_{M1} ganglioside in the bilayer, and on the electrical charge (neutral liposomes are more prone to aggregation than the charged ones). In these conditions,

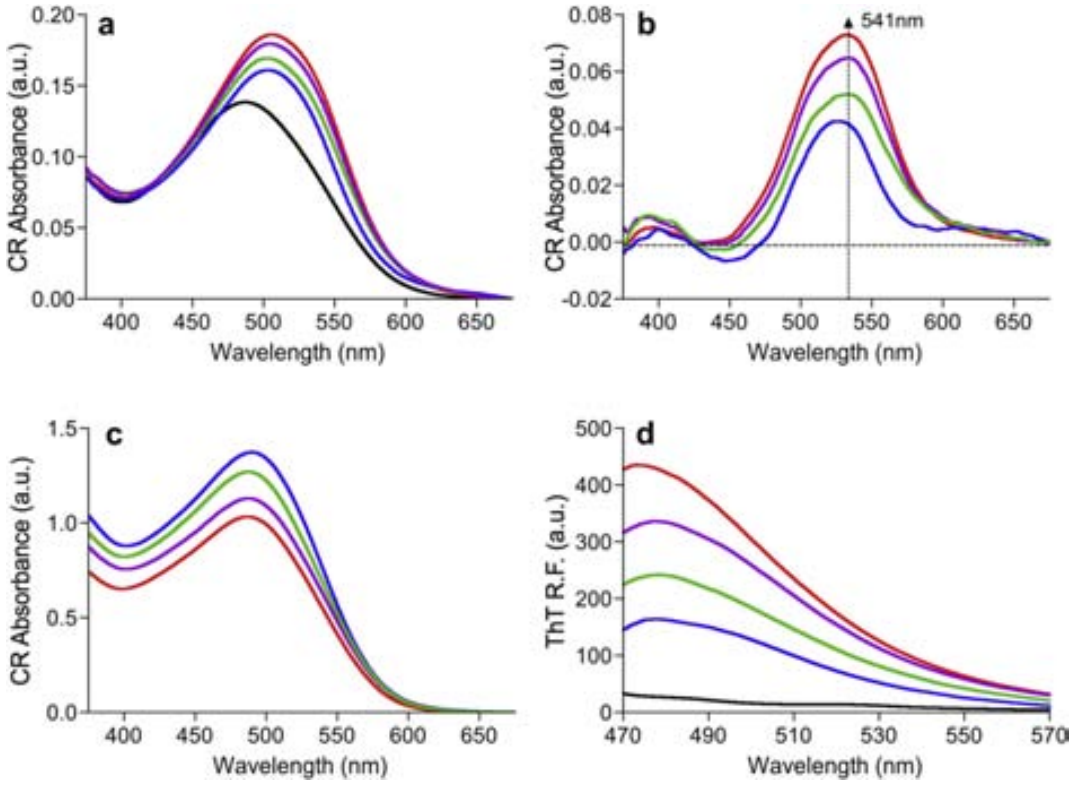

Fig. 3. Aβ40 binding to specific amyloid-like dyes in absence (red) and in presence of PC:PS 100:0 (blue), PC:PS 75:25 (green) and PC:PS 50:50 (violet) liposomes. (a) Absorbance spectra of CR; (b) Differential spectra of CR; (c) CR spectra of the supernatants obtained by centrifugation; (d) Relative fluorescence of Th-T. When required, free Th-T and CR were shown in black. (For interpretation of the references to colour in this figure legend, the reader is referred to the web version of this article.)

this event, which occurs prior to the formation of aggregates, may interfere with the results concerning the interaction liposome-Aβ. We have not observed an appreciable aggregation in the course of permeability studies, as evidenced by measurements by dynamic light scattering.

Aβ is able to form many different self-assembled structures on (or off) the pathway to amyloid fibril formation. It is still unclear which of these structures interact with membranes and whether this interaction may cause disruption of the bilayer. In this way, whereas the mature fibrils of Aβ40 have a weak effect in the liposome aggregation, soluble species promote a drastic liposome aggregation. Lin et al. showed by AFM that membrane pore formation could be considered a direct consequence of the interaction of Aβ soluble species with membranes [36]. To measure the ability of Aβ40 to permeabilize bilayer membranes, liposomes encapsulating a self-quenching fluorescent dye (calcein, CL) at high concentration were prepared. The leakage of CL is consequence of the destabilization of liposomes. In absence of peptides (or other membrane-disturbing agents), the instability of liposomes is due mainly to aggregation and fusion processes. Aggregation, always previous to the fusion and linked to Van der Waals interactions, is a natural and unavoidable phenomenon in neutral liposomes. The simplest way to overcome this effect is to introduce charge in the liposomal composition, which makes electrostatic repulsion become the driving force that keeps the suspension stable [51]. In consequence, the slower release of CL from charged liposomes, as compared to neutral liposomes, finds a more likely explanation in intrinsic destabilization of liposomes due to aggregation and fusion processes. Here, soluble Aβ40 was prepared in Tris–HCl buffer (10 mM, pH 7.4) at a final concentration of 20 μM and then added to

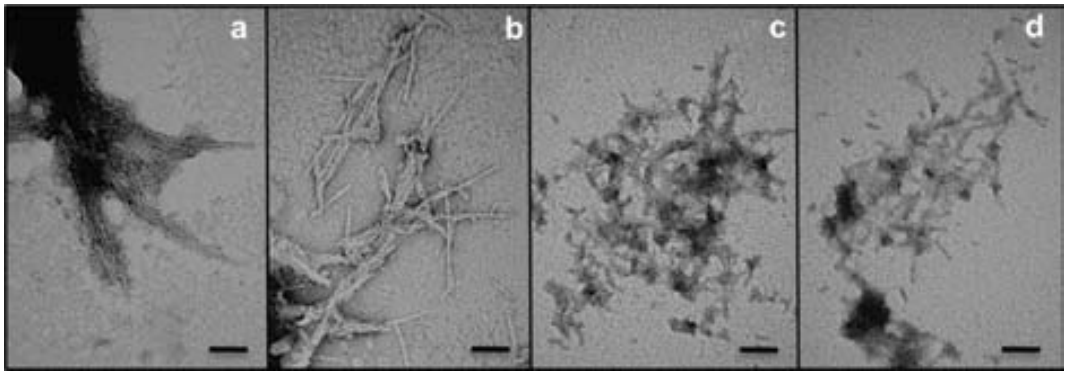

Fig. 4. Transmission electron micrographs of Aβ40 fibrils in absence (a) and presence of of PC:PS 100:0 (b), PC:PS 75:25 (c) and PC:PS 50:50 (d) Liposomes. (Scale bar: 100 nm).

CL-containing liposomes (lipid concentration 10 mM). The change in CL fluorescence was recorded over a period of 6 h. After this time point, the efflux of CL was extremely slow, which was made clear by a fluorescence plateau. The fluorescence obtained after addition of Triton X-100 was taken as 100% of liposome leakage. As can be seen in Fig. 5, whereas 50% of CL is released in 120 min from neutral liposomes, a two-fold delay in CL release was observed for negatively charged ones. The addition of Aβ to liposomes caused an immediate increase in the rate of CL efflux, compared with the slow release from liposomes without peptide. Thus, the presence of Aβ40 promoted changes in the membrane structure of liposomes, possibly by bringing the vesicles into close proximity with each other and thereby allowing them to fuse more rapidly or by causing defects within the membrane that allow CL leakage. The presence of Aβ40 peptide reduced 2.5-fold the time at which 50% of CL was released from negatively charged liposomes (from 205 to 85 min), whereas the effect was more moderate for neutral liposomes, with a 1.5-fold reduction (from 120 to 85 min). Together with the kinetic aggregation data, this suggests a preferential interaction of Aβ40 with negatively charged membranes.

4. Discussion

Aβ40 peptides are amphiphilic and highly surface-active, and, in consequence, they adsorb unspecifically at the air/water interface

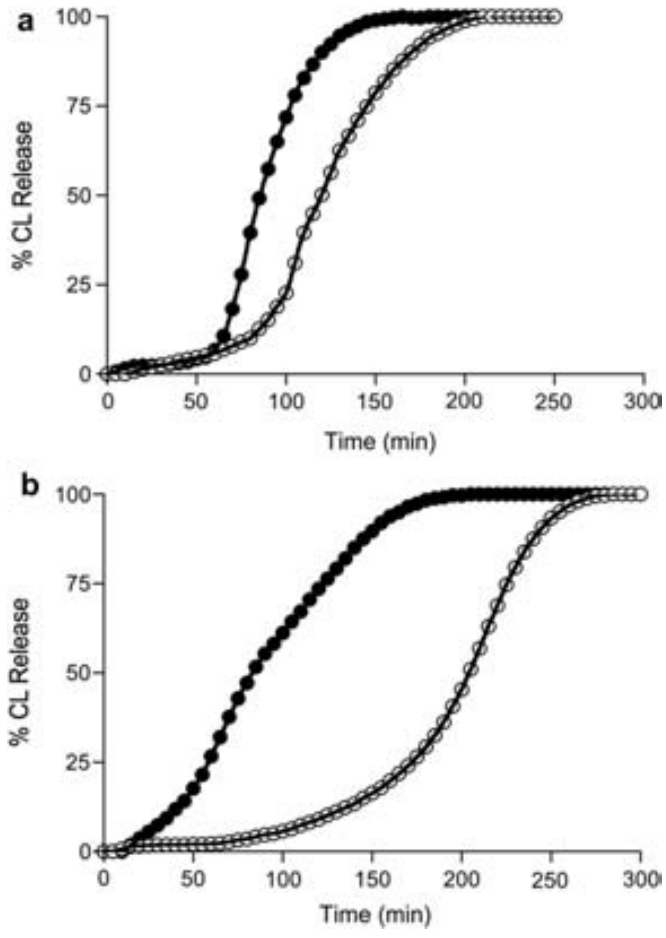

Fig. 5. Calcein fluorescence emission showing the effect of Aβ40 on liposomes with time. The value of fluorescence at 300 min was considered as 100% of the calcein released. (a) Neutral liposomes; (b) Liposomes with 25% negative charge. (—O— liposomes alone), (—●— liposomes with Aβ40).

and penetrate into uncompressed monolayers formed by zwitterionic and anionic phospholipids [52], and the same behaviour can be expected in their interaction with liposomes. We have demonstrated that the presence of liposomes slows down Aβ40 aggregation. This delay depends on the amount of negative charge present in the membranes. At first glance, this seems somewhat surprising, since the estimated net charge of Aβ at pH 7.4 is −2.8. Hence, the Aβ-bilayer interaction is moderately attractive (charge–dipole) for neutral liposomes and repulsive (charge–charge) for negative liposomes (PS has a net charge of −1). Despite this repulsion, the insertion of Aβ into monolayers of negative phospholipids in fluid phase has been described [53]. This suggests that the electrostatic repulsion between Aβ peptide and the negatively charged liposomes is overcome by other highly favourable interactions, e.g., between the hydrophobic tail of Aβ peptide and the interior of the membrane. That is, both the electrostatic and hydrophobic forces play important roles in the organization of Aβ-membrane complexes.

The interaction of Aβ peptide with membranes represents a critical step in fibrillogenesis and membrane disruption [27,54,55]. Such interaction might result from two different scenarios [11]: first, an electrostatic adsorption to membrane surfaces. The adsorption is facilitated by the presence of a negative surface potential in the membrane. In this way, an increase in acidic lipids would promote a significant increase in the proportion of surface-associated peptide; second, an insertion of Aβ peptide into membranes. In neutral bilayers only a short part of the hydrophobic segment would be inserted, since the hydrophilic part is stabilized in the bulk solution. Increasing the surface potential induces electrostatic anchoring of charged residues close to the surface thereby facilitating an increased insertion of the hydrophobic segment into the membrane core. As proposed by Bokvist et al. [11], the affinity of the peptide to negative charged bilayers arises from electrostatic coupling of the positively charged residue Lys28 with the negatively charged lipid phosphate group. The effect of each type of interaction on fibrillogenesis is different: The surface association (adsorption) causes an acceleration of the fibrillation, whereas the insertion produces a retard of the aggregation. Hence, the lag time increases observed in our study will be mainly due to the insertion of Aβ peptide in the bilayer (in neutral and negative liposomes) without excluding the possibility that an amount of the peptide is associated with the negatively charged membrane (Fig. 6). Apart from modifying the kinetics of the aggregation reaction, the presence of Aβ peptide in the trans-membrane region of the membrane can induce ion-channel formation and membrane disruption [36,56,57].

As indicated above, the presence of liposomes delays Aβ40 aggregation in a charge-dependent manner. Negative charge of the membrane should provoke an increase in Aβ40 association to membranes, since the highest increase of the lag time occurs when Aβ40 interacts with PC:PS 50:50 liposomes. The increase of the lag time in a lipid concentration-dependent manner was also previously observed in presence of neutral liposomes [19], which suggests that, the amount of available soluble Aβ peptide is a determinant factor in its amyloid nucleation. Hellstrand et al. described that the aggregation lag time increased in presence of neutral lipid vesicles, but, contrarily to our findings, no significant difference was detected when increasing amount of negative charge was incorporated into the membrane [15]. Among other aspects, the lower peptide concentration used in this study (380 nM–12 μM) might account for the observed differences. In fact, Hellstrand and co-workers do not exclude the possibility that lipid membranes have accelerating effects at different peptide and lipid concentrations, or in the presence of other solution components.

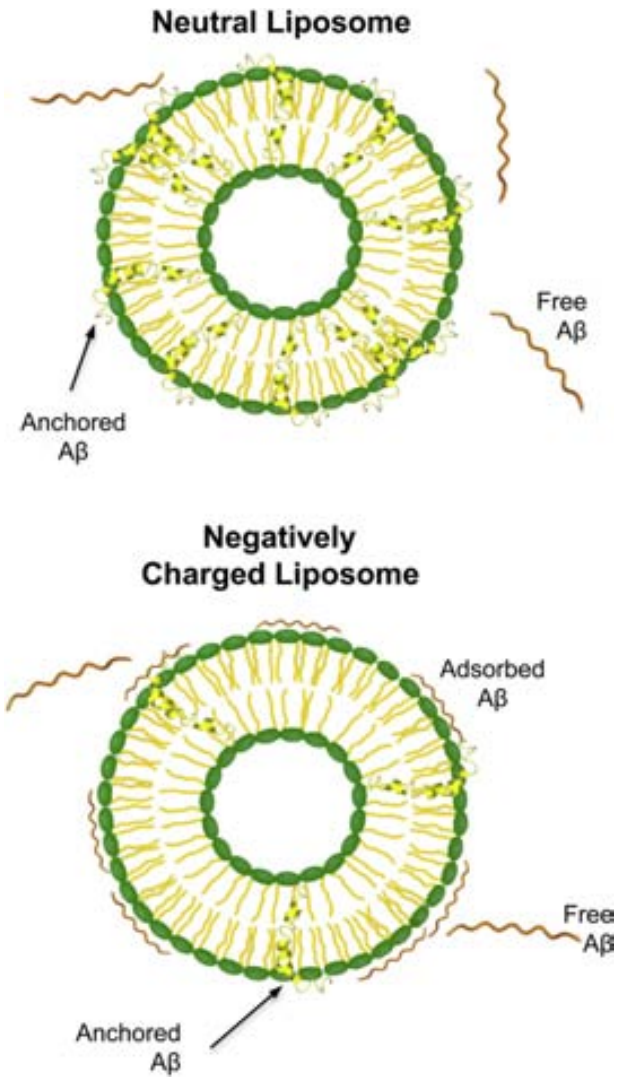

Fig. 6. Schematic model for the interaction of Aβ40 with liposomes. Top: neutral liposomes (the peptide is anchored in the membrane). Bottom: Negatively charged liposomes (the peptide is anchored in the membrane but it is also adsorbed by electrostatic forces on the external monolayer of the liposome).

The next point that we must to clarify is which kind of amyloid species is inserted in the bilayer. Although different amyloid species, like oligomers, may contribute to amyloid toxicity and could be related to membrane poration and disruption [58] several studies point to tetramers and hexamers bound to membrane as the main responsibles of membrane poration and subsequent disruption [36]. As showed in Table 1, while k_n is clearly affected by liposomes and their net charge, k_e is practically unaltered by the presence of liposomes. This suggests that the mechanism behind the observed increase in lag time must originate from interferences taking place during the build up of small oligomers from monomers. This implies that are the soluble Aβ40, and not the mature fibrils, the species that interact with membranes. Also, the permeability studies (Fig. 5) allow us to affirm that the first membrane disruption events occur before amyloid aggregation can be observed, suggesting that membrane disruption could be due to the binding of initially soluble Aβ40 species, without a requirement for the formation of structured species. Determination of CL release shows a clear acceleration of membrane disruption in presence of charged liposomes, in which a higher concentration of Aβ peptide is expected to be fixed to the membrane.

The association of soluble Aβ peptide to the bilayer is also modulated by the colloidal characteristics of the peptide, which forms micelles at concentrations above 17.5 μM (the corresponding critical micellar concentration (*cmc*)) [59–61]. Such micelles can act as a reservoir of soluble material available for subsequent fibrillogenesis. It should be noted that, at peptide concentrations above the *cmc*, the lag time of the reaction remains essentially constant, but at peptide concentrations below 17.5 μM, the lag time correlates with the peptide concentration. The association (adsorption and/or insertion) of the Aβ40 to membranes may to reduce the effective concentration of soluble Aβ40 peptide in the solution, and, in such circumstances, the peptide concentration might become below the *cmc*, with a concomitant reduction in the nucleation rate of the reaction.

Other important finding derived from our study is the observation that the interaction of the peptide with liposomes results in an increase in the β-sheet content of the peptide. It is known from CD measurements that Aβ peptide has mainly random-coil secondary structure in solution, while it adopts β-sheet conformation oriented almost parallel to the monolayer surface in the adsorbed state [22,23]. The increase in β-sheet conformation in the presence of liposomes could be caused either by the adsorption of peptide on the external monolayer of liposomes, in which well-formed fibrils could grow, or by the nucleation delay that favours better peptide accommodation and well-formed amyloid fibrils. Factors that delay the nucleation process tend to increase the levels of β-sheet in unrelated amyloidogenic polypeptide systems. For instance, the influence of temperature on the nucleation rates correlates well with changes in the morphology of the fibrils formed by barstar, insulin, α-synuclein and HET-s (218–289) [62–65]. Also, for the PI3-SH3 domain, pH values promoting fast aggregation reactions were shown to cause disorganized fibrillar structures, whereas pH values allowing slow polymerization led to well-ordered fibrils [66]. The interaction of the β-peptide with neutral liposomes illustrate how the increase in the lag time results in amyloid species displaying higher inter-molecular β-sheets, whereas with negatively charged liposomes both scenarios (adsorption on the liposome and delay in the fibrillation rate) might contribute to increase in β-sheet conformation with negatively charged with.

Dye-binding assays have shown that the presence of liposomes reduces the concentration of fibrils. This is in agreement with an insertion of Aβ40 peptides into the membrane, since it would result in a reduction in the amount of soluble Aβ40 available to form amyloid fibrils. Interestingly enough, a direct relationship between the amount of amyloid-like aggregates and the negative charge increment can be observed. This is likely due to the fact that in neutral liposomes most of the membrane-associated peptide is hidden inside the liposome core and therefore not available for amyloid formation, whereas in negative liposomes, the peptide associated to the membrane is prone to undergo a conversion into amyloid structures. Since fibril concentration can be directly related to the amount of available soluble peptide [60], more amyloid fibril mass is expected when the aggregation is carried out without liposomes, a condition in which all soluble species are available for taking part in the polymerization reaction. As observed by TEM, the peptide–phospholipid interaction leads to a dramatic alteration in size and shape of fibrils. Long amyloid fibrils are observed in absence or presence of neutral liposomes. A reduction in fibril size is observed in presence of negatively charged liposomes. As noted above, in absence and in presence of neutral liposomes only the soluble species present in the bulk solution participate in amyloid polymerization, whereas extended peptides fixed in the liposome surface participate in the elongation process in presence of charged liposomes. Our data demonstrates that the way Aβ40 interacts with

membranes critically influences its morphological properties, which may have important functional consequences.

5. Conclusions

Aβ40 polymerization is delayed by the presence of liposomes in a charge-dependent manner. Interestingly, while the nucleation process is dramatically altered by the interaction with liposomes, the elongation step remains practically unaltered. This suggests that the interaction between Aβ40 and liposome surface occurs at the initial stage of the reaction, probably promoting the incorporation of soluble Aβ40 species into the liposomal membrane. The peptide–phospholipid interaction entailing a reduction in the available soluble Aβ40 in the bulk might be considered as the main factor accounting for reduction in nucleation rates.

The peptide–membrane interaction modulates the amyloid fibril morphology, structure and concentration, as well as membrane integrity. On the one hand, as observed in CL release, the accumulation of Aβ40 peptide on the bilayer favours membrane disruption. The disruption effect is clearly more prominent in the presence of negatively charged membranes, since the Aβ-liposome interaction is favoured by the presence of negative phospholipids in the bilayer. On the other hand, the secondary structure and size of the formed amyloid fibrils depend on the amount of anchored and/or surface-associated peptide to bilayer. The final concentration of amyloid-like species is directly related to the concentration of free Aβ peptide, whereas the increment in β-sheet structure is linked to reduction in nucleation rates and, the fibrils size seems to be connected to the concentration of surface-associated Aβ peptide.

Acknowledgements

This study was supported by grants BIO2007-68046 and MAT2009-13155-C04-03 (Spain's Ministerio de Ciencia e Innovación, MICINN) and grants BFU2010-14901 from the Ministerio de Ciencia e Innovación (Spain) and 2009-SGR-760 and 2009-CTP-00004 from AGAUR (Generalitat de Catalunya). R.S. was the beneficiary of an I3 contract (Universitat Autònoma de Barcelona-Generalitat de Catalunya). SV was granted an ICREA Academia award (ICREA).

Appendix A. Supplementary material

Supplementary material associated with this article can be found, in the online version, at doi:10.1016/j.biochi.2012.03.027.

References

[1] F. Chiti, C.M. Dobson, Protein misfolding, functional amyloid, and human disease, Annu. Rev. Biochem. 75 (2006) 333–366.
[2] C.M. Dobson, Protein misfolding, evolution and disease, Trends Biochem. Sci. 24 (1999) 329–332.
[3] P.J. Thomas, B.H. Qu, P.L. Pedersen, Defective protein folding as a basis of human disease, Trends Biochem. Sci. 20 (1995) 456–459.
[4] M. Hashimoto, E. Rockenstein, L. Crews, E. Masliah, Role of protein aggregation in mitochondrial dysfunction and neurodegeneration in Alzheimer's and Parkinson's diseases, Neuromolecular Med. 4 (2003) 21–36.
[5] M.L. Kerr, D.H. Small, Cytoplasmic domain of the beta-amyloid protein precursor of Alzheimer's disease: function, regulation of proteolysis, and implications for drug development, J. Neurosci. Res. 80 (2005) 151–159.
[6] B.A. Yankner, New clues to Alzheimer's disease: unraveling the roles of amyloid and tau, Nat. Med. 2 (1996) 850–852.
[7] W.L. Klein, G.A. Krafft, C.E. Finch, Targeting small Abeta oligomers: the solution to an Alzheimer's disease conundrum? Trends Neurosci. 24 (2001) 219–224.
[8] L. Mucke, E. Masliah, G.Q. Yu, M. Mallory, E.M. Rockenstein, G. Tatsuno, K. Hu, D. Kholodenko, K. Johnson-Wood, L. McConlogue, High-level neuronal expression of abeta 1–42 in wild-type human amyloid protein precursor transgenic mice: synaptotoxicity without plaque formation, J. Neurosci. 20 (2000) 4050–4058.
[9] C. Haass, D.J. Selkoe, Soluble protein oligomers in neurodegeneration: lessons from the Alzheimer's amyloid beta-peptide, Nat. Rev. Mol. Cell Biol. 8 (2007) 101–112.
[10] G. Merlini, V. Bellotti, Molecular mechanisms of amyloidosis, N. Engl. J. Med. 349 (2003) 583–596.
[11] M. Bokvist, F. Lindstrom, A. Watts, G. Grobner, Two types of Alzheimer's beta-amyloid (1–40) peptide membrane interactions: aggregation preventing transmembrane anchoring versus accelerated surface fibril formation, J. Mol. Biol. 335 (2004) 1039–1049.
[12] A. Chauhan, I. Ray, V.P. Chauhan, Interaction of amyloid beta-protein with anionic phospholipids: possible involvement of Lys28 and C-terminus aliphatic amino acids, Neurochem. Res. 25 (2000) 423–429.
[13] S. Dante, T. Hauss, A. Brandt, N.A. Dencher, Membrane fusogenic activity of the Alzheimer's peptide A beta(1–42) demonstrated by small-angle neutron scattering, J. Mol. Biol. 376 (2008) 393–404.
[14] C. Ege, K.Y. Lee, Insertion of Alzheimer's A beta 40 peptide into lipid monolayers, Biophys. J. 87 (2004) 1732–1740.
[15] E. Hellstrand, E. Sparr, S. Linse, Retardation of Abeta fibril formation by phospholipid vesicles depends on membrane phase behavior, Biophys. J. 98 (2010) 2206–2214.
[16] J.D. Knight, J.A. Williamson, A.D. Miranker, Interaction of membrane-bound islet amyloid polypeptide with soluble and crystalline insulin, Protein Sci. 17 (2008) 1850–1856.
[17] K. Matsuzaki, C. Horikiri, Interactions of amyloid beta-peptide (1–40) with ganglioside-containing membranes, Biochemistry 38 (1999) 4137–4142.
[18] J. McLaurin, A. Chakrabartty, Membrane disruption by Alzheimer beta-amyloid peptides mediated through specific binding to either phospholipids or gangliosides. Implications for neurotoxicity, J. Biol. Chem. 271 (1996) 26482–26489.
[19] R. Sabate, M. Gallardo, J. Estelrich, Spontaneous incorporation of beta-amyloid peptide into neutral liposomes, Colloids and Surfaces A 270–271 (2005) 13–17.
[20] Y. Sun, C.C. Lee, T.H. Chen, H.W. Huang, Kinetic process of beta-amyloid formation via membrane binding, Biophys. J. 99 (2010) 544–552.
[21] E. Terzi, G. Holzemann, J. Seelig, Alzheimer beta-amyloid peptide 25–35: electrostatic interactions with phospholipid membranes, Biochemistry 33 (1994) 7434–7441.
[22] E. Terzi, G. Holzemann, J. Seelig, Self-association of beta-amyloid peptide (1–40) in solution and binding to lipid membranes, J. Mol. Biol. 252 (1995) 633–642.
[23] E. Terzi, G. Holzemann, J. Seelig, Interaction of Alzheimer beta-amyloid peptide(1–40) with lipid membranes, Biochemistry 36 (1997) 14845–14852.
[24] J. Vargas, J.M. Alarcon, E. Rojas, Displacement currents associated with the insertion of Alzheimer disease amyloid beta-peptide into planar bilayer membranes, Biophys. J. 79 (2000) 934–944.
[25] M.J. Widenbrant, J. Rajadas, C. Sutardja, G.G. Fuller, Lipid-induced beta-amyloid peptide assemblage fragmentation, Biophys. J. 91 (2006) 4071–4080.
[26] T.L. Williams, I.J. Day, L.C. Serpell, The effect of Alzheimer's Abeta aggregation state on the permeation of biomimetic lipid vesicles, Langmuir 26 (2010) 17260–17268.
[27] P.T. Wong, J.A. Schauerte, K.C. Wisser, H. Ding, E.L. Lee, D.G. Steel, A. Gafni, Amyloid-beta membrane binding and permeabilization are distinct processes influenced separately by membrane charge and fluidity, J. Mol. Biol. 386 (2009) 81–96.
[28] N. Arispe, H.B. Pollard, E. Rojas, Giant multilevel cation channels formed by Alzheimer disease amyloid beta-protein [A beta P-(1–40)] in bilayer membranes, Proc. Natl. Acad. Sci. U. S. A. 90 (1993) 10573–10577.
[29] N. Arispe, E. Rojas, H.B. Pollard, Alzheimer disease amyloid beta protein forms calcium channels in bilayer membranes: blockade by tromethamine and aluminum, Proc. Natl. Acad. Sci. U. S. A. 90 (1993) 567–571.
[30] A. Demuro, E. Mina, R. Kayed, S.C. Milton, I. Parker, C.G. Glabe, Calcium dysregulation and membrane disruption as a ubiquitous neurotoxic mechanism of soluble amyloid oligomers, J. Biol. Chem. 280 (2005) 17294–17300.
[31] A. Deshpande, E. Mina, C. Glabe, J. Busciglio, Different conformations of amyloid beta induce neurotoxicity by distinct mechanisms in human cortical neurons, J. Neurosci. 26 (2006) 6011–6018.
[32] S. Florent-Bechard, C. Desbene, P. Garcia, A. Allouche, I. Youssef, M.C. Escanye, V. Koziel, M. Hanse, C. Malaplate-Armand, C. Stenger, B. Kriem, F.T. Yen-Potin, J.L. Olivier, T. Pillot, T. Oster, The essential role of lipids in Alzheimer's disease, Biochimie 91 (2009) 804–809.
[33] R. Kayed, Y. Sokolov, B. Edmonds, T.M. McIntire, S.C. Milton, J.E. Hall, C.G. Glabe, Permeabilization of lipid bilayers is a common conformation-dependent activity of soluble amyloid oligomers in protein misfolding diseases, J. Biol. Chem. 279 (2004) 46363–46366.
[34] J.I. Kourie, A.L. Culverson, P.V. Farrelly, C.L. Henry, K.N. Laohachai, Heterogeneous amyloid-formed ion channels as a common cytotoxic mechanism: implications for therapeutic strategies against amyloidosis, Cell Biochem. Biophys. 36 (2002) 191–207.
[35] H.A. Lashuel, D. Hartley, B.M. Petre, T. Walz, P.T. Lansbury Jr., Neurodegenerative disease: amyloid pores from pathogenic mutations, Nature 418 (2002) 291.
[36] H. Lin, R. Bhatia, R. Lal, Amyloid beta protein forms ion channels: implications for Alzheimer's disease pathophysiology, FASEB J. 15 (2001) 2433–2444.
[37] A. Quist, I. Doudevski, H. Lin, R. Azimova, D. Ng, B. Frangione, B. Kagan, J. Ghiso, R. Lal, Amyloid ion channels: a common structural link for protein-misfolding disease, Proc. Natl. Acad. Sci. U. S. A. 102 (2005) 10427–10432.

[38] X.D. Sun, Z.L. Mo, B.M. Taylor, D.E. Epps, A slowly formed transient conformer of Abeta(1–40) is toxic to inward channels of dissociated hippocampal and cortical neurons of rats, Neurobiol. Dis. 14 (2003) 567–578.
[39] R. Capone, F.G. Quiroz, P. Prangkio, I. Saluja, A.M. Sauer, M.R. Bautista, R.S. Turner, J. Yang, M. Mayer, Amyloid-beta-induced ion flux in artificial lipid bilayers and neuronal cells: resolving a controversy, Neurotox Res. 16 (2009) 1–13.
[40] S.M. Ennaceur, J.M. Sanderson, Micellar aggregates formed following the addition of hexafluoroisopropanol to phospholipid membranes, Langmuir 21 (2005) 552–561.
[41] L.D. Mayer, M.J. Hope, P.R. Cullis, Vesicles of variable sizes produced by a rapid extrusion procedure, Biochim. Biophys. Acta 858 (1986) 161–168.
[42] M. Biancalana, K. Makabe, A. Koide, S. Koide, Molecular mechanism of thioflavin-T binding to the surface of beta-rich peptide self-assemblies, J. Mol. Biol. 385 (2009) 1052–1063.
[43] R. Sabate, M. Gallardo, J. Estelrich, An autocatalytic reaction as a model for the kinetics of the aggregation of beta-amyloid, Biopolymers 71 (2003) 190–195.
[44] D.W. Fry, J.C. White, I.D. Goldman, Rapid separation of low molecular weight solutes from liposomes without dilution, Anal. Biochem. 90 (1978) 809–815.
[45] M. Morell, A. Espargaro, F.X. Aviles, S. Ventura, Detection of transient protein-protein interactions by bimolecular fluorescence complementation: the Abl-SH3 case, Proteomics 7 (2007) 1023–1036.
[46] G. Zandomeneghi, M.R. Krebs, M.G. McCammon, M. Fandrich, FTIR reveals structural differences between native beta-sheet proteins and amyloid fibrils, Protein Sci. 13 (2004) 3314–3321.
[47] V. Castillo, S. Ventura, R. Sabate, Dye-liposome interactions: dye localization in neutral lipid bilayers, Int. Rev. Biophysical Chem. 1 (2010) 7–13.
[48] R. Khurana, C. Coleman, C. Ionescu-Zanetti, S.A. Carter, V. Krishna, R.K. Grover, R. Roy, S. Singh, Mechanism of thioflavin T binding to amyloid fibrils, J. Struct. Biol. 151 (2005) 229–238.
[49] M.J. Sanchez-Martin, P. Urban, M. Pujol, I. Haro, M.A. Alsina, M.A. Busquets, Biophysical investigations of GBV-C E1 peptides as potential inhibitors of HIV-1 fusion peptide, Chem. Phys. Chem 12 (2011) 2816–2822.
[50] B. Kurganov, M. Doh, N. Arispe, Aggregation of liposomes induced by the toxic peptides Alzheimer's Abetas, human amylin and prion (106–126): facilitation by membrane-bound GM1 ganglioside, Peptides 25 (2004) 217–232.
[51] E. Casals, A.M. Galan, G. Escolar, M. Gallardo, J. Estelrich, Physical stability of liposomes bearing hemostatic activity, Chem. Phys. Lipids 125 (2003) 139–146.
[52] A. Relini, O. Cavalleri, R. Rolandi, A. Gliozzi, The two-fold aspect of the interplay of amyloidogenic proteins with lipid membranes, Chem. Phys. Lipids 158 (2009) 1–9.
[53] E.Y. Chi, C. Ege, A. Winans, J. Majewski, G. Wu, K. Kjaer, K.Y. Lee, Lipid membrane templates the ordering and induces the fibrillogenesis of Alzheimer's disease amyloid-beta peptide, Proteins 72 (2008) 1–24.
[54] C.M. Yip, A.A. Darabie, J. McLaurin, Abeta42-peptide assembly on lipid bilayers, J. Mol. Biol. 318 (2002) 97–107.
[55] C.M. Yip, J. McLaurin, Amyloid-beta peptide assembly: a critical step in fibrillogenesis and membrane disruption, Biophys. J. 80 (2001) 1359–1371.
[56] N. Demeester, G. Baier, C. Enzinger, M. Goethals, J. Vandekerckhove, M. Rosseneu, C. Labeur, Apoptosis induced in neuronal cells by C-terminal amyloid beta-fragments is correlated with their aggregation properties in phospholipid membranes, Mol. Membr. Biol. 17 (2000) 219–228.
[57] M. Kawahara, Y. Kuroda, N. Arispe, E. Rojas, Alzheimer's beta-amyloid, human islet amylin, and prion protein fragment evoke intracellular free calcium elevations by a common mechanism in a hypothalamic GnRH neuronal cell line, J. Biol. Chem. 275 (2000) 14077–14083.
[58] D.M. Walsh, I. Klyubin, J.V. Fadeeva, M.J. Rowan, D.J. Selkoe, Amyloid-beta oligomers: their production, toxicity and therapeutic inhibition, Biochem. Soc. Trans. 30 (2002) 552–557.
[59] A. Lomakin, D.S. Chung, G.B. Benedek, D.A. Kirschner, D.B. Teplow, On the nucleation and growth of amyloid beta-protein fibrils: detection of nuclei and quantitation of rate constants, Proc. Natl. Acad. Sci. U. S. A. 93 (1996) 1125–1129.
[60] R. Sabate, J. Estelrich, Evidence of the existence of micelles in the fibrillogenesis of beta-amyloid peptide, J. Phys. Chem. B 109 (2005) 11027–11032.
[61] W. Yong, A. Lomakin, M.D. Kirkitadze, D.B. Teplow, S.H. Chen, G.B. Benedek, Structure determination of micelle-like intermediates in amyloid beta-protein fibril assembly by using small angle neutron scattering, Proc. Natl. Acad. Sci. U. S. A. 99 (2002) 150–154.
[62] S. Kumar, S.K. Mohanty, J.B. Udgaonkar, Mechanism of formation of amyloid protofibrils of barstar from soluble oligomers: evidence for multiple steps and lateral association coupled to conformational conversion, J. Mol. Biol. 367 (2007) 1186–1204.
[63] L. Nielsen, R. Khurana, A. Coats, S. Frokjaer, J. Brange, S. Vyas, V.N. Uversky, A.L. Fink, Effect of environmental factors on the kinetics of insulin fibril formation: elucidation of the molecular mechanism, Biochemistry 40 (2001) 6036–6046.
[64] R. Sabate, V. Castillo, A. Espargaro, S.J. Saupe, S. Ventura, Energy barriers for HET-s prion forming domain amyloid formation, FEBS J. 276 (2009) 5053–5064.
[65] V.N. Uversky, A.L. Fink, Conformational constraints for amyloid fibrillation: the importance of being unfolded, Biochim. Biophys. Acta 1698 (2004) 131–153.
[66] J. Zurdo, J.I. Guijarro, J.L. Jimenez, H.R. Saibil, C.M. Dobson, Dependence on solution conditions of aggregation and amyloid formation by an SH3 domain, J. Mol. Biol. 311 (2001) 325–340.

BLOQUE II: **Estudio de la agregación proteica *in vivo.* Propiedades biofísicas de los cuerpos de inclusión.**

FEBS Letters 582 (2008) 3669–3673

Kinetic and thermodynamic stability of bacterial intracellular aggregates

Alba Espargaró[1], Raimon Sabaté[1], Salvador Ventura*

Departament de Bioquímica i Biologia Molecular and Institut de Biotecnologia i de Biomedicina, Universitat Autònoma de Barcelona, 08193 Bellaterra, Barcelona, Spain

Received 4 July 2008; revised 4 September 2008; accepted 25 September 2008

Available online 7 October 2008

Edited by Jesus Avila

Abstract Protein aggregation is related to many human disorders and constitutes a major bottleneck in protein production. However, little is known about the conformational properties of in vivo formed aggregates and how they relate to the specific polypeptides embedded in them. Here, we show that the kinetic and thermodynamic stability of the inclusion bodies formed by the Aβ42 Alzheimer peptide and its Asp19 alloform differ significantly and correlate with their amyloidogenic propensity and solubility inside the cell. Our results indicate that the nature of the polypeptide chain determines the specific conformational properties of intracellular aggregates. This implies that different protein inclusions impose dissimilar challenges to the cellular quality-control machinery.

Keywords: Inclusion body; Protein aggregation; Protein folding; Protein stability; Recombinant protein expression

1. Introduction

Aggregation of misfolded proteins that escape the cellular quality-control mechanisms is a common feature during recombinant protein production. Importantly, this process is also linked to the onset of a wide range of debilitating and increasingly prevalent diseases as Alzheimer, Parkinson, Huntington or prion diseases [1]. In this way, the deposition of β-amyloid peptide (Aβ), a hydrophobic 40–43 amino acid peptide, appears as a major causative agent of Alzheimer's disease [2,3].

Not all regions of a polypeptide are equally important for determining its aggregation tendency [4]. In this way, very short specific amino acid stretches can act as facilitators or inhibitors of amyloid fibril formation [5,6]. The presence of aggregation-prone regions has been described in most of the peptides and proteins underlying neurodegenerative and systemic amyloidogenic disorders [7]. In Aβ peptide, the central hydrophobic core (CHC) (Leu17-Ala21) plays a crucial role in its folding, assembly and amyloid fibril structure [8]. Accordingly, we have shown that substitution of central residue in this region (Phe19) by Asp strongly reduces the in vitro amyloid propensity of Aβ [9].

*Corresponding author. Fax: +34 93 5811264.
E-mail address: salvador.ventura@uab.es (S. Ventura).

[1]These authors have contributed equally to this work.

Intracellular aggregates and specifically the inclusion bodies (IBs) formed inside bacterial cells during the expression of eukaryotic proteins have been traditionally regarded as non-specific associations of misfolded polypeptides. In contrast to amyloid fibrils, the extended view of IBs as amorphous supramolecular structures has precluded the detailed characterization of their conformational properties and how they relate to the specific proteins inside them. Nevertheless, it has been demonstrated that the intracellular aggregates formed by different proteins share significant internal order and secondary structure content [10,11]. Moreover, using a fusion of the amyloidogenic Aβ42 species to green fluorescent protein (GFP) as a model system we have recently shown that in vivo protein aggregation inside bacteria displays a remarkable specificity that depends on the establishment of selective molecular interactions and results in the formation of oligomeric and fibrillar structures with conformational properties very similar to those of amyloid fibrils [12]. Being stabilized by rather selective contacts, it is likely that, as it happens in globular proteins or amyloid fibrils, the IBs formed by different proteins should display specific stability features. To address this question, here we characterize the thermodynamic and, for the first time, the kinetic stability of intracellular bacterial aggregates. The properties of the IBs formed by Aβ42-GFP (WT) and by a variant of the fusion containing a single Phe19Asp mutation in the Aβ42 moiety (F19D) are compared.

2. Materials and methods

2.1. Protein expression

The plasmids encoding for Aβ42-GFP and the Phe19Asp mutant are as previously described [13,14]. Competent *Escherichia coli* BL21(D3) cells were transformed with plasmids encoding for the desired fusion proteins and incubated in Luria–Bertani medium (LB) with the appropriate antibiotic (50 μg/ml kanamycin) at 37 °C. Recombinant gene expression was induced with 1 mM of isopropyl-1-thio-b-d-galactopyranoside (IPTG) when the A_{600nm} reached 0.6. Cells were cultured at 37 °C for 16 additional hours.

2.2. IBs purification

IBs are purified from overnight cell extracts after the induction of gene expression, by detergent-based procedures as described [15]. Briefly, cells were harvested by centrifugation at $12000 \times g$ (at 4 °C) for 15 min and resuspended in 200 μL of lysis buffer (50 mM Tris–HCl, pH 8, 1 mM EDTA, 100 mM NaCl), plus 30 μL of 100 mM protease inhibitor PMSF and 6 μL of 10 mg/mL lysozyme. After 30 min of incubation at 37 °C under gentle agitation, NP-40 was added at 1% (v/v) and the mixture incubated at 4 °C for 30 min. Then, 3 μL of DNase I and RNase from 1 mg/mL stock (25 μg/mL final concentration) and 3 μL of 1 M $MgSO_4$ were added and the resulting mixture was further incubated at 37 °C for 30 min. Protein aggregates were separated by centrifugation at $12000 \times g$ for 15 min at 4 °C. Finally, IBs were

0014-5793/$34.00
doi:10.1016/j.febslet.2008.09.049

washed once with the same buffer containing 0.5% Triton X-100 and once with sterile PBS. After a final centrifugation at $12000 \times g$ for 15 min, pellets were stored at −80 °C until analysis.

2.3. Thermodynamic and kinetic stabilities

For stability assays, purified IBs were prepared at $OD_{350nm} = 1$ in phosphate-buffered saline (PBS) solution at pH 7.0 containing selected concentrations of guanidine hydrochloride (Gdn · HCl) ranging from 0 to 4 M. For equilibrium denaturation experiments, the reactions were allowed to reach equilibrium by incubating them for 20 h at room temperature. The fraction of solubilized protein (f_D) was calculated from the fitted values using equation: $f_D = 1 - ((y_D - y)/(y_D - y_N))$, where y_D and y_N are the absorbance at 350 nm of the solubilized and aggregated protein, respectively, and y is the absorbance of protein as a function of denaturant concentration. A non-linear least-squares analysis was used to fit the denaturation curves to the equation: $y = ((y_N + m_N \cdot [D]) + (y_D + m_D \cdot [D])\exp(A \cdot ([D] - m_{1/2})/R \cdot T))/(1 + \exp(A \cdot ([D] - m_{1/2})/R \cdot T))$, where y is the observed absorbance at 350 nm, y_N and y_D are the intercepts and m_N and m_D are the slopes of the pre- and post-transition baselines, $[D]$ is the guanidine hydrochloride (Gdn · HCl) concentration, $m_{1/2}$ is the Gdn · HCl concentration at the midpoint of the curve, and A is a constant generated by the fitting [16–18]. For kinetic measurements a concentrated IBs and Gdn · HCl solutions in PBS, pH 7.0, were mixed rapidly to obtain an $OD_{350nm} = 1$ and the desired denaturant concentration. The solubilization reaction was monitored for 100 min after mixing by measuring the changes in OD_{350nm} in a Cary-400 Varian spectrophotometer (Varian Inc.). Double-exponential decay curves were fitted to the data using GraphPad Prism 3.02 (GraphPad Software, La Jolla, CA, USA) and apparent rate constants were derived from these regressions.

2.4. Western blots

For Western blot, the protein cellular extract was lysed using Novagen Bug Buster protein extraction reagent with benzonase nuclease and protease inhibitory cocktail set III (Calbiochem). Insoluble and soluble fractions were resolved on 15% SDS–PAGE gels, transferred on to PVDF membranes, and recombinant proteins detected with a polyclonal anti-GFP antibody. The membranes were developed with the ECL method [19].

2.5. GFP relative fluorescence determination and Thermal denaturation

Emission spectra of GFP in WT and F19D IBs were measured on a Varian spectrofluorimeter (Cary Eclipse) from 500 to 600 nm at 25 °C using an excitation wavelength of 488 nm. A slit width of 5 nm was used and the maximum of emission, at 512 nm, was recorded. Thermal transition curves were obtained at a heating rate of 1 °C/min by measuring the GFP emission at 512 nm after excitation at 488 nm.

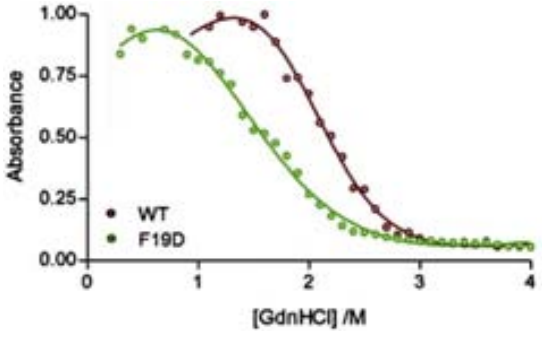

Fig. 1. Stability of WT and F19D IBs in front of Gnd · HCl denaturation at equilibrium monitored by changes in turbidity at 350 nm.

2.6. Secondary structure determination

Protein inclusion bodies purified as described above were washed twice with distilled water, 10 μl of suspension were deposited on the spectrometer window and dried at room temperature for 10 min for spectroscopy measurements. The purity of IBs was routinely checked by SDS–PAGE and Coomassie staining. ATR FT-IR spectroscopy analysis samples of IBs were performed using a Bruker Tensor 27 FT-IR Spectrometer (Bruker Optics Inc.) with a Golden Gate MKII ATR accessory. Each spectrum consists of 125 independent scans, measured at a spectral resolution of $2\ cm^{-1}$ within the 1800–1500 cm^{-1} range. All spectral data were acquired and normalized using the OPUS MIR Tensor 27 software. The fourth derivative FTIR spectra of IBs indicate that they were constituted by four principal bands. Hence, FTIR spectra were fitted to four overlapping Gaussian curves and the amplitude, center and bandwidth at half of the maximum amplitude and area of each Gaussian function were calculated using a non-linear peak fitting program (PeakFit package, Systat Software, San Jose, CA, USA). Second derivatives of the spectra were also used to determine the frequencies at which the different spectral components were located.

3. Results and discussion

For globular proteins, the study of their unfolding transition induced by denaturants is one of the most useful ways to address their stability. In the present work, we have used this approach to study the unfolding (i.e. solubilization) of IBs. Equilibrium denaturation was measured by monitoring the IBs absorbance at 350 nm after incubation at selected Gdn · HCl concentrations. This chaotropic agent has been used recently to study the resistance to solubilization of the IBs and thermal aggregates formed by different proteins [20,21]. We assumed a two-state mechanism in which the protein is either in an aggregated state that contributes to turbidity or in a soluble state with no contribution to the signal, independently of the conformational properties of the polypeptides in these states. Although this assumption represents a simplification of the effect of the chaotropic agent on the aggregates, the curves could be fitted accurately to a two states model. Accordingly, a cooperative unfolding transition could be observed for both IBs (Fig. 1). The free energy of the reaction (ΔG) was calculated and found to vary linearly with Gdn·HCl concentration using the linear extrapolation model:

$$\Delta G = \Delta G(H_2O) - m(\text{Gdn} \cdot \text{HCl})$$

where m measures the cooperativity of the transition and $\Delta G(H_2O)$ is the free energy change in the absence of denaturant [16,18]. From the data it can be clearly inferred that the aggregates formed by these two closely related proteins exhibit dramatic differences in the thermodynamic stability. WT IBs displayed a much higher stability against chemical denaturation as well as a higher unfolding cooperativity reaction than

Table 1
Kinetic and equilibrium denaturation parameters of Aβ42-GFP and F19D-GFP inclusion bodies.

Protein type	Thermodynamic parameters		Kinetic parameters				
	ΔG/kJ mol^{-1}	m/M^{-1}	K_U/10^3 min^{-1}	ΔG_U/kJ mol^{-1}	m_U/kJ mol^{-1} M^{-1}	$t_{1/2}$/days	k_F^*/10^3 min^{-1}
WT	−16.74	2.0	0.19	−21.28	2.08	3.7	159.59
F19D	−5.11	1.0	0.79	−17.70	1.67	0.9	6.20

F19D ones (Table. 1). In globular proteins, the unfolding cooperativity, expressed as m value, correlates very strongly with the amount of new protein surface exposed to solvent upon unfolding. By analogy, the higher m value of WT IBs suggests that the polypeptide chains inside these aggregates are more protected from the solvent before denaturation, and therefore more compacted than those in the mutant IBs.

The kinetic stability of an aggregate is a measure of how rapidly it is unfolded (i.e. solubilized) and corresponds to the activation free energy (ΔG_U) of the process. The kinetic stability, rather than equilibrium stability, is likely to be relevant for the in vivo fate of protein aggregates, since it is related to their half-lives and probably to the energetic barrier that chaperones have to face to disaggregate them. Surprisingly, no data on the kinetic stability properties of in vivo aggregates are available to date.

Kinetic chemical denaturation of IBs at different denaturant concentration (Fig. 2) has been analyzed using a classical two-phase exponential decay curve and the kinetic constants (k_1 and k_2) have been determined [22].

Fitting of the kinetic data traces (Fig. 3) to a two-states transition allowed the determination of the denaturation rates (k_U), the kinetic stability (ΔG_U), as well as the estimated half-life ($t_{1/2}$) and the kinetic m-values for the unfolding reaction (m_U) for both aggregates (Table 1).

Intracellular aggregates turned to have large activation free energies to unfolding. When compared with globular proteins, usually with $t_{1/2}$ between seconds and hours, the solubilization of IBs is a slow process with $t_{1/2}$ in the order of days. These high barriers to disaggregation account for their prevalent accumulation inside the cells.

In agreement with the equilibrium data, the kinetic barrier to unfolding and the cooperativity of the reaction were significantly lower for the mutant IBs. As a consequence, their solubilization reaction is strongly accelerated, resulting in a 4-fold shorter half-life than WT IBs. This suggests that, in the cell,

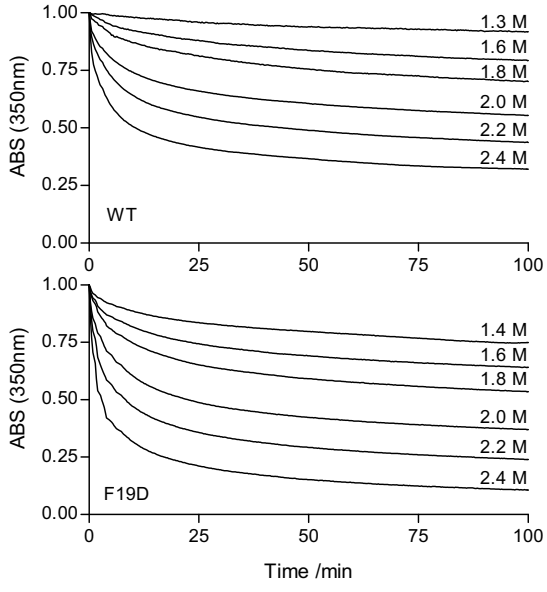

Fig. 2. Kinetic chemical denaturation curves of WT and F19D IBs at different Gdn · HCl concentration monitored by a time dependent decrease of turbidity at 350 nm.

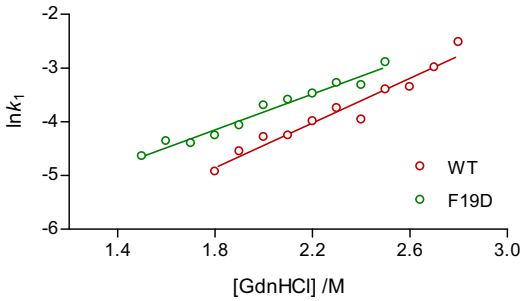

Fig. 3. Unfolding kinetic rates of WT and F19D IBs determined by linear extrapolation of the fast rate constants of their respective kinetic denaturation curves at different Gdn · HCl concentrations.

the proteins embedded in F19D IBs can be more easily solubilized, either passively or by the disaggregating action of molecular chaperones, than those in WT aggregates. Confirming this hypothesis, although the majority of both protein fusions is located in the insoluble fraction, a higher level of soluble protein was detected in cells expressing the F19D fusion than in those expressing the WT form, 1.2% and 0.3% of total recombinant protein, respectively, as quantified by Western blotting against the GFP moiety and densitometry (Fig. 4A).

Although the kinetics of IBs formation (i.e. aggregation) cannot be experimentally addressed in vitro, they can be theoretically inferred from the unfolding thermodynamic and kinetic stabilities of the aggregates, assuming a two-state model ($\Delta G = -RT\ln(k_F^*/k_U)$). The theoretical aggregation kinetic constant (k_F^*) for WT fusion is about 25-fold higher than in the F19D one. These values are clearly an approximation to the real constants, but they still suggest a significantly decreased aggregation propensity in the mutant fusion, in good agreement with the in vivo aggregation rates and the amyloidogenicity of both Aβ42 peptide variants [9].

We have shown previously, that during IBs formation, aggregation and folding reactions compete inside the cell in such a way that the fluorescence emission of IBs relates to the time the GFP fusion was soluble after its synthesis and before to its aggregation in the cytoplasm [23]. The mutant IBs express about 5-fold higher fluorescence than the WT ones (Fig. 4B). This indicates that F19D aggregation into IBs is a slower in vivo reaction than this of the WT form and supports the significance of the theoretically derived aggregation kinetic constants.

The stability of functional GFP domains inside both IBs contexts was measured by monitoring the loss of the fluorescence signal upon thermal denaturation. A melting point of ~85 °C was obtained for both fusions (Fig. 4C). These results are in agreement with those obtained using differential scanning calorimetry on purified and soluble GFP [24] and suggest a native structure in the GFP moiety that contributes little to the observed differential stability of the aggregates. Therefore, it is suggested that the different contacts established by the two Aβ42 peptides, and specifically those in the CHC region, account for the striking difference in consistence of both IBs.

Fourier-transform infrared (FTIR) spectroscopy has proved to be a powerful tool for investigation of the structural characteristics of aggregated proteins. We used this technique to further analyze the structure of both types of aggregates. The deconvoluted FTIR spectra as well as the second

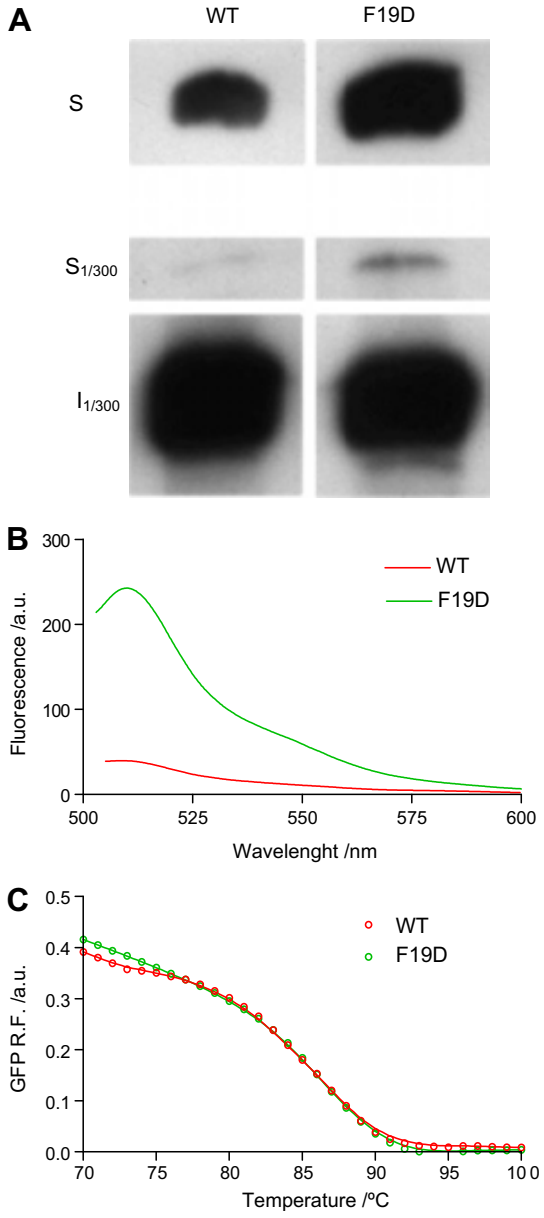

Fig. 4. Conformational properties of WT and F19D IBs. (A) Western blot of the soluble fraction of cells expressing WT and F19D fusions detected with anti-GFP antibody (up). 1/300 dilution of the soluble fraction (middle). 1/300 dilution of the correspondent insoluble fraction (down). (B) GFP fluorescence emission spectra of IBs excited at 488 nm. (C) Thermal denaturalization curves of GFP embedded in IBs followed by measuring the relative changes in GFP fluorescence emission.

derivative of the absorbance spectra are shown in Fig. 5. The F19D and WT IBs spectra are very similar, the amide I region contains four main components at 1692, 1679, at 1650, and at 1625 cm^{-1} indicating a dominance of beta conformations together with unordered components. In fact, the bands at 1692, 1679 and 1625 cm^{-1} correspond to an intermolecular β-structure similar to that present in amyloid fibrils (Fig. 5). This data indicates an overall common backbone polypeptide conformation in both aggregates and suggests that the stability of IBs is modulated by subtle changes in packing driven by specific side-chain interactions.

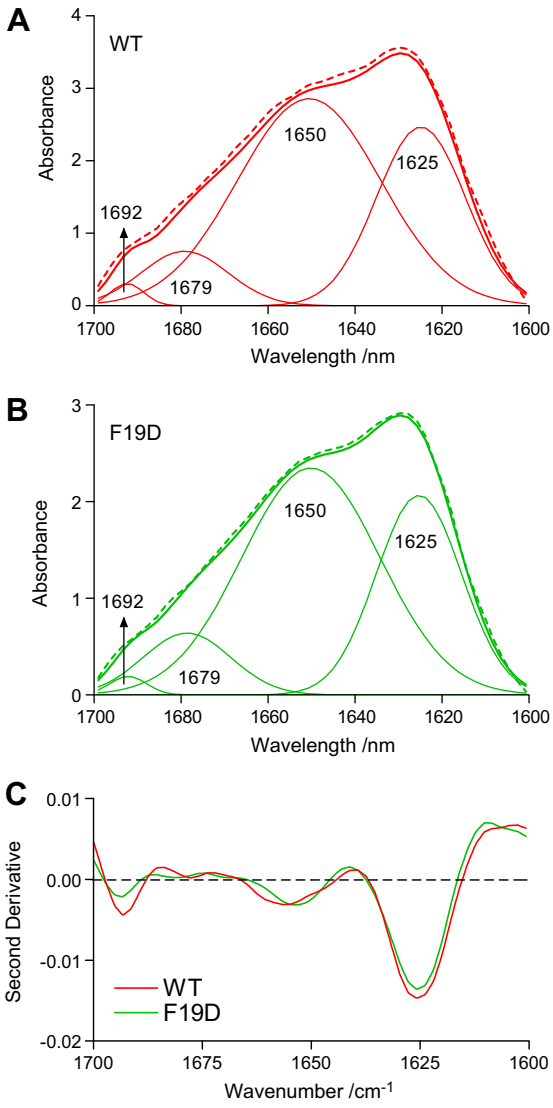

Fig. 5. Analysis of the secondary structure of IBs by ATR-FTIR spectroscopy. Absorbance FTIR spectra of the amide I′ region of WT (A) and F19D (B) (solid thick lines) showing the component bands (solid thin lines). The sum (dashed lines) of individual spectral components after Fourier self-deconvolution closely matches the experimental data. (C) Second derivatives of the respective absorbance spectra shown in panels A and B.

4. Conclusions

Overall, our results argue that the intracellular aggregates formed by different polypeptides in vivo cannot be treated as a homogeneous entity, even if they all present a common morphology and amyloid-like secondary structure content. Like in amyloid fibrils or in globular proteins, the fine structure of these aggregates depends on the specific intrinsic properties of the embedded polypeptides, as demonstrated by the fact that a point mutation is able to highly destabilize the whole aggregate ensemble. Importantly, a major energy consuming step for in vivo disaggregation by the action of molecular chaperones consists in the separation of individual polypeptide chains from aggregates and their unfolding. A recent study using in vitro protein aggregates formed under different

protein denaturation conditions suggest that the action of chaperones depend on the specific structural properties of the aggregates [25]. Our demonstration that in in vivo formed protein inclusions polypeptide chains are glued by differential and specific interactions suggests that the aggregates of different proteins impose dissimilar challenges to the cellular quality-control machinery. Our data have important implications for conformational diseases, because they suggest that single point genetic mutations cannot only increase the aggregation propensity of a protein, but at the same time they might result in the formation of significantly more resistant and difficult to handle intracellular aggregates. In addition, the correlation between amyloid propensity and IBs stability observed here for the Alzheimer related Aβ42 peptide validates bacterial systems as fast, simple and biologically relevant experimental models to study protein aggregation.

Acknowledgements: We gratefully thank Dr. Francesc X. Aviles and Dr. Josep Vendrell for lab facilities. We thank Natalia S. de Groot for cloning the Ab42-GFP fusions. This work has been supported by Grants BIO2007-68046 (MEC, Spain) and 2005-SGR00037 (Generalitat de Catalunya).

References

[1] Polverino de Laureto, P. et al. (2003) Protein aggregation and amyloid fibril formation by an SH3 domain probed by limited proteolysis. J. Mol. Biol. 334, 129–141.
[2] Glenner, G.G. and Wong, C.W. (1984) Alzheimer's disease: initial report of the purification and characterization of a novel cerebrovascular amyloid protein. Biochem. Biophys. Res. Commun. 120, 885–890.
[3] Walsh, D.M. and Selkoe, D.J. (2004) Deciphering the molecular basis of memory failure in Alzheimer's disease. Neuron 44, 181–193.
[4] de Groot, N., Pallares, I., Aviles, F., Vendrell, J. and Ventura, S. (2005) Prediction of "hot spots" of aggregation in disease-linked polypeptides. BMC Struct. Biol. 5, 18.
[5] Ivanova, M.I., Thompson, M.J. and Eisenberg, D. (2006) A systematic screen of beta(2)-microglobulin and insulin for amyloid-like segments. Proc. Natl. Acad. Sci. USA 103, 4079–4082.
[6] Ventura, S. et al. (2004) Short amino acid stretches can mediate amyloid formation in globular proteins: the Src homology 3 (SH3) case. Proc. Natl. Acad. Sci. USA 101, 7258–7263.
[7] Conchillo-Sole, O., de Groot, N.S., Aviles, F.X., Vendrell, J., Daura, X. and Ventura, S. (2007) AGGRESCAN: a server for the prediction and evaluation of "hot spots" of aggregation in polypeptides. BMC Bioinformatics 8, 65.
[8] Wurth, C., Guimard, N.K. and Hecht, M.H. (2002) Mutations that reduce aggregation of the Alzheimer's Abeta42 peptide: an unbiased search for the sequence determinants of Abeta amyloidogenesis. J. Mol. Biol. 319, 1279–1290.
[9] de Groot, N.S., Aviles, F.X., Vendrell, J. and Ventura, S. (2006) Mutagenesis of the central hydrophobic cluster in Abeta42 Alzheimer's peptide. Side-chain properties correlate with aggregation propensities.. FEBS J. 273, 658–668.
[10] Doglia, S.M., Ami, D., Natalello, A., Gatti-Lafranconi, P. and Lotti, M. (2008) Fourier transform infrared spectroscopy analysis of the conformational quality of recombinant proteins within inclusion bodies. Biotechnol. J. 3, 193–201.
[11] Carrio, M., Gonzalez-Montalban, N., Vera, A., Villaverde, A. and Ventura, S. (2005) Amyloid-like properties of bacterial inclusion bodies. J. Mol. Biol. 347, 1025–1037.
[12] Morell, M., Bravo, R., Espargaro, A., Sisquella, X., Avilés, F.X., X., F.-B. and Ventura, X. (2008) Inclusion Bodies: specificity in their aggregation process and amyloid-like structure. Biochim. Biophys. Acta. 1783, 1815–1825.
[13] Wurth, C., Guimard, N.K. and Hecht, M.H. (2002) Mutations that reduce aggregation of the Alzheimer's Abeta42 peptide: an unbiased search for the sequence determinants of Abeta amyloidogenesis. J. Mol. Biol. 319, 1279–1290.
[14] Garcia-Fruitos, E., Gonzalez-Montalban, N., Morell, M., Vera, A., Ferraz, R.M., Aris, A., Ventura, S. and Villaverde, A. (2005) Aggregation as bacterial inclusion bodies does not imply inactivation of enzymes and fluorescent proteins. Microb. Cell Fact. 4, 27.
[15] Carrio, M.M., Cubarsi, R. and Villaverde, A. (2000) Fine architecture of bacterial inclusion bodies. FEBS Lett. 471, 7–11.
[16] Pace, C.N. et al. (1998) Conformational stability and thermodynamics of folding of ribonucleases Sa, Sa2 and Sa3. J. Mol. Biol. 279, 271–286.
[17] Koditz, J., Ulbrich-Hofmann, R. and Arnold, U. (2004) Probing the unfolding region of ribonuclease A by site-directed mutagenesis. Eur. J. Biochem. 271, 4147–4156.
[18] Santoro, M.M. and Bolen, D.W. (1988) Unfolding free energy changes determined by the linear extrapolation method. 1. Unfolding of phenylmethanesulfonyl alpha-chymotrypsin using different denaturants.. Biochemistry 27, 8063–8068.
[19] Morell, M., Espargaro, A., Aviles, F.X. and Ventura, S. (2007) Detection of transient protein–protein interactions by bimolecular fluorescence complementation: the Abl-SH3 case. Proteomics 7, 1023–1036.
[20] Rinas, U., Hoffmann, F., Betiku, E., Estape, D. and Marten, S. (2007) Inclusion body anatomy and functioning of chaperone-mediated in vivo inclusion body disassembly during high-level recombinant protein production in *Escherichia coli*. J. Biotechnol. 127, 244–257.
[21] de Groot, N.S. and Ventura, S. (2006) Effect of temperature on protein quality in bacterial inclusion bodies. FEBS Lett. 580, 6471–6476.
[22] Ventura, S., Vega, M.C., Lacroix, E., Angrand, I., Spagnolo, L. and Serrano, L. (2002) Conformational strain in the hydrophobic core and its implications for protein folding and design. Nat. Struct. Biol. 9, 485–493.
[23] de Groot, N.S. and Ventura, S. (2006) Protein activity in bacterial inclusion bodies correlates with predicted aggregation rates. J. Biotechnol. 125, 110–113.
[24] Nagy, A., Malnasi-Csizmadia, A., Somogyi, B. and Lorinczy, D. (2004) Thermal stability of chemically denatured green fluorescent protein (GFP). A preliminary study. Thermochim. Acta 410, 161–163.
[25] Lewandowska, A., Matuszewska, M. and Liberek, K. (2007) Conformational properties of aggregated polypeptides determine ClpB-dependence in the disaggregation process. J. Mol. Biol. 371, 800–811.

Microbial Cell Factories

BioMed Central

Research

Characterization of the amyloid bacterial inclusion bodies of the HET-s fungal prion

Raimon Sabaté*[1], Alba Espargaró[1], Sven J Saupe[2] and Salvador Ventura*[1]

Address: [1]Departament de Bioquímica I Biologia Molecular and Institut de Biotecnologia i de Biomedicina, Universitat Autònoma de Barcelona, 08193 Bellaterra, Barcelona, Spain and [2]Laboratoire de Génétique Moléculaire des Champignons, IBGC, UMR5095, Université Victor Segalen Bordeaux 2 et CNRS, 1 rue Camille Saint-Saëns, 33077 Bordeaux Cedex, France

Email: Raimon Sabaté* - Raimon.Sabate@uab.cat; Alba Espargaró - Alba.Espargaro@campus.uab.cat; Sven J Saupe - sven.saupe@ibgc.u-bordeaux2.fr; Salvador Ventura* - salvador.ventura@uab.es

* Corresponding authors

Published: 28 October 2009

Microbial Cell Factories 2009, **8**:56 doi:10.1186/1475-2859-8-56

Received: 20 July 2009
Accepted: 28 October 2009

This article is available from: http://www.microbialcellfactories.com/content/8/1/56

Abstract

The formation of amyloid aggregates is related to the onset of a number of human diseases. Recent studies provide compelling evidence for the existence of related fibrillar structures in bacterial inclusion bodies (IBs). Bacteria might thus provide a biologically relevant and tuneable system to study amyloid aggregation and how to interfere with it. Particularly suited for such studies are protein models for which structural information is available in both IBs and amyloid states. The only high-resolution structure of an infectious amyloid state reported to date is that of the HET-s prion forming domain (PFD). Importantly, recent solid-state NMR data indicates that the structure of HET-s PFD in IBs closely resembles that of the infectious fibrils. Here we present an exhaustive conformational characterization of HET-s IBs in order to establish the aggregation of this prion in bacteria as a consistent cellular model in which the effect of autologous or heterologous protein quality machineries and/or anti-aggregational and anti-prionic drugs can be further studied.

Background

Protein misfolding and aggregation have become very active areas of research during the last decade. The large efforts devoted in this period to understand the determinants of polypeptide aggregation are justified by the tight connection between the formation of insoluble protein deposits in human tissues and the development of dozens of conformational diseases. These protein deposits are constituted mainly by fibrillar structures known as amyloids with a common cross-β supramolecular organisation [1]. Protein aggregation is also an important problem in biotechnology because during recombinant expression in prokaryotic systems many heterologous proteins misfold and accumulate as insoluble protein deposits named inclusion bodies (IBs) limiting in this way the use of bacteria for the production of therapeutically relevant proteins [2].

IBs formation has long been regarded as an unspecific process relaying on the establishment of hydrophobic contacts [3]. However, an increasing body of evidence suggests that bacterial IBs share a number of common features with the highly ordered and pathogenic amyloid fibrils linked to human diseases [4]. Both processes have been shown to be nucleation driven, sequence specific and lead to the formation of β-sheet enriched structures. However, the detailed structural characterisation of bacterial aggregates is extremely challenging and to which

extend a polypeptide embedded in IBs and the same molecule polymerized into amyloids are structurally related has remained essentially unknown.

Prions represent a particular subclass of amyloids for which the aggregation process becomes self-perpetuating *in vivo* and thus infectious [5]. Fungal prions are infectious filamentous polymers of proteins. Among these prions are the [*PSI*$^+$], [URE3] and [*PIN*$^+$] yeast prions [6,7] and HET-s that is a prion of the filamentous fungus *Podospora anserina* involved in a fungal specific non-self discrimination phenomenon [8]. HET-s is a 289 residues polypeptide. Residues 1-227 form a well-folded globular domain in the soluble HET-s conformation. In contrast the C-terminal region is highly flexible and unstructured. Previous studies have identified the C-terminal region of HET-s spanning residues 218 to 289 as the prion forming domain (PFD) responsible for amyloid formation and prion propagation [9,10]. *In vivo*, this PFD forms dot like aggregates, whereas a longer version in which the globular domain has been truncated, comprising residues 157-289, forms elongated fibrillar aggregates, suggesting that the ability to adopt this supramolecular organization is conferred *in vivo* by the sequences appended to the amyloid core PFD region [11]. The structure of the infectious amyloid fold of HET-s PFD have been solved recently by solid state NMR and represents the only atomic-resolution structure of an infectious fibrillar conformation reported to date [12]. Under close to physiological conditions, the protein adopts a β-solenoid structure with two layers of β-strand per monomer and a characteristic triangular hydrophobic core (Figure 1) [12]. These *in vitro* assembled fibrils are infectious [13,14]. This prion character is strictly associated to the fibril structure obtained at neutral pH since the highly ordered, but conformationally different, HET-s PFD fibrils formed at acidic pH are not infectious [14,15]. HET-s PFD accumulates as IBs when it is over-expressed in *E. coli*. Recently, Wasmer and co-workers, used H/D exchange and solid-state NMR to characterize the HET-s PFD conformation in IBs, demonstrating that it very closely resembles to that in the fibrils, explaining why HET-s PFD IBs are infectious [16]. These results strongly suggest that bacterial cells expressing the infectious form of this eukaryotic prion could provide a simple and powerful system to study how the autologous or heterologous protein quality machinery modulates the *in vivo* assembly, toxicity and infectivity of amyloids. In addition, this cellular model could be a convenient platform for the screening of generic anti-amyloid or specific anti-prion compounds. Towards these aims we present here an exhaustive biophysical and physicochemical characterization of the IBs formed by the different amyloidogenic forms of HET-s in order to establish which are the conformational signatures of these aggregates in a standard cellular background and culture conditions.

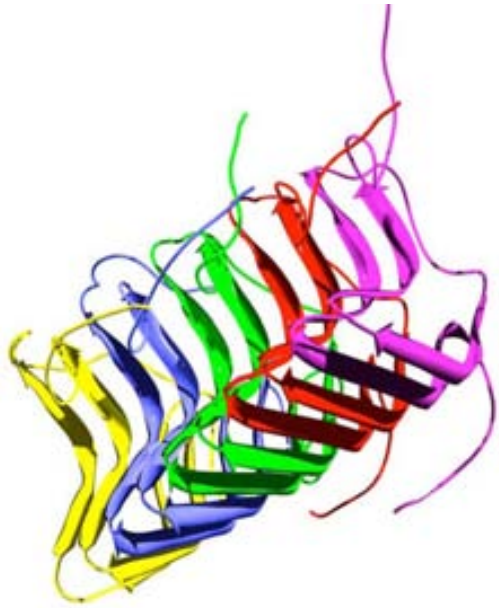

Figure 1
Three-dimensional structure of the infectious HET-s PFD fibrils. Ribbon representation the five central molecules corresponding to the lowest energy structure of the HET-s PFD heptamer as calculated from NMR restraints (PDB ID: 2RNM).

Results and Discussion

HET-s PFD assembles into a -sheet enriched structure in bacterial IBs

The aggregation of soluble proteins into amyloid fibrils invariably results in an increase in their β-sheet content [1]. In this way, the soluble and unstructured HET-s PFD undergoes a transition towards a β-sheet enriched conformation upon *in vitro* fibrillation [14,17]. The far-UV CD spectrum of HET-s mature fibrils displays a negative band at ~217 nm characteristic of β-sheet structures [14,17]. In the CD spectrum of HET-s PFD IBs the band is shifted 6 nm and centred at 223 nm (Figure 2A). This shift in the β-sheet signal in the far-UV CD spectra of aggregated amyloid proteins has been shown to be related to differences in the macroscopic morphology of the fibrils and thought to arise from the superposition of the aromatic CD band on the classical β-sheet CD spectrum as a result of changes in the stacking of the polypeptide aromatic side-chains in the fibrils [18]. FTIR spectroscopy allows more accurate assignment of the secondary structure elements in protein aggregates than CD. The FTIR spectrum of the infectious fibrillar form of HET-s PFD is dominated in the amide I region by a peak at ~1629 cm^{-1}. This signal was associated to the presence of a cross-β-sheet structure in the fibrils [14]. The spectrum of HET-s PFD IBs closely resembles that of the fibrils (Figure 2B and 2C), with a main band at

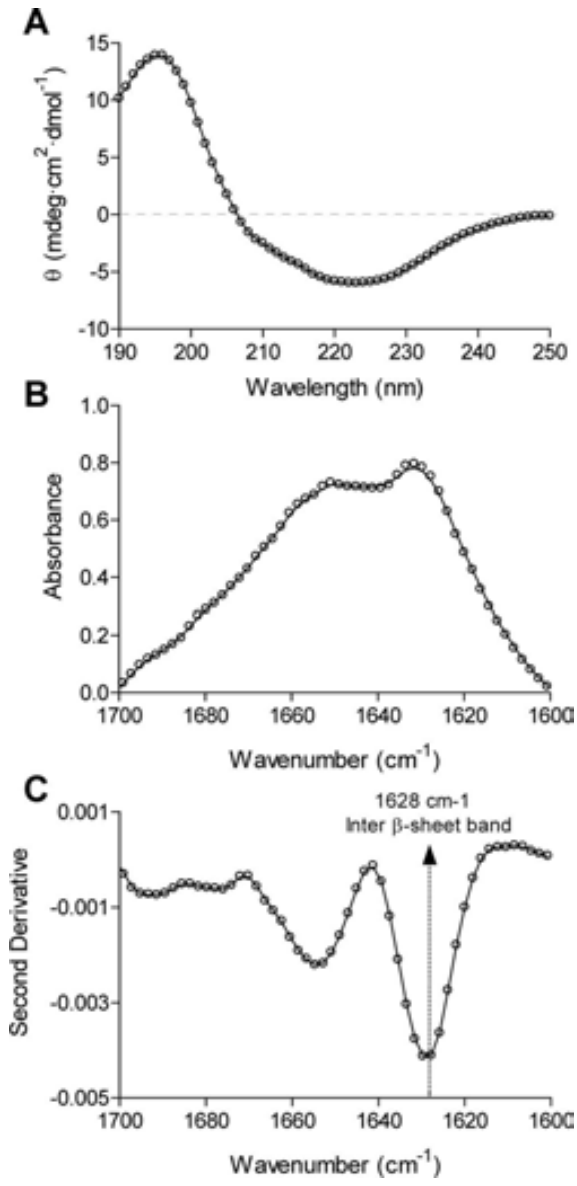

Figure 2
Secondary structure of HET-s PFD IBs. (A) Circular dichroism spectra, and (B and C) FTIR absorbance and second derivative spectra in the amide I region of the spectra showing the characteristic spectral bands of β-sheet conformations.

~1628 cm^{-1} confirming thus the predominance of a β-sheet architecture in these intracellular aggregates.

Amyloid properties of HET-s IBs

We used the amyloid specific dye Congo Red (CR) to verify that the detected IBs β-sheet structures display typical amyloid properties. The absorbance of CR increases and the spectrum maximum red-shifts to ~508 nm in the presence of HET-s PFD IBs (Figure 3A). This spectral change is identical to that observed in the presence of the infectious fibrils formed by the prion domain [14]. In addition, the difference spectrum between the dye in the presence and absence of IBs allows detecting the characteristic amyloid band at ~540 nm (Figure 3B). HET-s amyloid fibrils [19] exhibit CR birefringence, which is accepted to be one of the most stringent diagnostics for amyloid conformation [1]. As shown in Figure 3C and 3D, HETs PFD IBs also show a strong green-gold birefringence upon incubation with CR and illumination under cross-polarized light.

The structural properties of the bacterial IBs formed by the full-length HET-s prion and HET-s (157-289) have not been explored previously. However, it was shown that they display a common proteinase K (PK) resistant core which likely corresponds to the PFD region [16]. Therefore, one might expect that the IBs formed by these two proteins would also display amyloid features. In agreement with this hypothesis, both types of IBs bind CR (Figure 3A and 3B). Interestingly, the change in the CR signal correlates with the proportion of amyloidogenic versus non-amyloidogenic regions in the polypeptides. In this way, the CR signal in the presence of PFD IBs is three fold that of the dye in the presence of the full-length prion IBs. The IB-stretch hypothesis postulates that not necessarily all the polypeptide chain is involved in the network of contacts that sustain the β-core of an IB but rather that specific contacts between certain aggregation-prone regions keep the aggregate in a compact state [20]. For HET-s, the data suggest that the PFD is responsible for maintaining the detected IBs β-sheet architecture, as likely happens in the aggregates formed by the prion in its physiological environment.

A striking characteristic of HET-s PFD infectious fibrils is that, in contrast to most amyloid structures, they do not induce Thioflavin-T (Th-T) fluorescence [14], a dye widely used for amyloid diagnostic. Interestingly, in contrast with the IBs formed by other amyloidogenic peptides like the Aβ peptide [21], none of the three assayed HET-s IBs specifically induces Th-T fluorescence (data not shown). Overall, HET-s IBs display affinities for amyloid dyes that closely resemble that of the protein in its infectious fibrillar form.

The fibrillar core of HET-s IBs

Proteinase K is a protease usually used to map the protected core of amyloid fibrils because in spite of being highly active against peptidic bonds it cannot attack the highly packed backbones in amyloid β-sheet structures. We have shown that PK digestion also allows to reveal the existence of a fibrillar core in Aβ peptide IBs [21]. We used the same approach to asses if the presence of a similar fibrillar material might account for the amyloid conformational properties of HET-s IBs. All purified HET-s IBs

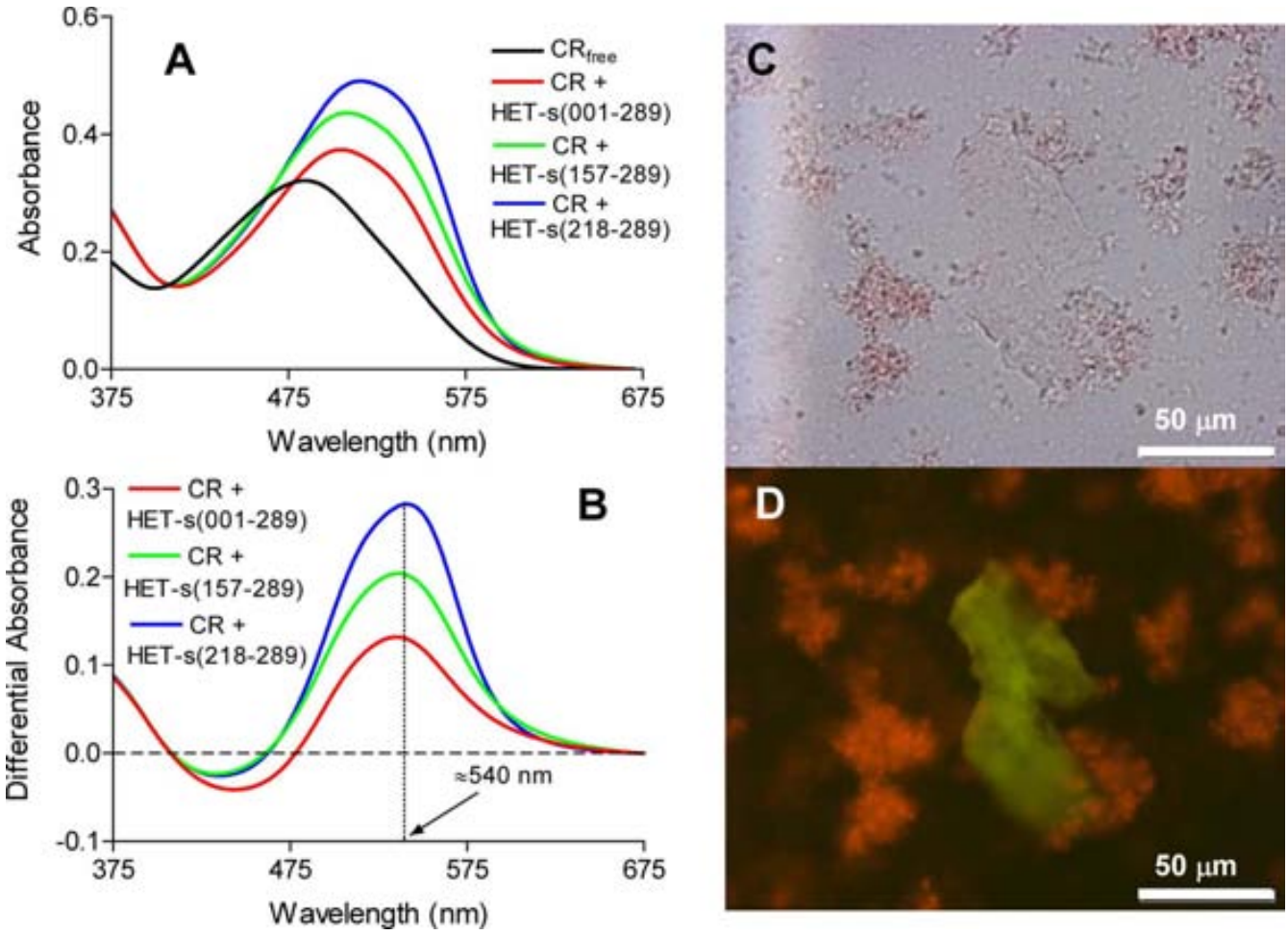

Figure 3

Congo-Red (CR) binding to different HET-s IBs by UV/Vis spectroscopy and staining and birefringence under cross-polarized light using an optic microscope. (A and B) CR spectral changes in the presence of different HET-s IBs; (A) Changes in λ_{max} and intensity in CR spectra in the presence of IBs; (B) Difference absorbance spectra of CR in the presence and absence of IBs showing in all cases the characteristic amyloid band at ~540 nm. (C) HET-PFD IBs stained with Congo red and observed at 40× magnification and in (D) the same field observed between crossed polarizers displaying the green birefringence characteristic of amyloid structures.

displayed a typical compact and electrodense structure (Figure 4, left panel). The progress of the digestion reaction was followed by monitoring the changes in the solution turbidity at 350 nm. The reaction reached a plateau after ~60 min (data not shown). We imaged samples taken at $t_{1/2}$. The aggregates were partially digested and the presence of abundant fibrillar structures could be observed in the IBs formed by all HET-s polypeptides (Figure 4, central and right panel). It is important to note that amyloid fibrils do not form spontaneously from soluble HET-s in the presence of the PK concentrations used to digest IBs [see Additional file 1] and therefore that the observed fibrillar material is not the result of the release HET-s fragments into solution and its subsequent reassembly. The fibrils are associated with apparently amorphous material and in some micrographs fibrils emerging from the preformed compact IBs are seen. The fibrils dimensions and morphology are very similar to that of the infectious amyloid fibrils formed *in vitro* at pH 7.0: the elementary fibrils are ~5 nm in diameter and tend to associate laterally into bundles or stacks [14,22]. Overall, it appears that the different HET-s IBs constitute a bacterial reservoir of amyloid structures that coexist with more disordered and PK susceptible protein regions.

Stability of HET-s PFD IBs towards chemical denaturation

We have previously characterized the stability of HET-s PFD fibrils towards chemical denaturation with Gdn · HCl. At pH 7, we found that the midpoint ($m_{1/2}$) of the transition between the aggregated and soluble states of

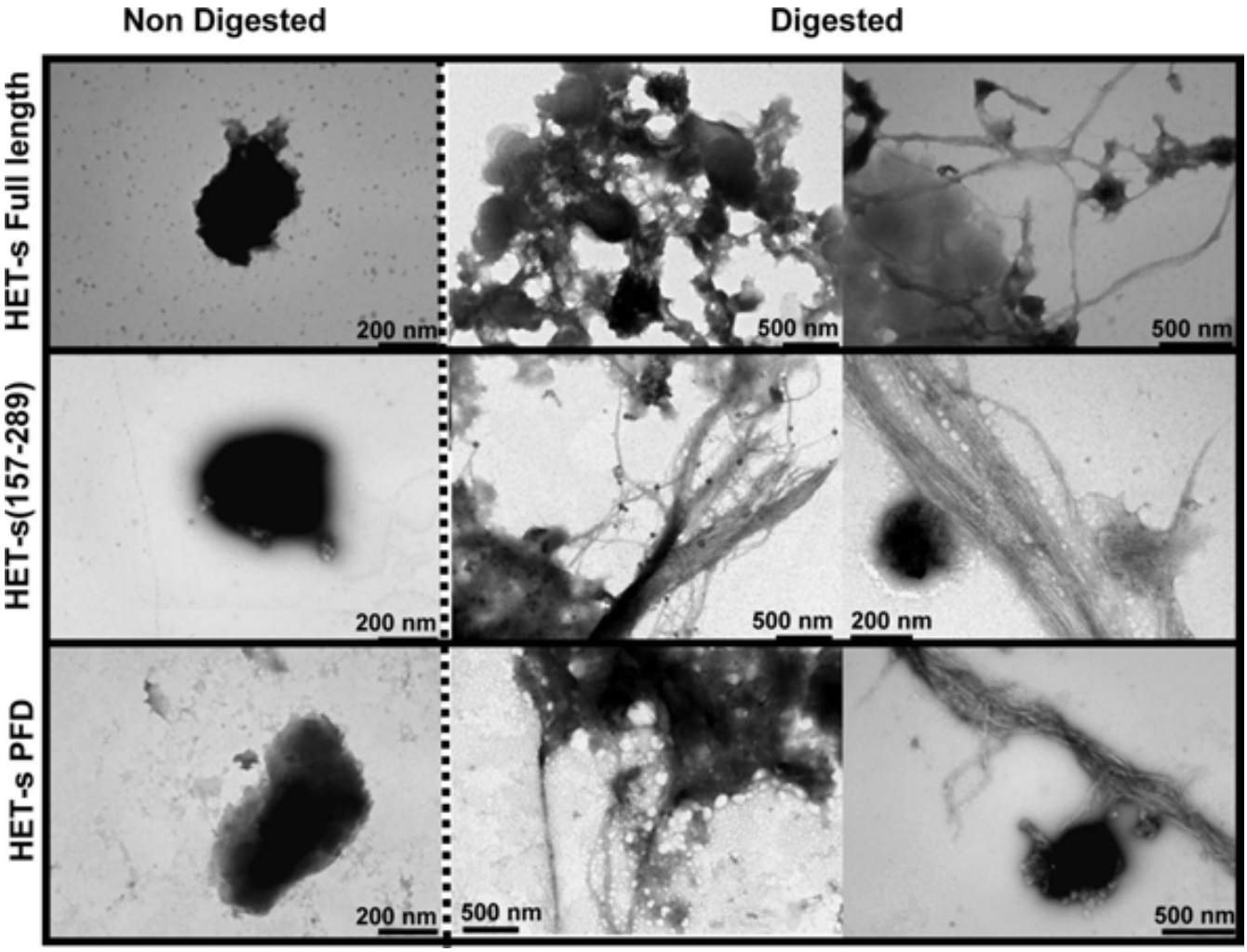

Figure 4
HET-s IBs structure before (left panel) and after 30 min of proteinase K digestion (central and right panel) as monitored by transmission electronic microscopy.

the prion domain is attained at a Gdn · HCl concentration of ~3.5 M [14]. In a recent study we demonstrated that the same approach can be used to approximate the stability of bacterial IBs [23]. This provides us with an opportunity to compare the strength of the contacts stabilizing HET-s PFD IBs with that established by the same polypeptide in the amyloid fibrillar state. IBs denaturation was measured by monitoring the changes in absorbance at 350 nm in the presence of 0 to 8 M Gdn · HCl. As for fibrils, we assumed that only aggregated states contribute significantly to the signal. To determine the incubation time necessary to reach equilibrium we followed the kinetics of IBs solubilization in the presence of different Gdn · HCl concentrations. We observed that, as happens in the denaturation of globular proteins, both the amplitude and the fast rate constant of the reaction increased with increasing chaotropic agent concentrations (Figure 5A). In all cases the reaction was complete before 10 h of incubation. We calculated $m_{1/2}$ for IBs solubilization under equilibrium conditions (20 h incubation) to be ~1.5 M (Figure 5B). Therefore, the *in vivo* formed aggregates are significantly less resistant than *in vitro* fibrils to chemical denaturation [14]. The reduced stability of IBs relative to the fibrils is not surprising if we take into account the PK digestion experiments discussed above which show that ordered stable fibrillar and, amorphous and probably less stables structures coexist in IBs. The presence of minor contaminants might also condition the stability of IBs.

Amyloid seeding capacity of HET-s IBs

The kinetics of amyloid fibril formation usually follow a sigmoidal curve that reflects a nucleation-dependent growth mechanism [24]. The assembly of HET-s PFD fibrils *in vitro* at pH 7.0 follows this kinetic scheme (Figure

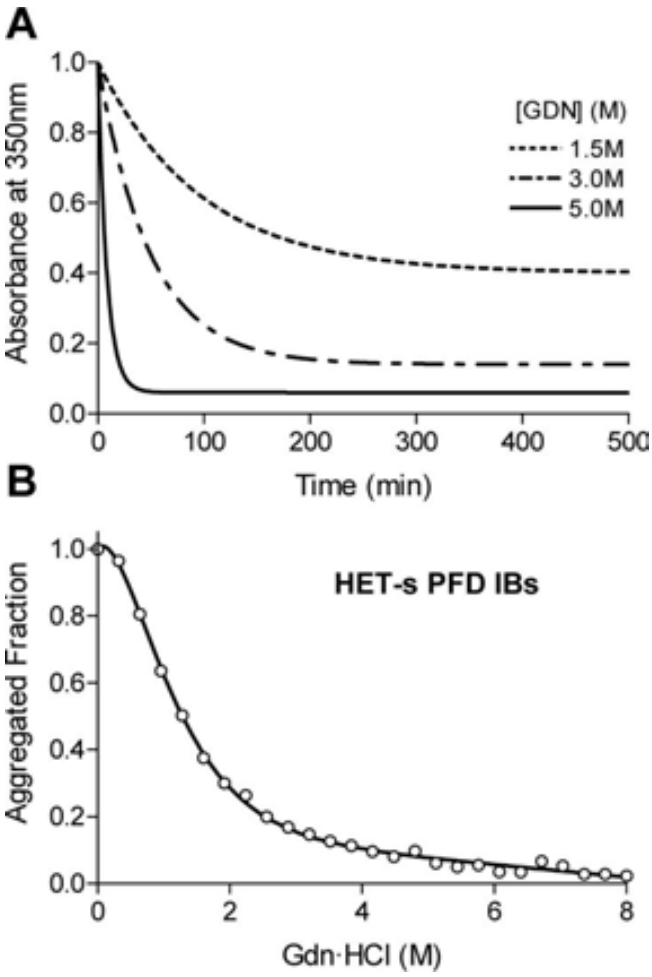

Figure 5
HET-s IBs stability. (A) Kinetics of chemical solubilization of HET-s PFD IBs at different Gdn·HCl, monitored by a time dependent decrease in light scattering at 350. (B) Solubilization at the equilibrium of HET-s PFD IBs in the presence of increasing concentrations of Gdn·HCl monitored by light scattering at 350 nm.

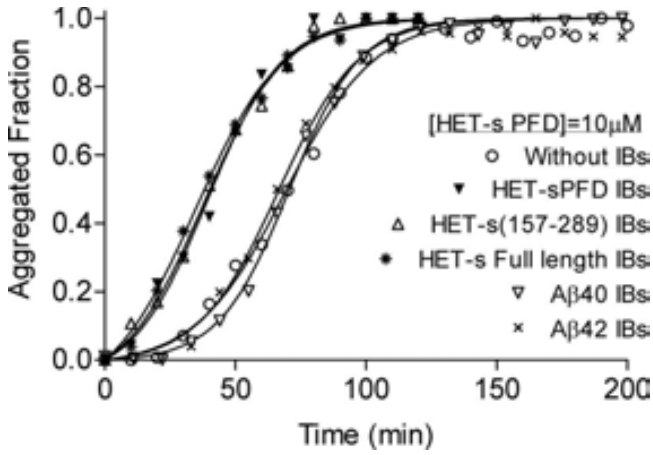

Figure 6
Seeding-dependent maturation of HET-s PFD amyloid growth. The aggregation reaction was seeded with HET-s(001-289), HET-s(157-289), HET-s(218-289), Aβ40 or Aβ42 IBs. The fibrillar fraction of HET-s PFD is represented as a function of time. The formation of HET-s PFD amyloid fibrils is accelerated only in the presence of HET-s IBs.

6). The detected lag phase corresponds to the formation of the initial nuclei on which the polymerization or fibril growth spontaneously proceeds. This step is considerably shortened by the presence of preformed fibrils than can act as seeds for the polymerization reaction. As previously reported by Wasmer and co-workers [16], the presence of limited amounts of HET-s PFD IBs also promotes a dramatic acceleration in the nucleation rate of soluble HET-s PFD amyloid formation (Figure 6). Interestingly enough, the IBs formed by the full-length prion protein and HET-s 157-298 promote exactly the same effect: the lag phase is shortened from 30 to 10 min and the total reaction time from 110 to 70 min. To ensure that the increase in aggregation rates results from a faster growth of amyloid material and not from the formation of amorphous assemblies, the morphology of the aggregates present in seeded solutions was analyzed by EM at the end of the reaction. As it is shown in Figure 7, independently of the HET-s IBs used to seed the reaction, the presence of abundant fibrillar structures with a morphology closely resembling that of unseeded fibrils was observed in all cases.

Amyloid formation is a highly specific process that can be accelerated only by homologous fibrils, but not by fibrils from unrelated polypeptides. This is because the amino acid sequence dictates the fibril conformation and it is in fact the fibril structure which determines seeding ability [1]. To test if this selectivity also applies in the case of IBs we performed cross-seeding experiments of soluble HET-s PFD with the IBs formed by the two amyloidogenic variants of the Alzheimer's related peptides Aβ40 and Aβ42. The presence of Aβ IBs does not affect the nucleation or the elongation rates (Figure 6) confirming that a highly specific molecular recognition between soluble and aggregated states is indispensable for seeding to occur. Therefore, the cross-reactivity observed for the different HET-s forms strongly suggests that the β-solenoid supramolecular disposition proposed for HET-s PFD IBs [16] is also present in the bacterial aggregates formed by the full-length HET-s prion. Structural similarity of the 218-289 region in PFD alone and full length HET-s *in vitro* amyloids was recently evidenced by ssNMR [25].

Conclusion

Prions are misfolded, self-propagating, infectious proteins. The HET-s PFD of *Podospora anserina* constitutes the

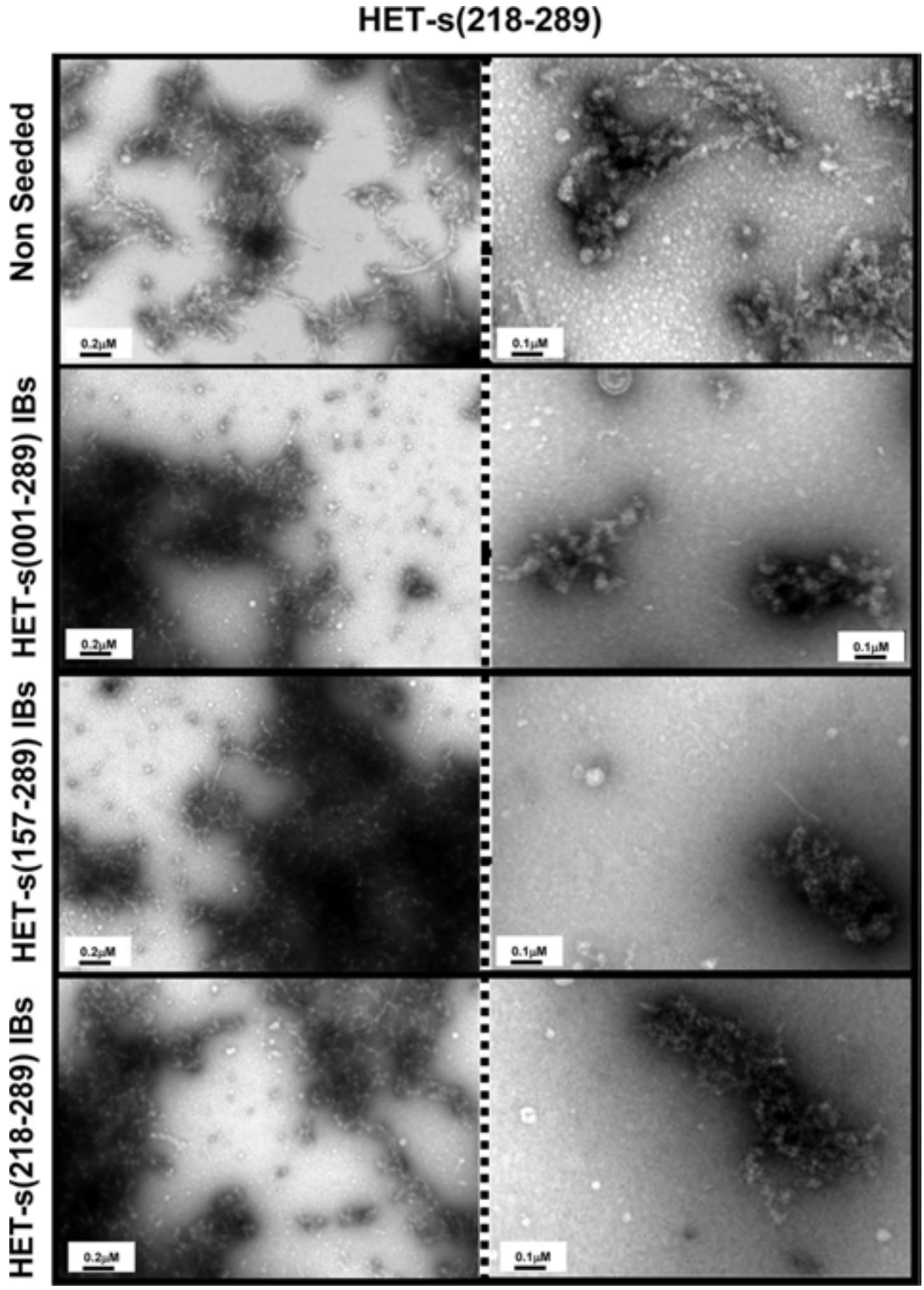

Figure 7
Morphological properties of HET-s PFD aggregates present at the final time point of soluble monomer non-seeded aggregation reactions (top panel) or at the final stage of reactions seeded with HET-s(001-289) (top-middle panel), HET-s(157-289) (bottom-middle panel) and HET-s(218-289) IBs (bottom panel) as monitored by transmission electronic microscopy.

only model for which the infectious fold is known to date at atomic resolution. Moreover, the same fold appears to be conserved in the IBs it forms in bacteria. We show here that the IBs formed by the full-length prion display very similar amyloid characteristics, becoming thus an interesting model to study amyloid formation in bacteria. The formation of prionic infectious folds is known to be tightly controlled by the cellular folding machinery [26]. For HET-s, this propagation depends on molecular chaperones and more specifically on Hsp104 as has been shown not only in *P. anserina* but also when this prion is heterologously expressed in yeast. The data in the present study supports the use bacterial systems to study how the very well characterized homologous prokaryotic chaperones, for example ClpB (a Hsp104 homolog), recombinant eukaryotic chaperones or small chemical compounds modulate the formation and structure of infectious prions in a more simple cellular background. Although solid state NMR provides a detailed view of the conformational properties of IBs at the molecular level, it requires specific equipment, labelling of the proteins, growing of the bacterial cells in non physiological minimal media and is overall a slow technique not suitable for large scale screening. The set of biophysical approaches described in the present work accurately report on the conformational properties of prionic HET-s IBs allowing to monitor how bacterial backgrounds modulate their properties in a faster and simpler manner.

Methods

Protein expression

Plasmids encoding for C-terminally histidine-tagged HET-s full-length, HET-s(157-289) and HET-s PFD polypeptides have been previously described [9,11,19]. They were cloned into the NdeI and HindIII sites of the pET21a vector (Novagen) and transformed into BL21(DE3) pLysS cells. The C-terminal histidine tag does not affect the biological activity of HET-s in *P. anserina* [19]. For protein expression, 10 mL overnight culture of transformed cells was used to inoculate 2 L of DYT medium, which was further incubated at 37°C and 200 rpm. At an OD_{600} of 0.5, protein expression was induced with 1 mM of isopropyl-1-thio-β-D-galactopyranoside for 3 h at 37°C, then the cultures were centrifuged and the cell pellet frozen at -20°C.

IB purification

IBs were purified from induced cell extracts by detergent-based procedures as previously described [27]. Briefly, cells were harvested by centrifugation at 12 000 × *g* (at 4°C) for 15 min and resuspended in 200 μL of lysis buffer (50 mM Tris-Cl pH 8, 1 mM EDTA, 100 mM NaCl), plus 30 μL of 100 mM protease inhibitor PMSF and 6 μL of 10 mg/mL lysozyme. After 30 min of incubation at 37°C under gentle agitation, NP-40 was added at 1% (v/v) and the mixture incubated at 4°C for 30 min. Then, 3 μL of DNase I and RNase from 1 mg/mL stock (25 μg/mL final concentration) and 3 μL of 1 M $MgSO_4$ were added and the resulting mixture was further incubated at 37°C for 30 min. Protein aggregates were separated by centrifugation at 12 000 × *g* for 15 min at 4°C. Finally, IBs were washed once with the same buffer containing 0.5% Triton X-100 and once with sterile PBS. After a final centrifugation at 12 000 × *g* for 15 min, pellets were stored at -20°C until analysis. The frozen pellets were reconstituted in PBS buffer. SDS-PAGE analysis revealed that in all cases HET-s proteins were the major polypeptidic components of the respective aggregates.

Secondary structure determination

ATR FT-IR spectroscopy analyses of HET-s IBs were performed using a Bruker Tensor 27 FT-IR Spectrometer (Bruker Optics Inc) with a Golden Gate MKII ATR accessory. Each spectrum consists of 20 independent scans, measured at a spectral resolution of 2 cm^{-1} within the 1800-1500 cm^{-1} range. All spectral data were acquired and normalized using the OPUS MIR Tensor 27 software. Second derivatives of the spectra were used to determine the frequencies at which the different spectral components were located.

CD spectra were collected in the 200 - 250 nm range at 25°C and measured at a spectral resolution of 1 cm^{-1}, and a scan rate of 15 nm min^{-1} using a Jasco 810 spectropolarimeter with a quartz cell of 0.1 cm path length.

Chemical denaturation

For stability assays, purified IBs were prepared at $OD_{350\ nm}$ = 1 in PBS solution at pH 7.0 containing selected concentrations of guanidine hydrochloride (Gdn · HCl) ranging from 0 to 8 M. For equilibrium denaturation experiments, the reactions were allowed to reach equilibrium by incubating them for 20 h at room temperature. The fraction of soluble protein (f_S) was calculated from the fitted values using equation: $f_S = 1-((\gamma_S-\gamma)/(\gamma_S-\gamma_A))$, where γ_S and γ_A are the absorbance at 350 nm of the soluble and aggregated protein, respectively, and γ is the absorbance of the protein solution as a function of denaturant concentration. The value $m_{1/2}$ was calculated as the denaturant concentration at which $f_S = 1/2$. $OD_{350\ nm}$ changes were monitored in a Cary-400 Varian spectrophotometer (Varian Inc.).

For kinetic experiments, purified IBs were prepared at $OD_{350\ nm}$ = 1 in PBS solution at pH 7.0 containing selected concentrations of Gdn · HCl. The reaction was monitored by measuring the changes in $OD_{350\ nm}$. Double-exponential decay curves were fitted to the data using Sigmaplot non-linear regression software (Jandel Scientific, San

Rafael, CA, USA), and apparent rate constants were derived from these regressions.

Limited proteolysis

HET-s IBs (to a final $OD_{350\ nm}$ = 0.125) were digested at 37°C with 10 μg/mL of proteinase K (PK) in pH 7.0 PBS buffer and the digestion was followed by UV/Vis spectroscopy at 350 nm. After 30 min of reaction, fractions of the samples were centrifuged and the insoluble part resuspended in water, placed on carbon-coated copper grids, and left to stand for five minutes. The grids were washed with distilled water and stained with 2% (w/v) uranyl acetate for another two minutes before analysis using a HitachiH-7000 transmission electron microscope operating at accelerating voltage of 75 kV.

Congo Red binding

Congo-Red (CR) interaction with different HET-s IBs was tested using a Cary100 (Varian) UV/Vis spectrophotometer by recording the absorbance spectra from 375 nm to 675 nm using a matched pair of quartz cuvettes of 1 cm optical length placed in a thermostated cell holder at 25°C. In order to detect the typical amyloid band at ~540 nm, differential CR spectra in the presence and absence of protein were used.

HET-s IBs were incubated for 1 h in the presence of 50 μM CR. After centrifugation (14 000 × *g* for 5 min), the precipitated fraction was placed on a microscope slide and sealed. The CR birefringence was detected under cross-polarized light using an optic microscope (Leica DMRB, Heidelberg, Germany).

Seeding assays

HET-s PFD aggregation from soluble monomer was monitored by measuring the transition from non-aggregated to aggregated state by UV/Vis spectrophotometry at 350 nm. In the seeding assay, a solution of different HET-s IBs (to a final OD_{350} = 0.125) was also added at the beginning of the reaction. Cross-seeding assays with Aβ40 and Aβ42 IBs were performed in the same manner. All experiments were carried out at 40°C and 1400 rpm with an initial soluble monomer concentration of 10 μM.

HET-s PFD aggregation process may be studied as an autocatalytic reaction using the equation f = ({exp [(1+)kt]-1})/{1+ *exp[(1+)kt]} under the boundary condition of t = 0 and f = 0, where $k = k_e$a (when a is the protein concentration) and represents the dimensionless value to describe the ratio of k_n to k. By non-linear regression of f against t, values of and k can be easily obtained, and from them the rate constants, k_e (elongation constant) and k_n (nucleation constant). The extrapolation of the growth portion of the sigmoid curve to abscissa (f = 0), and to the highest ordinate value of the fitted plot, afforded two values of time (t_0 and t_1), which correspond to the lag time and to the time at which the aggregation was almost complete [28].

Competing interests

The authors declare that they have no competing interests.

Authors' contributions

RS and SV directed the work and prepared the manuscript, AE performed experimental work and SJS contributed to the analysis and interpreation of the data.

Additional material

Additional file 1

Effect of Proteinase K on HET-s PFD soluble monomer aggregation. *Aggregation of HET-s PFD soluble monomer in the absence (top panel) and presence of 5 g/mL of proteinase K (bottom panel) as imaged by electronic microscopy. The aggregation assay was realized at 37°C and pH7 for 24 h.*

Click here for file

[http://www.biomedcentral.com/content/supplementary/1475-2859-8-56-S1.TIFF]

Acknowledgements

We gratefully thank Dr. Francesc X. Aviles and Dr. Josep Vendrell for lab facilities. We thank Dr. Bernd Reif for generously providing us the plasmid encoding for Aβ40 peptide. This work has been supported by grants BIO2007-68046 (Spanish Ministry for Science and Innovation) and 2009-SGR 760 (Generalitat de Catalunya).

References

1. Chiti F, Dobson CM: **Protein misfolding, functional amyloid, and human disease.** *Annu Rev Biochem* 2006, **75:**333-366.
2. Ventura S, Villaverde A: **Protein quality in bacterial inclusion bodies.** *Trends Biotechnol* 2006, **24(4):**179-185.
3. de Groot NS, Espargaro A, Morell M, Ventura S: **Studies on bacterial inclusion bodies.** *Future Microbiol* 2008, **3:**423-435.
4. Carrio M, Gonzalez-Montalban N, Vera A, Villaverde A, Ventura S: **Amyloid-like properties of bacterial inclusion bodies.** *J Mol Biol* 2005, **347(5):**1025-1037.
5. Prusiner SB: **Shattuck lecture--neurodegenerative diseases and prions.** *N Engl J Med* 2001, **344(20):**1516-1526.
6. Wickner RB: **[URE3] as an altered URE2 protein: evidence for a prion analog in Saccharomyces cerevisiae.** *Science* 1994, **264(5158):**566-569.
7. Wickner RB, Edskes HK, Shewmaker F, Nakayashiki T: **Prions of fungi: inherited structures and biological roles.** *Nat Rev Microbiol* 2007, **5(8):**611-618.
8. Coustou V, Deleu C, Saupe S, Begueret J: **The protein product of the het-s heterokaryon incompatibility gene of the fungus Podospora anserina behaves as a prion analog.** *Proc Natl Acad Sci USA* 1997, **94(18):**9773-9778.
9. Balguerie A, Dos Reis S, Ritter C, Chaignepain S, Coulary-Salin B, Forge V, Bathany K, Lascu I, Schmitter JM, Riek R, *et al.*: **Domain organization and structure-function relationship of the HET-s prion protein of Podospora anserina.** *Embo J* 2003, **22(9):**2071-2081.
10. Ritter C, Maddelein ML, Siemer AB, Luhrs T, Ernst M, Meier BH, Saupe SJ, Riek R: **Correlation of structural elements and infectivity of the HET-s prion.** *Nature* 2005, **435(7043):**844-848.
11. Balguerie A, Dos Reis S, Coulary-Salin B, Chaignepain S, Sabourin M, Schmitter JM, Saupe SJ: **The sequences appended to the amyloid**

core region of the HET-s prion protein determine higher-order aggregate organization in vivo. *J Cell Sci* 2004, **117(Pt 12):**2599-2610.
12. Wasmer C, Lange A, Van Melckebeke H, Siemer AB, Riek R, Meier BH: **Amyloid fibrils of the HET-s(218-289) prion form a beta solenoid with a triangular hydrophobic core.** *Science* 2008, **319(5869):**1523-1526.
13. Maddelein ML, Dos Reis S, Duvezin-Caubet S, Coulary-Salin B, Saupe SJ: **Amyloid aggregates of the HET-s prion protein are infectious.** *Proc Natl Acad Sci USA* 2002, **99(11):**7402-7407.
14. Sabate R, Baxa U, Benkemoun L, Sanchez de Groot N, Coulary-Salin B, Maddelein ML, Malato L, Ventura S, Steven AC, Saupe SJ: **Prion and non-prion amyloids of the HET-s prion forming domain.** *J Mol Biol* 2007, **370(4):**768-783.
15. Wasmer C, Soragni A, Sabate R, Lange A, Riek R, Meier BH: **Infectious and noninfectious amyloids of the HET-s(218-289) prion have different NMR spectra.** *Angew Chem Int Ed Engl* 2008, **47(31):**5839-5841.
16. Wasmer C, Benkemoun L, Sabate R, Steinmetz MO, Coulary-Salin B, Wang L, Riek R, Saupe SJ, Meier BH: **Solid-State NMR Spectroscopy Reveals that E. coli Inclusion Bodies of HET-s(218-289) are Amyloids.** *Angew Chem Int Ed Engl* 2009, **48(26):**4858-4860.
17. Sabate R, Saupe SJ: **Thioflavin T fluorescence anisotropy: an alternative technique for the study of amyloid aggregation.** *Biochem Biophys Res Commun* 2007, **360(1):**135-138.
18. Nyrkova IA, Semenov AN, Aggeli A, Boden N: **Fibril stability in solutions of twisted *b*-sheet peptides: a new kind of micellization in chiral systems.** *Eur Phys J B* 2000, **17:**481-497.
19. Dos Reis S, Coulary-Salin B, Forge V, Lascu I, Begueret J, Saupe SJ: **The HET-s prion protein of the filamentous fungus Podospora anserina aggregates in vitro into amyloid-like fibrils.** *J Biol Chem* 2002, **277(8):**5703-5706.
20. De Groot NS, Sabate R, Ventura S: **Amyloids in bacterial inclusion bodies.** *Trends Biochem Sci* 2009 in press.
21. Morell M, Bravo R, Espargaro A, Sisquella X, Aviles FX, Fernandez-Busquets X, Ventura S: **Inclusion bodies: specificity in their aggregation process and amyloid-like structure.** *Biochim Biophys Acta* 2008, **1783(10):**1815-1825.
22. Sen A, Baxa U, Simon MN, Wall JS, Sabate R, Saupe SJ, Steven AC: **Mass analysis by scanning transmission electron microscopy and electron diffraction validate predictions of stacked beta-solenoid model of HET-s prion fibrils.** *J Biol Chem* 2007, **282(8):**5545-5550.
23. Espargaro A, Sabate R, Ventura S: **Kinetic and thermodynamic stability of bacterial intracellular aggregates.** *FEBS Lett* 2008, **582(25-26):**3669-3679.
24. Jarrett JT, Lansbury PT Jr: **Seeding "one-dimensional crystallization" of amyloid: a pathogenic mechanism in Alzheimer's disease and scrapie?** *Cell* 1993, **73(6):**1055-1058.
25. Wasmer C, Schutz A, Loquet A, Buhtz C, Greenwald J, Riek R, Bockmann A, Meier BH: **The Molecular Organization of the Fungal Prion HET-s in Its Amyloid Form.** *J Mol Biol* 2009, **394(1):**119-127.
26. Chien P, Weissman JS, DePace AH: **Emerging principles of conformation-based prion inheritance.** *Annu Rev Biochem* 2004, **73:**617-656.
27. Carrio MM, Cubarsi R, Villaverde A: **Fine architecture of bacterial inclusion bodies.** *FEBS Lett* 2000, **471(1):**7-11.
28. Sabate R, Gallardo M, Estelrich J: **An autocatalytic reaction as a model for the kinetics of the aggregation of beta-amyloid.** *Biopolymers* 2003, **71(2):**190-195.

Microbial Cell Factories

BioMed Central
The Open Access Publisher

Yeast prions form infectious amyloid inclusion bodies in bacteria

Microbial Cell Factories 2012, **11**:89 doi:10.1186/1475-2859-11-89

Alba Espargaró (alba.espargaro@uab.cat})
Anna Villar-Piqué (anna.villar@uab.cat})
Raimon Sabaté (raimon.sabate@uab.cat})
Salvador Ventura (salvador.ventura@uab.es})

ISSN 1475-2859

Article type Research

Submission date 5 February 2012

Acceptance date 27 May 2012

Publication date 25 June 2012

Article URL http://www.microbialcellfactories.com/content/11/1/89

Yeast prions form infectious amyloid inclusion bodies in bacteria

Alba Espargaró[1]
Email: alba.espargaro@uab.cat

Anna Villar-Piqué[2]
Email: anna.villar@uab.cat

Raimon Sabaté[3,4,**]
Email: raimon.sabate@uab.cat

Salvador Ventura[1,2,*]
Email: salvador.ventura@uab.es

[1] Institut de Biotecnologia i de Biomedicina, Universitat Autònoma de Barcelona, E-08193 Bellaterra, Spain

[2] Departament de Bioquímica i Biologia Molecular, Facultat de Ciències, Universitat Autònoma de Barcelona, E-08193 Bellaterra, Spain

[3] Departament de Fisicoquímica, Facultat de Farmàcia, Universitat de Barcelona, Avda. Joan XXIII s/n, E-08028 Barcelona, Spain

[4] Institut de Nanociència i Nanotecnologia (IN2UB), Barcelona, Spain

[*] Corresponding author. Institut de Biotecnologia i de Biomedicina, Universitat Autònoma de Barcelona, E-08193 Bellaterra, Spain

[**] Corresponding author. Institut de Nanociència i Nanotecnologia (IN2UB), Barcelona, Spain

Abstract

Background

Prions were first identified as infectious proteins associated with fatal brain diseases in mammals. However, fungal prions behave as epigenetic regulators that can alter a range of cellular processes. These proteins propagate as self-perpetuating amyloid aggregates being an example of structural inheritance. The best-characterized examples are the Sup35 and Ure2 yeast proteins, corresponding to [*PSI+*] and [*URE3*] phenotypes, respectively.

Results

Here we show that both the prion domain of Sup35 (Sup35-NM) and the Ure2 protein (Ure2p) form inclusion bodies (IBs) displaying amyloid-like properties when expressed in bacteria. These intracellular aggregates template the conformational change and promote the aggregation of homologous, but not heterologous, soluble prionogenic molecules. Moreover,

in the case of Sup35-NM, purified IBs are able to induce different [*PSI*+] phenotypes in yeast, indicating that at least a fraction of the protein embedded in these deposits adopts an infectious prion fold.

Conclusions

An important feature of prion inheritance is the existence of strains, which are phenotypic variants encoded by different conformations of the same polypeptide. We show here that the proportion of infected yeast cells displaying strong and weak [*PSI*+] phenotypes depends on the conditions under which the prionogenic aggregates are formed in *E. coli*, suggesting that bacterial systems might become useful tools to generate prion strain diversity.

Keywords

Protein aggregation, Inclusion bodies, Prions, Sup35-NM, Ure2p, Amyloid fibrils, *E. coli*

Background

Mammalian prions cause fatal neurodegenerative disorders, like Creutzfeldt–Jacob disease in humans, bovine spongiform encephalopathy and scrapie in sheep [1]. In yeast, several polypeptides can form prions that behave as dominant non-Mendelian cytoplasmic genetic elements. The best-characterized yeast prionogenic proteins are Sup35 and Ure2, which, in their aggregated state, form two cytosolic inheritable elements named [*PSI*+] and [*URE3*], respectively. Whether this property is detrimental and prion formation constitutes a pathological yeast trait or it is, in contrast, associated to beneficial phenotypes is controversial [2]. The fact that in wild-type yeast, the [*PSI*+] or [*URE3*] prions were initially not found was interpreted in favour of the first possibility [3,4], but a recent study by the Lindquist's group demonstrates that various yeast prions can be found in several isolates of wild type yeast [5], favouring thus the second possibility. Regardless of their cellular effects, both mammalian and fungal prion proteins are characterized by a high propensity to assemble into amyloid-like aggregates under physiological conditions both *in vitro* and in the cell [6]. Prions represent a particular subclass of amyloids for which the aggregation process becomes self-perpetuating *in vivo* and therefore infectious [7]. *In vitro*, the assembly of prions into amyloid aggregates displays a characteristic lag phase, which is abrogated in the presence of preformed fibres [8-10]. This seeded catalysis of the polymerization reaction underlies prion conformational replication and infectivity [6]. Reconstitution of *in vivo* infectivity from *in vitro* aggregates formed by recombinant purified prions has definitively proven the protein only hypothesis for prion formation and the connection between amyloid conformations and prion spreadable species [11,12]. Prion assemblies of the same protein might lead to phenotypically different transmissible states or strains [13]. It is suggested that this phenomenon results from a single protein being able to adopt multiple misfolded conformations, each one corresponding to a specific strain.

The formation of inclusion bodies (IBs) in bacteria has long been regarded as an unspecific process depending on the establishment of hydrophobic contacts between partially or totally unfolded species after protein synthesis at the ribosome [14]. However, an increasing body of evidence indicates that bacterial IBs share a number of common structural features with the highly ordered and, in many cases, pathogenic amyloid fibrils [15-18]. So far, the conformational and functional characteristics of the IBs formed by prions in bacteria have

been only explored in detail for the HET-s prion of the filamentous fungus *Podospora anserina* [19,20]. The HET-s prion functions in a genetically programmed cell-death phenomenon, which occurs when two fungal strains of different genotypes fuse [21]. For this particular prionogenic protein, the formation of IBs and amyloid fibrils seem to be a remarkably similar process as IBs display a highly ordered amyloid-like conformation at the molecular level [19,20], are able to seed the polymerization of amyloid-fibrils *in vitro* [19,20] and turn to be infectious *in vivo* [20]. This suggests that the aggregates formed by other prionogenic proteins in bacteria might exhibit equal properties. We show here that this is the case for the yeast prion domain of Sup35 (Sup35-NM) and the Ure2 protein (Ure2p).

Results and discussion

Ure2p and Sup35-NM form β-sheet enriched IBs

We analyzed the cellular distribution of Ure2 and Sup35-NM proteins when expressed recombinantly in bacteria at 37°C. Western blotting and densitometry of the soluble and insoluble fractions indicate that about 50% of Ure2p and 40% of Sup35-NM recombinant proteins reside in the insoluble cellular fraction in these conditions (Figure 1A). Accordingly, bacterial cells expressing these polypeptides form birefringent IBs, located predominantly at the cell poles, as shown by phase contrast microscopy (Figure 1B).

Figure 1 Solubility properties of recombinant Sup35-NM (left panel) and Ure2 (right panel) proteins. (A) Western blot of the soluble and insoluble fractions of cells expressing Sup35-NM and Ure2p at 37°C detected with an anti-histag antibody and quantified by densitometry using the Quantity-One software (Bio-Rad). (B) Localization of cytoplasmic IBs at the poles of cells expressing Sup35-NM and Ure2p proteins, as imaged by phase contrast microscopy

The aggregation of proteins into amyloid fibrils results in the formation of intermolecular β-sheets [22,23]. Fourier-transform infrared (FT-IR) spectroscopy allows addressing structural features of protein aggregates [24,25]. Specifically, the amide I region corresponding to the absorption of the carbonyl peptide bond group of the protein main chain is a sensitive marker of the protein secondary structure. To decipher the secondary structure in Sup35-NM and Ure2p IBs, we purified them from bacterial cell extracts and analyzed their FT-IR spectra (Figure 2A, B and C). Deconvolution of the absorbance spectrum in the amide I region for Sup35-NM and Ure2p IBs permitted to identify the individual secondary structure components and their relative contribution to the main absorbance signal. Both IBs exhibit FT-IR bands that can be assigned to the presence of intermolecular β-sheets (Table 1). These signals are absent or display a low intensity in the FT-IR of purified, initially soluble and monomeric, Sup35-NM and Ure2p species (Figure 2A and B). Therefore, as reported for other amyloid proteins [15,18,19,26], aggregation of Sup35-NM and Ure2p into IBs results in the formation of a supra-molecular structure in which at least part of the polypeptide chains adopt a disposition similar to this in amyloids. The IBs of the two yeast prionogenic proteins display, however, certain differences in secondary structure (Table 1 and Figure 2C); Ure2p IBs being slighted enriched in intermolecular β-sheet structure relative to Sup35-NM aggregates. The secondary structure content of Sup35-NM IBs closely resembles the one we observed for fibrils under agitation conditions [27]. In the case of Ure2p IBs, their secondary structure is more similar to that in fibrils formed under quiescent conditions [28]. In fact we

have shown that, in contrast to Sup35-NM, the secondary structure content of Ure2p is strongly dependent on the aggregation conditions [27].

Figure 2 Conformational properties of soluble and aggregated Sup35-NM and Ure2 proteins. Secondary structure of Sup35-NM (A) and Ure2 (B) yeast proteins in their soluble forms and inside the IBs formed at 37°C as determined FT-IR spectroscopy in the amide I region of the spectrum. Empty circles, solid thick lines and solid thin line show the absorbance spectra, the sum of individual spectral components and the inter-molecular β-sheet band, respectively; note that whereas Sup35-NM and Ure2p IBs display the typical inter-molecular β-sheet band at 1625–1630 cm^{-1}, this signal is low or absent in soluble species. (C) Comparative analysis of the secondary structure of Sup35-NM and Ure2p IBs. Empty circles, solid thick lines and solid thin lines show the absorbance spectra, the sum of individual spectral components and the deconvolved component bands, respectively. (D) Stability of yeast prionogenic IBs in front of Gdn·HCl denaturation at equilibrium monitored by changes in turbidity at 350 nm

Table 1 Secondary structure bands in the absorbance FT-IR spectra of purified *E. coli* Sup35-NM and Ure2p IBs

18°C		37°C				
Sup35-NM IBs		Sup35-NM IBs		Ure2p IBs		
Band (cm^{-1})	Area (%)	Band (cm^{-1})	Area (%)	Band (cm^{-1})	Area (%)	Structure
1615	4	1617	7	1617	8	Tyrosine ring
1629	29	1628	21	1629	26	β-sheet (inter-molecular)
1652	51	1653	65	1650	45	
1665	2	1676	6	1664	10	loop/β-turn/bend/α-helix
1677	12	1682	1	1677	11	

The presence of regular secondary structure inside IBs implies the existence of cooperative interactions involving the main and side chains of the polypeptides embedded in these aggregates. To confirm this extent, we used chemical denaturation with guanidine hydrochloride (Gdn·HCl). We have shown before that this approach allows to approximate the conformational stability of intracellular aggregates [29]. Ure2p and Sup35-NM IBs denaturation was measured by monitoring the changes in absorbance at 350 nm in a Gdn·HCl range from 0 to 8 M. We calculated $[Gdn{\cdot}HCl]_{1/2}$ for IBs solubilization under equilibrium conditions (20 h incubation) to be 1.8 M and 2.1 M for Sup35-NM and Ure2p IBs, respectively (Figure 2D). These values are close to the one observed for HET-s PFD IBs (1.6 M) [19] and in agreement with their relative intermolecular β-sheet content. The cooperative denaturation transitions observed for both IBs support the presence of selective contacts in at least a fraction of the molecules deposited inside them.

Amyloid properties of Sup35-NM and Ure2p IBs

We used the amyloid-specific dyes Congo red (CR), thioflavin T (Th-T) and S (Th-S) to confirm that the detected β-sheet secondary structure in Sup35-NM and Ure2p IBs is organized into an amyloid-like suprastructure. The absorbance of CR increases and the spectrum maximum red-shifts to 510 nm in the presence of both IBs (Figure 3A). This spectral change corresponds to that observed in the presence of the fibrils formed *in vitro* by both proteins [27,30,31]. Moreover, the difference spectra of the dye in the presence and absence of IBs exhibit the characteristic amyloid band at 541 nm (Figure 3B).

Figure 3 Specific amyloid dyes staining of yeast prion IBs. (A) CR spectral changes in the presence of each IB; displaying the characteristic red-shift in λ_{max} and intensity increase in CR spectra in the presence of IBs. (B) Difference absorbance spectra of CR in presence and absence of IBs showing the characteristic amyloid band at 541 nm for both yeast proteins. (C) Fluorescence emission spectrum of Th-T in the presence of each IB when excited at 445 nm; note the characteristic maximum at ~ 480 nm upon binding to amyloid structures. (D) Yeast prions IBs stained with Th-S and observed at 40x magnification by phase contrast and fluorescence microscopy displaying the green fluorescence characteristic of amyloid structures

Th-T fluorescence emission is enhanced in the presence of yeast prion amyloid fibrils [27,30,31]. The same behaviour is observed upon incubation of Th-T with yeast proteins IBs (Figure 3C). The Th-T fluorescence at the 480 nm spectral maximum increases 20- and 40-folds for Sup35-NM and Ure2p IBs, respectively. Furthermore, binding of Th-S to IBs was visualized by fluorescence microscopy (Figure 3D). For both IBs, areas rich in fibrous material were stained with Th-S to yield a bright green–yellow fluorescence against a dark background. Therefore, consistently with the secondary structure data and the existence of selective interactions, the dye binding results indicate that both IBs possess detectable amounts of amyloid structure.

Sup35-NM and Ure2p IBs selectively seed amyloid formation

The kinetics of amyloid fibril formation usually results in a sigmoid curve that reflects a nucleation-dependent growth mechanism [29]. We have shown previously that the *in vitro* assembly of Sup35-NM and Ure2p fibrils follows this kinetic scheme [27]. The detected lag phase corresponds to the formation of the initial nuclei on which the polymerization or fibril growth would further spontaneously proceed. Seeded protein polymerization is a well-established mechanism for *in vivo* amyloid fibril formation and underlies prion propagation [32-34]. In Figure 4, it is shown, the effect of the presence of preformed amyloid Sup35-NM and Ure2p fibrils on the kinetics of fibril formation. In the presence of a 10% of preformed fibrils, the apparent nucleation constant (k_n) increases by three- and five-fold for Sup35-NM and Ure2p, respectively (Table 2). As a result, the lag phase of the reaction is shortened by 22 min for Sup35-NM and by 62 min for Ure2p. As expected, no significant changes in the apparent elongation constants (k_e) were detected since fibril seeds act preferentially at the nucleation stage.

Figure 4 Aggregation kinetics of Sup35-NM and Ure2p. The aggregation reactions of 20 μM yeast prionogenic proteins were carried out under agitation at 37°C. 2 μM of *in vitro* formed fibrils (representing 10% of the final protein concentration) or IBs (at a final OD_{350nm} of 0.125) were used for seeding and cross-seeding assays. The fibrillar fraction of Sup35-NM (A) and Ure2p (B) is represented as a function of time. The formation of Sup35-NM and Ure2p amyloid fibrils are accelerated only in the presence of pre-aggregated homologous protein, either fibrils or IBs

Table 2 Kinetic parameters of Sup35-NM and Ure2p aggregation reactions

Protein	Parameters	Non seeded	Sup35-NM Fibrils	Sup35-NM IBs	Ure2p IBs
Sup35-NM	k_n /10^6·s^{-1}	0.35	1.07	1.00	0.45
	k_e /M^{-1}·s^{-1}	37.54	36.08	36.67	36.07
	c·k_e /10^6·s^{-1}	750.83	721.50	733.33	721.33
	t_0 /s	124.0	102.5	98.6	123.0
	$t_{1/2}$ /s	169.9	150.1	149.6	171.0
	t_1 /s	215.8	197.8	200.7	219.1
Protein	Parameters	Non seeded	Ure2p Fibrils	Ure2p IBs	Sup35-NM IBs
Ure2p	k_n/10^6·s^{-1}	2.13	11.46	14.24	2.62
	k_e /M^{-1}·s^{-1}	22.33	23.40	21.49	22.53
	c·k_e /10^6·s^{-1}	446.67	468.00	429.83	450.50
	t_0 /s	122.9	60.8	54.9	114.5
	$t_{1/2}$ /s	199.9	131.2	129.5	190.3
	t_1 /s	276.8	201.6	204.2	266.0

To test if the detected amyloid-like structures in Sup35-NM and Ure2p IBs were able to template the conformational conversion of their respective soluble species into amyloid fibrils we performed aggregation experiments in the presence of preformed and purified IBs. The effect exerted by these aggregates on fibril formation kinetics is analogous to that promoted by the corresponding fibrillar states. Their presence do not affect k_e but increases k_n by three- and seven-fold for Sup35-NM and Ure2p reactions, respectively; shortening the respective lag phases in 26 min and 68 min (Figure 4). Interestingly enough, fibrils and IBs have quantitatively similar effects on the reaction constants for amyloid formation of yeast prionogenic proteins (Table 2).

In contrast to amorphous aggregation, amyloid formation is a specific process that can be seeded by homologous fibrils, but not by fibrils from unrelated polypeptides, even if they share a cross β-sheet conformation [35]. To test if this selectivity also applies in the case of IBs, we performed cross-seeding experiments, seeding the aggregation reaction of Sup35-NM with preformed Ure2p IBs and vice-versa. Importantly, the presence of heterologous prionogenic IBs does not affect the nucleation rates or lag times (Figure 4 and Table 2). This confirms that, as for fibrils, a specific molecular recognition between the soluble species and aggregated polypeptides underlies IBs-promoted fibril seeding.

The morphology of the aggregates in seeded and non-seeded reactions was analyzed by transmission electronic microscopy (TEM) to make sure that the observed increase in aggregation rates results from a faster growth of amyloid material and not from a rapid formation of amorphous assemblies. As shown in Figure 5, regular fibrillar structures were observed in all cases. Interestingly, the morphology of the fibrils formed by seeding with fibrils and IBs of the same protein were similar. Overall, the data allow concluding that the selective intra- and inter-molecular contacts that characterize yeast prions fibrils are established as well by at least a fraction of the polypeptide chains embedded in the intracellular aggregates formed by these proteins in bacteria.

Figure 5 Sup35-NM and Ure2p amyloid fibrils. Morphology of Sup35-NM (A) and Ure2p (B) amyloid-like aggregates observed at the final time point of the aggregation kinetics. Fibrils in un-seeded, seeded and cross-seeded reactions were monitored by transmission electronic microscopy

Sup35-NM IBs are infectious

The Sup35 protein is an eukaryotic release factor, which is required for translation termination in yeast [36,37]. In contrast to [*psi*-] cells, where the Sup35 protein is soluble and functional, [*PSI*+] cells exhibit a nonsense suppressor phenotype due to reduced translation termination efficiency as consequence of the sequestration of native Sup35 into insoluble amyloid structures [38,39]. Both the cellular content of yeast [*PSI*+] cells and the amyloid fibrils formed *in vitro* by purified and soluble Sup35-NM are infectious and suffice to promote the transformation of the [*psi*-] phenotype into the [*PSI*+] if they enter into the cell [40].

The biophysical characterization of Sup35-NM and Ure2p aggregates suggests that these proteins might get access to prion conformations when expressed recombinantly in bacteria. As described above, in the case of Sup35-NM this property can be assessed monitoring the conversion of [*psi*-] yeast cells into [*PSI*+] ones. To test this possibility, we fractionated bacterial cells expressing Sup35-NM. The resulting soluble and insoluble fractions were used to transform spheroplasts of a [*psi*-] yeast strain as described in the Methods section. Bacterial cells expressing an insoluble variant of the spectrin SH3 domain (MAXF-SH3) [41] were processed in the same manner as a control, to make sure that phenotypic conversion is not caused by endogenous bacterial material or by the presence of a generic aggregation-prone protein in the transformation solution. A pESC-URA3 plasmid that allows selecting for the reduced fraction of transformed cells by uracil auxotrophy was added to each of the fractions. Upon spheroplast transformation, yeast cells were grown in uracil-deprived plates. Subsequently, they were streaked in ¼YPD plates. On these plates, [*psi*-] cells are of an intense red color whereas [*PSI*+] cells appear white or pink, depending if they convert to strong or weak [*PSI*+] strains, respectively [42]. No [*PSI*+] colonies were observed for transformations with any of the fractions of MAXF-SH3 expressing cells. In contrast, transformation with the soluble and insoluble fractions of Sup35-NM expressing bacteria resulted in a 1.7% and 3.5% of [*PSI*+] colonies, respectively (Figure 6 and Additional file 1: Table S1). These results are reminiscent of those recently reported by Hochschild and co-workers using a fusion of a Sup35-NM^{R2E2} variant, containing extra copies of the critical oligopeptide repeat region and displaying an increased propensity to convert spontaneously into the prion form in yeast [43], to GFP. They convincingly demonstrated the formation of prionic variants of this protein fusion in bacteria [44]. In our study, we confirmed this behaviour using the wild type Sup35-NM domain without any mutation or fusion that might modify its intrinsic aggregation or conversion propensity [45].

Figure 6 Infectivity of Sup35-NM IBs. Induction of different [*PSI*+] strains upon transformation of a [*psi*-] yeast strain with the soluble (S), insoluble (I) fractions of *E. coli* cells expressing Sup35-NM protein at 18 and 37 º C or purified Sup35-NM IBs. After PEG transformation with the indicated material, yeast cells were recovered on SD-URA and randomly selected colonies were spotted onto ¼ YPD plates to identify [*PSI* $^{+}$] converted colonies. [*psi*-] and [*PSI*+] columns correspond to the parental negative and positive control strains. Transformation with the bacterial material induced pink (weak) and white (strong)

[*PSI*+] phenotypes. Representative images of spots corresponding to distinct strains are shown for each transformed material (see Additional file 1: Table S1 for quantitative data)

An important difference between the results in both studies is that, in the case of the Sup35-NM^{R2E2} -GFP fusion, the co-expression of the yeast New1 prionogenic protein in bacteria appeared as a requirement for prion formation. In contrast, our data argue that the natural bacterial protein machinery suffices to support the formation of prionic conformations, without a requirement for exogenous factors. This apparent discrepancy in the genetic background required for prion formation in bacteria might arise, among other reasons, from the fact that, in our hands, the Hochschild fractionation protocol causes precipitation and loss of most IBs. We thought that, according to their amyloid-like properties, the polypeptides embedded in these aggregates might contribute significantly to infectivity. To confirm this point, we purified Sup35-NM IBs from the insoluble fraction of cells cultured at 37°C and transformed them in [*psi*-] yeast spheroplasts. [*PSI*+] strain conversion occurred at a frequency of 5.6%. 65% of the transformed cells exhibited a weak pink [*PSI*+] phenotype and the rest where white (Figure 6 and Additional file 1: Table S1). Both Sup35-NM IBs induced weak and strong [*PSI*+] phenotypes could be cured when the transformed yeast cells were transiently grown on a medium containing guanidine hydrochloride (Figure 7). Moreover, when cellular extracts of [*PSI*+] yeast cells resulting from IBs transformation were used to transform [*psi*-] spheroplasts, 40% of the resulting colonies converted to [*PSI*+]. These two features are characteristic of [*PSI*+] strains and support an infective prion nature for at least a fraction of the protein embedded in Sup35-NM IBs. Overall, independently of methodological differences, the data in the two studies converge to demonstrate that the bacterial cytosol supports the formation of infective amyloid-like structures.

Figure 7 Curing the Sup35-NM IBs induced [*PSI*+] phenotype. Comparison of spots of control [*psi*-] and [*PSI*+] strains with cells displaying weak and strong [*PSI*+] phenotypes obtained by infection with Sup35-NM IBs. Cells were spotted on ¼ YPD before (left) and after (right) culture on a medium containing 3 mM Gdn·HCl

Temperature dependence of the infectious properties of Sup35-NM aggregates

It is postulated that the existence of distinct amyloid conformations of Sup35-NM accounts for the different [*PSI*+] phenotypes that this prionogenic protein induces in yeast [40,46,47]. *In vitro*, the temperature at which the aggregation of prionogenic proteins occurs might influence the conformational properties of the resulting fibrils [27]. Accordingly, Weissman and co-workers demonstrated that Sup35-NM fibrils formed *in vitro* at different temperatures rendered different [*PSI*+] phenotypes when transformed into [*psi*-] cells. Fibrils formed at 4°C resulted in a majority of [*PSI*+] cells displaying a strong (white) phenotype whereas fibrils formed at 37°C rendered mostly weak (pink) strains [40]. This result is in agreement with our observation that most of the [*PSI*+] yeast strains obtained after transformation with the content of bacterial cells expressing Sup35-NM at 37°C displayed a weak phenotype. We wondered if, by analogy to fibrils, cultivation of Sup35-NM expressing cells at lower temperature would result in a significant increase of transformed cells displaying a strong phenotype. To this aim, Sup35-NM was expressed in bacterial cells grown at 18°C. First, we addressed if production at lower temperature modifies the distribution of recombinant Sup35-NM between the soluble and insoluble fractions. As it can be seen in Figure 8A, at 18°C the fraction of Sup35-NM protein residing in the insoluble fraction is reduced by about five-fold relative to that observed at 37°C, representing 8% of the total recombinant protein. This solubilizing effect of reduced temperature is well-documented for the expression of different

model proteins [48]. Still, when the cellular fractions of these bacterial cells were used to transform [*psi*-] spheroplasts, the conversion efficiency into [*PSI+*] phenotypes was about five-fold higher for the insoluble fraction than for the soluble one (Figure 6 and Additional file 1: Table S1), arguing that Sup35-NM aggregates are enriched in prion conformations relative to the corresponding soluble species. Interestingly enough, the reduction in the production temperature results in a significant increase in the proportion of white colonies (44%) among [*PSI+*] cells (Figure 6 and Additional file 1: Table S1), relative to those observed at 37°C (25%). These data suggest that, in principle, one can modulate the infective properties of prionogenic proteins produced in bacteria by tuning the production conditions. In an effort to decipher the conformational determinants of the differential infective properties of 37 and 18°C insoluble fractions, we purified IBs from the low temperature insoluble fraction, analyzed their FT-IR in the amide I region of the spectra and compared it with the one of IBs obtained at 37°C (Figure 8B). The shapes of both spectra were fairly similar. This is in agreement with previous data in which we show that changes in the temperature of aggregation of Sup35-NM fibrils do not induce dramatic changes in their secondary structure content, as assessed by FT-IR [27]. Nevertheless, certain differences in the contribution of the spectral components to the main spectra could be detected. In particular, the ratio between the contribution of the band at 1628–1629 cm^{-1} and that at 1652–1653 cm^{-1} is higher in the IBs formed at 18°C (0.56) than in the IBs formed at 37°C (0.32) indicating a relative enrichment in intermolecular β-sheet in the 18°C aggregates [49] (Table 1). However, it is important to note that, despite the differences detected in IBs secondary structure content might contribute to the observed phenotypic differences between insoluble fractions, they might also be caused by more subtle conformational features to which FT-IR is blind, as shown for Sup35-NM amyloid fibrils [13].

Figure 8 Solubility and conformational properties of Sup35-NM as a function of the temperature. (A) Western blot of the soluble and insoluble fractions of cells expressing Sup35-NM at 18 and 37°C detected with anti-histag antibody and quantified by Quantity One software. (B) Comparative analysis of the secondary structure of Sup35-NM IBs formed at 18°C and 37°C as determined FT-IR spectroscopy in the amide I region of the spectrum. Empty circles, solid thick lines and solid thin lines show the absorbance spectra, the sum of individual spectral components and the deconvolved component bands, respectively

Conclusions

Prions are misfolded, self-propagating, infectious proteins. The bacterial IBs formed by HET-s PFD have been shown to display an amyloid fold and to be infective [19,20]. We show here that the IBs formed by the yeast Ure2 and Sup35-NM prionogenic proteins have an amyloid nature, while confirming the previous observation that bacteria supports the formation of Sup35-NM prion conformations. Moreover, we prove that a major fraction of the recombinant infective species is embedded in IBs. The formation of infectious prion folds in bacteria can be modulated by the expression conditions, as illustrated here using different growth temperatures. Since proteins accumulate in IBs at high levels and these biological particles are easily purified, it is suggested that they might become a convenient source to obtain prion particles exhibiting strain diversity. Besides, prion producing bacterial cells can potentially be used to develop screens for anti-prion drugs; an approach already validated in yeast models [50,51].

Methods

Protein expression and purification

Plasmids encoding Sup35-NM residues 1 to 254 (NM) C-terminally tagged with 7x-histidine and Ure2p N-terminally tagged with 6x-histidine have been described previously [13,52,53]. The histidine tag does not affect the biological activity of Sup35-NM and Ure2p in *Saccaromyces cerevisiae* [13,54]. The plasmids were transformed into BL21(DE3) pLysS *E. coli* cells. For protein expression, 10 mL overnight culture of transformed cells was used to inoculate 2 L of DYT medium, which was further incubated at 37°C and 250 rpm. At an OD_{600nm} of 0.5, protein expression was induced with 1 mM of isopropyl-1-thio-β-D-galactopyranoside (IPTG) at 37°C for 3 h and 14 h for soluble protein and IBs purification, respectively. The cultures were centrifuged at 8 000 x*g* for 10 min, then resuspended in 20 mL of deionized water, centrifuged at 15 000 x*g* for 10 minutes and the cell pellet frozen at −80°C. For expression experiments at low temperature, cells were initially grown at 37°C until an OD_{600nm} of 0.4, transferred to 18°C for 20 min, induced with 1 mM IPTG and incubated for 14 h.

Ure2p and Sup35-NM proteins were purified from the soluble and insoluble cell fractions, respectively, essentially as previously described [27]. For lysis, cells were resuspended in 5 mL of deionized water and 45 mL of non-denaturing washing buffer (20 mM Tris·HCl at pH 8.0, 0.5 M NaCl) was further added. The cell suspension was placed under gentle agitation for 15 min. Finally, the samples were sonicated with a Branson Sonifier® ultrasonic cell disruptor for 3 min on ice. Soluble and insoluble fractions were separated after cell lysis by centrifugation at 15 000 x*g* for 30 minutes. When required, the insoluble fraction was resuspended in denaturing washing buffer. Affinity chromatography on FF-Histrap resin (Amersham, Uppsala, Sweden) under denaturing (20 mM Tris·HCl at pH 8.0, 0.5 M NaCl, 6 M Gdn·HCl, and 20 mM or 500 mM imidazole for washing and elution buffer, respectively) and non-denaturing conditions (20 mM Tris·HCl at pH 8.0, 0.5 M NaCl, and 20 mM or 500 mM imidazole for washing and elution buffer, respectively) was used for Sup35-NM and Ure2p purfication, respectively. Buffer was exchanged by gel filtration on Sephadex G-25 column (Amersham, Uppsala, Sweden) for native buffer (50 mM Tris·HCl and 150 mM NaCl at pH 7.4).

Sup35-NM and Ure2p IBs purification

IBs were purified from induced cell extracts by detergent-based procedures as previously described [16]. Briefly, cells in a 10 mL culture were harvested by centrifugation at 12 000 x*g* (at 4°C) for 15 min and resuspended in 200 µL of lysis buffer (50 mM Tris·HCl pH 8.0, 1 mM EDTA, 100 mM NaCl), plus 30 µL of 100 mM protease inhibitor PMSF and 6 µL of a 10 mg/mL lysozyme solution. After 30 min of incubation at 37°C under gentle agitation, NP-40 was added at 1% (v/v) and the mixture was incubated at 4°C for 30 min. Then, 3 µL of DNase I and RNase from a 1 mg/mL stock (25µg/mL final concentration) and 3 µL of 1 M $MgSO_4$ were added and the resulting mixture was further incubated at 37°C for 30 min. Protein aggregates were separated by centrifugation at 12 000 x*g* for 15 min at 4°C. Finally, IBs were washed once with the same buffer containing 0.5% Triton X-100 and once with sterile native buffer. After a final centrifugation at 12 000 x*g* for 15 min, pellets were stored at −20°C until analysis. The frozen pellets were reconstituted in native buffer. SDS-PAGE

analysis revealed that in all cases the yeast proteins were the major polypeptidic components of the aggregates.

Fibril formation: aggregation kinetics and seeding assays

For aggregation reactions, 20 μM of soluble Sup35-NM and Ure2p in native buffer were placed under agitation (~750 rpm with micro-stir bars) at 25°C. Conversion of soluble species to aggregates was monitored by quantification of the relative Th-T fluorescence at 480 nm when exciting at 445 nm. In the seeding assay, a solution of yeast prion IBs (to a final OD_{350nm} = 0.125) or 2 μM of preformed fibrils was also added at the beginning of the reaction. Cross-seeding assays were performed in the same manner. Yeast prions aggregation process, as other related amyloid processes, may be modeled as an autocatalytic reaction using the equation $f = (\rho\{\exp[(1 + \rho)kt]-1\})/\{1 + \rho*\exp[(1 + \rho)kt]\}$ under the boundary condition of $t = 0$ and $f = 0$, where $k = k_e a$ (when a is the protein concentration) and ρ represents the dimensionless value to describe the ratio of k_n to k. By non-linear regression of f against t, values of ρ and k can be easily obtained, and from them the rate constants, k_e (elongation constant) and k_n (nucleation constant). The extrapolation of the growth portion of the sigmoid curve to abscissa ($f = 0$), and to the highest ordinate value of the fitted plot, afforded two values of time (t_0 and t_1), which correspond to the lag time and to the time at which the aggregation was almost complete [9,27,55].

Western blots

For Western blotting, bacterial cells were resuspended in lysis buffer and sonicated with a Branson Sonifier® ultrasonic cell disruptor for 3 min on ice. The cellular extract was centrifuged at 12 000 x*g* for 30 min. The soluble fraction was separated and pellet was resuspended exactly in the same volume of lysis buffer. To 50 μL of the soluble and resuspended insoluble fractions, it was added 25 μL of loading buffer (180 mM Tris–HCl pH 7, 30% glycerol, 0.05% bromophenol blue, 9% sodium dodecyl sulfate (SDS) and 15% β-mercaptoethanol) and the mixture was heated at 95°C for 10 minutes. Insoluble and soluble fractions were resolved on 15% SDS–PAGE gels, transferred on to PVDF membranes, and recombinant proteins detected with a polyclonal anti-histag antibody. The membranes were developed with the ECL method [56]. The proportion of proteins in each fraction was determinated using Quantity-One analysis software (Bio-Rad, Hercules, CA, USA).

Spheroplast preparation for transformation

Yeast cells culture

Yeast strains L1749 (*MATα ade1-14 ura3-52 leu2-3,112 trp1-289 his3-200*, [*psi*-], [*PIN*+]) and L1762 (*MATα adel-14 ura3-52 leu2-3,112 trp1-289 his3-200*, Strong [*PSI*+], [*PIN*+]) were kindly provided by Susan Liebman. Yeast strains were grown in solid YEPD medium for 48 h at 30°C; then a colony was inoculated in 10 mL liquid YEPD medium and incubated overnight at 30°C and agitation of 250 rpm. 5 mL of this culture were used to inoculate 50 mL of liquid YEPD at 30°C and 250 rpm. When an OD_{600nm} = 0.5 was reached, the culture was centrifuged at 1 500 x*g* and room temperature for 10 min. Cells were successively washed with 20 mL of sterile water and 1 M sorbitol, and centrifuged at 1500 x*g* and room temperature for 5 min. Yeast cells were resuspended in SCE buffer (1 M sorbitol, 10 mM EDTA, 10 mM DTT, 100 mM sodium citrate at pH 5.8) and divided in 2 tubes.

Lyticase preparation

Lyticase from *Arthrobacter luteus* obtained as lyophilized powder, ≥200 units/mg solid (L4025: Sigma) was prepared at a final concentration of 10 000 units·mL^{-1} in phosphate buffer at pH 7.4 with 50% glycerol and kept at −80°C.

Spheroplast preparation

The first yeast cell tube was used to calculate the optimal spheroplast lyticase digestion time, according to the provider instructions. The second one was incubated with 10 µL of lyticase at 30°C until 85-90% of spheroplasts were reached. The spheroplasts solution was then centrifuged at 750 x*g* and room temperature for 10 minutes. The spheroplasts were gently resuspended and washed successively with 10 mL of 1 M sorbitol and STC buffer (1 M sorbitol, 10 mM $CaCl_2$ and 10 mM Tris·HCl, pH 7.4), and centrifuged at 750 x*g* and room temperature for 10 min. Finally, the spheroplasts were gently resuspended in 100 µL of STC and immediately used.

Spheroplast transformation

25 µL of pelleted spheroplats resuspended in STC buffer were mixed with 3µL of sonicated soluble, insoluble fractions or IBs of Sup35-NM, URA3-marked plasmid (pRS316) (20 µg/mL) and salmon sperm DNA (100 µg/mL). Fusion was induced by addition of 9 volumes of PEG buffer (20% (w/v) PEG 8000, 10 mM $CaCl_2$, 10 mM Tris·HCl at pH 7.5) for 30 min. Cells were centrifuged at 750 x*g* and room temperature for 10 min, and resuspended in SOS buffer (1 M sorbitol, 7 mM $CaCl_2$, 0.25% yeast extract, 0.5% bacto-peptone), incubated at 30°C for 30 min and plated on synthetic medium lacking uracil overlaid with top agar (2.5% agar).

Analysis of prion phenotypes

After growth on synthetic medium lacking uracil (for >5 days), the efficiency of conversion from [*psi*-] to [*PSI*+] was tested by the following colour assay. Transformants were randomly selected and streaked onto ¼ YPD plates to enhance the colour phenotype. After 3 days the streaked colonies were classified as strong [*PSI*+] (white), weak [*PSI*+] (pink) and [*psi*-] (red) strains. The obtained conversion percentages result from the analysis of >500 colonies for each transformation assay.

Conversion from [PSI+] to [psi-] strains

Yeast strains with different phenotypes were grown in YEPD medium containing 3 mM of Gdn·HCl for 48 h at 30°C to cure the [*PSI*+] phenotype. The conversion from [*PSI*+] to [*psi*-] phenotype was assessed by spotting cells onto ¼ YPD plates.

Secondary structure determination

ATR FT-IR spectroscopy analyses of Sup35-NM and Ure2p IBs were performed using a Bruker Tensor 27 FT-IR Spectrometer (Bruker Optics Inc) with a Golden Gate MKII ATR accessory. Each spectrum consists of 16 independent scans, measured at a spectral resolution of 1 cm^{-1} within the 1700–1500 cm^{-1} range. All spectral data were acquired and normalized

using the OPUS MIR Tensor 27 software. FT-IR spectra were fitted to five overlapping Gaussian curves and the amplitude, centre, and bandwidth at half of the maximum amplitude and area of each Gaussian function were calculated using a nonlinear peak fitting program (PeakFit package, Systat Software, San Jose, CA).

Chemical denaturation

For stability assays, purified IBs were prepared at OD_{350nm} = 1 in native buffer containing selected concentrations of guanidine hydrochloride (Gdn·HCl) ranging from 0 to 8 M. The reactions were allowed to reach equilibrium by incubating them for 20 h at room temperature. The fraction of soluble protein (f_S) was calculated from the fitted values using equation: $f_S = 1-((y_S-y)/(y_S-y_A))$, where y_S and y_A are the absorbance at 350 nm of the soluble and aggregated protein, respectively, and y is the absorbance of the protein solution as a function of the denaturant concentration.

The value $m_{1/2}$ was calculated as the denaturant concentration at which $f_S = 1/2$. $OD_{350\ nm}$ changes were monitored with a Cary400 Varian spectrophotometer.

Binding of amyloid dyes to Sup35-NM and Ure2p IBs and amyloid fibrils

The interaction of 10 μM of Congo-Red (CR) with Sup35-NM and Ure2p IBs and fibrils was tested using a Cary100 UV/Vis spectrophotometer (Varian, Palo Alto, CA, USA) by recording the absorbance spectra from 375 nm to 675 nm using a matched pair of quartz cuvettes of 1 cm optical length placed in a thermostated cell holder at 25°C. In order to detect the typical amyloid band at ~541 nm, differential CR spectra in the presence and absence of protein were used.

The binding of 25 μM of Thioflavin-T (Th-T) to Sup35-NM and Ure2p was recorded using a Cary Eclipse spectrofluorometer (Varian, Palo Alto, CA, USA) with an excitation wavelength of 445 nm and emission range from 470 nm to 570 nm at 25°C in native buffer. For the staining assays with Thioflavin-S (Th-S), Sup35-NM and Ure2p IBs were incubated for 1 h in the presence of 125 μM of dye. After centrifugation (14 000 x*g* for 5 min), the precipitated fraction was placed on a microscope slide and sealed. Images of Sup35-NM and Ure2p IBs and fibrils bound to Th-S were obtained at 40-fold magnification under UV light or using phase contrast in a Leica fluorescence microscope (Leica DMRB, Heidelberg, Germany).

Transmission electronic microscopy

Fibrils containing solutions were placed on carbon-coated copper grids, and left to stand for five minutes. The grids were washed with distilled water and stained with 2% (w/v) uranyl acetate for another two minutes before analysis using a HitachiH-7000 transmission electron microscope (Hitachi, Tokyo, Japan) operating at accelerating voltage of 75 kV.

Competing interests

The authors declare that they have no competing interests.

Authors' contributions

SV and RS supervised the project, designed the study and drafted the manuscript. AE carried out most of the experiments. AVP participated in the experimental work. All authors read and approved the final manuscript.

Acknowledgements

This work was supported by grants BFU2010-14901 from Ministerio de Ciencia e Innovación (Spain) and 2009-SGR 760 from AGAUR (Generalitat de Catalunya). RS is beneficiary of a contract from the Ramón y Cajal Programme from Ministerio de Ciencia e Innovación. SV has been granted an ICREA ACADEMIA award (ICREA).

References

1. Aguzzi A, Weissmann C: **Prion diseases.** *Haemophilia* 1998, **4**(4):619–627.

2. Wickner RB, Edskes HK, Shewmaker F, Nakayashiki T: **Prions of fungi: inherited structures and biological roles.** *Nat Rev Microbiol* 2007, **5**(8):611–618.

3. McGlinchey RP, Kryndushkin D, Wickner RB: **Suicidal [PSI+] is a lethal yeast prion.** *Proc Natl Acad Sci U S A* 2011, **108**(13):5337–5341.

4. Wickner RB, Edskes HK, Bateman D, Kelly AC, Gorkovskiy A: **The yeast prions [PSI+] and [URE3] are molecular degenerative diseases.** *Prion* 2011, **5**(4**)**.

5. Halfmann R, Jarosz DF, Jones SK, Chang A, Lancaster AK, Lindquist S: **Prions are a common mechanism for phenotypic inheritance in wild yeasts.** *Nature* 2012, **482**(7385):363–368.

6. Shorter J, Lindquist S: **Prions as adaptive conduits of memory and inheritance.** *Nat Rev Genet* 2005, **6**(6):435–450.

7. Prusiner SB, Scott MR, DeArmond SJ, Cohen FE: **Prion protein biology.** *Cell* 1998, **93:**337–348.

8. Baskakov IV, Legname G, Baldwin MA, Prusiner SB, Cohen FE: **Pathway complexity of prion protein assembly into amyloid.** *J Biol Chem* 2002, **277**(24):21140–21148.

9. Sabate R, Castillo V, Espargaro A, Saupe SJ, Ventura S: **Energy barriers for HET-s prion forming domain amyloid formation.** *FEBS J* 2009, **276**(18):5053–5064.

10. Patino MM, Liu JJ, Glover JR, Lindquist S: **Support for the prion hypothesis for inheritance of a phenotypic trait in yeast.** *Science* 1996, **273**(5275):622–626.

11. Legname G, Baskakov IV, Nguyen HO, Riesner D, Cohen FE, DeArmond SJ, Prusiner SB: **Synthetic mammalian prions.** *Science* 2004, **305**(5684):673–676.

12. Castilla J, Saa P, Hetz C, Soto C: **In vitro generation of infectious scrapie prions.** *Cell* 2005, **121**(2):195–206.

13. Tanaka M, Chien P, Naber N, Cooke R, Weissman JS: **Conformational variations in an infectious protein determine prion strain differences.** *Nature* 2004, **428**(6980):323–328.

14. Sabate R, de Groot NS, Ventura S: **Protein folding and aggregation in bacteria.** *Cell Mol Life Sci* 2010, **67**(16):2695–2715.

15. de Groot NS, Sabate R, Ventura S: **Amyloids in bacterial inclusion bodies.** *Trends Biochem Sci* 2009, **34**(8):408–416.

16. Morell M, Bravo R, Espargaro A, Sisquella X, Aviles FX, Fernandez-Busquets X, Ventura S: **Inclusion bodies: specificity in their aggregation process and amyloid-like structure.** *Biochim Biophys Acta* 2008, **1783**(10):1815–1825.

17. Carrio M, Gonzalez-Montalban N, Vera A, Villaverde A, Ventura S: **Amyloid-like properties of bacterial inclusion bodies.** *J Mol Biol* 2005, **347:**1025–1037.

18. Wang L, Maji SK, Sawaya MR, Eisenberg D, Riek R: **Bacterial inclusion bodies contain amyloid-like structure.** *PLoS Biol* 2008, **6**(8):e195.

19. Sabate R, Espargaro A, Saupe SJ, Ventura S: **Characterization of the amyloid bacterial inclusion bodies of the HET-s fungal prion.** *Microb Cell Fact* 2009, **8:**56.

20. Wasmer C, Benkemoun L, Sabate R, Steinmetz MO, Coulary-Salin B, Wang L, Riek R, Saupe SJ, Meier BH: **Solid-state NMR spectroscopy reveals that E. coli inclusion bodies of HET-s(218–289) are amyloids.** *Angew Chem Int Ed Engl* 2009, **48**(26):4858–4860.

21. Ritter C, Maddelein ML, Siemer AB, Luhrs T, Ernst M, Meier BH, Saupe SJ, Riek R: **Correlation of structural elements and infectivity of the HET-s prion.** *Nature* 2005, **435**(7043):844–848.

22. Nelson R, Sawaya MR, Balbirnie M, Madsen AO, Riekel C, Grothe R, Eisenberg D: **Structure of the cross-beta spine of amyloid-like fibrils.** *Nature* 2005, **435**(7043):773–778.

23. Fernandez-Busquets X, de Groot NS, Fernandez D, Ventura S: **Recent structural and computational insights into conformational diseases.** *Curr Med Chem* 2008, **15**(13):1336–1349.

24. Fink AL: **Protein aggregation: folding aggregates, inclusion bodies and amyloid.** *Fold Des* 1998, **3:**R9–23.

25. Ami D, Natalello A, Taylor G, Tonon G, Maria Doglia S: **Structural analysis of protein inclusion bodies by Fourier transform infrared microspectroscopy.** *Biochim Biophys Acta* 2006, **1764**(4):793–799.

26. Dasari M, Espargaro A, Sabate R, Lopez Del Amo JM, Fink U, Grelle G, Bieschke J, Ventura S, Reif B: **Bacterial Inclusion Bodies of Alzheimer's Disease beta-Amyloid**

Peptides Can Be Employed To Study Native-Like Aggregation Intermediate States. *ChemBioChem* 2011, **12**(3):407–423.

27. Sabate R, Villar-Pique A, Espargaro A, Ventura S: **Temperature dependence of the aggregation kinetics of Sup35 and Ure2p yeast prions.** *Biomacromolecules* 2012, **13**(2):474–483.

28. Bousset L, Briki F, Doucet J, Melki R: **The native-like conformation of Ure2p in fibrils assembled under physiologically relevant conditions switches to an amyloid-like conformation upon heat-treatment of the fibrils.** *J Struct Biol* 2003, **141**(2):132–142.

29. Espargaro A, Sabate R, Ventura S: **Kinetic and thermodynamic stability of bacterial intracellular aggregates.** *FEBS Lett* 2008, **582**(25–26):3669–3673.

30. Bousset L, Thomson NH, Radford SE, Melki R: **The yeast prion Ure2p retains its native alpha-helical conformation upon assembly into protein fibrils in vitro.** *EMBO J* 2002, **21**(12):2903–2911.

31. Hess S, Lindquist SL, Scheibel T: **Alternative assembly pathways of the amyloidogenic yeast prion determinant Sup35-NM.** *EMBO Rep* 2007, **8**(12):1196–1201.

32. Caughey B, Raymond GJ, Callahan MA, Wong C, Baron GS, Xiong LW: **Interactions and conversions of prion protein isoforms.** *Adv Protein Chem* 2001, **57:**139–169.

33. Wickner RB, Taylor KL, Edskes HK, Maddelein ML, Moriyama H, Roberts BT: **Yeast prions act as genes composed of self-propagating protein amyloids.** *Adv Protein Chem* 2001, **57:**313–334.

34. Serio TR, Lindquist SL: **The yeast prion [PSI+]: molecular insights and functional consequences.** *Adv Protein Chem* 2001, **59:**391–412.

35. Krebs MR, Morozova-Roche LA, Daniel K, Robinson CV, Dobson CM: **Observation of sequence specificity in the seeding of protein amyloid fibrils.** *Protein Sci* 2004, **13**(7):1933–1938.

36. Frolova L, Le Goff X, Rasmussen HH, Cheperegin S, Drugeon G, Kress M, Arman I, Haenni AL, Celis JE, Philippe M, *et al*: **A highly conserved eukaryotic protein family possessing properties of polypeptide chain release factor.** *Nature* 1994, **372**(6507):701–703.

37. Stansfield I, Jones KM, Kushnirov VV, Dagkesamanskaya AR, Poznyakovski AI, Paushkin SV, Nierras CR, Cox BS, Ter-Avanesyan MD, Tuite MF: **The products of the SUP45 (eRF1) and SUP35 genes interact to mediate translation termination in Saccharomyces cerevisiae.** *EMBO J* 1995, **14**(17):4365–4373.

38. Liebman SW, Derkatch IL: **The yeast [PSI+] prion: making sense of nonsense.** *J Biol Chem* 1999, **274**(3):1181–1184.

39. Eaglestone SS, Cox BS, Tuite MF: **Translation termination efficiency can be regulated in Saccharomyces cerevisiae by environmental stress through a prion-mediated mechanism.** *EMBO J* 1999, **18**(7):1974–1981.

40. Tanaka M, Collins SR, Toyama BH, Weissman JS: **The physical basis of how prion conformations determine strain phenotypes.** *Nature* 2006, **442**(7102):585–589.

41. Castillo V, Espargaro A, Gordo V, Vendrell J, Ventura S: **Deciphering the role of the thermodynamic and kinetic stabilities of SH3 domains on their aggregation inside bacteria.** *Proteomics* 2010, **10**(23):4172–4185.

42. Serio TR, Cashikar AG, Moslehi JJ, Kowal AS, Lindquist SL: **Yeast prion [psi +] and its determinant, Sup35p.** *Methods Enzymol* 1999, **309:**649–673.

43. Liu JJ, Lindquist S: **Oligopeptide-repeat expansions modulate 'protein-only' inheritance in yeast.** *Nature* 1999, **400**(6744):573–576.

44. Garrity SJ, Sivanathan V, Dong J, Lindquist S, Hochschild A: **Conversion of a yeast prion protein to an infectious form in bacteria.** *Proc Natl Acad Sci U S A* 2010, **107**(23):10596–10601.

45. Bulone D, Masino L, Thomas DJ, San Biagio PL, Pastore A: **The interplay between PolyQ and protein context delays aggregation by forming a reservoir of protofibrils.** *PLoS One* 2006, **1:**e111.

46. King CY, Diaz-Avalos R: **Protein-only transmission of three yeast prion strains.** *Nature* 2004, **428**(6980):319–323.

47. Diaz-Avalos R, King CY, Wall J, Simon M, Caspar DL: **Strain-specific morphologies of yeast prion amyloid fibrils.** *Proc Natl Acad Sci U S A* 2005, **102**(29):10165–10170.

48. Sorensen HP, Mortensen KK: **Soluble expression of recombinant proteins in the cytoplasm of Escherichia coli.** *Microb Cell Fact* 2005, **4:**1.

49. Gonzalez-Montalban N, Garcia-Fruitos E, Ventura S, Aris A, Villaverde A: **The chaperone DnaK controls the fractioning of functional protein between soluble and insoluble cell fractions in inclusion body-forming cells.** *Microb Cell Fact* 2006, **5:**26.

50. Bach S, Talarek N, Andrieu T, Vierfond JM, Mettey Y, Galons H, Dormont D, Meijer L, Cullin C, Blondel M: **Isolation of drugs active against mammalian prions using a yeast-based screening assay.** *Nat Biotechnol* 2003, **21**(9):1075–1081.

51. Bach S, Tribouillard D, Talarek N, Desban N, Gug F, Galons H, Blondel M: **A yeast-based assay to isolate drugs active against mammalian prions.** *Methods* 2006, **39**(1):72–77.

52. DePace AH, Santoso A, Hillner P, Weissman JS: **A critical role for amino-terminal glutamine/asparagine repeats in the formation and propagation of a yeast prion.** *Cell* 1998, **93**(7):1241–1252.

53. Ross ED, Baxa U, Wickner RB: **Scrambled prion domains form prions and amyloid.** *Mol Cell Biol* 2004, **24**(16):7206–7213.

54. Immel F, Jiang Y, Wang YQ, Marchal C, Maillet L, Perrett S, Cullin C: **In vitro analysis of SpUre2p, a prion-related protein, exemplifies the relationship between amyloid and prion.** *J Biol Chem* 2007, **282**(11):7912–7920.

55. Sabate R, Gallardo M, Estelrich J: **An autocatalytic reaction as a model for the kinetics of the aggregation of beta-amyloid.** *Biopolymers* 2003, **71**(2):190–195.

56. Morell M, Espargaro A, Aviles FX, Ventura S: **Detection of transient protein-protein interactions by bimolecular fluorescence complementation: the Abl-SH3 case.** *Proteomics* 2007, **7**(7):1023–1036.

Additional file

Additional_file_1 as DOC

Additional file 1: Table S1 Apparition frequencies of weak and strong [*PSI+*] phenotypes in the transformation of [*psi-*] yeast strain with the soluble, insoluble fractions of *E. coli* cells expressing Sup35-NM protein at 18º and 37ºC or purified Sup35-NM IBs.

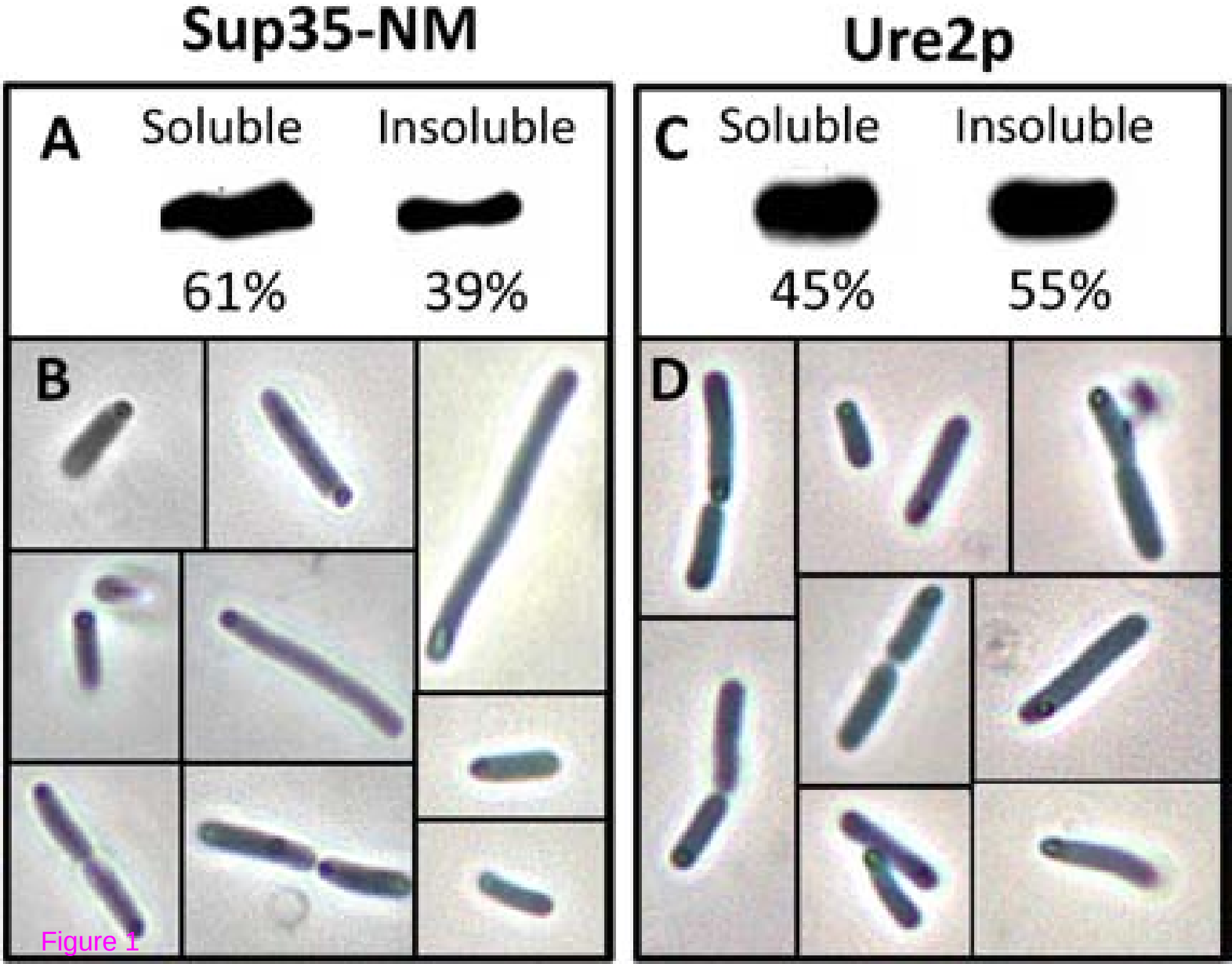
Sup35-NM
Ure2p
A
Soluble
Insoluble
61%
39%
C
Soluble
Insoluble
45%
55%
B
D

Figure 1

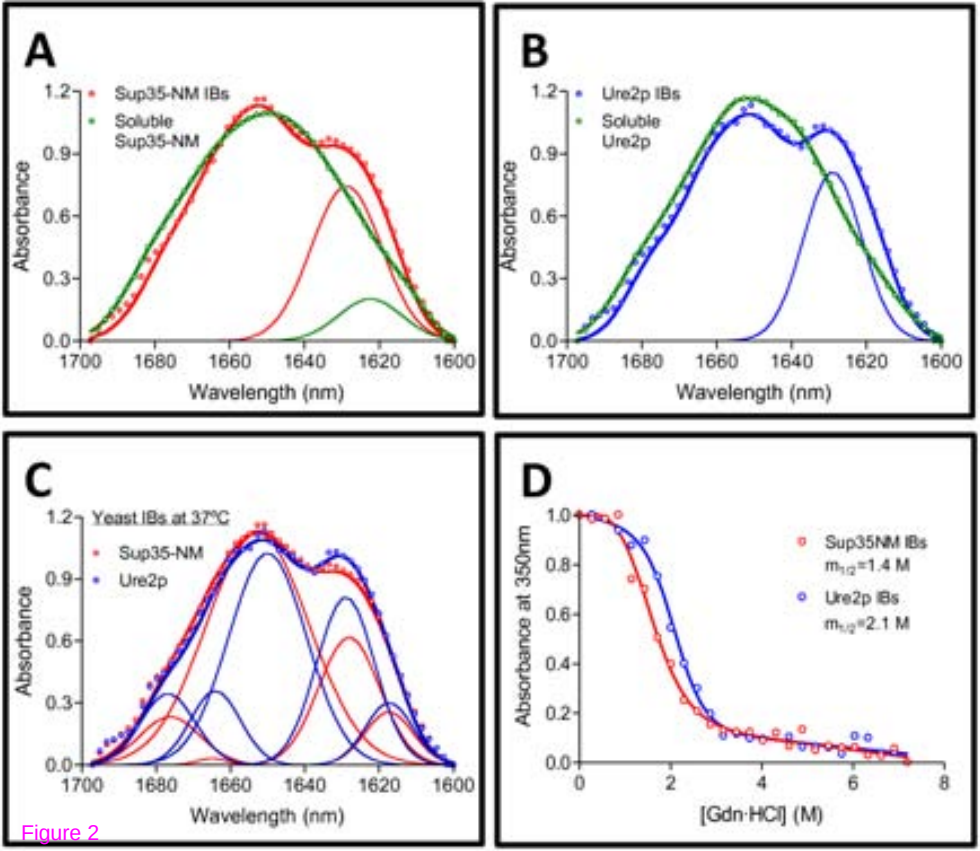
A
Sup35-NM IBs
Soluble Sup35-NM
Absorbance
Wavelength (nm)
B
Ure2p IBs
Soluble Ure2p
Absorbance
Wavelength (nm)
C
Yeast IBs at 37°C
Sup35-NM
Ure2p
Absorbance
Wavelength (nm)
D
Sup35NM IBs
m1/2=1.4 M
Ure2p IBs
m1/2=2.1 M
Absorbance at 350nm
[Gdn·HCl] (M)

Figure 2

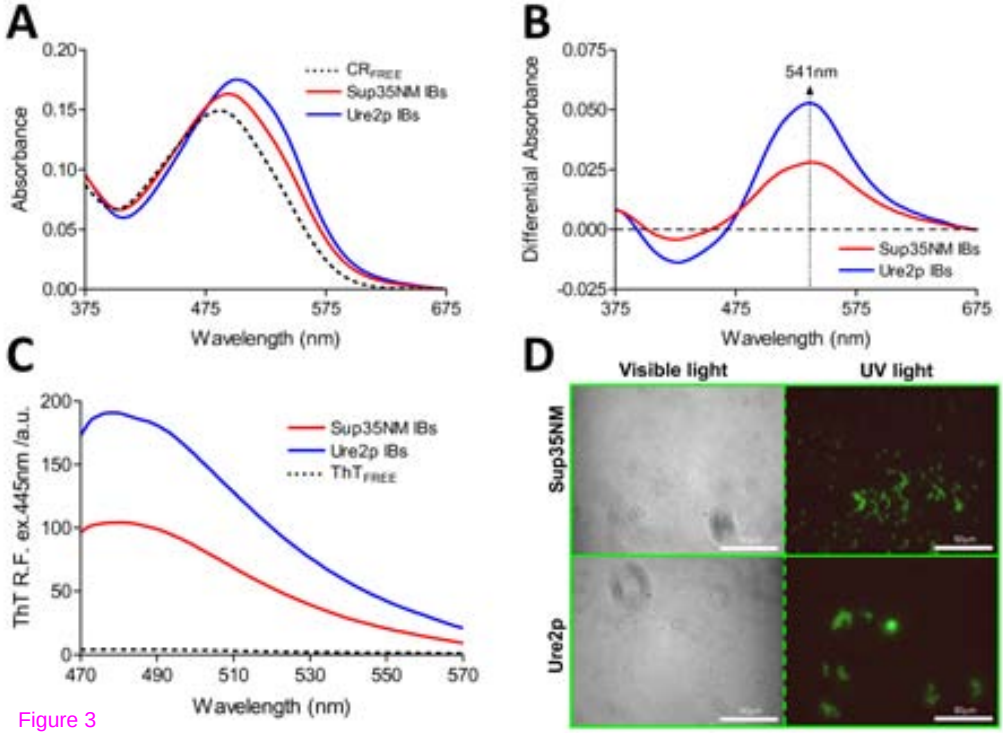
A
Absorbance
0.20
0.15
0.10
0.05
0.00
375
475
575
675
Wavelength (nm)
CR FREE
Sup35NM IBs
Ure2p IBs
B
Differential Absorbance
0.075
0.050
0.025
0.000
-0.025
541nm
375
475
575
675
Wavelength (nm)
Sup35NM IBs
Ure2p IBs
C
ThT R.F. ex.445nm /a.u.
200
150
100
50
0
470
490
510
530
550
570
Wavelength (nm)
Sup35NM IBs
Ure2p IBs
ThT FREE
D
Visible light
UV light
Sup35NM
Ure2p

Figure 3

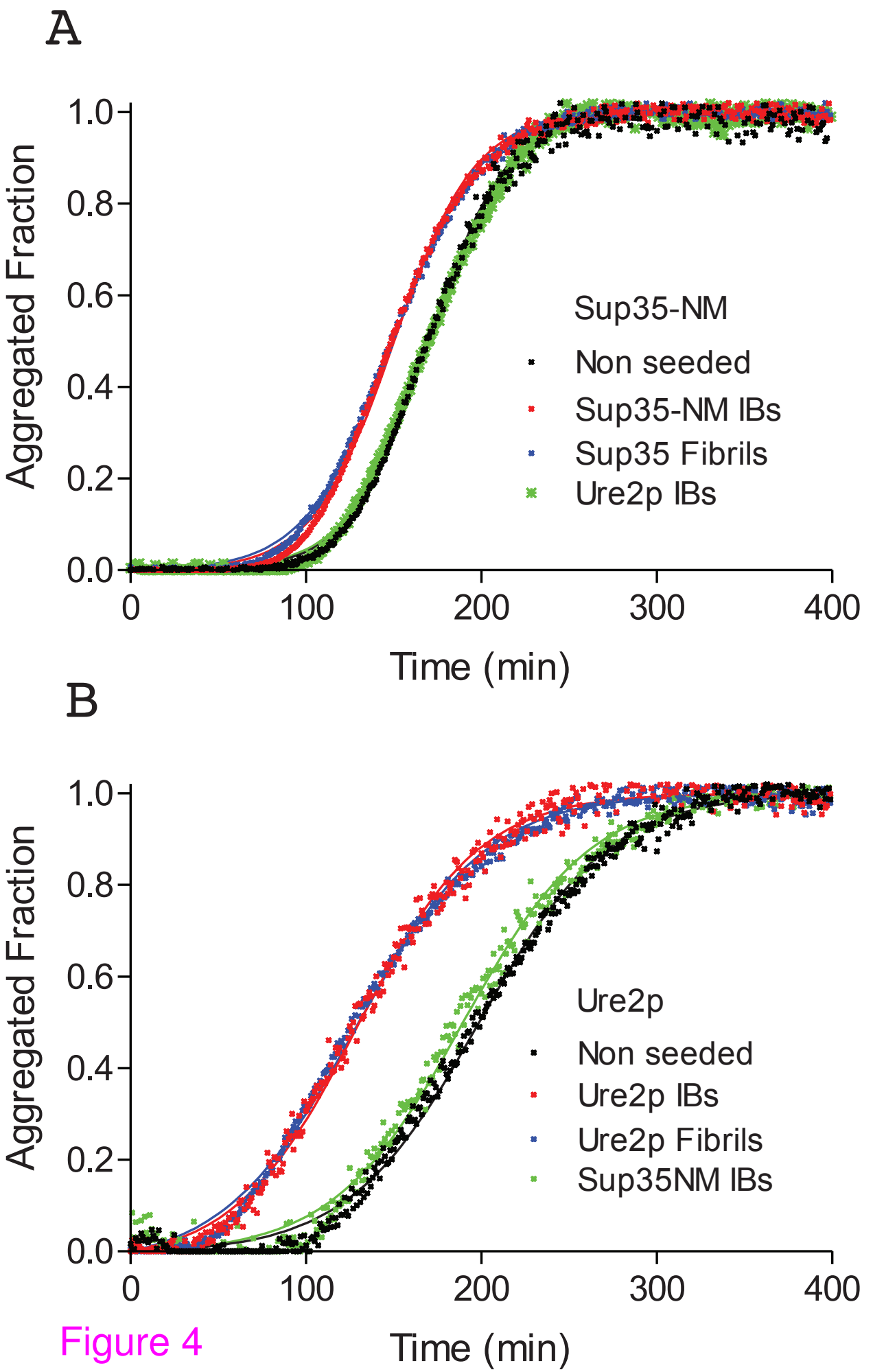
A
1.0
0.8
0.6
0.4
0.2
0.0
Aggregated Fraction
Sup35-NM
Non seeded
Sup35-NM IBs
Sup35 Fibrils
Ure2p IBs
0
100
200
300
400
Time (min)
B
1.0
0.8
0.6
0.4
0.2
0.0
Aggregated Fraction
Ure2p
Non seeded
Ure2p IBs
Ure2p Fibrils
Sup35NM IBs
0
100
200
300
400
Time (min)

Figure 4

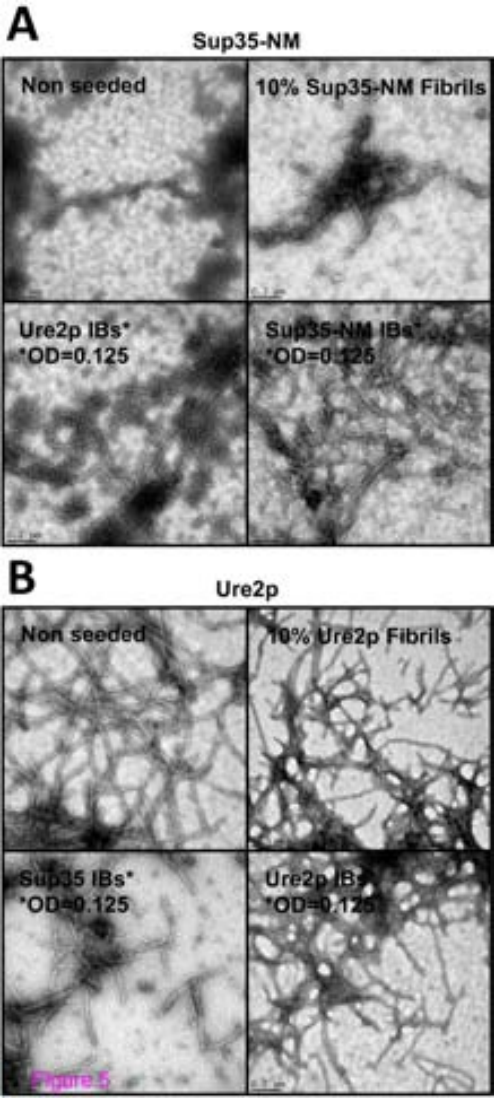
A
Sup35-NM
Non seeded
10% Sup35-NM Fibrils
Ure2p IBs*
*OD=0.125
Sup35-NM IBs*
*OD=0.125
B
Ure2p
Non seeded
10% Ure2p Fibrils
Sup35 IBs*
*OD=0.125
Ure2p IBs*
*OD=0.125
Figure 5

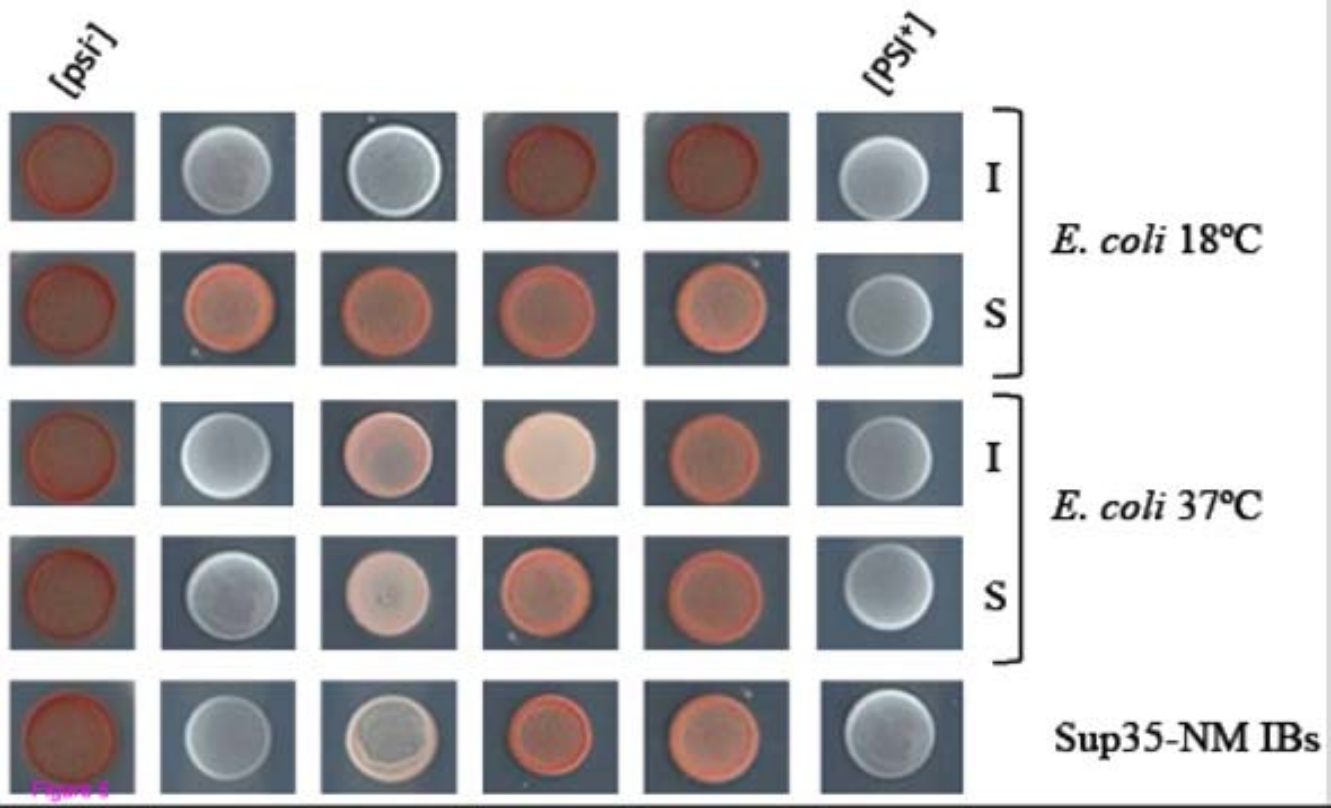
[psi⁻]
[PSI⁺]
I
S
E. coli 18°C
I
S
E. coli 37°C
Sup35-NM IBs

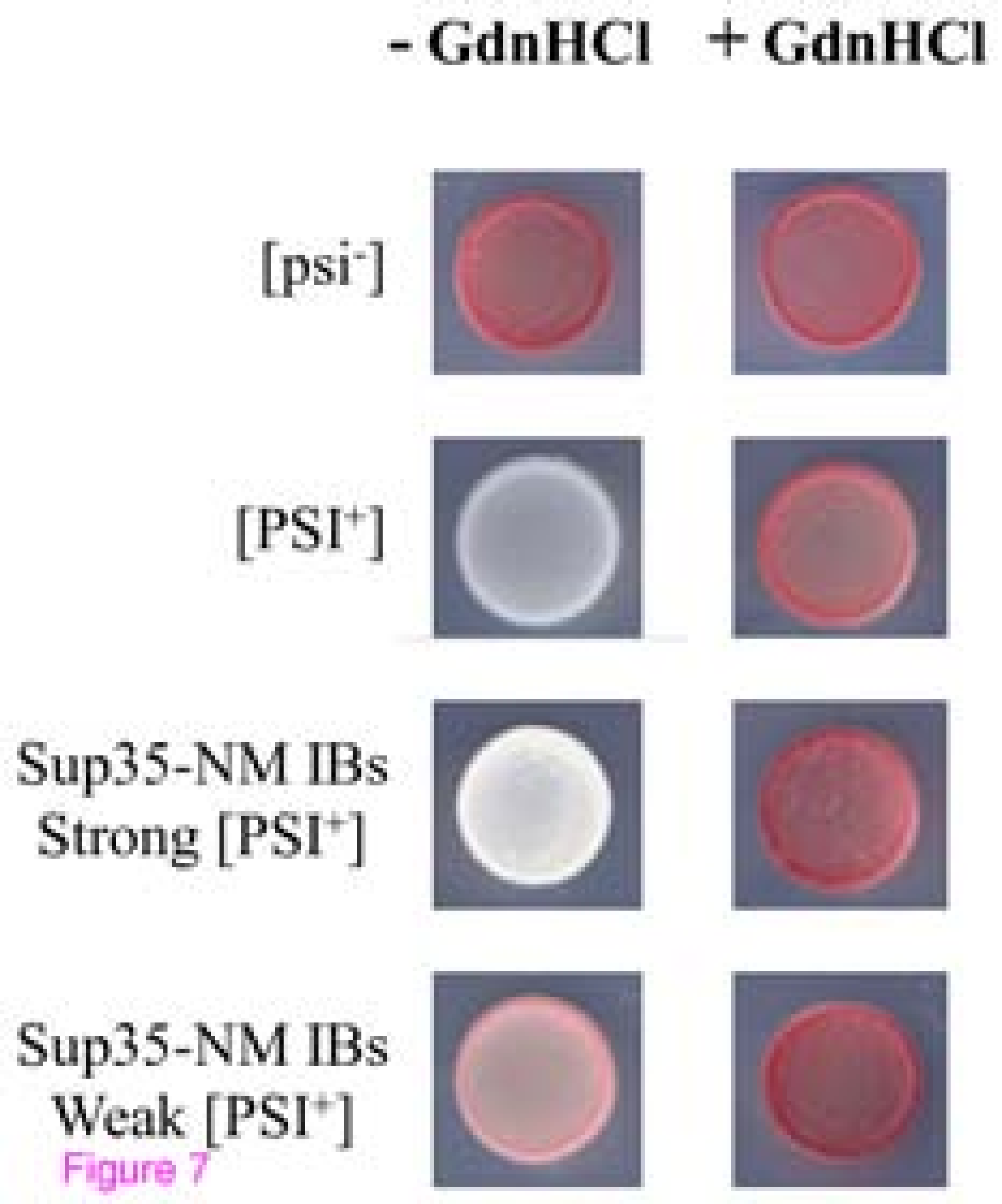
- GdnHCl
+ GdnHCl
[psi-]
[PSI+]
Sup35-NM IBs
Strong [PSI+]
Sup35-NM IBs
Weak [PSI+]

Figure 7

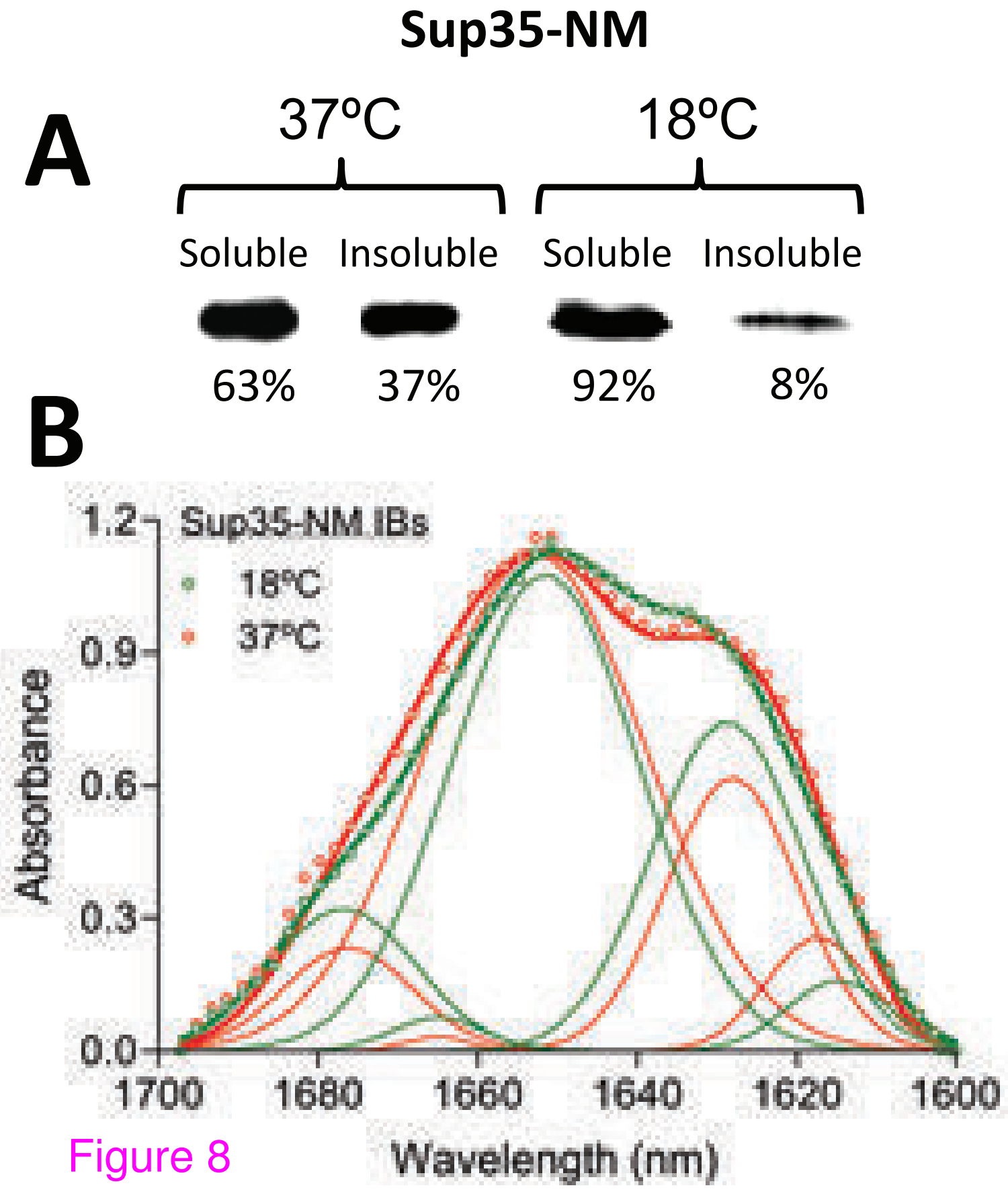
Sup35-NM
A
37ºC
18ºC
Soluble
Insoluble
Soluble
Insoluble
63%
37%
92%
8%
B
Sup35-NM IBs
18ºC
37ºC
Absorbance
1.2
0.9
0.6
0.3
0.0
1700
1680
1660
1640
1620
1600
Wavelength (nm)

Figure 8

Additional files provided with this submission:

Additional file 1: 1633404618672777_add1.doc, 161K
http://www.microbialcellfactories.com/imedia/2059202001753456/supp1.doc

Molecular BioSystems

Cite this: DOI: 10.1039/c2mb25214g

www.rsc.org/molecularbiosystems

METHOD

Thioflavin-S staining coupled to flow cytometry. A screening tool to detect *in vivo* protein aggregation

Alba Espargaró,[a] Raimon Sabate*[bc] and Salvador Ventura*[ad]

Received 30th May 2012, Accepted 23rd July 2012
DOI: 10.1039/c2mb25214g

Amyloid deposits are associated with an increasing number of human disorders, including Alzheimer's and Parkinson's diseases. Recent studies provide compelling evidence for the existence of amyloid-like conformations in the insoluble bacterial inclusion bodies (IBs) produced during the recombinant expression of amyloidogenic proteins. This makes prokaryotic cells a physiologically relevant system to study the mechanisms of *in vivo* amyloid deposition. We show here that the application of flow cytometry to detect Thioflavin-S (Th-S) fluorescence provides a fast, robust, quantitative, non-invasive method to screen for the presence of *in vivo* intracellular amyloid-like aggregates in bacteria, with potential application in the analysis of the impact of genetic mutations or chemical compounds on the aggregation of disease-associated polypeptides.

Introduction

Protein misfolding and aggregation into fibrillar structures appear as the fundamental cause behind multiple human disorders of growing incidence in our aging society, such as Alzheimer's (AD) and Parkinson's (PD) diseases.[1,2] Amyloid fibrils are thread-like protein aggregates with a core region formed by repetitive arrays of β-sheets oriented perpendicular to the fibril axis, forming a characteristic cross-β structure.[3] Since in 1855 Virchow first identified amyloid deposits on the basis of a blue staining reaction with iodine followed by treatment with acid,[4] large efforts have been devoted to the detection of *in vitro* and *ex vivo* amyloid-like aggregates. Although many dyes, like acridine orange,[5] chrysamine G,[6] pinacyanol[7] or Nile red,[8] have been shown to be useful for amyloid detection; Congo Red (CR)[9–11] and thioflavins *viz.* Thioflavin-S and T (Th-S and Th-T)[9,12] have become the most popular amyloid specific dyes for histology staining and biophysical studies. Upon binding to amyloids, thioflavins experiment an intensity increase and a maximum shift of their fluorescence spectra when excited using UV or blue light.[13] Th-S is a homogenous mixture of compounds that results from the methylation of dehydrothiotoluidine with sulfonic acid. It binds to amyloid fibrils, but not to soluble monomers and oligomers.[14] Whereas Th-T is the preferred dye for *in vitro* studies, it is not usually used as histological stain for amyloid. In contrast, Th-S, together with CR, is a routine diagnostic compound for the presence of plaques and tangles in post-mortem brain sections of AD patients[15] and the preferred thioflavin for *in vivo* amyloid staining.[16,17]

Recombinant protein production is an essential tool for the biotechnology industry and also supports expanding areas of basic and biomedical research, including structural genomics and proteomics.[18] A common limitation for the production of eukaryotic proteins in bacteria is the formation of insoluble protein aggregates known as inclusion bodies (IBs).[19] Although IBs were considered as "molecular dust-balls" composed of disorderly deposited proteins joined by unspecific hydrophobic contacts, recent studies provide compelling evidence for the existence of highly ordered amyloid-like structures inside these intracellular aggregates.[20–22] This is particularly true, for amyloidogenic proteins and peptides.[19,23–25] In this way, using H/D exchange NMR experiments we have been able to show that for the AD linked peptide Aβ42, the conformations inside IBs resemble at the molecular level those present in neurotoxic fibrils, explaining why these bacterial intracellular aggregates are highly toxic to neuroblastoma cells.[25] Moreover, we have shown that the accumulation of amyloidogenic IBs in bacteria impairs cellular division and promote aging.[26] Therefore, prokaryotic cells have become a powerful system to study the mechanisms of *in vivo* amyloid aggregation as well as their cellular effects.

In the present work, we exploit the unique ability of Th-S to penetrate biological membranes and accumulate in amyloid deposits[27] to develop a technically straightforward method that allows detecting the presence of amyloid-like protein conformations inside living bacterial cells using the high-speed

[a] *Institut de Biotecnologia i Biomedicina, Universitat Autònoma de Barcelona, 08193-Bellaterra, Barcelona, Spain. E-mail: salvador.ventura@uab.es; Fax: +34-935811264; Tel: +34-935868147*
[b] *Departament de Fisicoquímica, Facultat de Farmàcia, Universitat de Barcelona, Avda. Joan XXIII s/n, E-08028-Barcelona, Spain. E-mail: rsabate@ub.edu; Fax: +34-93-4035987; Tel: +34-934035986*
[c] *Institut de Nanociència i Nanotecnologia (IN²UB), Spain*
[d] *Departament de Bioquímica i Biologia Molecular, Universitat Autònoma de Barcelona, 08193-Bellaterra, Barcelona, Spain*

multi-parametric data acquisition and analysis properties of Flow Cytometry (FC).

Results and discussion

The spectrin SH3 (SPC-SH3) is a small globular 62-residue protein domain. It consists of two β-sheets that form an orthogonal sandwich structure.[28] In previous works we have designed and produced a large number of SPC-SH3 mutants displaying a broad range of solubility when produced in *E. coli*, from totally soluble to totally insoluble.[2,29,30] For this work we have selected the C8A-I53V, Best2 and D48G-2Y variants. C8A-I53V is highly stable and soluble *in vitro* and localizes preferment in the soluble fraction when expressed in bacteria. Best2 and D48G-2Y variants are destabilized domains that form amyloid structures *in vitro* and amyloid-like IBs inside bacteria. We tested if Th-S staining allows visualizing the intracellular aggregated state of the amyloidogenic mutants using microscopy under UV-light. As it can be seen in Fig. 1, Best2 and D48G-2Y IBs are selectively stained inside living bacterial cells yielding a strong green-yellow fluorescence. In contrast, no specific staining was observed in cells expressing the soluble C8A-I53V variant. Therefore, Th-S allows us to distinguish between the intracellular accumulation of soluble and amyloidogenic SH3 variants.

As stated above, the aggregation of amyloidogenic polypeptides inside bacteria might promote severe cell division defects.[26] The use of Th-S staining allows monitoring this effect *in vivo*. In Fig. 1 it can be observed how cells expressing the highly amyloidogenic D48G-2Y domain[30] become elongated and accumulate multiple Th-S positive IBs as a result of their inability to divide.

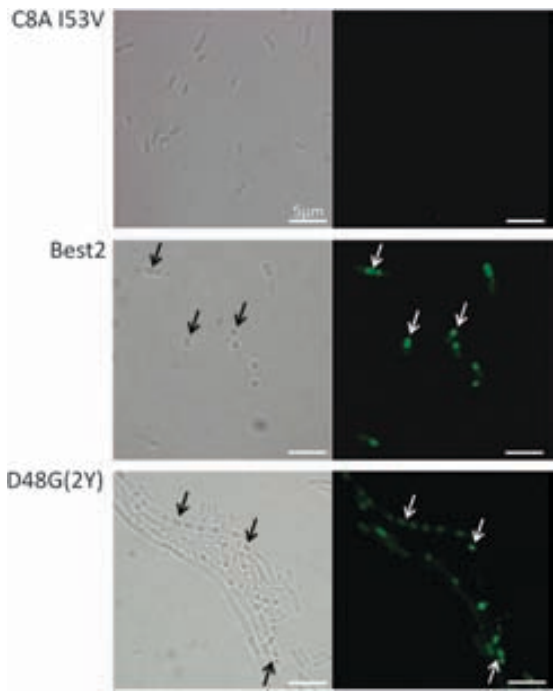

Fig. 1 Optical fluorescence microscopy images of bacterial cells expressing SPC-SH3 mutants stained with Th-S. Left and right panels correspond to phase-contrast microscopy and fluorescence microscopy under UV light, respectively. Arrows indicate the position of IBs. Scale bars correspond to 5 μm.

To confirm that the capacity of Th-S to stain intracellular amyloid-like IBs is a generic property of the dye, we further analyzed two related, physiologically relevant, model peptides: Aβ40 and Aβ42. We have shown before that inside bacteria these peptides form small IBs that once purified fulfil all the requirements to be classified as amyloids: they seed fibril growth, are Congo red positive and show characteristic β-sheet-rich circular dichroism and infra red spectra.[25] In Fig. 2A we show that these IBs also bind Th-S yielding a bright green-yellow fluorescence against a dark background when illuminated with UV-light. We used confocal microscopy to test whether Th-S can also stain these aggregates when they are inside living cells. In Fig. 2B it is shown that a significant proportion of induced bacterial cells form aggregates located at the cellular poles, which display high fluorescence, confirming thus that *in vivo* Th-S binding is aggregation dependent but protein independent and can be easily monitored using both confocal and optical microscopes. In the light of these results we decided to investigate the impact of the presence of cells containing amyloid-like aggregates on the excitation and emission spectra of Th-S. The presence of cells expressing either Aβ40 or Aβ42 peptides promotes important bathochromic effects in both the excitation and emission maximum wavelengths of Th-S, which shift from 342 and 436 nm to 375 and 455 nm in the presence of cells containing IBs (Fig. 3). In addition, a dramatic fluorescence enhancement is observed in the presence of bacterial cells expressing either of the recombinant Aβ peptides compared to non-expressing cells (Fig. 3).

The above-described spectroscopy- and microscopy-based Th-S fluorescence detection methods cannot be easily adapted for large-scale analysis. Thus, we sought to test whether FC has the potential to detect Th-S binding to IBs inside cells. FC is a powerful method allowing the analysis of complete cell populations based on the characteristics of single cells flowing through an optical and/or electronic detector. Flow cytometers are able to analyze thousands of cells per second and therefore are suitable for high-throughput analysis.[31] We compared the fluorescence properties of *E. coli* cells expressing Aβ40 and Aβ42 peptides with those of non-induced cells (containing the plasmid encoding for Aβ42) in the presence and absence of Th-S (Fig. 4). For FC fluorescence measurements an excitation wavelength of 355 nm was used and emission was collected at 530 nm to take profit of the Th-S spectral shift promoted by cells containing IBs (Fig. 3). In the absence of Th-S no differences among the three bacterial cell populations exist, all displaying almost identical dot plots and histograms, indicating essentially the absence of background fluorescence emission (Fig. 4 and Table 1); this allowed defining the threshold (P2) for gating the fluorescent cellular populations in the presence of Th-S. In the presence of the dye, induced and non-induced cells exhibit clearly different cell frequency histograms (Fig. 4). In non-induced bacteria, 5% of the cells are found in P2, whereas this value increases to 90% and 97% in cells expressing Aβ40 and Aβ42 peptides, respectively (Table 1). In addition, the mean fluorescence of non-induced cells is about 20 and 30 times lower than the signal of cells expressing Aβ40 and Aβ42 peptides, respectively.

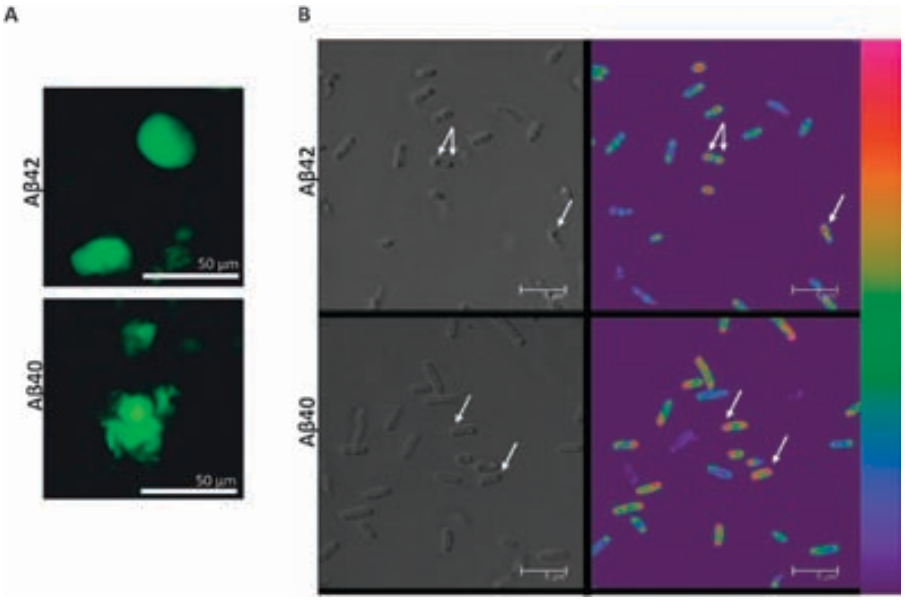

Fig. 2 Th-S staining of purified Aβ40 and Aβ42 IBs and confocal microscopy images of bacterial cells expressing Aβ40 and Aβ42 peptides. (A) Th-S fluorescence of purified Aβ40 and Aβ42 IBs under UV light. Scale bars 50 μm. (B) Left and right panels correspond to the phase-contrast and confocal laser microscopy image, respectively. Image color-code with intensity LUT (Pcolor4) in which purple was used to encode background, and blue, green and red to encode increasing Th-S fluorescence. Arrows indicate the position of IBs. Scale corresponds to 5 μm.

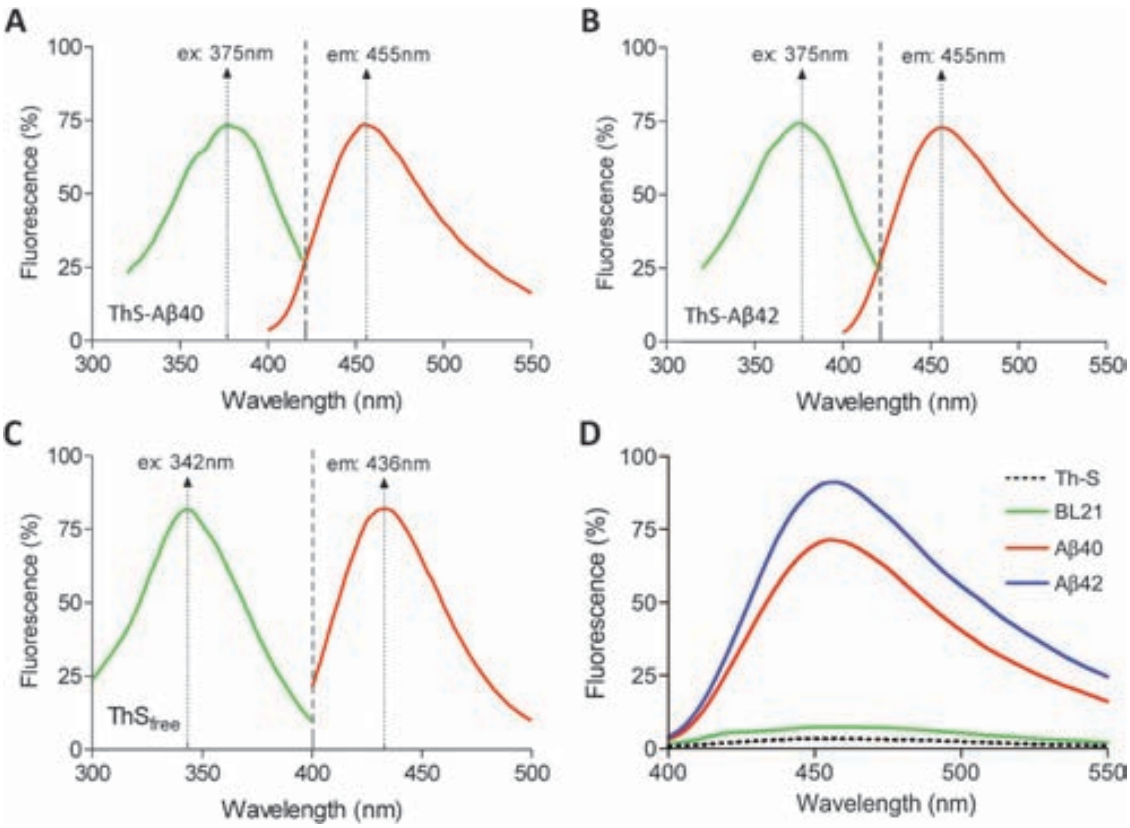

Fig. 3 Emission and excitation spectra of Th-S in the presence of bacterial cells expressing Aβ40 and Aβ42 peptides. Normalized excitation and emission Th-S fluorescence spectra: In the presence of bacterial cells expressing Aβ40 (A) and Aβ42 (B) peptides and in their absence (C). Above each graph the excitation or emission wavelength used to record the emission and excitation spectrum is indicated. (D) Emission spectra of Th-S alone and in the presence of non-induced BL21 cells or BL21 cells expressing Aβ peptides.

Importantly, the ratio between the mean fluorescence of cells expressing the more amyloidogenic Aβ42 variant and the signal of cells expressing Aβ40 coincides exactly with that observed by spectroscopy, 1.3 in both cases (Fig. 3 and Table 1).

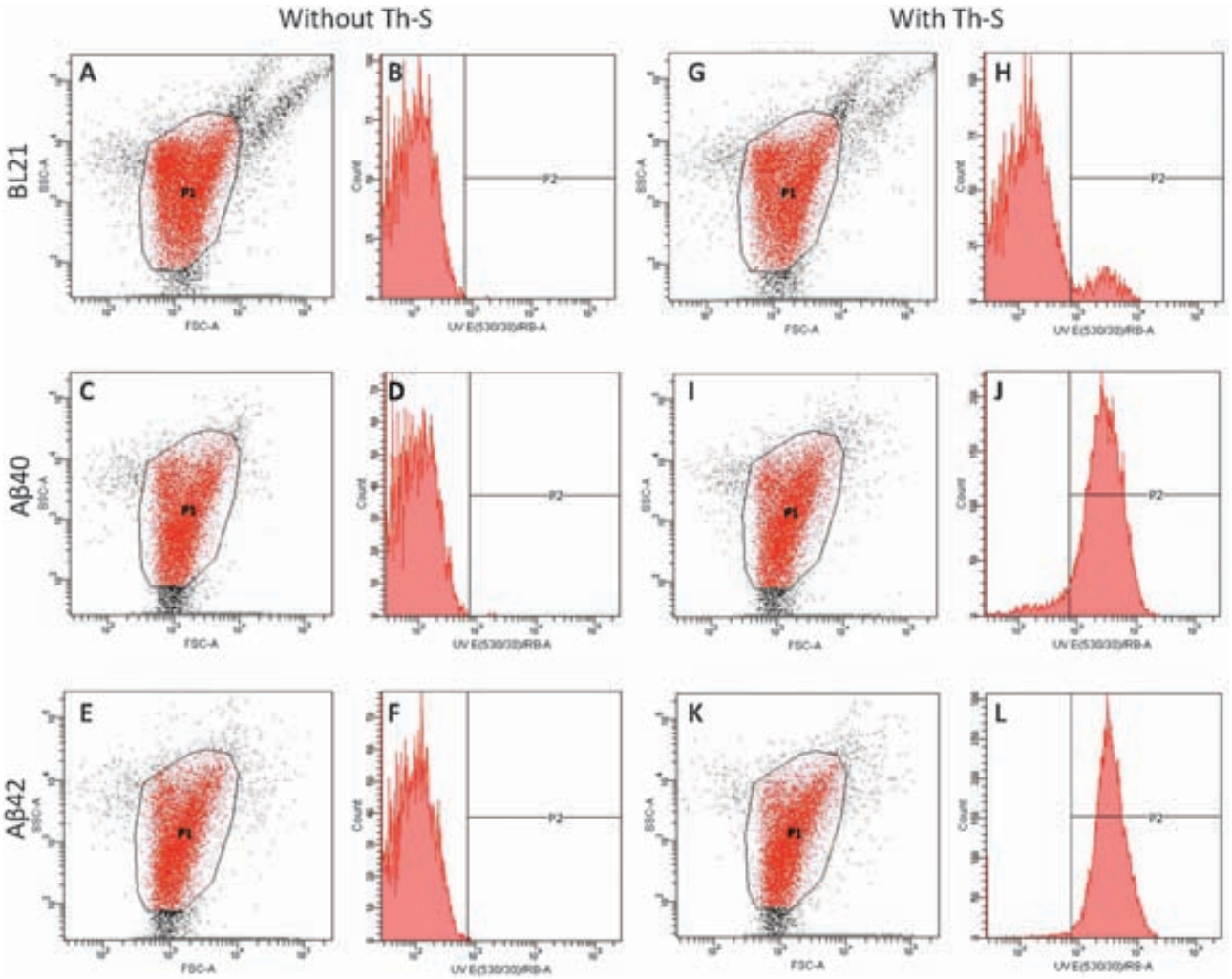

Fig. 4 Flow cytometry detection of cells expressing amyloid Aβ peptides. Left and right panels correspond to analysis in the absence and presence of Th-S, respectively. A, C, E, G, I and K correspond to forward scatter (FSC) *vs.* side scatter (SSC) dot-plots showing the P1 gate. Cells in P1 were analyzed by fluorescence emission at 530 nm upon excitation at 355 nm. Panels B, D, F, H, J and L correspond to cell frequency histograms. Non-induced BL21 cells (A, B, G and H), BL21 cells expressing Aβ40 (C, D, I and J) and BL21 cells expressing Aβ42 (E, F, K and L).

Table 1 Detection of cells containing amyloid-like IBs using Th-S and flow cytometry. The population in P2 corresponds to cells exhibiting fluorescence emission at 530 nm upon excitation at 355 nm

Sample	% Population in P2 gate	Th-S intensity mean
BL21	0	0
BL21 + Th-S	5	218
Aβ40	0	0
Aβ40 + Th-S	90	4905
Aβ42	0	0
Aβ42 + Th-S	97	6265

Overall, the data indicate that FC of Th-S stained bacterial cells provides a sensitive and selective approach to identify the formation of intracellular amyloid-like aggregates.

FC offers advantages for the analysis of biological samples over conventional single-cell measurements or approaches that rely on averaged population properties. Specifically, when compared with alternative automated technologies available for cell-based screening, like fluorescent plate reader assays, the analysis of a large number of cells in FC averages experimental variability, providing more consistent and reproducible results. In this way, the signals of cells actively expressing the recombinant protein and not expressing it, *i.e.* because they have lost the plasmid, are averaged in plate reader assays, biasing the measurements and making the assay dependent on the culture and induction conditions. In contrast, the two populations are easily distinguished using FC and can be analyzed independently. In cell-based plate reader assays, light scattering by cells in suspension might interfere significantly with fluorescence emission/detection and therefore cell concentrations have to be determined accurately and controls performed to correct the scattering effect. This problem is avoided in FC assays. Moreover, the amount of laser light that is scattered by cells is routinely measured in FC, providing data as the relative cell size when captured in line with the incident light (forward scatter), or the amount of cellular complexity when captured at a 90° angle (side scatter), and these parameters can be correlated with the fluorescent emission of individual cells. Additionally, only the fluorescence that is associated with cells is measured by FC, so that

background fluorescence in the fluid goes undetected. This FC property is important for amyloid inhibitor's screening since many active compounds have an aromatic character[32] and are intrinsically fluorescent, potentially interfering with thioflavin emission in solution. Finally, FC allows performing multiple analyses on each cell in a sample. Multiplex analysis results in a gain in productivity since recording two or more fluorescent probes in one flow assay is equivalent to performing two or more independent experiments on a plate reader. Combining Th-S detection of intracellular aggregates with simultaneous measurement of cell viability and/or metabolic cellular state in FC assays is a promising strategy to gain insight into the cytotoxic effects of amyloids (Navarro *et al.*, unpublished data).

Plate reader assays are the default election method for *in vitro* screening of amyloid inhibitors. In this line, we have shown that purified Aβ42-GFP IBs can be used to screen for inhibitors of Aβ42 aggregation in a plate-based assay by monitoring the recovery of GFP fluorescence upon unfolding.[33] This assay exploits the kinetic competition between the rates of GFP folding and of Aβ42 aggregation.[34,35] The same principle has been used to track the aggregation of GFP fusions to amyloid proteins inside living cells,[36] to identify inhibitors of intracellular amyloid formation[37] or to monitor the effect of chaperones on intracellular aggregation.[26] However, it is important to note that any factor that would impact GFP folding or aggregation rates would lead to a biased readout in these approaches, independently of the aggregation propensity of the target protein. The method presented here overcomes this problem since it monitors directly the presence of amyloid-like aggregates inside cells without the need for a protein reporter.

Conclusions

Bacteria have become model organisms to study the effect of genetic mutations on the aggregation propensities of proteins,[30,34,38,39] to screen for anti-aggregational drugs[37] to analyze the impact of the protein quality machinery on protein aggregation,[26,40] to study how protein aggregation relates to aging[41] or to understand the relationship between aggregation and the evolution of protein sequences.[42] We show here using bacterial cells as a model system that the use of the amyloid specific dye Th-S, coupled to flow cytometry provides a fast, high-throughput, quantitative and non-invasive technique to monitor the *in vivo* intracellular aggregation of unrelated amyloidogenic proteins. The method might contribute to clarify the mechanisms of *in vivo* amyloid aggregation of peptides and proteins related to conformational diseases in the simple, yet physiologically relevant intracellular prokaryotic environment.

Experimental

Chemicals and proteins

Th-S (T1892) and other chemical reagents were purchased from Sigma (St. Louis, MO). Solutions were prepared in double-distilled water purified through a Milli-Q system (Millipore, USA).

For expression of Aβ40 and Aβ42 peptides and SPC-SH3 mutants in *E. coli*, competent cells BL21 (DE3) were transformed with a pET28a vector (Novagen, Madison, WI) carrying the DNA sequences of Aβ40 and Aβ42 as inserts and with pBAT4-derived plasmid encoding SPC-SH3 mutants. Cultures were grown up at 37 °C in Luria medium (LB) to an optical density (OD_{600nm}) of 0.5. Protein expression was induced by the addition of isopropyl β-D-thiogalactopyranoside (IPTG) at a final concentration of 1 mM for 12 hours at 37 °C. Cells were centrifuged at 8000 × *g*, 4 °C, for 10 min. The cell pellet was re-suspended in phosphate buffer saline (PBS) and diluted in the same buffer at an $OD_{600\ nm}$ of 1.

IBs purification

IBs were purified from cell extracts expressing the recombinant proteins by detergent-based procedures as described.[43] Cells were centrifuged at 12 000 × *g*, 4 °C for 15 min and resuspended in lysis buffer (50 mM Tris-HCl pH 8, 1 mM EDTA, 100 mM NaCl), plus protease inhibitor PMSF and lysozyme at the final concentrations of 15 mM and 300 μg mL^{-1}, respectively. After 30 min of incubation at 37 °C under agitation, detergent NP-40 was added at 1% and the cells were incubated at 4 °C for 50 min under mild agitation. Then mixtures were treated with DNase and RNase at 15 μg mL^{-1} and $MgSO_4$ at 15 μM for 30 min at 37 °C to remove nucleic acids. Protein aggregates were collected by centrifugation at 12 000 × *g* for 15 min and washed in lysis buffer with 0.5% Triton X-100. Finally IBs were washed three times with PBS and pellets were stored at −20 °C until analysis.

Thioflavin-S steady-state fluorescence

Fluorescent spectral scans of Th-S were analyzed using a Varian spectrofluorometer (Cary Eclipse, Varian, Palo Alto, CA). For emission scans, the excitation wavelengths were 342 nm and 375 nm for free and bound Th-S, respectively, and emission range from 400 to 500 nm. For excitation scans, the emission wavelengths were 436 nm and 455 nm for free and bound Th-S, respectively, and excitation range from 300 to 400 nm. Slit widths of 5 nm were used for excitation and emission. Spectra were acquired at 1 nm intervals, 600 nm min^{-1} rate and 0.1 s averaging time.

In order to test Th-S fluorescence in the absence and presence of bacterial cell containing IBs 1 mL of bacterial culture was centrifuged at 12 000 × *g*, 4 °C for 15 min. The supernatant was discarded and the bacterial cells were re-suspended in PBS at an $OD_{600\ nm}$ of 1. Th-S and bacterial cells were mixed to obtain Th-S and bacteria concentrations in PBS of 25 μM (from a stock solution of 250 μM in Milli-Q water) and an $OD_{600\ nm}$ of 0.1, respectively. Spectra were recorded after 15 min equilibration. Excitation and emission slit widths of 5 nm were used.

Optical fluorescence microscopy

Cells and purified IBs were incubated for 1 h in the presence of 125 μM of Th-S, pelleted by centrifugation and re-suspended in PBS. 10 μL of sample was deposited on top of glass slides. Images were obtained under UV light using a filter for GFP excitation (450–500 nm) and an emission filter (515–560 nm) or using phase-contrast microscopy in a Leica fluorescence DMBR microscope (Leica Microsystems, Mannheim, Germany).

Confocal microscopy

The bacterial cells expressing the recombinant proteins were incubated for 1 h in the presence of 125 μM of Th-S, pelleted by centrifugation, re-suspended in PBS and placed in glass slides at 37 °C in the incubation chamber of a TCS-SP5 AOBS confocal laser scanning microscope (Leica Microsystems Heidelberg 575 GmbH, Mannheim, Germany). Th-S fluorescence was excited using a 488 nm argon laser and the emission was collected in a range from 515 to 540 nm. Images were digitally captured and analysed with LAS AF 579 Lite Software (Leica Microsystems CMS GmbH, Mannheim, Germany).

Flow cytometry

Flow cytometry (FC) was performed using a FacsAria SORP, flow cytometer (BD Biosciences, San Jose, CA, USA) equipped with a 355 nm-UV laser. Cells were first gated (P1) by forward scatter (FSC) and side scatter (SCC) signals. Cells in P1 were then analyzed for yellow/green Th-S fluorescence emission measured on an FL1 detector (530/30 nm band pass filter). Data analysis was performed with the FACSDiva Version 6.1.1 (BD Biosciences, San Jose, CA, USA). The final Th-S concentration was 125 μM and bacteria were diluted at an $OD_{600\ nm}$ of 0.05 in PBS.

Acknowledgements

We thank Susanna Navarro for help in the flow cytometry data analysis. This work was supported in part by grants BFU2010-14901 from Ministerio de Ciencia e Innovacion (Spain), by grant 2009-SGR 760 from AGAUR (Agencia de Gestio d'Ajuts Universitaris i de Recerca-Generalitat de Catalunya). RS is the beneficiary of a contract from the Ramón y Cajal Programme from Ministerio de Ciencia e Innovación. SV has been granted an ICREA-ACADEMIA award (Institució Catalana de Recerca I Estudis Avançats). The authors declare no conflict of interest.

References

1 X. Fernandez-Busquets, N. S. de Groot, D. Fernandez and S. Ventura, *Curr. Med. Chem.*, 2008, **15**, 1336–1349.
2 F. Chiti and C. M. Dobson, *Annu. Rev. Biochem.*, 2006, **75**, 333–366.
3 N. Carulla, G. L. Caddy, D. R. Hall, J. Zurdo, M. Gairi, M. Feliz, E. Giralt, C. V. Robinson and C. M. Dobson, *Nature*, 2005, **436**, 554–558.
4 H. LeVine 3rd., *Protein Sci.*, 1993, **2**, 404–410.
5 D. Stiller, D. Katenkamp and K. Thoss, *Acta Histochem.*, 1970, **38**, 18–30.
6 W. E. Klunk, M. L. Debnath and J. W. Pettegrew, *Neurobiol. Aging*, 1995, **16**, 541–548.
7 R. Sabate and J. Estelrich, *Biopolymers*, 2003, **72**, 455–463.
8 R. Mishra, D. Sjolander and P. Hammarstrom, *Mol. Biosyst.*, 2011, **7**, 1232–1240.
9 G. Kelenyi, *Acta Neuropathol.*, 1967, **7**, 336–348.
10 W. E. Klunk, R. F. Jacob and R. P. Mason, *Anal. Biochem.*, 1999, **266**, 66–76.
11 M. Wolman and J. J. Bubis, *Histochemie*, 1965, **4**, 351–356.
12 H. Naiki, K. Higuchi, M. Hosokawa and T. Takeda, *Anal Biochem.*, 1989, **177**, 244–249.
13 H. LeVine 3rd., *Methods Enzymol.*, 1999, **309**, 274–284.
14 R. Kayed, E. Head, J. L. Thompson, T. M. McIntire, S. C. Milton, C. W. Cotman and C. G. Glabe, *Science*, 2003, **300**, 486–489.
15 S. R. Choi, J. A. Schneider, D. A. Bennett, T. G. Beach, B. J. Bedell, S. P. Zehntner, M. J. Krautkramer, H. F. Kung, D. M. Skovronsky, F. Hefti and C. M. Clark, *Alzheimer Dis. Assoc. Disord.*, 2012, **26**, 8–16.
16 H. J. Lee and S. J. Lee, *J. Biol. Chem.*, 2002, **277**, 48976–48983.
17 D. M. Fowler, A. V. Koulov, C. Alory-Jost, M. S. Marks, W. E. Balch and J. W. Kelly, *PLoS Biol.*, 2006, **4**, e6.
18 S. Ventura and A. Villaverde, *Trends Biotechnol.*, 2006, **24**, 179–185.
19 N. S. de Groot, R. Sabate and S. Ventura, *Trends Biochem. Sci.*, 2009, **34**, 408–416.
20 M. Carrio, N. Gonzalez-Montalban, A. Vera, A. Villaverde and S. Ventura, *J. Mol. Biol.*, 2005, **347**, 1025–1037.
21 M. Morell, R. Bravo, A. Espargaro, X. Sisquella, F. X. Aviles, X. Fernandez-Busquets and S. Ventura, *Biochim. Biophys. Acta*, 2008, **1783**, 1815–1825.
22 L. Wang, S. K. Maji, M. R. Sawaya, D. Eisenberg and R. Riek, *PLoS Biol.*, 2008, **6**, e195.
23 R. Sabate, A. Espargaro, S. J. Saupe and S. Ventura, *Microb. Cell Fact.*, 2009, **8**, 56.
24 C. Wasmer, L. Benkemoun, R. Sabate, M. O. Steinmetz, B. Coulary-Salin, L. Wang, R. Riek, S. J. Saupe and B. H. Meier, *Angew. Chem., Int. Ed.*, 2009, **48**, 4858–4860.
25 M. Dasari, A. Espargaro, R. Sabate, J. M. Lopez Del Amo, U. Fink, G. Grelle, J. Bieschke, S. Ventura and B. Reif, *ChemBioChem*, 2011, **12**, 407–423.
26 A. Villar-Pique, N. S. de Groot, R. Sabate, S. P. Acebron, G. Celaya, X. Fernandez-Busquets, A. Muga and S. Ventura, *J. Mol. Biol.*, 2012, **421**, 270–281.
27 B. Urbanc, L. Cruz, R. Le, J. Sanders, K. H. Ashe, K. Duff, H. E. Stanley, M. C. Irizarry and B. T. Hyman, *Proc. Natl. Acad. Sci. U. S. A.*, 2002, **99**, 13990–13995.
28 A. Musacchio, M. Noble, R. Pauptit, R. Wierenga and M. Saraste, *Nature*, 1992, **359**, 851–855.
29 S. Ventura, M. C. Vega, E. Lacroix, I. Angrand, L. Spagnolo and L. Serrano, *Nat. Struct. Biol.*, 2002, **9**, 485–493.
30 A. Espargaro, V. Castillo, N. S. de Groot and S. Ventura, *J. Mol. Biol.*, 2008, **378**, 1116–1131.
31 M. Morell, A. Espargaro, F. X. Aviles and S. Ventura, *Nat. Protocols*, 2008, **3**, 22–33.
32 M. Levy-Sakin, M. Shreberk, Y. Daniel and E. Gazit, *Islets*, 2009, **1**, 210–215.
33 A. Villar-Pique, A. Espargaro, R. Sabate, N. S. de Groot and S. Ventura, *Microb. Cell Fact.*, 2012, **11**, 55.
34 N. S. de Groot and S. Ventura, *J. Biotechnol.*, 2006, **125**, 110–113.
35 N. S. de Groot and S. Ventura, *FEBS Lett.*, 2006, **580**, 6471–6476.
36 N. S. de Groot, F. X. Aviles, J. Vendrell and S. Ventura, *FEBS J.*, 2006, **273**, 658–668.
37 W. Kim, Y. Kim, J. Min, D. J. Kim, Y. T. Chang and M. H. Hecht, *ACS Chem. Biol.*, 2006, **1**, 461–469.
38 G. Calloni, S. Zoffoli, M. Stefani, C. M. Dobson and F. Chiti, *J. Biol. Chem.*, 2005, **280**, 10607–10613.
39 S. Mayer, S. Rudiger, H. C. Ang, A. C. Joerger and A. R. Fersht, *J. Mol. Biol.*, 2007, **372**, 268–276.
40 A. Mogk, D. Huber and B. Bukau, *Cold Spring Harbor Perspect. Biol.*, 2011, 3.
41 A. B. Lindner, R. Madden, A. Demarez, E. J. Stewart and F. Taddei, *Proc. Natl. Acad. Sci. U. S. A.*, 2008, **105**, 3076–3081.
42 N. S. de Groot and S. Ventura, *PLoS One*, 2010, **5**, e9383.
43 M. M. Carrio, R. Cubarsi and A. Villaverde, *FEBS Lett.*, 2000, **471**, 7–11.